

# **Design study of a horizontal axis tidal turbine blade**

Siddharth Suhas Kulkarni

A thesis submitted in partial fulfilment of the requirement of

Birmingham City University for the degree of

DOCTOR OF PHILOSOPHY

January 2016

Faculty of Computing, Engineering, and the Built Environment

Birmingham City University

## **DECLARATION**

I hereby declare that work done in this thesis has been entirely written by myself. No part of this thesis has been reproduced or submitted for any other degree or professional qualification at this university or any other technological institution.

The work submitted in this thesis is an original piece of work, all other results indicated in the text other than mine are clearly quoted, and the sources are always given.

Siddharth Suhas Kulkarni

To mum and dad.

कर्मण्येवाधिकारस्ते मा फलेषु कदाचन ।  
मा कर्मफलहेतुर्भूर्मा ते सङ्गोऽस्त्वकर्मणि ॥ २-४७ ॥

**“Do your duty and be detached from its outcome,**

**Do not be driven by the end product,**

**Enjoy the process of getting there.**

**(Shree Krishna, Bhagavad Gita, Chapter 2, Verse: 47)**

## ABSTRACT

Tidal current power generation offers a prospect of renewable energy which is predictable, and has lower CO<sub>2</sub> emissions than traditional energy generation sources. It also has the potential to fulfil a significant part of the energy requirements of the UK and the rest of the world.

The horizontal axis tidal turbine (HATT) acts as one of the means to convert the kinetic energy available in seawater into mechanical energy, and this research explores the hydrodynamics and the Computational Fluid Analysis (CFD) based design study of this. The first aim of this research was to develop a novel HATT blade shape through bio-mimicking a curved caudal fin shape to produce improved power coefficient. A second aim was to compare two different turbulence modelling techniques to enable the comparison of the power coefficients with the standard HATT models in tidal turbine blade literature.

There were two types of numerical approaches used: The SST model and a more complex mathematical model, LES-Smagorinsky, to perform steady state and transient CFD analysis respectively on the designed blades using ANSYS CFX. The initial default HATT was designed, parameterised, and represented as a straight blade following to the standard HATT literature. The airfoil centres of the straight blade are built around the centreline, where the centreline acts as the master, and a novel third order polynomial function was integrated on the centreline to model the Blue Marlin fish caudal fin look-alike target shape. This approach was used to model the further 3 sets of curved blade shapes in percentage wise chord lengths.

The CFD analysis of the two dimensional airfoils was conducted using ANSYS CFX, and compared against the literature. A further comparative analysis was performed with different mesh settings, and using the SST turbulence model. The comparative analysis formed an integral part of the CFD analysis to define the boundary conditions and the verification of the three dimensional CFD based HATT design study. The design strategy to move the curved blade backwards to the straight blade was also developed. The results obtained from the three dimensional comparative CFD analysis show good agreement between the two different turbulence modelling techniques used also producing an improved curved blade shape achieving the power coefficient of 0.5073% for SST simulations and 0.5178% for the LES-Smagorinsky CFD simulations. It is seen that LES-Smagorinsky CFD results produce slightly greater efficiency than the SST simulations, but the computational overhead required is massive. Finally, after comparing the improved efficiency of the bio-mimicked curved blade with the standard HATT models in the literature, it can be proved that bio-mimicking the caudal fin look-alike blade produces a higher power coefficient than the standard HATT blade.

## **ACKNOWLEDGEMENTS**

I am most grateful to my supervisor Professor Craig Chapman, for proposing this thesis topic and for his excellent support and guidance throughout my PhD. I have been very fortunate to work under his supervision, and I would like to thank him sincerely for his advice, encouragement and for his unorthodox insight.

I would like to thank my second supervisor Professor Hanifa Shah, Associate Dean (Research and Enterprise), Faculty of Computing, Engineering and the Built Environment, for her guidance, advice, and financial support for the PhD project.

I also want to thank Professor Peter Larkham for his patience and doing a thankless job of proof reading the draft versions of this doctoral thesis.

A very special thanks is due to my friends Sikander Khan, and Mani Seethapathy for the moral support, and their enthusiasm as I navigated through the PhD process.

Last but not the least, and on a personal level, I am most indebted to my mother Sangeeta, and my father Suhas, without whose support, motivation, encouragement and forbearance, I wouldn't have been able to achieve so much.

## LIST OF SYMBOLS

Symbol	Symbol name	S.I. units
$\rho$	Water density	Kg/m <sup>3</sup>
P	Power	kW
A	Cross sectional area	m <sup>2</sup>
$V_{in}$	Seawater velocity	m/s
$\lambda$	Tip Speed Ratio (TSR)	-
$\omega$	Angular velocity	rad/s
r	Rotor radius	m
$C_P$	Power coefficient	-
$\theta$	Blade pitch angle	°
c	Airfoil chord length	m
dr	Radial length of the blade section	m
$P_0$	Ambient pressure	Bar
$u_1$	Upstream pressure of fluid	Bar
$T_{thrust}$	Axial thrust force	N
a	Axial interference factor	-
$P_{Betz}$	Betz power limit	kW
$C_{PBetz}$	Betz limit power coefficient	-
L	Lift force	kN
D	Drag force	kN
Re	Reynolds number	-
$\mu$	Dynamic viscosity	kg/ms
$C_L$	Lift coefficient	-

$C_D$	Drag coefficient	-
$C_M$	Torque coefficient	-
$C_T$	Thrust coefficient	-
$p$	Static pressure	bar
T	Temperature	K
$W_{out}$	Work energy output	kilowatts/hour
$E_{tw}$	Energy loss	joule
$R_v$	The required chord length value	mm
$Ed_{val}$	The end value of target shape chord length value	mm
$St_{val}$	The starting chord length value of the initial blade	mm
$R_p$	The required chord length percentage	%
$T_{ASTN}$	The required airfoil station value	-
$T_{SXC}$	The target shape X-coordinate value	mm
$F$	Force	kN
Q	Volumetric flow rate	m <sup>3</sup> /s
t	Time	sec

# Table of Contents

LIST OF SYMBOLS .....	v
1 Introduction .....	1
1.1 The need for renewable energy.....	1
1.2 Advantages and disadvantages of tidal energy .....	1
1.3 Tidal energy physics and its applications.....	2
1.4 Tidal energy resources in the UK .....	7
1.5 Types of tidal turbines .....	8
1.6 Aims and objectives .....	13
1.7 Structure of the thesis .....	14
2 Seawater Environment, Hydrodynamics of Horizontal Axis Tidal Turbines, and Bio-mimicry .....	16
2.1 Introduction .....	16
2.2 The Seawater Environment.....	16
2.2.1 Introduction .....	16
2.2.2 Maximum theoretical power generation from moving water.....	17
2.2.3 Tidal energy assessment in the <i>Marine Energy Atlas</i> in the UK .....	19
2.2.4 Properties of seawater required for CFD analysis .....	20
2.2.5 Tidal flow analysis methods .....	23
2.2.6 Numerical tidal characteristics and site selection .....	25
2.3 Hydrodynamics of horizontal axis tidal turbines .....	29
2.3.1 Introduction .....	29
2.3.2 Blade Element Momentum theory .....	29
2.3.3 Airfoils and Non-dimensional forces of tidal turbines .....	31
2.4 Sensitivity analysis of tidal turbine blades.....	36
2.5 Bio-mimicry: Using Nature as a model to generate an efficient tidal turbine blade.....	46
2.5.1 Introduction .....	46
2.5.2 Bio-mimicry examples.....	46
2.5.3 Work input vs Work output .....	49
2.5.4 Marine vertebrates synopsis and their locomotion characteristics .....	50
2.5.5 Justification of the fish selection .....	56
2.6 Chapter summary.....	59
3 Application of Computational Fluid Dynamics in tidal energy.....	60
3.1 Introduction .....	60

3.2	Principle CFD theories.....	60
3.3	Turbulence modelling in CFD.....	62
3.3.1	Turbulent and Laminar Flow.....	62
3.3.2	Numerical description of turbulence.....	64
3.3.3	The Reynolds-Averaged-Navier-Stokes (RANS) equations.....	65
3.4	Turbulence models.....	66
3.4.1	Introduction.....	66
3.4.2	The Boussinesq approximation.....	67
3.4.3	Prandtl's mixing length models.....	67
3.4.4	The turbulent kinetic energy governing equations.....	68
3.4.5	Standard k- $\epsilon$ model.....	68
3.4.6	Wilcox's k- $\omega$ model.....	69
3.4.7	Shear Stress Transport (SST) model.....	69
3.4.8	Large eddy simulation (LES).....	70
3.4.9	Flow modelling near the turbulence wall.....	72
3.5	Discretisation in CFD.....	73
3.5.1	Finite Element Method (FEM).....	73
3.5.2	Finite Difference Method (FDM).....	74
3.5.3	Finite Volume Method (FVM).....	74
3.5.4	Transient term.....	75
3.5.5	Convection term.....	76
3.5.6	Pressure-Velocity coupling.....	76
3.6	Errors and uncertainty in CFD.....	77
3.6.1	Differentiating errors and uncertainties.....	77
3.6.2	Physical Modelling errors.....	78
3.6.3	Verification and Validation.....	79
3.7	Application of CFD in turbine blade design.....	80
3.7.1	CFD in the tidal energy conversion.....	80
3.7.2	CFD based design studies in tidal energy.....	86
3.8	Chapter summary.....	90
4	Design and Analysis of tidal turbine blades.....	91
4.1	Introduction.....	91
4.2	Direct design method.....	91
4.3	Designing the default tidal turbine blade.....	93

4.3.1	Introduction .....	93
4.3.2	Three dimensional default tidal turbine blade modelling based on literature.....	93
4.4	CFD simulations setup.....	101
4.4.1	Introduction .....	101
4.4.2	2D CFD study of NACA 0018 airfoil .....	101
4.4.3	Design of the computational domain .....	104
4.5	Strategy to move the default straight blade to the curved caudal fin shaped blade .....	106
4.5.1	Mesh Independency study and boundary conditions .....	106
4.6	Design strategy and sensitivity analysis.....	109
4.6.1	Saving the results of the curved blade.....	111
4.7	Comparison of the CFD results .....	111
4.7.1	Power, lift coefficient comparisons .....	111
4.8	Chapter summary.....	112
5	CFD analysis of airfoils .....	113
5.1	Introduction .....	113
5.2	The NACA 0018 airfoil .....	113
5.3	Geometry specification.....	114
5.4	Grid generation .....	115
5.5	Boundary conditions, turbulence model, mesh convergence study .....	117
5.6	Comparison of the steady state simulations .....	118
5.7	Two domain grid design and verification of the O-C grid .....	123
5.8	Chapter summary.....	126
6	CFD based design studies of tidal turbines .....	127
6.1	Introduction .....	127
6.2	Design of the default straight blade .....	127
6.3	Classification of the sensitivity analysis variables.....	128
6.4	Boundary conditions, turbulence models, and seawater properties .....	128
6.5	Design of the curved caudal fin blades .....	130
6.5.1	Moving the centreline in percentage chord lengths and constant blade radius.....	131
6.5.2	Strategy to move the curved blade shape backwards to straight blade shape.....	133
6.6	Mesh independency study.....	135
6.6.1	Turbulence model comparison study .....	137
6.7	Steady State CFD analysis using Shear Stress Transport model .....	139
6.8	Transient CFD analysis using the LES-Smagorinsky model .....	146

6.9	Comparison of the forces on the straight blade and curved blades.....	153
6.10	Chapter summary.....	157
7	Conclusions .....	159
7.1	Thesis Contributions .....	159
7.2	Overall thesis conclusions.....	160
7.3	Future work suggestions.....	162
7.3.1	Development of a decision support methodology for optimisation through KBE-CFD closed loop system.....	163
7.3.2	CFD simulations for cavitation analysis.....	163
7.3.3	Structural analysis for designed tidal turbine blades.....	163
7.3.4	Manufacturing of the designed horizontal axis tidal turbine blades.....	164
Appendix A: GB Patent Application: GB1421623.8.....		165
Appendix B: Matlab programs .....		185
References .....		191

## Table of Figures

Figure 1 Gravitational and Centrifugal effects of the moon on tides (Rourke et al., 2010) .....	3
Figure 2 Generation of the neap and spring tides (James <i>et al.</i> , 2010).....	4
Figure 3 The La Rance tidal barrage system in France (Sheth & Shahidehpour, 2005).....	5
Figure 4 the Annapolis tidal barrage system (The Canadian Encyclopaedia, 2013) .....	6
Figure 5 Sketch of the Kislaya Bay tidal barrage system (Chaîneux & Charlier, 2008) .....	6
Figure 6 Mean Spring tide current velocities and specific regions of tidal sites (BERR Marine Atlas, 2008) .....	7
Figure 7 Seaflow turbine system by MCT (MCT, 2009).....	9
Figure 8 SeaGen turbine system (MCT, 2008) .....	9
Figure 9 Evopod tidal turbine system (Ocean Flow Energy Ltd, 2008) .....	10
Figure 10 Lunar Energy tidal turbine system and lunar energy farm (Lunar Energy Ltd, 2008).....	10
Figure 11.1 Swept blade concept (after Larwood & Zuteck, 2006), Figure 11.2 Manufactured STAR blades for flight testing (Ashwill <i>et al.</i> , 2010) .....	11
Figure 12 the Flygt banana blade propeller (Flygtus, 2011) .....	12
Figure 13 A100 three bladed and five bladed curved plate rotors (Nishizawa <i>et al.</i> 2013) .....	12
Figure 14 various efficiency limits of water turbines (after Vu & Retieb, 2002) .....	18
Figure 15 Theoretical Power Coefficient (after Robinson & Byrne, 2008) .....	19
Figure 16 Sea surface temperature across the globe (OSPO, NOAA; 2013) .....	22
Figure 17 Different lunar cycles (Kvale <i>et al.</i> , 1994) .....	24
Figure 18 the tidal current velocities in mean spring tide for the Pentland Firth, Scotland area (Shields <i>et al.</i> , 2009).....	26
Figure 19 Conceptual diagram of various turbines installed in a tidal channel and velocities interacting around a single turbine (Vennell, 2013).....	27
Figure 20 Effects of the mean neap tide on the energy flux (Bryden & Couch 2006) .....	28
Figure 21 Generated Bathymetry for the Pentland Firth using the ADCP (Baston & Harris 2011) .....	28
Figure 22 Illustration of the blade sections (after Manwell <i>et al.</i> , 2002) .....	29
Figure 23 Flow velocity in a control volume according to actuator disc theory (after Stoddard & Eggleston, 1985).....	30
Figure 24 Airfoil characteristics (Bavanish & Thyagarajan, 2013) .....	32
Figure 25 Different families of symmetric and non-symmetric NACA profiles (Mohamed, 2012) .....	33
Figure 26 Hydrodynamic forces acting on the airfoil.....	34
Figure 27 Pressure inclination effects on the surface of airfoil (Singh <i>et al.</i> , 2012) .....	35
Figure 28 Maximum velocity vs angle of attack simulated over different lengths of NACA 0018 sections (Mehmood <i>et al.</i> , 2012) .....	38
Figure 29.1 Comparison of lift and Figure 29.2 drag coefficients for trend line NACA 0012 (red), 0015 (black), 0018 (green) foils (Hameed & Afaq, 2013) .....	39
Figure 30 Turbulent stress components around NACA0018 airfoil for angle of attack = 6° (Kim <i>et al.</i> , 2006) .....	40
Figure 31 Fluid flow visualisation and velocity streamlines around NACA0018 foil (after Kim & Lee, 2013) .....	41
Figure 32 Relationship of Tip speed ratio and Power coefficient and validation of BEM-CFD model (Rossetti & Pavesi, 2013) .....	41
Figure 33 Hydrodynamic performance comparison (Yang & Shu, 2012) .....	42

Figure 34.1 Velocity vectors ( $Cl = 1.72$ , $\alpha = 30^\circ$ , $Re = 3000$ ); Figure 34.2 Velocity vectors ( $Cl = 1.20$ , $\alpha = 53^\circ$ , $Re = 3000$ ) (Murthy <i>et al.</i> , 2000) .....	43
Figure 35.1 Humpback whale pectoral flippers (Fish <i>et al.</i> 2011), and Figure 35.2 Manufactured adapted tubercles on the leading edge on WhalePower wind turbine blade (WhalePower, 2014)....	47
Figure 36.1 seven blade conventional propeller (Felice <i>et al.</i> , 2009), and Figure 36.2 the Faux Fish fish tailfin propeller (US Patent 6895108; 2004) .....	49
Figure 37 SHARC Vehicle (Watts <i>et al.</i> , 2006).....	49
Figure 38 The Blue Marlin Fish with its fins representing its propulsion movements (after King Sailfish Mounts, 2014).....	52
Figure 39 the locomotion forces acting on the fish whilst swimming (Sfakiotakis <i>et al.</i> , 1999) .....	53
Figure 40 the evolution of the pectoral (A), and dorsal (B) fins in different species (Jayne <i>et al.</i> , 1996) .....	54
Figure 41 Different swimming modes of fishes (Sagong <i>et al.</i> , 2013) .....	55
Figure 42 Biologically inspired application within various industries.....	58
Figure 43 Laminar and Turbulent flow (Reynolds, 1883).....	63
Figure 44 Wall turbulence in a pipe (Lathrop, 2006) .....	64
Figure 45 Free turbulence in a jet (Buhler <i>et al.</i> , 2010).....	64
Figure 46 A 2D control volume with mesh elements.....	75
Figure 47 Graphical overview of the CFD process used in this research .....	92
Figure 48 Description of the blade parameters like Total blade height, blade radius, root chord, and the distance from hub circle to root airfoil.....	94
Figure 49 Blade span airfoil distribution.....	95
Figure 50 NACA airfoils twisted about the central axis in blade.....	96
Figure 51 Defining the NACA airfoil stations along the entire length of the blade .....	97
Figure 52 Lofted surface blade profiles .....	100
Figure 53 Mesh block cutting scheme (Mehmood <i>et al.</i> , 2012) .....	102
Figure 54 Mesh created for NACA 0018 1m 0 degree of angle of attack .....	103
Figure 55 schematic of the boundary conditions (Mehmood <i>et al.</i> , 2012) .....	103
Figure 56 boundary conditions defined using named selections in CFX .....	104
Figure 57 Inlet, outlet and height extension from the tidal turbine blades .....	105
Figure 58 Rotating turbine domain around blades using unstructured mesh.....	105
Figure 59 3D plot of the curved caudal fin blade reproduced by MATLAB program.....	107
Figure 60 the y equation graph which constructs the third order polynomial.....	109
Figure 61 chord length variation of the straight blade to achieve the curved blade .....	110
Figure 62 NACA 0018 geometry specification replicating Mehmood <i>et al.</i> (2012) geometry.....	114
Figure 63 NACA 0018 0.5m and angle of attack zero degree dimensions.....	115
Figure 64 Block cutting mesh view .....	116
Figure 65 Velocity streamline of NACA 0018 0.5m and AOA $15^\circ$ (Mehmood <i>et al.</i> , 2012) .....	119
Figure 66 Velocity streamline for NACA 0018 chord length 500mm and angle of attack 15 degrees	119
Figure 67 Velocity streamline for NACA 0018 length 1000mm and AOA $16^\circ$ (Mehmood <i>et al.</i> , 2012) .....	120
Figure 68 Velocity streamline for NACA 0018 chord length 1000mm and angle of attack 16 degrees .....	120
Figure 69 Comparison of the maximum velocity values at different angles of attack .....	121
Figure 70 Comparison of the drag values at different angles of attacks .....	122

Figure 71 Boundary spacing for inlet and outlet walls .....	124
Figure 72 Velocity vectors around the NACA 0018 airfoil .....	125
Figure 73 Blade Spinal axis variation.....	134
Figure 74 the power coefficients of all the investigated meshes in mesh independency study.....	136
Figure 75 Torque coefficient versus Tip speed ratio for k- $\epsilon$ and SST model medium meshes.....	137
Figure 76 Power coefficient versus Tip speed ratio for k- $\epsilon$ and SST model medium meshes .....	138
Figure 77 a) Meshed SB with blades and hub, b) SB meshed tip, c) Meshed CB 75% with blades and hub, d) CB 75% meshed tip.....	139
Figure 78 Blade pressure distributions (pressure side) on a) SB, b) CB 25 %, c) CB 50%, d) CB 75%, and e) CB 100% .....	141
Figure 79 SST mid-height lift coefficient distribution for five blade designs.....	143
Figure 80 SST model lift coefficient distribution for 5 designed blades .....	144
Figure 81 Steady state blade rotational velocity, streamlines for a) SB, b) CB 25 %, c) CB 50%, d) CB 75%, and e) CB 100% .....	145
Figure 82 CB 75% LES-Smagorinsky convergence monitoring with respect to the defined convergence criteria.....	148
Figure 83 Lift coefficient history convergence monitoring for the CB 75% transient solution. ....	149
Figure 84 Transient blade pressure distributions (pressure side) on a) SB, b) CB 25 %, c) CB 50%, d) CB 75%, and e) CB 100% .....	150
Figure 85 LES – Smagorinsky mid-height lift coefficient distribution for five blade designs.....	151
Figure 86 LES-Smagorinsky model lift coefficient distribution for the 5 designed blades .....	152
Figure 87 Transient blade rotational velocity, streamlines for a) SB, b) CB 25 %, c) CB 50%, d) CB 75%, and e) CB 100% .....	153
Figure 88 Lift coefficient versus angle of attack for SST and LES CFD simulations, at inlet velocity 2.5m/s.....	154
Figure 89 SST - power versus seawater velocities for the designed five blades.....	155
Figure 90 Power coefficient versus output power for the designed five blades.....	156

## Table of Tables

Table 1 Comparison of Pressure and Depth of seawater (UNESCO, 1983) .....	20
Table 2 Summary of the sources for NACA-4 digit foils.....	37
Table 3 Seawater environment and blade sensitivity variables derived from the literature .....	45
Table 4 Summary of the SST and LES simulations from the literature with the data analysed.....	82
Table 5 Summary of the CFD based design techniques used in the literature with the data analysed .....	87
Table 6 Three dimensional blade parameters .....	94
Table 7 Default blade parameters .....	97
Table 8 NACA Airfoil stations with the R values (worked at the 10% rule) .....	98
Table 9 Twist angle values for each NACA airfoil station.....	99
Table 10 Complete blade parameters .....	100
Table 11 default values for defining the curved blade shape.....	108
Table 12 Block edge parameters.....	116
Table 13 Reynolds number and advection time differences for case studies performed.....	118
Table 14 Available data set for validation.....	118
Table 15 Percentage based chord length values in four stages.....	132
Table 16 Mesh size, CFD simulation time, and estimated $C_p$ for SST model at $\lambda = 5$ .....	135
Table 17 Mesh size, CFD simulation time, and estimated $C_p$ for k- $\epsilon$ model at $\lambda = 5$ .....	135
Table 18 Mesh Parameters for all the designed blades (SST).....	140
Table 19 Mesh parameters for the designed blades (LES-Smagorinsky).....	147

# 1 Introduction

## 1.1 The need for renewable energy

Currently, the global energy requirements are met by consumption of the fossil fuels. As the heavy dependence on fossil fuel increases it is becoming a major concern and countries worldwide have now realised the need to incorporate renewable energy sources in their energy policies as an alternative to the fossil fuels (Shields *et al.*, 2011). With an increasing demand for energy, much of world's energy requirements are met through the heavy consumption of fossil fuels (Yuksel & Kaygusuz, 2011). The energy generated from fossil fuels has adverse effects on the environment causing greenhouse emissions and global warming with the potential for an environmental disaster (Stern, 2007). Fossil fuels are very limited with their potential and with the current percentage of fuel consumption, these resources would deplete in coming decades. Thus realising the change in energy policy, renewable energy technologies have become a favourable alternative to traditional energy sources.

As the search for alternative sources continues, renewable energy is the most desired one. Renewable energy plays a significant role to reduce the consumption of fossil fuels. Solar power, tidal energy, geothermal energy, and wind power are the primary sources of sustainable energy (Yuksel, 2008). In 2009, the European Union announced that “by 2020 at least 20% of the energy consumption of European union should be provided by renewable resources as well as mandating a reduction in greenhouse gas emissions of at least 20% from 1990” (Nagy & Kormendi, 2012). Tidal energy has advantages over wind energy, mainly because it is predictable and due to sea water being denser than wind, the available energy can be up to 835 times greater than wind power (Bryden *et al.*, 2007). Tidal energy is a renewable electricity source based on the conversion of kinetic energy of moving water into mechanical power to drive generators. It has fewer CO<sub>2</sub> emissions and it has minimal reliance on fossil fuels.

## 1.2 Advantages and disadvantages of tidal energy

Energy conversion from the tidal currents is similar to wind energy conversion, but tidal currents have a slight advantage over wind energy; tidal current speeds are lower than wind speeds and this is important because the power contained in flowing water currents is proportional to the cube of its velocity. The two main advantages of tidal energy are mentioned below:

- a) **Reliability and Predictability:** Tides are the results of the gravitation movements of the moon. “As 71% of the earth’s surface is covered by water, energy can be harnessed on a large scale through tides” (Blunden & Bahaj, 2007). Tides are predictable, which is also the greatest advantage that tidal energy has over other renewable sources like wind or solar power.
- b) **Renewable Energy:** Power generation from tides is clean; it has minimal reliance on the fossil fuels and has fewer CO<sub>2</sub> emissions. It does not emit any greenhouse gas or does not pollute the environment.

Tidal energy has disadvantages a number of which are highlighted below:

- a) **Installation costs:** The installation costs are very high as compared to traditional power plants using coal and gas. The transportation of the power generated is also very expensive. There are few locations where tidal turbines could be placed to produce electricity, which makes it localised to coastal regions.
- b) **Possible environmental damage:** The tidal turbine blade operation may lead to fish mortality. This can also lead to disruption in the migration pattern of the fish.
- c) **Economic costs:** The start-up costs are very expensive, but the maintenance low. This means that the profit will not be seen for some years. Thus it makes tidal energy generation is in its infancy.

### 1.3 Tidal energy physics and its applications

Tides are the results of rotational movements within the gravitational and centrifugal forces of the sun and the moon. Two high and two low tides pass through a point on equator, approximately because the moon rotates through the centre of the earth-moon system during this time; this cycle is never ending hence, tidal energy is a renewable energy. The gravitational and centrifugal effects of the moon on tides are shown in Figure 1.

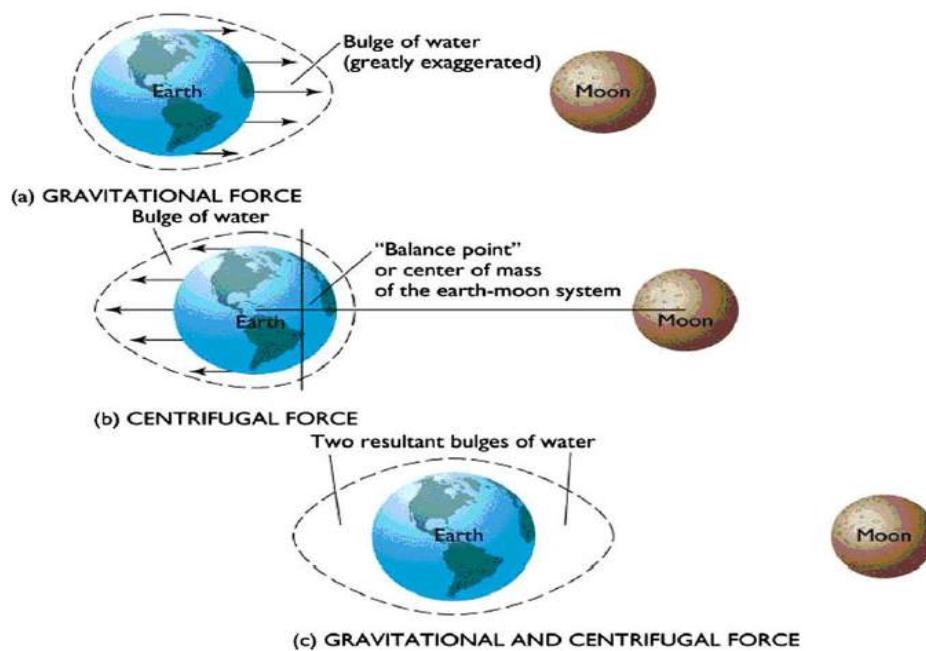


**Figure 1 Gravitational and Centrifugal effects of the moon on tides (Rourke et al., 2010)**

The fundamental lunar patterns in seawater energy are defined as follows (Herzfeld & Andrewartha, 2010)

- **Lunar day:** The time for a cycle of two high and two low tides is 24 hours and 50 minutes per tidal day, known as a lunar day in seawater energy context.
- **Synodic or Lunar cycle:** The period from full moon to full moon is 29.53 days, known as Synodic or Lunar month.
- **Diurnal tides:** One high and one low tide per tidal day. The time period is 24 hours and 50 minutes.
- **Semi diurnal tides:** Two equal high tides and two equal low tides per tidal day. The time period is 12 hours and 25 minutes.
- **Spring tides:** At the full moon, the moon is in between sun and earth, during this period, sun's gravitational field is in the same direction as the moons. At this time, the high tides are higher and low tides are lower known as Spring tides (Bahaj *et al.*, 2007). Spring tides are larger because tide generating forces of sun and moon is combined together.

- **Neap tides:** During the first or last quarter of the moon, the sun's gravitational forces are perpendicular. There is a partial cancellation of the tide generating forces resulting in lower high tides and higher low tides known as Neap tides (James *et al.*, 2010). Generation of the neap tides and spring tides is demonstrated in Figure 2.

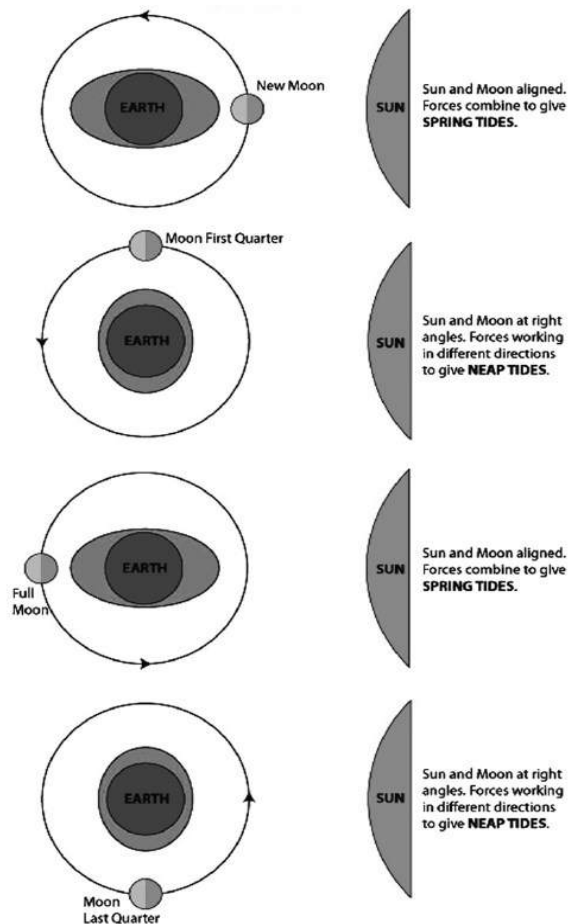


**Figure 2 Generation of the neap and spring tides (James *et al.*, 2010)**

As the energy generated from tides is renewable, tides are very predictable with as much as 98% accuracy (Ben Elghali, 2007). "The use of tidal energy is not a new idea" (Fraenkel, 1999). Traditionally, there are two methods of harnessing electricity from tides – a) Tidal barrages across estuaries b) more recently by using high fidelity tidal current turbine designs. Tidal barrages are massive and very expensive in terms of cost and building. Tidal barrages are built across bays and estuaries which have tidal range (water head) of 5m and up to 12m (Sutherland *et al.*, 2007). Tidal barrages share the same working principles as hydropower electricity generation (Clark, 2007). Tide water is stopped using sluice gates, as the water begins to fall a head of water gets created between the two sides of tidal barrage. Then water falls on the turbines at low heads to generate electricity.

According to Charlier (2003) currently, only four tidal barrages are functional; a) La Rance, France, b) Annapolis, Bay of Fundy, Canada, c) Jangxia creek, east china sea, d) Kislaya Guba, Russia.

- a) **La Rance, France:** This largest operating tidal barrage system in world is at the La Rance, Brittany. It has power generation capacity of 240 MW. “This barrage is 720 m long which encloses a surface area of 22 km<sup>2</sup>; this barrage contains 24 reversible 10 MW bulb turbines operating with a tidal head of 5 m” (Etemadi *et al.*, 2011). The La Rance, tidal barrage system produces approximately power output of 480 GW h per year. The La Rance tidal barrage system is shown in Figure 3.



**Figure 3 The La Rance tidal barrage system in France (Sheth & Shahidehpour, 2005)**

- b) **Annapolis tidal barrage system, Bay of Fundy, Canada:** It has a capacity of generating power of 20 MW, and is linked to the national grid. This tidal generation facility was built in between 1980 and 1984 (Nova Scotia Power, 2013). It has a tidal head of 16 m and produces 30 GW h of power per year. The Annapolis tidal barrage system is demonstrated in Figure 4.



**Figure 4 the Annapolis tidal barrage system (The Canadian Encyclopaedia, 2013)**

- c) **The Kislaya Bay tidal barrage system, Russia:** This tidal barrage system is located on the Kislaya Bay in the Russian Atlantic (Karasev *et al.*, 1996). This power plant is 40m wide and 3 – 5m deep and the water velocity is up to 4m/s; the water depth is 35m, it produces 400kW of power which makes it the smallest tidal barrage system in the world. The Kislaya bay tidal barrage system is illustrated in Figure 5.

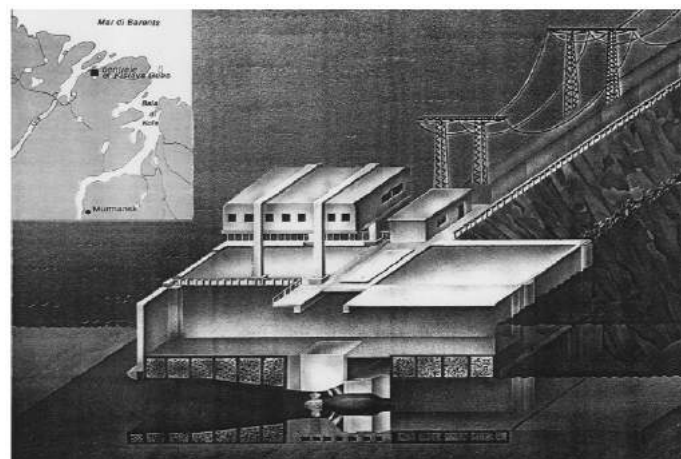


**Figure 5 Sketch of the Kislaya Bay tidal barrage system (Chaineux & Charlier, 2008)**

- d) **Jangxia Creek tidal barrage system, China:** This tidal barrage system is located at the East China Sea. It was constructed in 1960's (Tang & Skraatz, 2011). It has power generation capacity of 500kW.

## 1.4 Tidal energy resources in the UK

There are major efforts put in by the UK government to meet the 2020 target of having 15% renewable energy which would reduce 34% of the CO<sub>2</sub> emissions (UK Hydrographic office, 2013). In order to achieve these targets major investment is necessary, given the UK's large tidal energy resource. Due to the geographical advantage of the UK, it is a world leader in terms of tidal energy potential resources, which could provide power up to 50 TWh/annum. Black & Veatch (2005) identified the largest tidal energy sites in the UK where places like the Pentland Firth and Orkney Islands have tidal current velocities (Spring tides) up to 4.5 m/s (BERR Marine Atlas, 2008). Figure 6 shows the spring tide currents and their velocities.

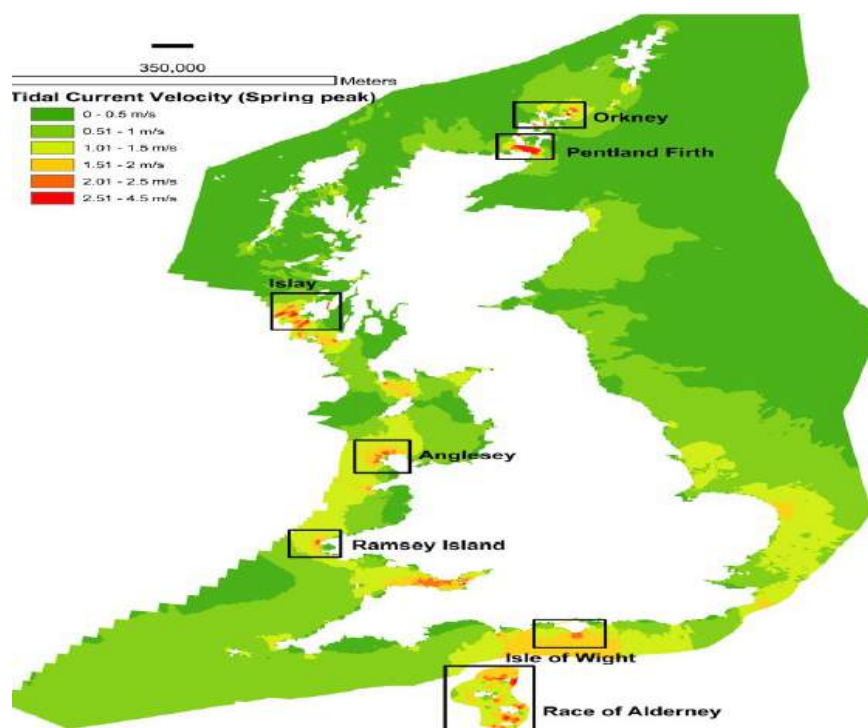


**Figure 6 Mean Spring tide current velocities and specific regions of tidal sites (BERR Marine Atlas, 2008)**

Iyer *et al.* (2013) suggest that the tidal energy sites would potentially produce 35 TWh/year of power through tidal turbines/devices per year. The Pentland Firth alone has the installation capacity of 4532 MW of power output with complete power output potential being 9.7 GWh/year (Iyer *et al.*, 2013). There is no doubt, that if this technology is developed to its full potential it would help the UK Government in achieving its 2020 renewable energy targets and would not compromise the energy demand for the future.

## 1.5 Types of tidal turbines

There are two types of tidal turbines: 1) Horizontal axis tidal turbines (HATT) and 2) Vertical axis tidal turbines (VATT), of which HATT's are the most efficient ones. The working principles of tidal turbines are similar to wind turbines, but sea water is nearly 835 times denser than wind (Cai *et al.* 2011). As the tidal turbines are submerged the working conditions are different from the wind energy environment, tidal turbines experience more forces and pressure than wind turbines. Due to these reasons tidal turbines can have smaller blades and rotate slower than but can still capture same amount of the kinetic energy to produce power. Flow under seawater cannot be unidirectional like wind; it can be bidirectional. Tidal turbines are capable of reversing their blades to suit the flow from any direction; it can be done by reversing the blades and by having a pitch of 180° to generate electricity on both flood tide and ebb tide. A sample of HATT applications including the curved HATT are discussed below.

- 1) Horizontal axis tidal turbines (HATT): Horizontal axis tidal turbines (HATT) are also known as axial flow turbines, they have rotational axis parallel to the tidal flow; thus makes them operate in only one flow direction. The principle operation of the HATT's is similar to the Horizontal axis wind turbine (HAWT), it has blades fitted to the hub, a generator to convert kinetic energy from the water to mechanical energy, and shaft to produce power and gearbox. HATT's are designed to operate in both the flow directions hence they can be fixed pitch or variable pitched.
  - i) The Marine Current Turbine (MCT), UK: The largest developer of full scale horizontal axis tidal turbines in the UK is MCT (Ben Elghali, 2007). MCT have developed two technologies which are explained below:-
    - a) *Seaflow*: Seaflow turbine system has an 11 m diameter turbine with power output of 300 kW. It has a complete span pitch control to face flow from any direction (MCT, 2008). It is installed at Foreland Point in North Devon, UK. Its significant feature is that it is not connected to grid but is installed on a tubular pile and the entire turbine can be raised up for maintenance (MCT, 2008). Fraenkel (2007) presented a graph of power available in shaft versus the speed of the tidal current which shows that the power coefficient for horizontal axis turbines is ideally in between 0.37 to 0.45. Figure 7 demonstrates the Seaflow turbine system.

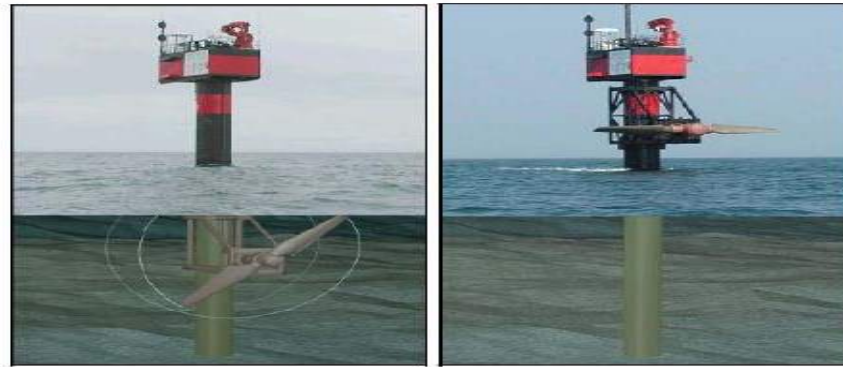


**Figure 7 Seaflow turbine system by MCT (MCT, 2009)**

b) *SeaGen*: *SeaGen* turbine system was a second development by MCT. It has two rotor blades 16 m each with power generation capacity of 600 kW. This gives the whole turbine system ability to produce power up to 1.2 MW. The turbine blades are pitch controlled so they can be operated in both ebb and flood tides. Figure 8 demonstrates the *SeaGen* turbine system.



**Figure 8 SeaGen turbine system (MCT, 2008)**

2) Evopod Tidal Turbine system, UK: This tidal turbine generation system was built by Ocean Flow Energy Ltd, UK. This turbine system has five blades and is a floating turbine, which allows it to maintain its optimal head in the seawater (Ocean Flow Energy Ltd, 2008). Figure 9 demonstrates artistic impression of the Evopod tidal turbine system.

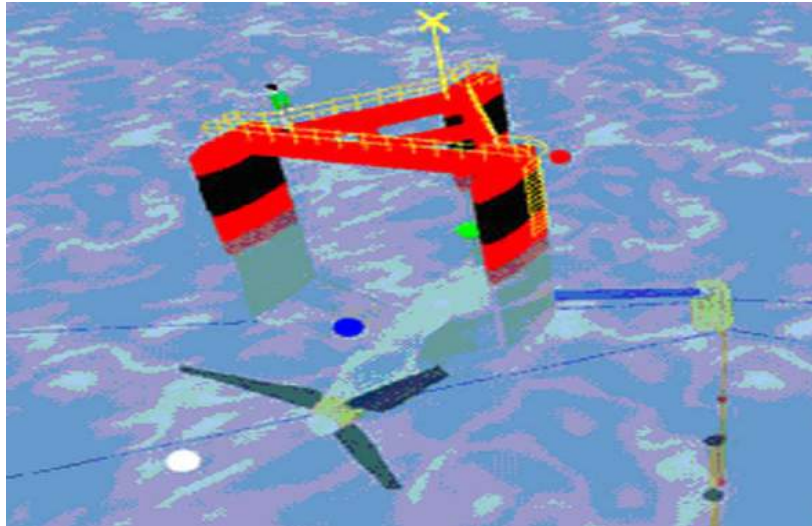


**Figure 9 Evopod tidal turbine system (Ocean Flow Energy Ltd, 2008)**

- 3) Lunar energy tidal turbine project, UK: This tidal turbine system was built by Lunar Energy Ltd, UK. These turbines ducted to seawater floor with a gravitational foundation. This system is a 1 MW bi-directional turbine, with 11.5 m diameter. As this turbine system has ducts, it is designed to produce maximum energy from the water flow (Lunar Energy Ltd, 2008). Figure 10 demonstrates an artistic illustration of the Lunar Energy tidal turbine system and a Lunar Energy farm.

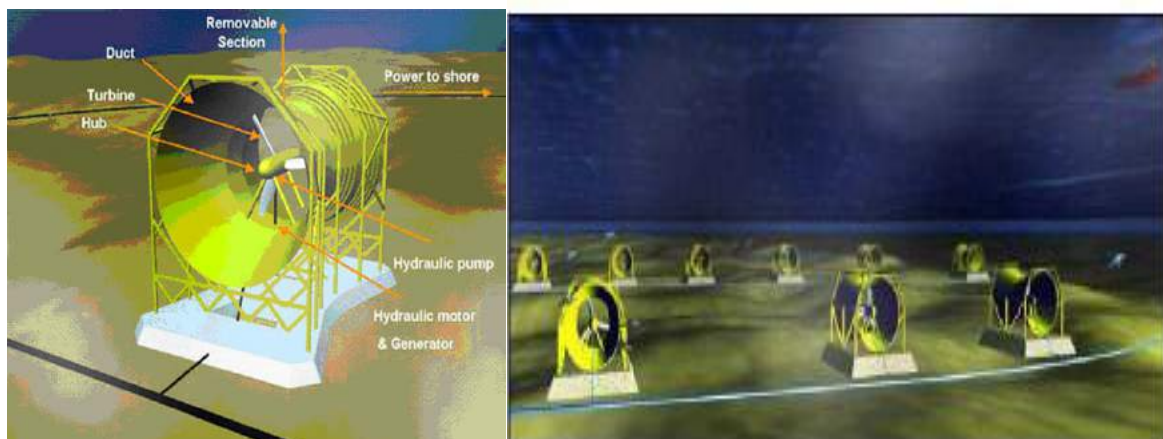


**Figure 10 Lunar Energy tidal turbine system and lunar energy farm (Lunar Energy Ltd, 2008)**

- 4) Swept Twist Adaptive Rotor (STAR) Blade: Sandia National Laboratories (SNL) partnering with Knight and Carver (K&C) modelled a horizontal axis wind turbine called the Swept Twist Adaptive Rotor (STAR) blade aiming to improve annual power production from low wind velocity sites (Ashwill *et al.*, 2010). The entire STAR project was funded by the US Energy Department's 'Wind and Water Program' to promote energy generation from wind from lower wind velocity areas. The STAR blade was inspired from a 'high lift generating bird feather' allowing the geometric sweep for longer blade fatigue life (Larwood & Zuteck, 2006). After conducting the parametric design of the STAR blade, an aero elastic analysis was conducted in order to fabricate the modelled blade. The operating loads and the power output were calculated using 'full flight tests' achieving their primary goal of improving the annual power output by 10 to 12%. The design variables used for the optimisation process were planform, airfoil thickness, sweep magnitude, airfoil and blade structural geometry, root airfoil forward sweep angle, and load reduction at the root airfoil station. Figure 11.1 shows the swept blade artistic concept from the 'high lift generating bird feather', and Figure 11.2 shows the manufactured STAR blade for flight testing.

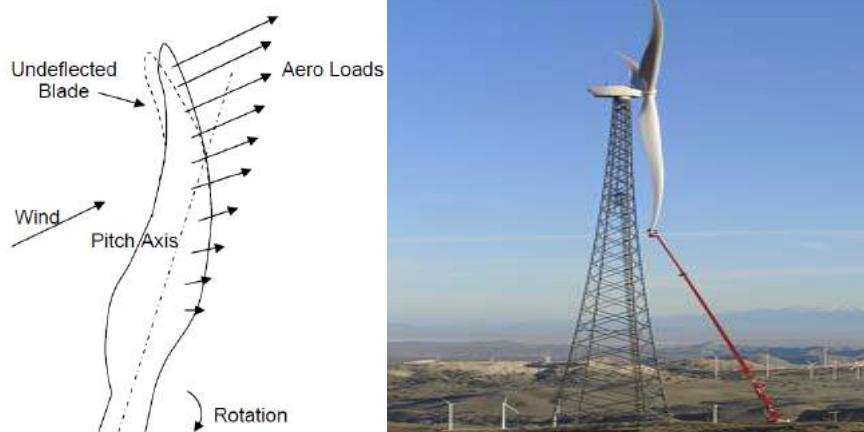


**Figure 11.1 Swept blade concept (after Larwood & Zuteck, 2006), Figure 11.2 Manufactured STAR blades for flight testing (Ashwill *et al.*, 2010)**

- 5) Flygt, USA: A propeller system, for small scale turbulence and clog free operations inspired from "a banana" was built by Flygt, USA. The energy saving propeller has been used for clog-free operations in debris-laden sewage mixing areas and claimed to be potentially operative in rivers as hydrokinetic turbines, but further research needs to be done as to how practical it can be to use these as hydrokinetic turbines (Anyi and Kirke, 2010). These swept back banana blade propellers (Figure 12) are designed to maximise the amount of thrust, and thus maximising the energy production.



**Figure 12 the Flygt banana blade propeller (Flygtus, 2011)**

- 6) Curved-plate bladed rotor: Nishizawa *et al.* (2013) proposed three and five bladed curved plate rotors (Figure 13) for power generation from wind. Both types of rotor blades were made from aluminium plate, and a Betz type manometer was used in the wind tunnel tests to measure the wind speed and the power coefficients of both the rotors measuring around 0.35. The authors claimed that curved bladed rotors would have a huge potential to generate electricity from wind in developing countries, and at the time be inspirational as educational materials.



**Figure 13 A100 three bladed and five bladed curved plate rotors (Nishizawa *et al.* 2013)**

## 1.6 Aims and objectives

The overall aim of this research is to develop a novel HATT blade shape through bio-mimicking a curved caudal fin shape to produce improved power coefficient from this research, using CFD based design studies. Such an aim requires further description, and decomposition, which is discussed in the following sections. Finally, the power coefficient of the highest power coefficient obtained curved caudal fin blade is to be compared with the standard HATT models available in the tidal turbine literature.

With the numerical model developed the author aims to develop better understanding of CFD based design study and realise the limitations of numerical simulation for this application. Hence the objectives are follows:

- 1) To conduct a literature review of current knowledge on the seawater environment, hydrodynamic design of tidal turbine blades, and CFD.
- 2) To critically review the design variables and their sensitivities in tidal turbine systems using CFD based design study.
- 3) To verify and compare the two dimensional NACA airfoil simulation against the literature, and perform comparative analysis for the three dimensional turbine CFD simulations.
- 4) To develop a novel horizontal axis tidal turbine blade shape using bio-mimicry to produce improved blade efficiency.

In order to simulate the designed turbine blades and find an improved blade efficiency, it was necessary to understand the seawater environment characteristics, as it is the most important concept to understand before designing a tidal turbine blade. For a chosen tidal site, the seawater flow velocity acts a function to define the inlet boundary conditions for CFD simulations; and determines the power potential from the chosen site. After understanding the seawater environment characteristics, a comprehensive literature review was carried out on the hydrodynamic design of tidal turbine blades, which also involves their working principles, mathematical modelling and identifying the most important design variables of HATT and their sensitivities that affect the power coefficient of the designed HATT.

A second aim was to compare two different turbulence modelling techniques to enable the comparison of the power coefficients. To achieve the main aim and the second aim a brief literature

review on bio-mimicry was carried out on the propulsion characteristics of marine vertebrates, justification of the fish selection, also including previous applications using this inspiration.

ANSYS CFX was used to set up the two dimensional and three dimensional CFD simulations, this means that the turbulence modelling set up presented through this thesis would be used as an industry standard for simulating the HATT's by using CFD. To mesh and set up the CFD simulations for steady state and transient CFD simulations completely the theory involved in the turbulence modelling in CFD was explained. To access the quality of the mathematical solutions presented by this research it was necessary to understand the CFD verification process, and the errors in CFD modelling were also explored. A mesh independency study was carried out to investigate the effects of the mesh resolution on the CFD results on the Straight Blade, using the standard k- $\epsilon$  model and SST turbulence model. The Straight blade was examined at coarse, medium, and fine mesh resolutions under two turbulence models thus creating six different meshes. Verification was done for all the steady state and transient CFD simulations performed in this research, also identifying the most important CFD based design study sensitivities in HATT's.

Although a number of authors have already presented results from CFD simulations of horizontal axis tidal turbine blade, either for tidal current or wind energy applications, this research aims to develop a novel blade shape using bio-mimicry for design and analysis of the tidal turbine rotors. This is done firstly, by designing an initial tidal turbine rotor based on the literature (which is called as Straight Blade or SB in this research), and secondly applying bio-mimicry to develop and test the curved caudal fin shape blade to improve the tidal turbine efficiency. The first task is divided into three stages: design, analysis, and verification (comparison) of the default horizontal axis tidal turbine blade system. Once the initial tidal turbine is simulated, a central line polynomial function is introduced at the root airfoil of the initial blade passing through all the airfoil stations to model the curved shape blade making sure the total blade height stays constant for all the designed blades. The second task is also divided into three stages: design, analysis, and verification of the curved shaped blade (Blue Marlin caudal fin look-alike), and thus performing a comparative analysis study for both the designed blades.

### **1.7 Structure of the thesis**

This PhD research is presented in seven chapters:

In Chapter 1, the need for renewable energy, background information on tidal energy has been presented like types of tidal turbines their advantages and disadvantages. The tidal current resources available in the UK, and finally the aims and objectives of this research are explained.

Chapter 2, discusses the literature review conducted in areas that influence this thesis; seawater environment, the hydrodynamic design of tidal turbines (with specifically focusing on HATT's), and background on bio-mimicry are demonstrated along with the fish selection justification and other applications inspired from bio-mimicry are also highlighted.

Chapter 3, examines the background theory on Computational Fluid Dynamics and on the other design studies of the tidal turbine blades. A brief review on the basic governing equations of the fluid dynamics, different turbulence modelling techniques, and finally a summary of different CFD based design study techniques used in the design of tidal turbine blade technology.

Chapter 4 mainly focuses on the design and analysis of a 2D and 3D CFD tidal turbine blades, for simulation and verification of the CFD based design strategy for this PhD thesis. The two dimensional mathematical model of the turbine blade is built and compared against the literature. The numerical simulation presented in this chapter is only intended to build an insight into the actual CFD simulation and the design of a novel tidal turbine blade shape using bio-mimicry.

In Chapter 5, a two dimensional CFD analysis of the NACA 0018 airfoil is presented which forms a starting point in designing the default three dimensional horizontal axis tidal turbine, and compares the turbulence model used along with the steady state simulations. The 2D CFD simulations are verified against the literature at a constant water velocity.

In Chapter 6, three dimensional modelling of default horizontal axis tidal turbine blade is presented, and initial CFD analysis consisting of a mesh independency study, steady state, and transient simulations using turbulence models SST, and LES respectively are performed. After simulating the default straight tidal turbine blade, the curved caudal fin blade is designed using the percentage wise chord length method, whilst keeping constant total blade height and the number of airfoil stations. Finally, a comparison of the blade performance is highlighted for power, lift coefficients, and thus allowing the comparison of power coefficient with the tidal turbine blade literature.

In Chapter 7, the original contributions made through this thesis, thesis conclusions and future work suggestions are demonstrated.

## **2 Seawater Environment, Hydrodynamics of Horizontal Axis Tidal Turbines, and Bio-mimicry**

### **2.1 Introduction**

This chapter examines the background knowledge on seawater environment and hydrodynamics of horizontal axis tidal turbines. A literature review on the seawater environment is conducted in order to achieve the aim of defining inlet boundary conditions for CFD simulations of the tidal turbine blade. Other concepts which include power potential from sea water, its properties, and site selection are based on the available sources of data are highlighted. A second literature reviews the hydrodynamic design of horizontal axis tidal turbine blades, involving their working principles, concepts involved on airfoil sections, and mathematical modelling of tidal turbines is also presented. The most important sensitivities related to the seawater environment, and design of the horizontal axis tidal turbine blades includes non-dimensional parameters drag coefficient, lift coefficient, torque, and power coefficient are explicitly discussed. Finally, a brief literature review on bio-mimicry is presented covering its application areas the synopsis of the marine vertebrate and their propulsion characteristics are also discussed.

### **2.2 The Seawater Environment**

#### **2.2.1 Introduction**

Tides are the results of the rotational movements within the gravitational and centrifugal forces of the sun and the moon. In this section, mathematical aspects of power generation are described, then a marine atlas section from where the inlet conditions boundary conditions required for CFD simulations are obtained. Properties of seawater which include density, viscosity, temperature, and thus salinity can be modelled from temperature and viscosity values are discussed as they have a significant effect on the CFD analysis of turbine blades. Further, tidal flow analysis techniques are explained. Other hydrodynamic modelling aspects: climate modelling, environmental and sediment transport are not discussed here, because of the limitations of the scope of the project. Various assumptions have been considered to simplify the computation and to implement boundary conditions for CFD analysis. Finally, a brief introduction to numerical modelling of tidal flows and the selection of site used in this research is discussed.

### 2.2.2 Maximum theoretical power generation from moving water

The available power in a flow of water can be calculated as the kinetic energy per unit time passing through the cross sectional area of the rotor. Therefore the available power for a tidal turbine can be calculated by using Equation 1 and the derivation follows (Mycek et al., 2013):

Assuming constant linear acceleration,

$$v^2 = u^2 + 2ax$$

$$v^2 = 2v \cdot \frac{dv}{dx} \cdot x$$

$$\therefore \frac{dv}{dx} = \frac{v^2}{2x}$$

And,

$$P = F \cdot V$$

$$= M \cdot \frac{dv}{dt} \cdot V$$

$$= M \cdot \frac{dv}{dx} \cdot V^2$$

$$= \rho V \cdot \frac{1}{2} \cdot \frac{v^2}{x} \cdot V^2$$

$$\mathbf{P = \frac{1}{2} \rho AV^3}$$

**Eqn. 1**

where P is available power (W),  $\rho$  is water density ( $\text{Kg/m}^3$ ), A is the cross sectional area perpendicular to water ( $\text{m}^2$ ), V is water velocity (m/s).

Tidal turbines and wind turbines share the same working principle. Although all the kinetic energy is available for power production, Betz's law states that the maximum efficiency of a turbine is 59.3%, which is discussed further in the section 2.2.6.2 (Betz, 1966). Keck & Sick (2008) suggest that, to allow variable speed operation; the mechanical rotor speed and the frequency of the electric supply grid must be decoupled. When the water velocity increases to levels above the flow water velocity, the power generated cannot be increased further, because this will lead to overloading of the generator. Therefore, the hydrodynamic efficiency of the tidal rotor must be reduced, in order to limit the power extracted from water to the maximum power of the tidal turbine. Vu & Retieb (2002) showed efficiencies of various tidal turbines in Figure 14.

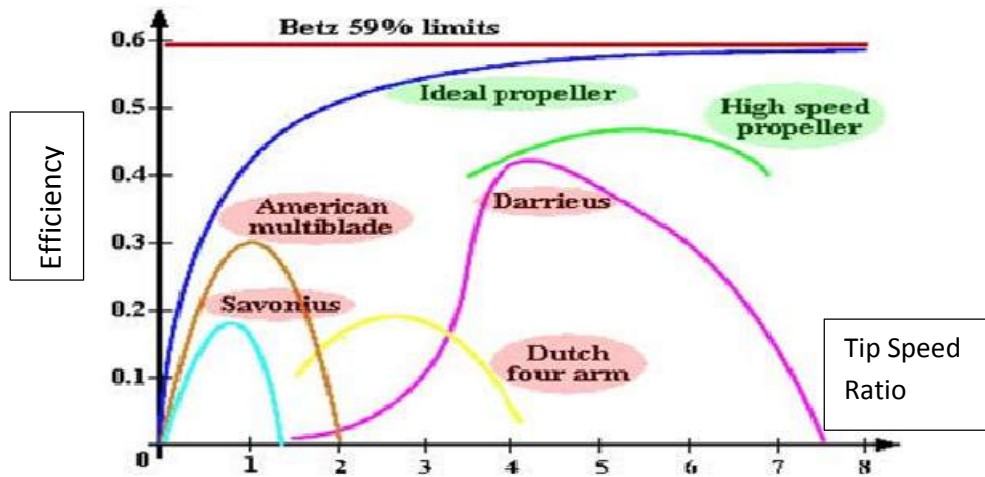


Figure 14 various efficiency limits of water turbines (after Vu & Retieb, 2002)

The relationship between fluid flow velocity and the angular velocity of the turbine blade is known as Tip Speed Ratio. “Tidal turbines must be designed to operate at an optimal water tip speed ratio in order to extract as much as power as possible” (Jahromi *et al.*, 2011). Therefore the tip speed ratio can be defined as;

$$\lambda = \frac{\text{velocity of the rotor tip}}{\text{water flow velocity}} = \frac{v}{V} = \frac{\omega r}{V} \quad \text{Eqn. 2}$$

where  $V$  is water velocity (m/s),  $v$  is rotor tip velocity (m/s),  $r$  is the rotor radius (m),  $\omega = 2\pi f$  is angular velocity (rad/s) and  $f$  is frequency of rotation (Hz).

The power coefficient indicates the percentage of power available in the water that is converted into mechanical power. Robinson & Byrne (2008) stated that the power coefficient of a tidal turbine was calculated based on available power in the fluid, with respect to the change in momentum of the sea water and the power output. Figure 15 shows the average power coefficients for various ranges of tip speed ratios.

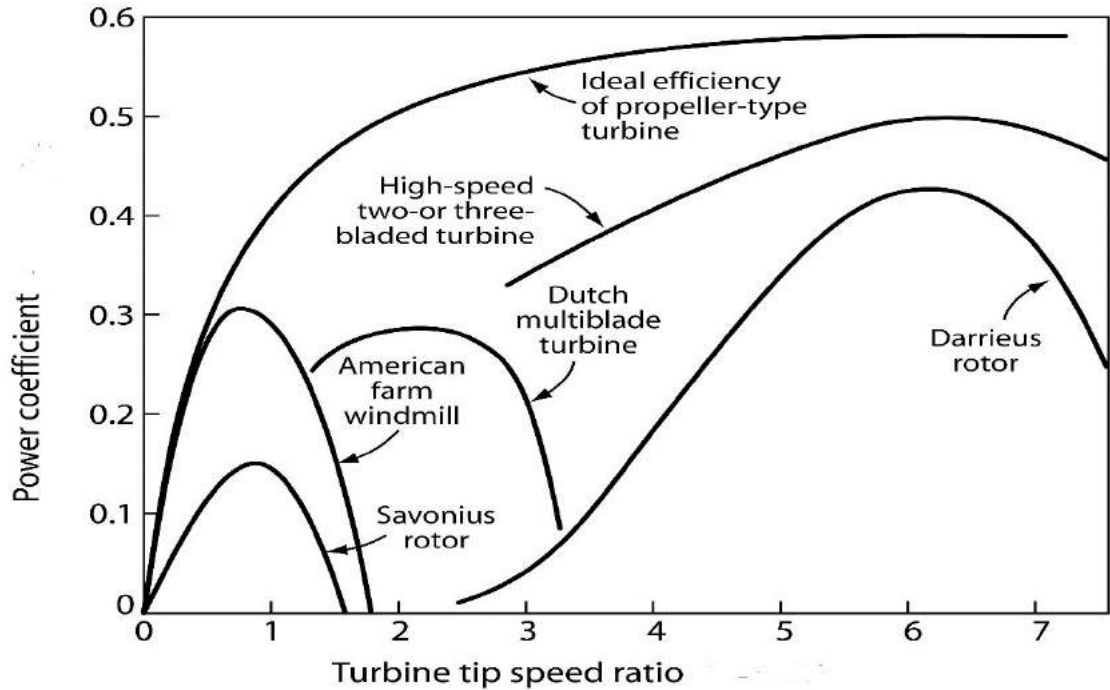


Figure 15 Theoretical Power Coefficient (after Robinson & Byrne, 2008)

Incorporating the power coefficient into Equation 1 leads to Equation 3;

$$P = \frac{\rho}{2} C_p(\lambda, \theta) A V^3 \quad \text{Eqn. 3}$$

where, P is available power output (W),  $\rho$  is water density (Kg/m<sup>3</sup>),  $C_p$  is power coefficient (unitless),  $\lambda$  is the tip speed ratio,  $\theta$  = the blade pitch angle (°), A is the cross sectional area (m<sup>2</sup>) and V is Velocity of water (m/s).

### 2.2.3 Tidal energy assessment in the *Marine Energy Atlas* in the UK

The UK Department of Trade and Industry in 2008 published an assessment of the waves and tide current marine energy resources for the UK coast. The average tidal power density (energy flux), is measured by the Waverider™ which is a buoy installed by the Institute of Oceanography, UK. The *Marine Renewable Atlas* used Geographical Information Services (GIS) technology to assess the tidal wave height, tidal wave direction and also the total period (Cooper *et al.*, 2006). According to Bryden & Couch (2006) in some sites the water velocity changes every day even on the same point and in the same tide cycle. The main reason for producing this atlas was to provide an insight into the tidal current resources surrounding the UK, for the government to use and make decisions on the

renewable energy policy. The *Marine Renewable Atlas* also provides additional properties like significant wave height, wave energy period, and the annual calculations for the velocity input data. Although modern technology was used to map the marine energy resources in the UK, due to the total grid size; highly constrained energy and rotary flows issues were not solved for specific sites provided.

#### 2.2.4 Properties of seawater required for CFD analysis

Seawater water is incompressible, with the surface pressure of  $10^4$  Pa. While performing the CFD analysis on tidal turbines water pressure, water density, water temperature and salinity play important roles in defining the inlet boundary conditions. Each property is discussed briefly below:

- a) **Water pressure:** “Pressure can be defined as force per unit area exerted by fluid” (or seawater pressure in this project). Atmospheric pressure is usually measured in bars, but seawater water pressure is measured in ‘dbars’. When tides hit the turbine blades the force due to pressure of tides creates a pressure difference between tides and turbine blades which is called as high pressure to low pressure. Lynchnos *et al.* (2010) suggest that in oceans the upward gradient force of pressure is maintained by the gravitational downward force, hence pressure in the seawater increases as the depth increases. This is also known as hydrostatic balance of pressure. Seawater pressure is generally measured by using a transducer. Seawater temperature, and density are related by the gas law; hence accurate measurements of pressure would be enough to define a good CFD analysis of turbine blades. UNESCO (1983) presented a comparison of pressure and depth at standard oceanographic depths.

**Table 1 Comparison of Pressure and Depth of seawater (UNESCO, 1983)**

Pressure (dbar)	Depth (m)	Difference (%)
0	0	0
100	99	1
200	198	1
300	297	1
500	495	1
1000	990	1
1500	1453	1.1
2000	1975	1.3
3000	2956	1.5
4000	3932	1.7
5000	4904	1.9
6000	5872	2.1

## 2. Seawater Environment, Hydrodynamics of Horizontal Axis Tidal Turbines, and Bio-mimicry

- b) **Water temperature:** “Temperature is a numerical (thermodynamic) property of fluid (sea water, in this case), due to the energy behaviour in the molecules in the fluid” (Behrendt *et al.*, 2011). In the Oceanography context, temperature (T) is measured in Degree Celsius (°C), although heat transfer in the flow of water is measured in Kelvin (K). The temperatures in the seawater typically range from -1.7°C (Antarctic region) to the maximum of 30°C (Indian Ocean); they are dependent on the salinity of the water (Robinson *et al.*, 2011). Figure 16 shows the sea surface temperatures across the globe for 5<sup>th</sup> October 2013.

## 2. Seawater Environment, Hydrodynamics of Horizontal Axis Tidal Turbines, and Bio-mimicry

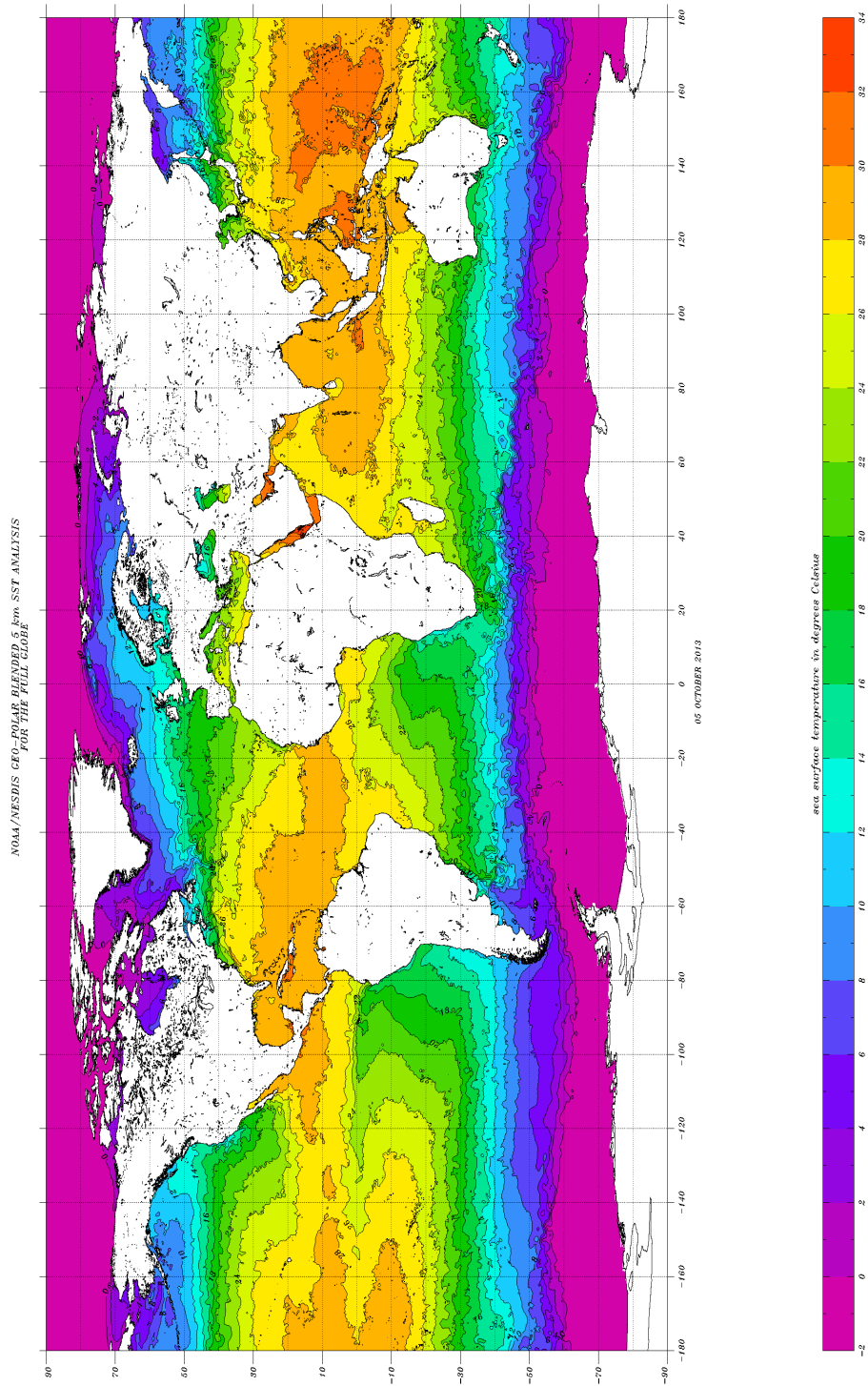


Figure 16 Sea surface temperature across the globe (OSPO, NOAA; 2013)

## 2. Seawater Environment, Hydrodynamics of Horizontal Axis Tidal Turbines, and Bio-mimicry

- c) **Water density:** The density of seawater is the most important property while performing the CFD analysis of tidal turbines, as it defines the depth of seawater at which tidal turbines can reach equilibrium. Seawater density is denoted by  $\rho$  and its unit is  $\text{kg/m}^3$ . The density for pure water (having no salt content) is  $1000 \text{ kg/m}^3$  at  $0^\circ\text{C}$ . Generally, sea water density is taken as  $1025 \text{ kg/m}^3$ , in CFD analysis. The density varies effectively when the flow is close to being isentropic.

### 2.2.5 Tidal flow analysis methods

Tides are produced by the gravitational interactions of the sun and moon which act on the ocean. Elevations of tides only occur when there is rise in oscillating forces produced by oceanic tides on the shallower continental shelf. It is assumed that tidal stream processes should have same analytical properties, hence in order to provide a good tidal flow analysis for a location; traditionally harmonic analysis of tides has been preferred especially for the ups and downs of the tides in “shallow water” areas (Arns *et al.*, 2013). The tidal waves are not directly influenced by gravitational/astronomical effects between sun and moon along the coastal and shallow water areas. The positions of the sun, the moon and the earth are not circular but elliptical due to this reason they all are inclined to each other and result in different lunar periods and cycles. The principal lunar periodicities and lunar forces for the sun-moon-earth system are discussed below:

- a) **Smaller periodic lunar cycles:** In the oceanographic context, when the orbital plane of the moon is inclined with the earth’s equatorial plane it results in tidal force generation and the moon is in the elliptical orbit of the sun-moon-earth system. At this time, the moon has maximum declination and the variations of the declinations during this period of time is called as a tropical month which has the same rotation as earth and the length is 27.32 days. The period of time from new moon to new moon, is called as the synodic month and the length of that month is 29.53 days.
- b) **Longer periodic lunar cycles:** When the earth revolves around the sun in an elliptical orbit, the length of time with respect to earth’s rotation is 365.2422 days. When the moon’s orbit intersects the earth it has an angle of  $5.15^\circ$  to the lunar plane of sun’s elliptic path. At this period of time, the moon’s orbit rotates slowly in that plane, the length of this period is 18.61 years which is also known as “the lunar node revolution”. The last concept of the longer periodic cycle known as “The Perihelion cycle”, at this period of time the earth’s orbit faces the effects from the earth’s revolution around the sun which is very slow at this period

## 2. Seawater Environment, Hydrodynamics of Horizontal Axis Tidal Turbines, and Bio-mimicry

of time and the length is 20940 years. The sun has similar periodic cycles. Figure 17 shows different lunar cycles.

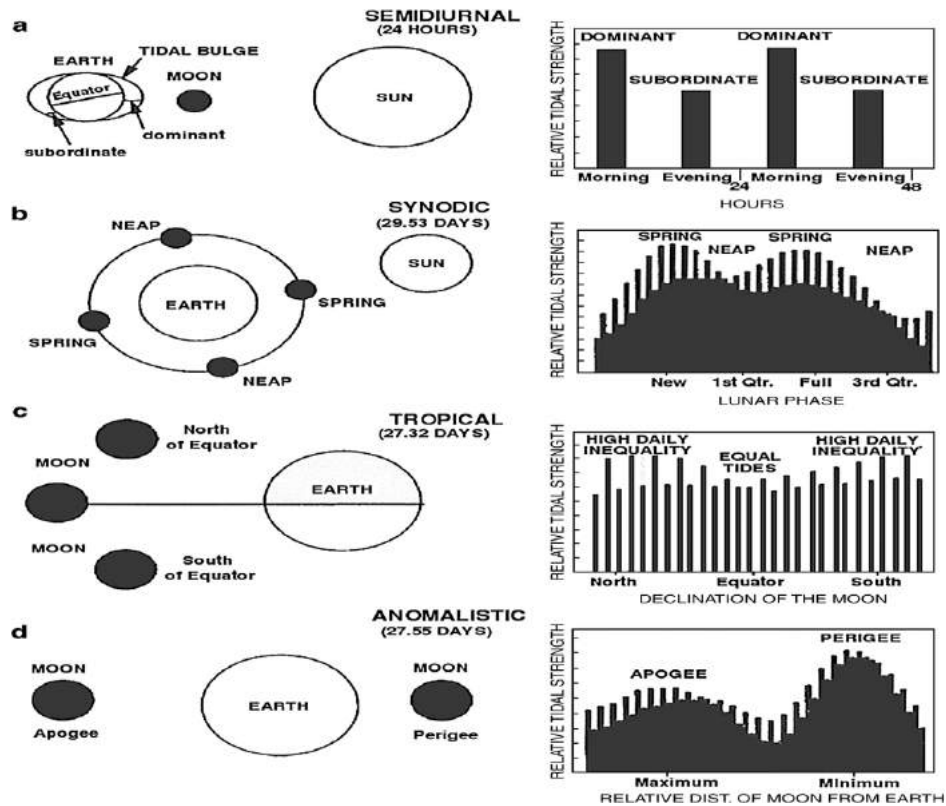


Figure 17 Different lunar cycles (Kvale *et al.*, 1994)

### 2.2.5.1 Harmonic analysis of tides

Leffler & Jay (2009) reported the need for analysis and understanding of the tidal behaviour because of the dynamic nature of coastal and estuary waters. They also reported that taking measurements for a longer period of tidal behaviour with appropriate accuracy is required for the prediction of tides. Traditionally, the astronomical effects on tides have been analysed by using harmonic analysis method (Cherniawsky *et al.*, 2010). While analysing the tides local bathymetry and the topology of the location are very important to the forces acting on the tidal constituents. A harmonic analysis of tides allows measuring of the periods, amplitudes, frequencies, and different phases of a tide at a particular location, by mapping a curve called “Nyquist frequency”.

### 2.2.5.2 *Response analysis of tides*

The response analysis of the tides is more precise than the traditional harmonic analysis of tides and has greater accuracy with analysing fewer tidal constituents. The mathematical formulation of the response method was done by Groves & Reynolds (1975), treating the seawater as an equilibrium system with tides as the input and tide flow velocity as the output.

Despite the response method being more accurate and precise than the harmonic analysis method for tides, it can also operate in shallow waters with low gravitational effects; the harmonic analysis remains the preferred method for analysing the tides because of its ease in computer analysis and simple conceptual understanding.

### 2.2.6 **Numerical tidal characteristics and site selection**

The work in this section considers the site selection of a suitable site for the purpose of this research, and the numerical modelling of the tidal characteristics such as inlet velocities, annual power potential from the tidal site chosen, depths and other parameters related to the CFD analysis are discussed in this section. Bryden & Couch (2006) state that selection of site is not an easy process, and the chosen site should have large tidal current producing capacity in order to generate electricity. Site selection and the power (energy) generation assessment is a tedious process and involves the following steps, which apply for the each individual site:

**Step 1** Site selection for placing turbine generators is the most important and vital step. This is the main concern as the mean cube flow of the water velocity is proportional to the turbine efficiency which affects the power output so a suitable depth at which turbine will be installed must be considered.

**Step 2** The size and the dimensions of the power generating turbine are important parameters to be considered because the turbine interaction effects on the ocean bed can maximise or minimise the power output.

**Step 3** Considering the design parameters above, optimising a rotor for maximum hydrodynamic efficiency does not necessarily create a turbine with the highest annual energy production. So a revision considering the changes of the design parameters might be essential to maximise the power output to match the local flow conditions of the site selected.

**Step 4** Lastly, Vennell (2011) suggested that width and depth of the chosen site can only estimate the power potential approximately and a tidal turbine operating at its full capacity at one location can lead to reduction in power generation capacity at another location. Robinson and Byrne (2008) suggested a methodology for performing numerical simulations on the tidal turbines but in their studies assumed generic blade profiles incorporated into different configurations for the use of a particular site. Thus the variations in velocities result a change of boundary conditions for the CFD analysis.

### 2.2.6.1 *Pentland Firth, Scotland (UK)*

In UK, the Pentland Firth is an area which meets all the above generic criteria for a site selection. It connects to the North Atlantic and lying in the South of Orkney Islands (Scotland, UK). The Pentland Firth is known for experiencing spring tide current velocities up to 7 m/s with power generation capacity approximately of 1GW over the year. “The Pentland Firth is around 23km long and varies in depth from 60m to 100m along its main axis. Its width varies considerably, with 7.5km being taken as representative of the width of the region of high flow along the Firth. Maximum flows can exceed 4.5m/s in some locations within the Firth at spring tides” (Vennell, 2013). Although a tidal site might experience higher tidal current velocities, the velocities are not continuously high; they vary throughout the year. Figure 18 shows the tidal current velocities in mean spring tide for the Pentland Firth, Scotland area.

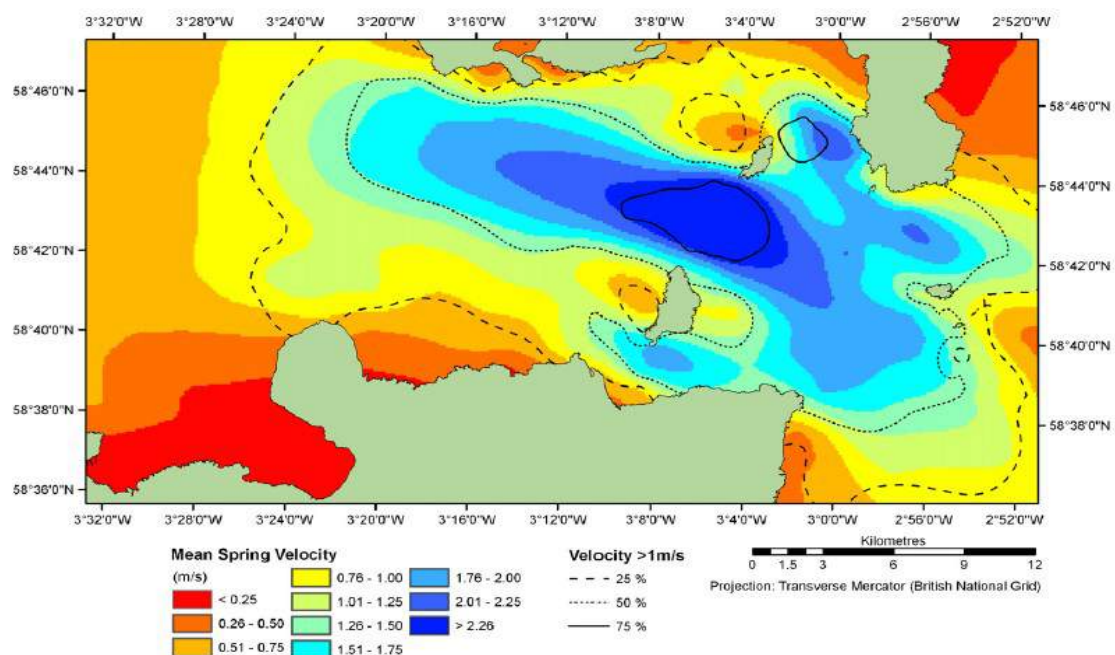


**Figure 18** the tidal current velocities in mean spring tide for the Pentland Firth, Scotland area (Shields *et al.*, 2009)

2.2.6.2 ***The Pentland Firth, UK sea water velocity variations and influence in setting CFD boundary conditions***

Black and Veatch (2005) conducted a survey on the energy estimates of UK seawater energy based on the kinetic energy flux. They reported that “approximately 20% of the UK tidal resource is within sites of depths 30 to 40 m and have the peak velocities up to 2.5 to 3.5 m/s”. Bryden *et al.* (2007) suggest that the kinetic energy flux is proportional to the water velocity passing through that channel. The variations and the directions of the seawater flow velocity, are highly non-linear and multi-directional, hence while performing CFD analysis of the turbine the flow variations must be considered, otherwise the results can be misleading (Garrett & Cummins, 2013). Betz (1920) and Lancaster (1915) proposed a maximum turbine efficiency called “Lancaster-Betz” limit. They proposed that when a single turbine is installed in an infinite ocean, the maximum turbine efficiency cannot exceed 59.3%. As the variations of flow, the force exerted by the turbine, the pressure of water velocity on the turbine blades which causes wake, and the transport of the electricity generated to the grid (coast) may cause energy losses. Figure 19 shows the conceptual diagram of the various turbines installed in a channel and the velocities around a single turbine.

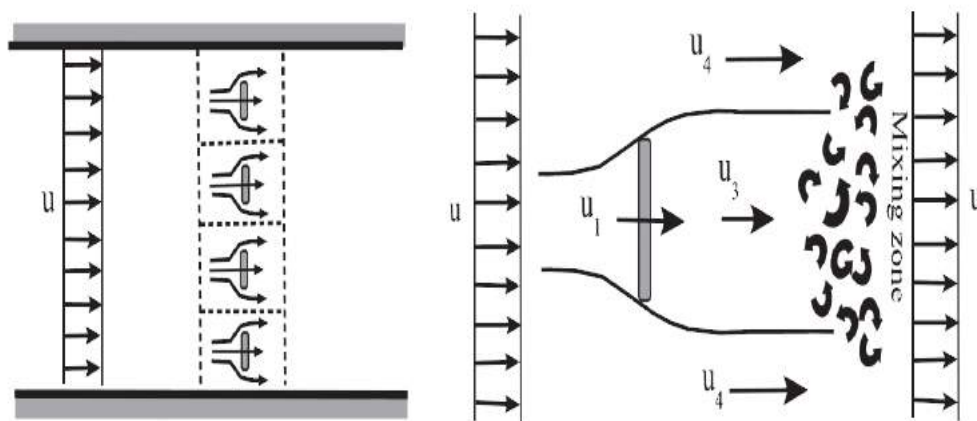


**Figure 19 Conceptual diagram of various turbines installed in a tidal channel and velocities interacting around a single turbine (Vennell, 2013)**

where  $u$  is free stream water velocity entering the tidal channel,  $u_1$  is the water velocity passes through the turbine,  $u_3$  is the water velocity wake caused in the downstream of the turbine, and  $u_4$  is the water velocity passing around the turbine.

Bryden *et al* (2007) generated water flow velocity graphs using UK admiralty charts and Marine Atlases around the Pentland Firth, UK. The tidal flow velocities range from 1 to 3.5 m/s for the

## 2. Seawater Environment, Hydrodynamics of Horizontal Axis Tidal Turbines, and Bio-mimicry

annual spring and neap tides around the Pentland Firth, Scotland which vary throughout the year. Bryden and Couch (2006) demonstrated a graph (Figure 20) how the mean energy flux behaves in a tidal channel which has width of 1000 m and depth of 40 m for the mean neap tide and assuming the peak spring tide of 3 m/s. They reported that the performance of the tidal rotor to harness the electricity and the turbine efficiency depends on the water flow velocity and its variation.

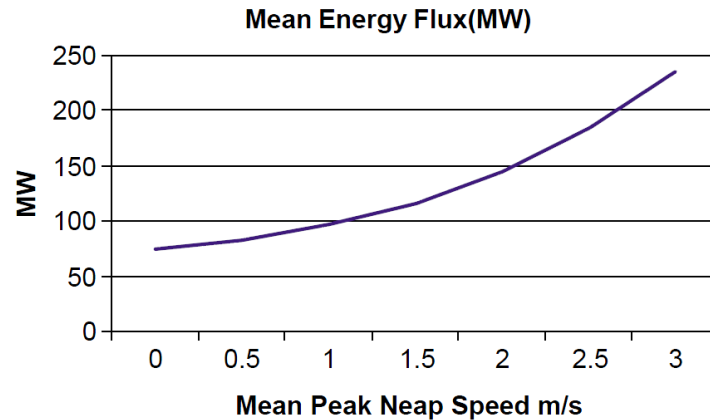


**Figure 20 Effects of the mean neap tide on the energy flux (Bryden & Couch 2006)**

Baston and Harris (2011) implemented a 3D numerical model using the “Stanford Unstructured Non-hydrostatic Terrain-following Adaptive Navier-Stokes Simulator (SUTANS)” to understand the non-linear tidal flow dynamics in the Pentland Firth area. They generated the bathymetry of the Pentland Firth area using the UK Admiralty charts and using the port authorities. Their study covered the depth between 60 m and 100 m. The bathymetry of the Pentland Firth (Figure 21) was generated by using Acoustic Doppler Current Profiler (ADCP).

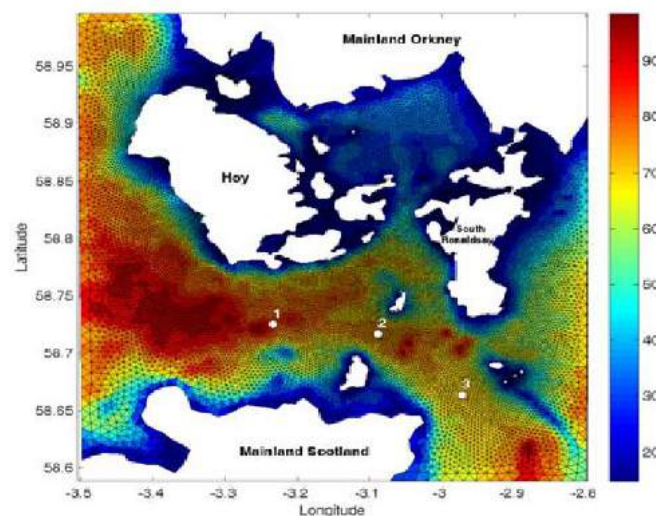


**Figure 21 Generated Bathymetry for the Pentland Firth using the ADCP (Baston & Harris 2011)**

## 2.3 Hydrodynamics of horizontal axis tidal turbines

### 2.3.1 Introduction

A broad literature review on hydrodynamics of horizontal axis tidal turbines was conducted in this section. This review only focuses on the horizontal axis tidal turbines as the main objective is to design an optimal HATT, therefore this review is broadly divided into HATT's concepts via Blade Element Momentum theory (BEM), Airfoil section theory, Hydrodynamic non-dimensional parameters such as drag, lift, torque, power coefficient etc. are reviewed. The literature on blade design for modern tidal turbines, with the aim of defining the ideal blade shape for tidal turbines has been examined. This section ends with defining the tidal turbine design procedure and performing the sensitivity analysis of the parameters involved in design and analysis of the HATT's which later forms the background for CFD modelling on HATT's.

### 2.3.2 Blade Element Momentum theory

Tidal turbine power generation depends on the interaction between the sea water and tidal turbine blade. Betz (1920) demonstrated the idealised simple model of ideal turbine, with ideal flow of fluid. This model of linearized blade momentum theory was developed in early 1920's to measure the performance of ship propellers. Manwell *et al.* (2002) suggested that using BEM theory loads and the thrust on the rotor blade can be calculated for various velocities, angular velocity and pitch angle. They demonstrated that a blade can be divided in N number of sections with assuming that each section is independent of other sections, and lift and drag on each section of the airfoil section defines the force acting. Figure 22 demonstrates various sections in a rotor blade and its angular velocity.

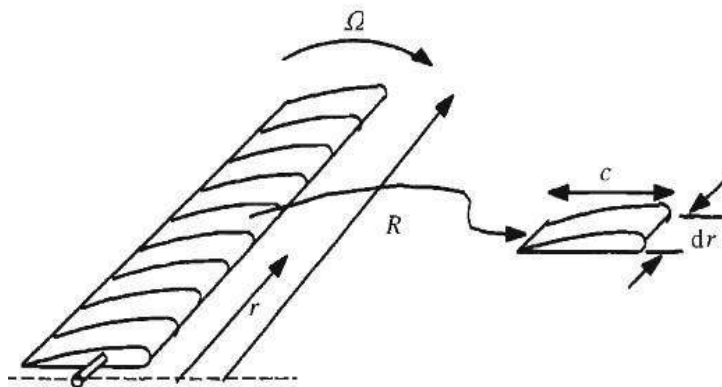
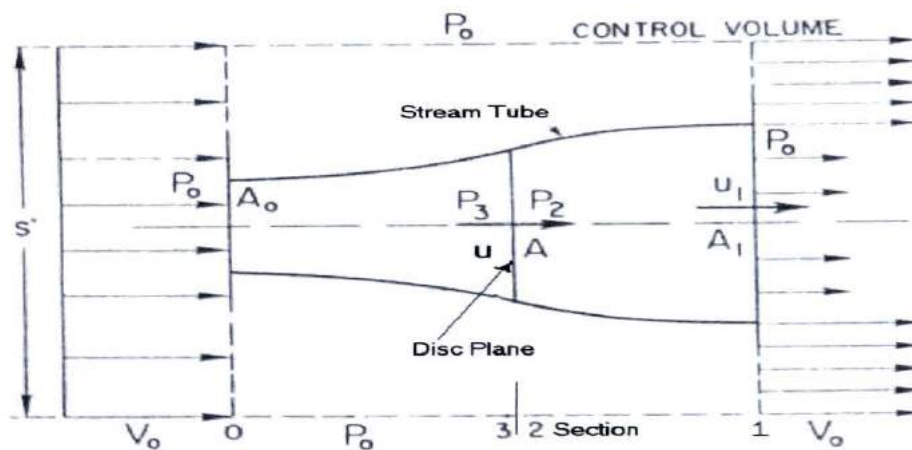


Figure 22 Illustration of the blade sections (after Manwell *et al.*, 2002)

where  $c$  is airfoil chord length,  $dr$  is the radial length of the blade section (m),  $r$  is the rotor radius (m), and  $\Omega$  is the angular velocity of the rotor (rad/s)

This theory it assumes the tidal rotor as the actuator disc and tidal rotor in a control volume (CV) boundaries (Figure 23). BEM theory is based on the following assumptions:

- The fluid flow should be steady, homogeneous and incompressible,
- The turbine disc has an infinite number of blades, with velocity being constant in the rotor area,
- The turbine should not produce any wake or rotational flow,
- The flow should not get obstructed either by downstream or upstream boundaries i.e. the static pressure should be equal to the ambient static pressure distributed across the control volume.



**Figure 23 Flow velocity in a control volume according to actuator disc theory (after Stoddard & Eggleston, 1985)**

where  $S$  is the control volume cross-sectional area (m),  $P_0$  is the ambient pressure of the atmosphere ( $N/m^2$ ),  $V_0$  is the fluid velocity at inlet and outlet of CV (m/s),  $u$  and  $u_1$  are the downstream and upstream fluid velocity of the CV (m/s),  $P_2$  and  $P_3$  are the downstream and upstream pressure of the rotor ( $N/m^2$ ),  $A$  is the area of the rotor ( $m^2$ ),  $A_0$  and  $A_1$  are the area of the inlet and outlet cross section of the tube.

As the water is moving towards the rotor plane area, Bernoulli's pressure theorem assumes that "the flow is frictionless". The atmospheric pressure is usually about 1atm which is equal to

## 2. Seawater Environment, Hydrodynamics of Horizontal Axis Tidal Turbines, and Bio-mimicry

101325Pa, and assuming that density of the fluid is constant, the upstream and the downstream pressure can be defined using Equations 4 and 5 respectively:

$$P_0 + \frac{1}{2}\rho V_0^2 = P_3 + \frac{1}{2}\rho u^2 \quad \text{Eqn. 4}$$

and

$$P_2 + \frac{1}{2}\rho u^2 = P_o + \frac{1}{2}\rho u_1^2 \quad \text{Eqn. 5}$$

Thus the axial force (thrust,  $T_{thrust}$ , N) can be defined as:

$$T_{thrust} = \frac{1}{2}\rho A(V_0^2 - u_1^2) \quad \text{Eqn. 6}$$

After defining the axial force in the tidal turbine axial interference factor can be defined as minute decrease in the water velocity in the free stream and rotor plane,

$$u = V_0(1 - a) \quad \text{Eqn. 7}$$

Tidal turbine is distinguished by its power coefficient  $C_p$  which can be defined as follows:

$$C_p = \frac{P}{\frac{1}{2}\rho V^3 A} = \frac{\text{Turbine Power}}{\text{Power in the sea water}} \quad \text{Eqn. 8}$$

In order to obtain an optimal  $C_p$ , Betz limit 16/27 or 0.593 should be considered while calculating the power coefficient with an axial interference factor giving  $a = 1/3$  or 0.33, then  $P_{Betz}$  can be calculated as:

$$P_{Betz} = C_{pBetz} \frac{1}{2}\rho V^3 A \quad \text{Eqn. 9}$$

where,  $P_{Betz}$  is the optimal power that can be produced by a tidal rotor (W),  $C_{pBetz}$  is the Betz limit power coefficient (16/27).

### 2.3.3 Airfoils and Non-dimensional forces of tidal turbines

A brief literature was carried out on the airfoil structures with specific focus on the four digit symmetrical NACA airfoil sections. Airfoils are the sections in a turbine blade with certain geometric shapes, which generate forces such as drag, lift, torque due to the interaction between fluid surrounding to the blade. Tidal turbine blades are cross sectioned in the form of various airfoils to generate mechanical power from seawater. The length and the thickness of the airfoil are the important functions to obtain the desired mechanical power from the rotor and this is purely based

on the assumption of the airfoil properties used. The review shows that the coefficients like drag, lift and power vary from source to source and also because of the deficiency of the scope.

### 2.3.3.1 *Airfoils and their design*

NACA profiles were created by The US National Advisory Committee for Aeronautics, which was later owned by NASA. As stated before, the literature review in this section solely concentrates on particular profile from the NACA 4 digit symmetrical series. This choice was made on the rationale of horizontal axis tidal turbine parameters where appropriate, and mainly because it high cavitation properties (Liu & Veitch, 2011). And also significant amount of data was available for validation purposes. An airfoil comprises of many terms to characterise it, this can be demonstrated in Figure 24.

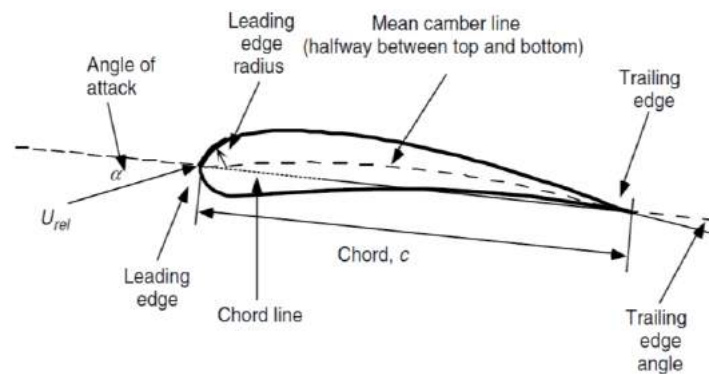


**Figure 24 Airfoil characteristics (Bavanish & Thyagarajan, 2013)**

It can be noted from the above figure that airfoils have important geometric parameters that have an effect on the hydrodynamic performance of the airfoil which include, leading and trailing edge, thickness, chord length and the angle of attack. There are many families of airfoils (Figure 25) like five digit series, six digit series etc. NACA 4 digit symmetrical series have the following parameters: the first digit specifies the maximum value of camber (mean line) in percentage of the chord (airfoil length), the second digit specifies the distance to the location of maximum camber from leading edge in the tenths of the chord, and the last two digits specify the maximum section thickness of the airfoil in the percentage of the chord. For example NACA 0018 has a maximum thickness of 18% and is a symmetric airfoil (Johnson *et al.*, 2004).

## 2. Seawater Environment, Hydrodynamics of Horizontal Axis Tidal Turbines, and Bio-mimicry

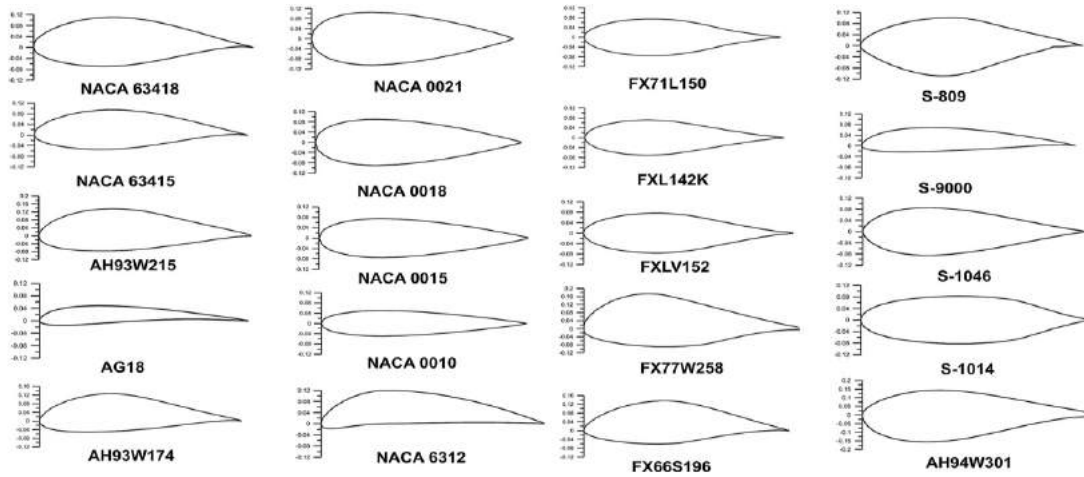


Figure 25 Different families of symmetric and non-symmetric NACA profiles (Mohamed, 2012)

### 2.3.3.2 Non-dimensional forces acting on tidal turbine blades

Water flow over an airfoil results in production of forces which are distributed over airfoil surfaces. As the fluid velocity increases over the airfoils, the ‘convex surface’ results in lower pressure on the ‘suction’ side when compared to the ‘pressure side’ of airfoil. Hydrodynamic forces such as drag lift and torque (Figure 26) act on the airfoils when immersed with sea water due to its relative motion. These hydrodynamic forces arise due to pressure on the surface of airfoil and the shear forces. Those forces are explained below:

- Lift force: Lift force can be defined as the force that is perpendicular to the oncoming flow direction. The lift force is a result of the distribution of uneven pressure on the both upper and lower surfaces of the airfoil. Mathematically,

$$L = \frac{1}{2} \rho V^2 A C_L \quad \text{Eqn. 10}$$

- Drag force: Drag force can be defined as the force that is parallel to the oncoming flow direction. The drag force is a result of both the distribution of uneven pressure on the both upper and lower surfaces of the airfoil and due to the viscous forces on the surface of the airfoil. Mathematically,

$$D = \frac{1}{2} \rho V^2 A C_D \quad \text{Eqn. 11}$$

- Pitching Moment (Torque) force: Torque force can be defined as the force which rotates around perpendicular axis to the airfoil section.

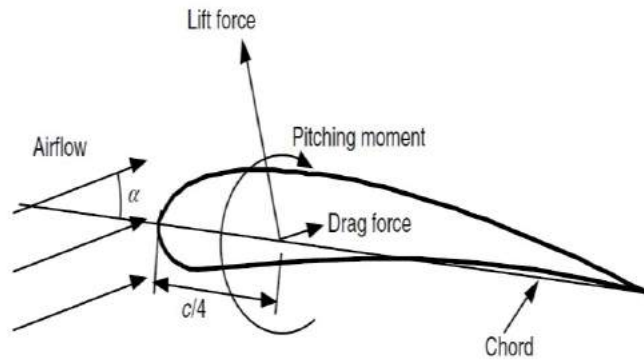


**Figure 26 Hydrodynamic forces acting on the airfoil**

Another important non-dimensional parameter which defines the airfoil flow characteristics is Reynolds number, which can be defined as “the ratio of inertial forces to viscous forces and consequently quantifies the relative importance of these two types of forces for given flow conditions”. Reynolds number is also used to differentiate the different flow patterns like Turbulent or Laminar flow. Thus the Reynolds number ( $Re$ ) can be defined as:

$$Re = \frac{\rho V L}{\mu} \quad \text{Eqn. 12}$$

where,  $\rho$  is the density of the sea water ( $\text{kg/m}^3$ ),  $\mu$  is the dynamic viscosity of sea water ( $\text{kg/ms}$ ),  $V$  is the velocity of the sea water ( $\text{m/s}$ ),  $L$  is the characteristic length ( $\text{m}$ ).

It is now possible to define the lift coefficient for a tidal turbine blade which can be expressed as:

$$C_L = \frac{L}{\frac{1}{2} \rho V^2 A} \quad \text{Eqn. 13}$$

The drag coefficient for a tidal turbine blade is defined as:

$$C_D = \frac{D}{\frac{1}{2} \rho V^2 A} \quad \text{Eqn. 14}$$

and the pitching moment (torque) coefficient for a tidal turbine blade can be defined as:

$$C_M = \frac{M}{\frac{1}{2} \rho V^2 A} \quad \text{Eqn. 15}$$

where,  $\rho$  is the density of the sea water ( $\text{kg/m}^3$ ),  $V$  is the non-uniform velocity of sea water ( $\text{m/s}$ ),  $A$  is the area of turbine blades ( $\text{m}^2$ ),  $M$  is the torque ( $\text{N.m}$ ).

### 2.3.3.3 Flow over an airfoil

The hydrodynamic forces drag, lift and pitching moment of the airfoil are generated due to the pressure differences on the airfoil surface and resistance between sea water and the airfoil. These pressure differences are caused due to the alterations in water velocity, which can be comprehended by using Bernoulli's theorem (Clancy, 1978). This can be shown as:

$$p + \frac{1}{2}\rho V^2 = \text{constant} \quad \text{Eqn. 16}$$

where,  $p$  is the static pressure of the sea water,  $V$  is the velocity interacting along the airfoil surface.

As the water flow increases around the cylindrical leading edge, it results in pressure drop and gives negative pressure inclination. As the water flow advances to the trailing edge, it reduces and the pressure rises, which concludes in positive pressure inclination. For the given airfoil design, if the water velocity, the angle of attack, water pressure is higher on the upper surface of the airfoil and also exceeds the force of gravity it results in generating lift force. Drag force is generated due to the uneven pressure distribution on the airfoil and the resistance between water velocity flow and the airfoil. The water pressure variations on the airfoil surface are represented by Eqn. 16, i.e. the Bernoulli's equation, which states that the increase in the water velocity decreases the pressure. The pressure inclination has a powerful development over the airfoil surface (Figure 27).

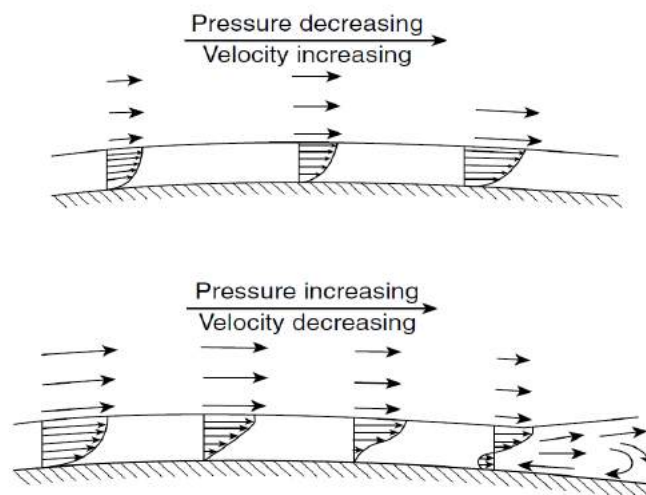


**Figure 27 Pressure inclination effects on the surface of airfoil (Singh *et al.*, 2012)**

The fundamental requirement when designing tidal turbine blades is to convert the kinetic energy available in the sea water into torque whilst maintaining its structural strength. Several commercial

companies have additional requirements for the tidal turbine design to be welcomed in the market, that the material and manufacturing should be low. The origin of the tidal turbine blade arrangement considers steady central flow on the upstream of the tidal turbine blades provided that the operating conditions are in steady state. For example, Tocardo B.V. (2013) designed a tidal turbine rotor for operating at a water velocity of 2.5 m/s and with an angular velocity of 17 rpm. These blades are designed to operate in many other off-shore design conditions and for non-uniform flows as well. Unsteady flow cause variations in shear stresses across the tidal rotor, as the turbulent boundary layer where water velocity and its direction vary in space and time.

### 2.3.3.4 *Tidal turbine design procedure*

Tidal turbine design procedure starts with choosing different parameters and the preferred airfoil. Then a basic shape of the blade is defined assuming that the blades have no wake rotation. The concluding blade shape and efficiency is measured by examining drag, lift, tip losses and torque. The following steps are considered while designing the tidal turbines:

- The most important to design a tidal turbine is to finalise the radius of the rotor, number of blades, the Tip Speed Ratio (TSR), the water velocity, the drag and lift coefficients of the airfoil. Then the number of sections the blades are substituted determine drive the tidal blade shape performance calculation. Huang & Wu (2013) suggested that for a tidal turbine harnessing generating electricity the chosen tip speed ratio,  $\lambda$  should be 4 if the number of blades is 3 or higher.
- The angle of attack is then calculated, to estimate the best lift to drag ratio, which is based on the hydrodynamic performance of the blade airfoil.
- After calculation of the tip loss factor, the axial induction factor is calculated.
- The inflow angle of the velocity is also calculated for additional convenience and if necessary the chord length and incidence angle are adjusted. Finally, the rotor performance is calculated and the blade shape is modified accordingly.

## 2.4 Sensitivity analysis of tidal turbine blades

This literature review is solely focused on the symmetrical NACA 4-digit series, with a view on identifying the most important tidal turbine blade design and analysis sensitivities affecting tidal turbine blades. Only NACA 0012 and NACA 0018 were of greater interest for validation and structure purposes. All of the published data which is considered suitable for this research has been

## 2. Seawater Environment, Hydrodynamics of Horizontal Axis Tidal Turbines, and Bio-mimicry

stated in the table 2. The data collected includes the calculation of lift, drag, and moment coefficients; also some data includes measurements of surface pressure distribution are described later on. Data obtained for the validation was of particular interest due to following reasons:

- Variation in the velocities, analysis done for over a wide range of angle of attack, analysis involving multiple blade sections,
- CFD analysis type (steady or unsteady), lift, drag, and torque characteristics.

**Table 2 Summary of the sources for NACA-4 digit foils**

Author	NACA foil thickness (%)	Angle of attack (°)	CFD analysis type	Notes
<b>Mehmood <i>et al.</i> (2012)</b>	18	0-16	2D (steady)	Various lengths and angles of attack for NACA profiles
<b>Hameed &amp; Afaq (2013)</b>	12, 18	0-10	2D (steady)	Structural integrity of the blade shape inspected
<b>Kim <i>et al.</i> (2006)</b>	18	0, 3, 6, 9	2D (steady)	CFD simulation carried out using LES and Reynolds shear stress measured
<b>Gim &amp; Lee (2013)</b>	18	10, 20	2D (steady)	Flow visualisation and velocity streamlines presented
<b>Rossetti &amp; Pavesi (2013)</b>	18	0	2D (unsteady)	Unsteady flow with unstructured mesh and grid refinements presented
<b>Rodriguez <i>et al.</i> (2013)</b>	12	9.25 and 12	2D (steady)	Direct Numerical Simulation (DNS) used for simulation
<b>Yang &amp; Shu (2012)</b>	12	0	2D (steady)	Parameterisation of the airfoil using GA
<b>Chen <i>et al.</i> (2006)</b>	12	0	2D (unsteady)	Cavitation analysis performed
<b>Murthy <i>et al.</i> (2000)</b>	12	30	2D (steady)	Flow characteristics examined to measure dynamic stall

Mehmood *et al.* (2012) examined the design of a diffuser for tidal current turbines using the NACA 0018 foil for the diffuser design. The purpose of their review was to examine the effect of length and angle of attack on NACA 0018 foil for diffuser design. 2D CFD simulations were carried out to investigate the velocity and mass flow rate at the throat of the diffuser. The CFD simulations carried out in this study was done using ANSYS CFX. By means of addressing the diffuser design problem this review identifies the use of NACA 0018 foil in tidal energy, and correlates the simulation data with

Mehmood *et al.* (2012 a). In particular, the airfoil analysis was carried out for various lengths i.e. 400, 500, 650, 900 and 1000 mm and the results show variations in:

- 1) Maximum velocity vs angle of attack (Figure 28),
- 2) Coefficient of velocity to angle of attack,
- 3) Maximum drag and,
- 4) Maximum drag to lift ratio

each of the above parameters versus maximum velocity. A structured mesh was created around the airfoil as 2D CFD analysis was done to see the pressure gradient effects. SST k- $\omega$  turbulence model was used due to “its good performance for predicting boundary layer separation problems as well as for pressure-velocity coupling” (pp. 4554).

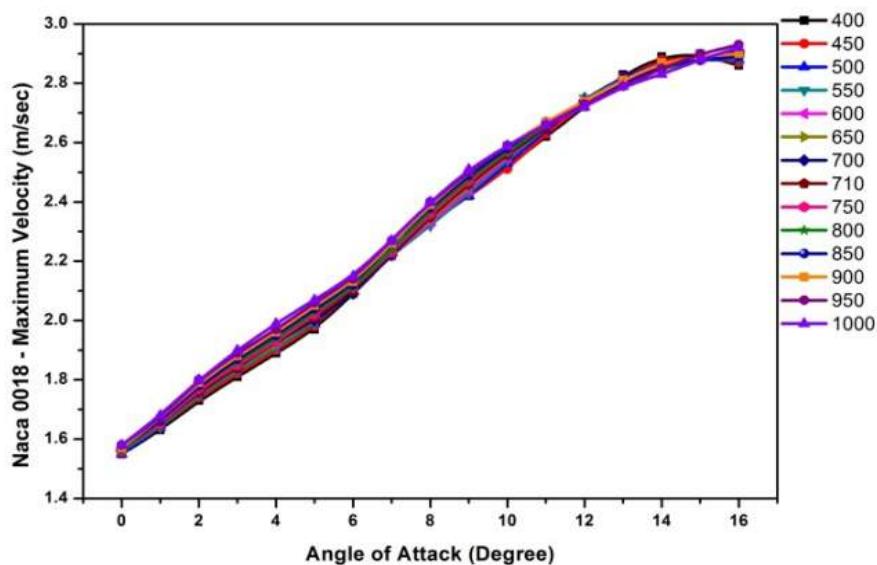


**Figure 28 Maximum velocity vs angle of attack simulated over different lengths of NACA 0018 sections (Mehmood *et al.*, 2012)**

Coefficient of mass flow rate and coefficient of velocity was also introduced to monitor the velocity at 10 different points of the NACA 0018 airfoil section. All the data given are corrected, but no reference is given. Their conclusion was that; velocity increases as the length and angle of attack are increased. This study was of a particular interest because it was used to validate the 2D CFD methodology, defined in this project using the same boundary conditions as authors.

The data reviewed by Hameed & Afaq (2013) included design and analysis of a symmetrical blade for a small vertical axis wind turbine, which applied BEM theory. Design constituents included solidity ratio, aspect ratio and the pressure coefficient with the aim of obtaining 1 KW power output through

## 2. Seawater Environment, Hydrodynamics of Horizontal Axis Tidal Turbines, and Bio-mimicry

the turbine. Aerodynamic and centrifugal forces were also considered in order to optimise the structural integrity of the blade so that manufacturing costs could be reduced. The effects of the larger centrifugal forces due to higher angular velocities result in higher torques which increases the stress failure at the same time, so the turbine design mechanism was designed to determine aerodynamic forces during its 360° rotation. The analytical results obtained were validated using ANSYS 11.0. Comparison of the lift and drag coefficients (Figure 29) was also presented for NACA 0012, 0015, 0018 airfoils and they also reported that symmetric airfoil was chosen in their analysis due to “the same characteristics of drag and lift in both upper and lower surfaces and also symmetrical airfoils provide lift from both sides of airfoil” (pp. 249).

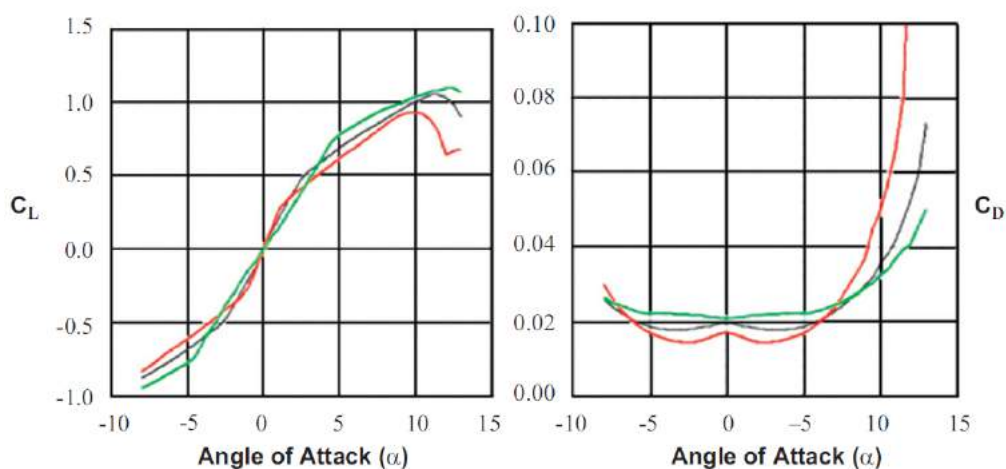


**Figure 29.1 Comparison of lift and Figure 29.2 drag coefficients for trend line NACA 0012 (red), 0015 (black), 0018 (green) foils (Hameed & Afaq, 2013)**

Their study concluded with observing the centrifugal forces for the Darrieus wind turbine and mentioning that bending stresses and deflections play a vital role while performing the stress analysis if the symmetrical airfoil blades in order to manufacture them by optimisation through weight reduction.

Kim *et al.* (2006) simulated uniform and non-uniform flow around NACA 0018 foil and studied the aerodynamic noise generation due to the vortex shedding on the pressure side on the trailing edge. The CFD simulations were carried out using Large Eddy simulation, for the angles of attack 0°, 3°, 6° and 9°. All the mathematical modelling of unsteady flow and turbulence around the airfoil was correlated to the ‘sub-grid scale model’ presented by Lee *et al.* (2004). As there is an increment in the angle of attack, the fluid flow velocity slows down on the suction surface of the airfoil and the pressure surface gains movement. Thus to give the complete picture (Figure 30) of the turbulent stress around the NACA0018 airfoil for 6° using LES which describes Reynolds shear stress.

## 2. Seawater Environment, Hydrodynamics of Horizontal Axis Tidal Turbines, and Bio-mimicry

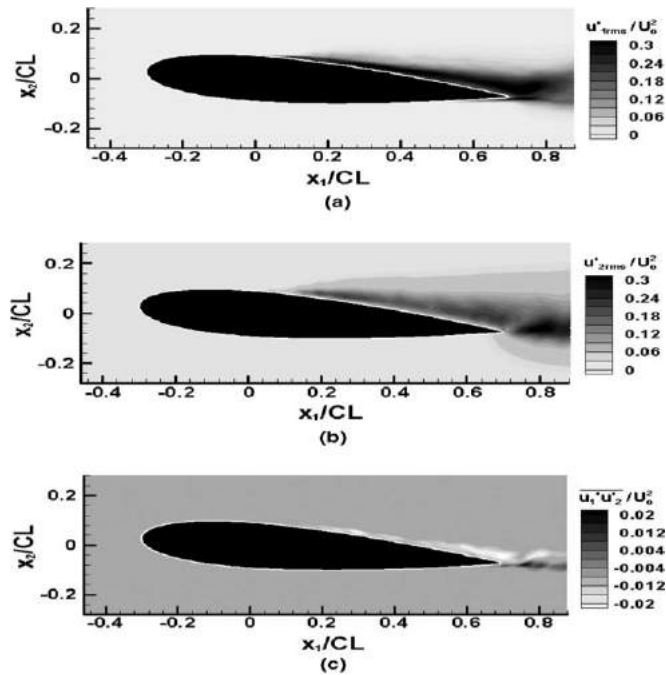


**Figure 30** Turbulent stress components around NACA0018 airfoil for angle of attack =  $6^\circ$  (Kim *et al.*, 2006)

From the unsteady state numerical analysis performed, positive vorticity shed from the pressure side on the leading edge of NACA0018 airfoil while negative vorticity shed on the suction side of the airfoil. To conclude their study, Green's function was applied to figure out the far field noise frequency; alternatively on the suction side of airfoil boundary layer of turbulence is formed because of the quasi-behaviour pressure vortex formation.

The data reported by Gim & Lee (2013) was of distinct interest because of the flow patterns and the use of NACA0018 foil for the design of the rudder model to be considered in the application of the propeller design in ships. The functional use of NACA0018 in design of rudders increases the stability, and work efficiency. The experiments were carried over a 'circulating free water channel (pp. 30),' and using Particle Image Velocimetry (PIV) flow using visualisation was presented (Figure 31), the 2D flow separation for the angles of attack  $10^\circ$  and  $20^\circ$ .

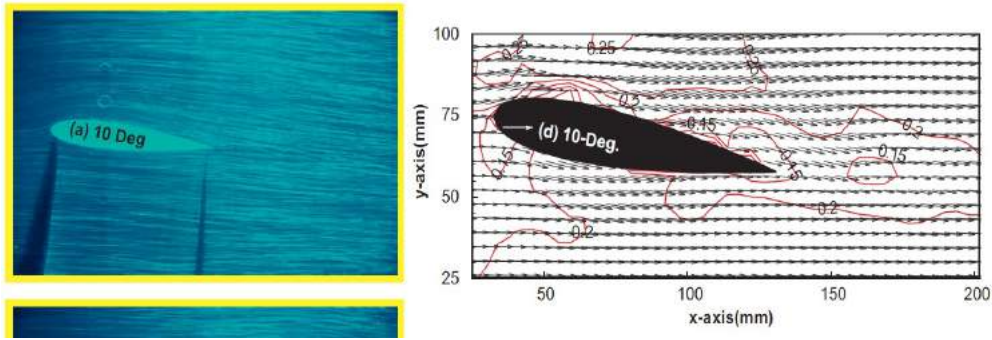


**Figure 31 Fluid flow visualisation and velocity streamlines around NACA0018 foil (after Kim & Lee, 2013)**

The behaviour of the turbulent flow near on the airfoil was discussed and their variations for different angles of attack along with Reynolds number were demonstrated. The Reynolds shear stress was stabilised which would prevent the cavitation (which is not modelled in the present study) and increased hydrodynamic performance was noted on the ‘high-lift’ foil.

Rossetti & Pavesi (2013) presented the comparative analysis of 2D and 3D numerical approaches to study the unsteady flow effects on NACA0018 in the design of H-Darrieus turbine. The 2D simulations presented provided the unsteady fluid flow effects on blades and the vortices patterns in a complex flow over the foil. A relationship of tip speed ratio with power coefficient curves (Figure 32) was presented and the integration of thrust force with blade shape iterations was highlighted.

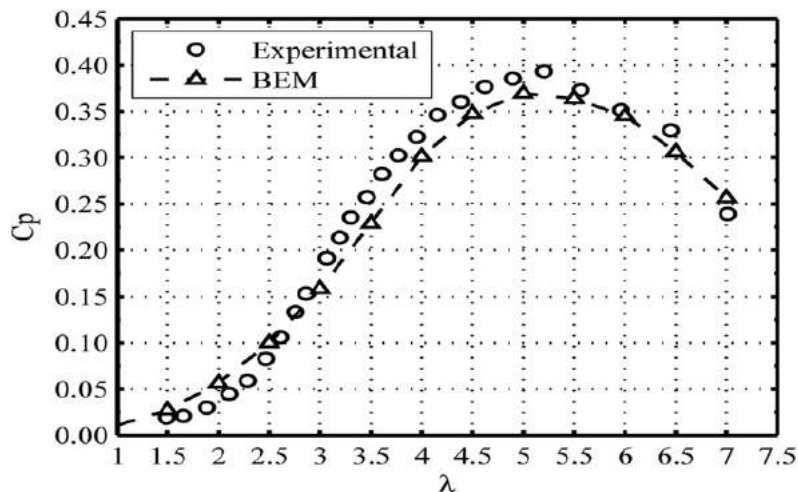


**Figure 32 Relationship of Tip speed ratio and Power coefficient and validation of BEM-CFD model (Rossetti & Pavesi, 2013)**

Unstructured mesh was applied, to the stationary domain (the hydrodynamic tunnel), and the rotating domain (turbine domain) and grid refinements were employed in the near wall areas,

## 2. Seawater Environment, Hydrodynamics of Horizontal Axis Tidal Turbines, and Bio-mimicry

especially near the rotor blade area to improve the accuracy of the results. Their work concluded with showing the advantages and disadvantages of applying BEM-CFD theory while analysing the turbine blades. 3D CFD simulations show compelling contraction of the intensity of vortices giving a clearer picture for unsteady flow conditions than performing 2D analysis.

The data reported by Rodriguez *et al.* (2013) investigated the phenomenon of turbulence separation in shear layer separated of NACA 0012 aerodynamic profile at low Reynolds number. They applied Direct Numerical Simulation (DNS) technique to simulate the flow around NACA 0012 foil at angles of attack  $9.25^\circ$  and  $12^\circ$ , and noticed vortex shedding causes forceful variations in drag and lift of the airfoil, which further leads to the flow partition on the suction side of the airfoil. Unstructured mesh technique was used to airfoil region as the fluid flow is turbulent in that area. The transition of the lift curve was presented for both angles of attack and the variation in the maximum lift was given, and hence they concluded by observing the separation of the flow at both angles of attack with minor variations in the integration of the flow over airfoil.

The data reported by Yang & Shu (2012) are of particular interest because of the airfoil optimisation done and the power coefficient results are presented for the case of different velocities. Parameterisation of the airfoil was done using Bezier curves and CFD analysis was performed to calculate the hydrodynamic performance. Flow visualisation was done using the PIV technique and later the CFD results of the optimised airfoil were compared with original NACA0012 profile CFD results. The hydrodynamic performance (coefficient of lift) was compared with the experimental data (Figure 33) provided by Cristzos *et al.* (1955) and the results show compliance with each other.

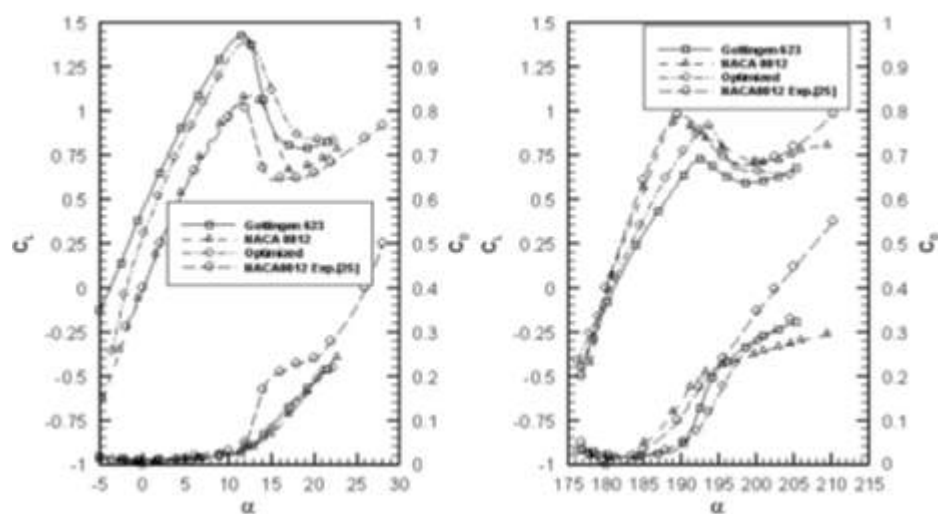


Figure 33 Hydrodynamic performance comparison (Yang & Shu, 2012)

## 2. Seawater Environment, Hydrodynamics of Horizontal Axis Tidal Turbines, and Bio-mimicry

Their study resulted with the development of the parameterised airfoil based on Bezier curves and proved that the optimisation variables were reduced and lift to drag ratio was put forward as a design variable under hydrodynamic conditions.

Chen *et al.* (2006) modelled cavitation unsteady turbulent flow around NACA0012 through 2D CFD simulations. They also investigated the numerical reliability of the RNG K- $\epsilon$  turbulence model with the SIMPLE scheme. The numerical code was treated in two phases of the cavitation analysis which linked to the barotropic law of pressure and links to the fluid flow density.

Murthy *et al.* (2000), review the data for the flow characteristics and steady analysis of NACA 0012 section for various ranges of angles of attacks. Their examination showed unsteadiness in CFD results which then led on to performing the unsteady analysis, to predict the stall on different angles of attack also examining the dynamic characteristics beyond stall. For addressing their problem, their review identifies and correlates with the empirical data, which allows calculating the overall lift characteristics around the airfoil. Their results show variations in:

- a) Maximum lift (Figure 34.1),
- b) Unsteadiness in flow at higher angles of attack (Figure 34.2),

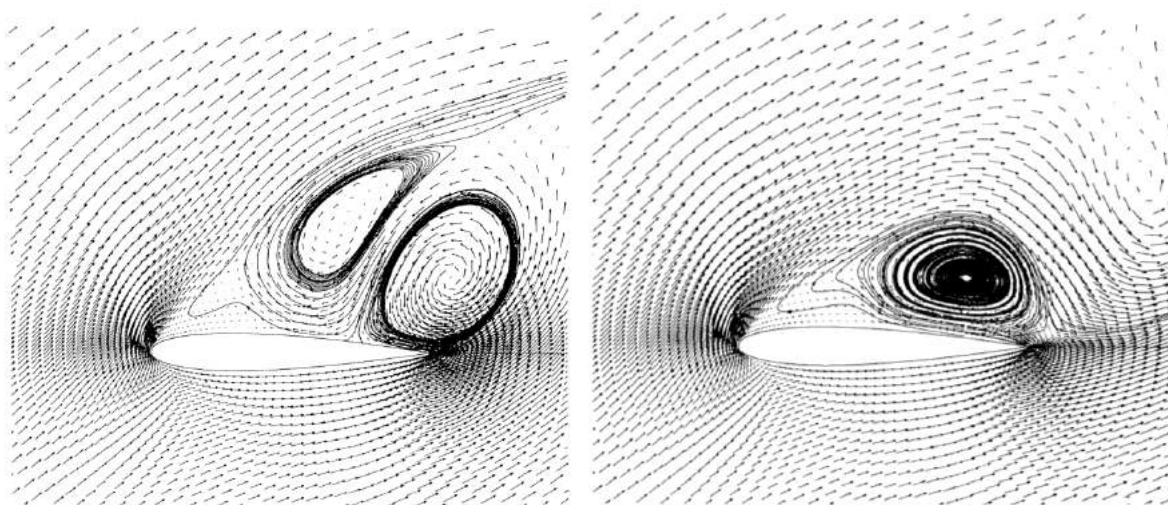


**Figure 34.1 Velocity vectors ( $C_l = 1.72$ ,  $\alpha = 30^\circ$ ,  $Re = 3000$ ); Figure 34.2 Velocity vectors ( $C_l = 1.20$ ,  $\alpha = 53^\circ$ ,  $Re = 3000$ ) (Murthy *et al.*, 2000)**

Their review concluded with the characterising the occurrence of laminar bubble partition under transient analysis. They compared the results lift and drag coefficients with Rumsey, and they showed agreement.

### Alternative data

A number of other references considered for the discussion of NACA 0012 and NACA 0018. The primary focus of Ferrer & Willden (2011) was to develop the unstructured high order Discontinuous Galerkin solver, for the computation of tidal turbine hydrodynamics. They validated their solver for NACA 0012 and NACA 0015 airflow flows, for various Reynolds numbers and turbulent regimes. They also investigated the wake characteristics for single and three bladed turbines, which they defined as “tidal fence concept”. They concluded with developing Discontinuous Galerkin unstructured high order solver which provides solutions with minimising numerical errors for complex flows. The sliding mesh capability cannot handle the flow phenomenon which is encountered in airfoil and cross flow turbines. Finally to minimise blade-wake reactions, the increased effective flow resistance of three bladed turbines relate to the solidity ratio and tip speed ratio.

Batten *et al.*, (2006) explained the hydrodynamics tidal turbines and developed a methodology for the design of horizontal axis tidal turbine. They built a numerical model of a 3D turbine rotor to show the variations of the design variables parametrically, while designing the tidal turbine rotor. In any hydrodynamic design of tidal turbine, the important parameters are the choice of diameter, pitch and revolutions for that application. Further investigation included stall investigation or preclusion of cavitation. They concluded their studies mentioning changes in the blade pitch angles alter the stall performance which also delays the possibility of cavitation on turbine blades. Myers & Bahaj (2006) built a 0.4m horizontal axis tidal turbine in diameter. They measured the power output over various velocities, blade pitch and various rotor angles. They measured power output from the CFD rotor analysis in comparison with the blade inflow angles. They concluded with representing 25% of the turbine rotor producing more power.

Lee *et al.* (2012) developed CFD theory to measure the efficiency of horizontal axis tidal turbine and later verified the approaches with the existing experimental data, and later amendments were made in the turbine design process. 2D CFD analysis was performed on the NACA 63-418 foil section using the k- $\omega$  SST turbulence model. They measured the pressure coefficient at the suction side of the turbine blade using structured and hybrid mesh techniques. Kim *et al.* (2012), presented two case studies; for a bidirectional cross flow turbine which was to be employed in larger channel area. The cross flow turbine presented in their studies was made up of 26 blades which were at an equivalent distance to each other, with the design of an enhanced channel consisting of nozzle at the inlet of the channel and diffuser at the outlet of the channel. As sea water is highly incompressible, especially when the flow experiences barriers it becomes highly unsteady and particularly increases the pressure drag at higher Reynolds number. They concluded with obtaining higher power

## 2. Seawater Environment, Hydrodynamics of Horizontal Axis Tidal Turbines, and Bio-mimicry

coefficient when utilising their cross flow turbine equipped in an augmented channel. Mason-Jones *et al.* (2012) studied the collision of the velocity and the local depth on the tidal turbine efficiency. The CFD simulations were applied on a scaled version of the actual turbine, and later compared with the experimental data. Non-dimensionless parameters like power coefficient, torque and thrust with increased diameters and velocities were simulated in a uniform tidal velocity flow. They concluded their studies with proving that the above mentioned dimensionless characteristics can be applied to diametrically similar turbines, set up on sea bed experiencing steady or non-steady currents, and with the consideration of volume averaged velocity.

Thus after conducting a comprehensive literature review on the seawater environment and the hydrodynamics of the HATT's it is now possible to identify important sensitivities related to HATT blade design in the Table 3.

**Table 3 Seawater environment and blade sensitivity variables derived from the literature**

<b>Seawater Environment, and Blade sensitivity variables</b>
<b>Fluid Velocity, <math>V_{in}</math> (m/s)</b>
<b>Fluid Density, <math>\rho</math> (kg/m<sup>3</sup>)</b>
<b>Fluid Dynamic Viscosity, <math>\mu</math> (Pa.s)</b>
<b>Fluid Pressure, <math>P_{water}</math> (atm)</b>
<b>Angle of attack, <math>\alpha</math> (°)</b>
<b>Airfoil chord length, <math>c</math> (m)</b>
<b>Blade twist angle, <math>\beta</math> (°)</b>
<b>Rotor Diameter, <math>D</math> (m)</b>
<b>Rotor swept area, <math>A</math> (m<sup>2</sup>)</b>
<b>Tip speed ratio, <math>\lambda</math> (-)</b>
<b>Hydrodynamic Lift, <math>L</math> (N)</b>
<b>Hydrodynamic Drag, <math>D</math> (N)</b>
<b>Hydrodynamic Torque, <math>M</math> (Nm)</b>
<b>Rotor Power, <math>P</math> (W)</b>
<b>Rotor Power Coefficient, <math>C_p</math> (-)</b>
<b>Rotor Lift Coefficient, <math>C_L</math> (-)</b>
<b>Rotor Drag Coefficient, <math>C_D</math> (-)</b>

## **2.5 Bio-mimicry: Using Nature as a model to generate an efficient tidal turbine blade**

### **2.5.1 Introduction**

This section of this research presents an introduction to bio-mimicry, and then various bio-mimicry examples which include the Humpback whale and wind turbines, and underwater propellers are discussed. This section also compares the synopsis of various marine vertebrates, and their swimming speeds, locomotion characteristics and their relation to the tidal turbine aerodynamics is also discussed. After presenting the understanding of these characteristics the lift based thrust characteristics of the caudal fin the selection of the fish caudal fin is justified.

Bio-mimicry is a field which studies nature, and later imitating its designs and models to solve complex human problems (University of Reading, 2014). The design process starts by looking at nature's ecosystem, self-healing abilities or a particular organism, to produce a design solution of the human need. To enable an optimal tidal turbine blade producing higher efficiency throughout the year, swimming speeds of the marine vertebrates are studied including their characteristics which allow swimming and producing highest propulsion efficiency. This section also includes a brief study on the fish locomotion which identifies the attributes of the swimming like lift based thrust, the locomotion driving factors: dorsal fins, caudal fins in propulsion, which enable the fish to be efficient even at low tidal velocities.

### **2.5.2 Bio-mimicry examples**

Before proceeding carrying out any research review on the marine vertebrate locomotion, a literature review was conducted to gain an understanding of the high propelling fish and their previous designs being adapted to others. The analysis of the lengths, and weights of fish species like Sword fish, and Sailfish have been performed by Lenarz & Nakamura in 1972, but the concept of using nature to solve complex human problems is a recent idea. The classic example of this is the Humpback Whale and Wind turbine blades (which is discussed below), and also the underwater propellers, which are the two most prominent marine and fish locomotion application, which directly relates to the aerodynamics, and thus are now being used to design modern wind turbines and marine propellers.

### 2.5.2.1 *Humpback whale and Wind turbine blades*

The primary application of the marine vertebrates and their locomotion was first explored by Dr Frank Fish, to design an efficient wind turbine blade adapting Humpback Whale's flippers and tubercles, in Toronto based company called WhalePower (WhalePower, 2014). Dr Fish along with his colleagues Dr Phil Watts, and Dr Lauren Howle in 2004 through their collaborative research proposed this new design of humpback whale wind turbine blade design and ultimately owned a patent for this bio-mimicry application, they also claimed that their design gives 20% extra annual power production as compared to other existing wind turbine blades, and also has a delayed stall (Fish *et al.*, 2011). Figure 35.1, and Figure 35.2 illustrate the humpback whale pectoral flippers, and manufactured adapted tubercles on the leading edge of the wind turbine blade.



**Figure 35.1 Humpback whale pectoral flippers (Fish *et al.* 2011), and Figure 35.2 Manufactured adapted tubercles on the leading edge on WhalePower wind turbine blade (WhalePower, 2014)**

After the initial experimentation on the newly designed wind turbine blade Dr Fish and his team found out compelling power coefficient differences between the traditionally designed wind turbine blade and the tubercle adapted wind turbine blade, the traditional wind turbine blade formed a laminar airflow pattern; whilst tubercles blade produced expedition of the air between the bumps hence reducing the tip vortex and thus reducing turbulent vibration and thus increasing the efficiency (Fish & Battle, 1995). Dr Fish also claimed that, introducing the tubercles at the tip of the blade forces air flow to decrease the turbine noise, and it works smoothly with less vibration and noise. The tubercle wind turbine blade accomplished the pitch angle of 28°, at the same inlet wind

velocity, when compared with the traditional wind turbine which produces the pitch angle of 16°. Their study concluded with conveying “20% gain in the overall efficiency, and reducing 1/5<sup>th</sup> of the vibrational noise in the tubercle wind turbine blade design” (Fish *et al.*, 2008; Fish, 2009).

### 2.5.2.2 *Underwater Propellers*

Underwater propellers are designed and developed for a wide range of marine applications like boats, ships, and submarines. Underwater propeller systems are used to travel long distances, and traditional propeller designs are only designed for two design constraints: maximum velocity which allows the submarines to travel long distances, and low velocity rotating propellers allowing finite range transportation. Thus there is a gap in between these two realms, and there is a need for better propulsion mechanisms (Liu & Hu, 2005). The underwater propulsion converts rotational shaft power to thrust propulsion, and thus the propulsion of the underwater vehicles is solely based on the control surface and thrust generation mechanism. The propulsion efficiency depends on the rotation of the propeller, and the majority of the propeller losses are incurred as the propeller only rotates in the flow direction, thus by designing the propeller for higher thrust efficiency automatically reduces the drag and improves the manoeuvre of the underwater systems.

Many designers have investigated the benefits of the biomimetic underwater propulsion mechanisms through the propulsion characteristics of the fishes like dolphins and tuna fish tail fins, to contribute better efficient propellers for both high and low design speeds. United States Navy, has heavily invested in the research of mimicking the tuna fish tail fin to design a highly efficient submarine termed as ‘Faux Fish’, which is demonstrated in Figure 36.2. The Faux Fish, submarine propulsion design system is now patented and owned by United States Navy, and the empirical results achieved remain highly confidential (US Patent 6895108; 2004). Figure 36.1 shows a conventional seven blade marine propeller, and Figure 36.2 illustrates the Faux Fish.

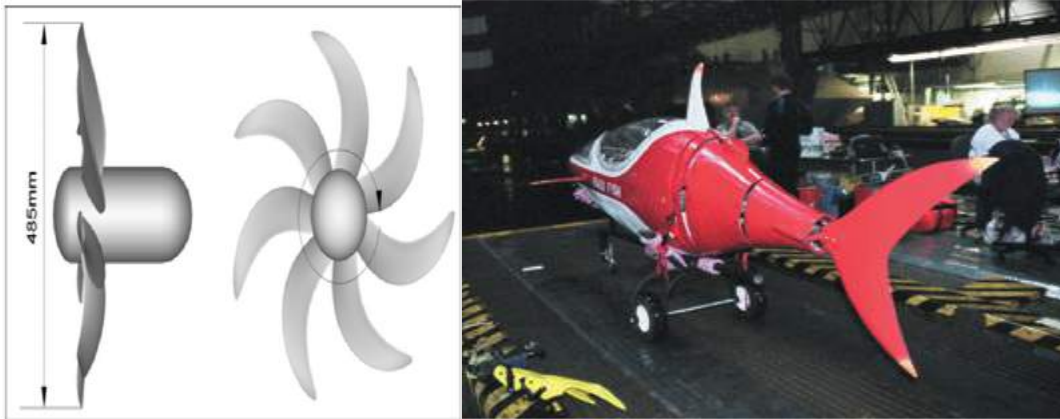


**Figure 36.1 seven blade conventional propeller (Felice *et al.*, 2009), and Figure 36.2 the Faux Fish fish tailfin propeller (US Patent 6895108; 2004)**

Other propulsion system applications which are inspired from bio-mimicry include SHARC (Submersible Hybrid Autonomous Rover Craft), developed by University of Glasgow, for the hybrid propulsion using bio-mimicry of a Tiger Shark. Figure 37 illustrates the SHARC vehicle.

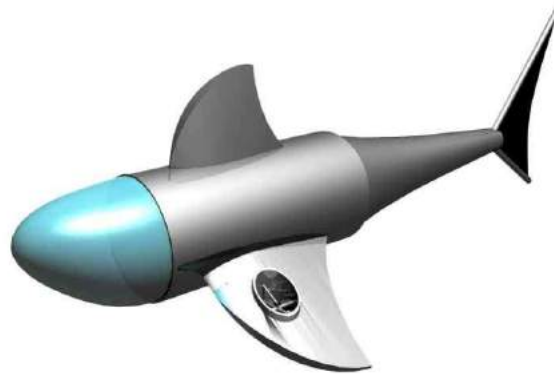


**Figure 37 SHARC Vehicle (Watts *et al.*, 2006)**

### 2.5.3 Work input vs Work output

Work input by a fan can be defined as the inward force acting through the input distance, whereas work output is the output force acting through the output distance dependent on the force to increase the output distance, by the turbine blades. Fans transfer energy into a flow and thus reducing the pressure, i.e. power is input to fans and output from turbines. Fans for e.g. an axial compressors use “back sweep” in 1D design phase and the blade twist angles are different on the

compressor leading and trailing edge, and the gases can reach higher velocities and energy levels. Thus, fans are not limited by the Betz limit and can have higher efficiencies than 58.3%. In the case of tidal turbines, the seawater rotates the turbine blades and the water is pulled out and replaced with the outside water. Fans offer high peak efficiency over wide range of rotational speed range, they have low starting power requirements, and have increased pressure rise due to increased number of stages with negligible losses. Thus, bio-mimicking the fans would be a good idea to design a horizontal axis tidal turbine blade as the seawater velocity varies throughout the year, and the tidal turbine blade would have high peak efficiency throughout the year, it would also have increased rotational velocity.

The above mentioned bio-mimicry examples contribute excellent evidence in improving the functioning and the efficiency to the conventional designs, and thus generating entirely new designs. The following section examines the underwater fish locomotion concepts and their characteristics which enable fast and efficient swimming speeds.

### 2.5.4 **Marine vertebrates synopsis and their locomotion characteristics**

The synopsis presented in this section regarding the marine vertebrate locomotion does not aim to review all marine fish and mammals. The research review rather focuses on the lift based thrust characteristics of the high speed swimming fishes Blue Marlin, Sail fish, and Sword fish, and the aspects of their locomotion. For this reason, the underwater marine locomotion of slow speed fish is not presented here. Before proceeding to the lift based thrust characteristics of the high speed swimming fish understanding the knowledge of the external anatomy which includes Pectoral, Dorsal, Anal, and Caudal fins which contribute in marine fish propulsion is discussed.

#### 2.5.4.1 ***Exclusive characteristics of marine vertebrates***

The swimming and locomotion characteristics of marine like most other mammals differ in size, weight, shape, nonetheless they all live and survive in the unsteady currents in the ocean. Thus certain marine vertebrates function accurately in unsteady and fast seawater currents like Sailfish, *Istiophorus Platypterus* which is the fastest fish with swimming speeds recorded up to 110 km/h (70 MPH), whereas the Blue Marlin fish, *Makaira nigricans* swimming speed has been recorded up to 80 km/h (50 MPH), thus these marine vertebrates employ the thrust manoeuvring or in other words they use their 'fins' for the propulsion (Lenarz & Nakamura, 1972). Marine vertebrate locomotion can be classified into two different taxonomic sections:

## 2. Seawater Environment, Hydrodynamics of Horizontal Axis Tidal Turbines, and Bio-mimicry

- 1) The first section dwells on marine animals jelly fish, jawless fish, squids, skates etc. These marine vertebrates reduce the volume of seawater by squeezing it (Flammang, 2013), and thus lead to the formation of the nozzle like design. A shear layer is formed during to the propulsion, which is also known as 'torodial vortex', this is also found in the jet concurrence which travels at a high momentum. However, due to the scope of the project only a brief introduction is given.
- 2) The second section covers marine vertebrates Blue Marlin, White Marlin, Tuna fish, Sailfish, Whale, Sharks and their locomotion characteristics are found in the larger part of the marine vertebrates involving pitching like a flexible foil like structures. Their locomotion is based on the paired fins which are also known as pectoral flippers, caudal fin, dorsal fins or flukes, which enable highest swimming propulsion efficiency (Long, 1992). For these reasons, these fish prove an excellent motivation for bio-mimicking nature to produce an inproved tidal turbine blade throughout the season. The fish caudal fin in a profile looks like a streamline, and these fish come in flexible fin shapes and sizes, which makes them adaptable to unsteady marine currents. The propulsion characteristics are discussed in the following section.

### 2.5.4.2 *Locomotion and Anatomy of the marine vertebrates*

The locomotion of the marine vertebrate Blue marlin fish (Figure 38) is generally based on the five fins namely; caudal, anal, pelvic, pectoral, and dorsal fins which are located around its body, and the movements caused because of these flexible fins act as the main source for propulsion at high swimming efficiency. Figure 38 illustrates the external anatomy of the Blue Marlin fish with its propulsion fins.

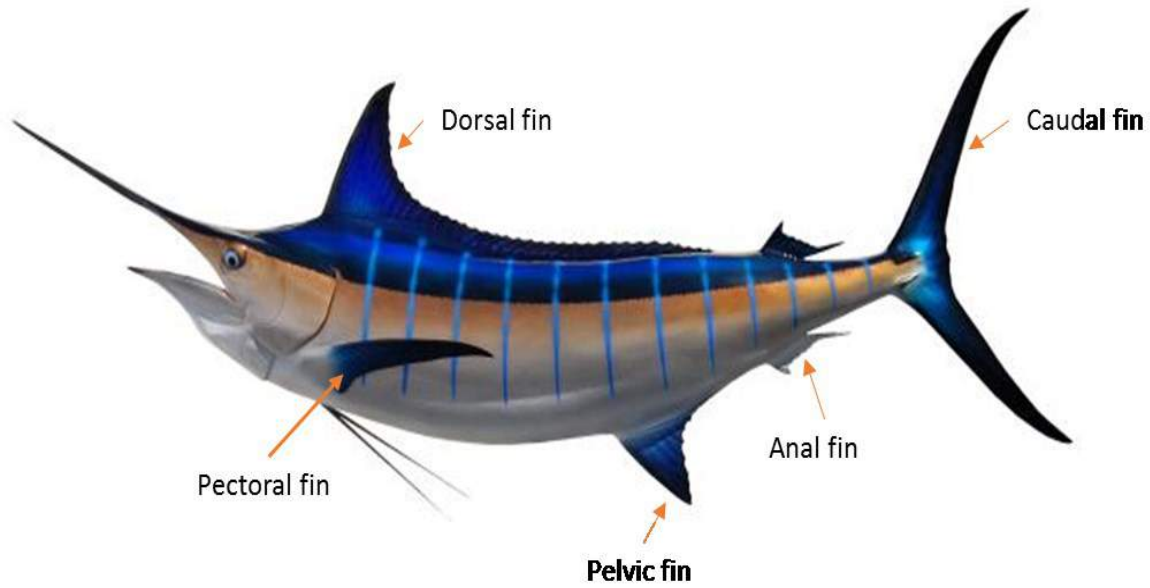


**Figure 38 The Blue Marlin Fish with its fins representing its propulsion movements (after King Sailfish Mounts, 2014)**

The pectoral and pelvic fins contribute to the manoeuvrability to swim at low velocity marine currents, with 'the caudal fin' actually causing the essential thrust for propulsion (Tokic & Yue, 2012). The caudal fin propulsion may represent a ship's rudder at high speed or an airplane movement operating with the same forces like pitch and thrust, including the transfer mechanisms like drag and lift (Figure 39). The pressure-related forces drag and lift originate due to the water flow acting on the fish body. This propulsion is also termed as the Body and/or Caudal Fin (BCF) propulsion, which may cause surface area increment or decrement; thus, the swimming movements may differ from species to fish species.

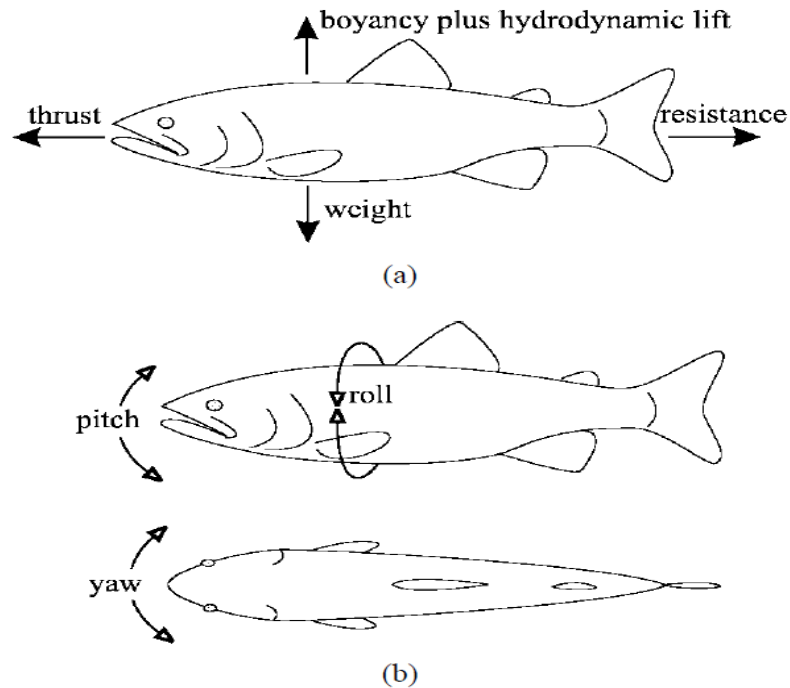


**Figure 39** the locomotion forces acting on the fish whilst swimming (Sfakiotakis et al., 1999)

Different fish species employ different swimming methods, the two most commonly employed marine vertebrates are 'Body and/or Caudal Fin (BCF), and Median and/or Paired fin (MPF) propulsion' (Sfakiotakis *et al.*, 1999). Greater thrust, and acceleration are generated by BCF, whilst MPF offers greater propulsion efficiency at low speeds.

#### 2.5.4.2.1 Pectoral Fins

Pectoral fins are located at the 'ventrolateral margin' of the fish body and vary with size, shape and function amongst different marine vertebrates as demonstrated in the Figure 40. The fundamental function of the pectoral fin is generating dynamic lift which allows fishes like sharks to maintain manoeuvrability at certain depths, and thus the dexterity to survive (Wilga & Lauder, 2001). The pectoral fins automatically adjust the angle of attack of the flow in order to create upward lift, thus act as an elementary fish propulsion fin. Figure 40 illustrates the evolution of the pectoral fins in different fish species.

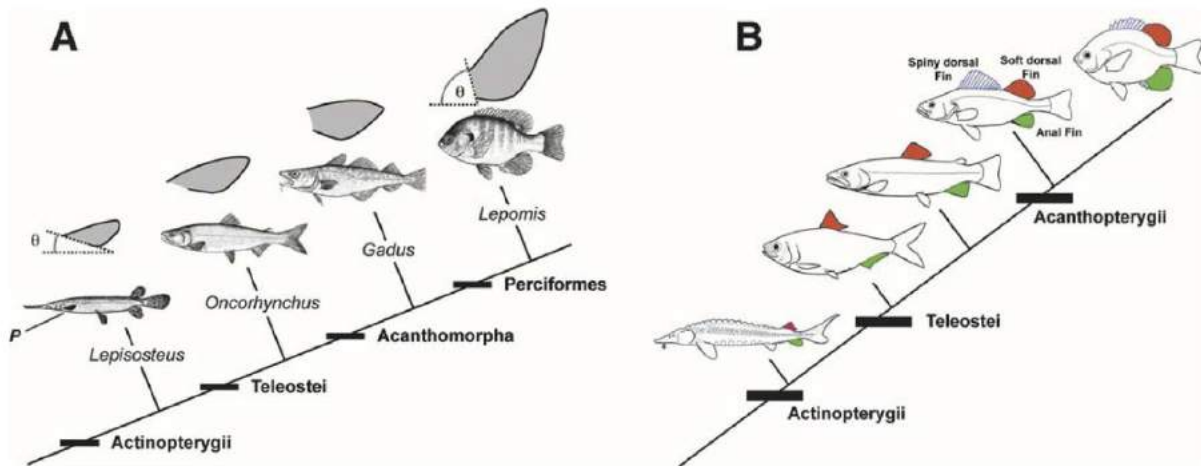


**Figure 40** the evolution of the pectoral (A), and dorsal (B) fins in different species (Jayne *et al.*, 1996)

#### 2.5.4.2.2 Pelvic, Dorsal and Anal fins

The pelvic fins are based near the mid fish body, and below the pectoral fins ventrally, the pelvic fins are relative to the centre of mass of the fish body which varies between different species like the pectoral fins. The pelvic fins boost fish from moving up and down to the water flow, and also avoid stopping quickly, by providing the braking power (Salumae & Kruusmaa, 2011). Dorsal fins are the easiest to locate in marine vertebrates as they are found in the dorsal part of the spinal cord in fish. The dorsal fins protect the fish from rolling, and help in turning, thus controlling the body at low speeds or to a complete stop (Jayne *et al.*, 1996). The anal fins are located ventrally in the anus region of the fish, and help managing the body orientation to maintain the stability when the swimming velocity increases (Zhou *et al.*, 2008).

#### 2.5.4.2.3 Caudal Fin and Caudal Fin propulsion

The caudal fin, which is also termed the tail fin, is located at the end of the fish's body (caudal pinnacle), and is the main fin that produces thrust propulsion through seawater. The caudal fin like pectoral fins come in various shapes, and sizes in different species. The caudal fin oscillates with the horizontal movements to produce the propulsion efficiency by accelerating the body forward in the seawater. The caudal fin based propulsion is caused due to the undulation in the fish body and this is represented by the Body Caudal Fin (BCF) propulsion. The undulatory swimming locomotion is divided into the following sections (Windsor *et al.*, 2010), and is demonstrated in Figure 41.

## 2. Seawater Environment, Hydrodynamics of Horizontal Axis Tidal Turbines, and Bio-mimicry

- 1) **Anguilliform:** In this type of undulatory swimming, the fish completes one wavelength with their entire body i.e. swimming is possible via both forward and backward movements for fishes like eels, and other jawless fishes.
- 2) **Carangiform and Subcarangiform:** The undulatory fish locomotion in this type is performed similarly to the Anguilliform type but these two types also form the hybrid type of swimming locomotion, due to 75% of the body being used to propagate the wave amplitude. The caudal fin thrust propulsion of this type is usually seen in trout.
- 3) **Thunniform:** This type of swimming mode is the most powerful and efficient marine vertebrate locomotion which is lift based thrust generation occurring due to the caudal fin. The evolution of Thunniform locomotion is found in sharks, marine mammals and other fishes, this thus allows the marine vertebrates to maintain high speed swimming under low water velocities as well. In the Blue Marlin fish the thrust propulsion is 80% efficient based on the caudal fin, and despite swimming at high speed its body is optimised for efficient locomotion in calm waters, as well as turbulent waters.

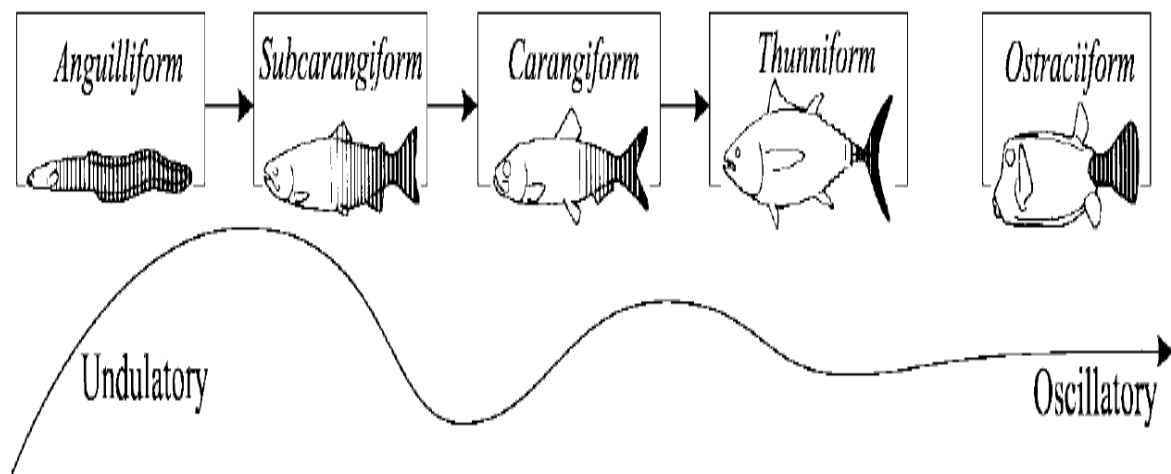


**Figure 41 Different swimming modes of fishes (Sagong *et al.*, 2013)**

The propulsive efficiency of the marine vertebrates is given in the Equation 19 (Suleman & Crawford, 2008; Shirgaonkar *et al.*, 2008):

$$\eta = \frac{W_{out}}{W_{out} + E_{lw}} \quad \text{Eqn. 17}$$

where,  $W_{out}$  is the work energy output of the marine vertebrate, and  $E_{lw}$  is the energy lost in the water due to fish locomotion.

The propulsive efficiency of the Thunniform (based on the caudal fin thrust propulsion) fishes like The Blue Marlin, Swordfish, Sailfish, and the Sunfish ranges in between “0.85 to 0.91 %” (Barbara *et al.*, 1992; Watanabe & Sato, 2008; Luthy, 2004).

### 2.5.5 Justification of the fish selection

Bio mimicking is a prominent trend in the aerospace industry, as morphing the aircraft wing design continues to change based on the shapes of bird’s wings (Abdulrahim and Lind, 2004). Modern aircraft designs are specifically morphed to make them highly adaptable to produce maximum lift and twisted for drag reduction for e.g. when eagles (Figure 42) are observed in the flight their wings are broadened when they are high in the sky, and when they are gliding their wings attempt to reduce the drag and thus increase the lift. By using the bird wing morphing principles the aircraft wings are highly adaptable to highly unsteady, time-differing, and uncertain dynamics, which also causes weight reduction and wingspan gaining enough lift and thrust (Han *et al.*, 2009). The Progress Eagle (US Army conventional UAV) uses ultralight materials in its designs, uses solar energy during flight and is also an example of bird morphing.

The aerospace industry inspires the wind turbine industry for turbine blade design. Airfoil theory is used to design fixed wing aircraft, whilst Helicopter blades and Wind turbine blades are designed using a more complex Blade Element Momentum theory to predict the aerodynamic forces. Helicopter blades which are stiff and have high aspect wing ratio rotate at a high speed to produce enough force. As illustrated in Figure 42, Whale humpbacks have recently inspired the creation of bio-mimicked helicopter and wind turbine blades to reduce the skin friction, and drag (Fish, 2006; Bhusan, 2009). Thus morphing the blade shapes to a humpback tubercles increased the efficiency of the blades by additional 20%, compared with the standard blade types in both the cases. Other examples which are inspired from aquatic animals are robotic fish (gold shiner fish inspiration), and school fish movement to understand the complex fish swimming in the water currents, and Lilly Impeller (Nautilus shell inspiration) for efficient energy water mixing in the storage tanks.

Marine vertebrates have the functionality to force their bodies throughout the ocean, and with the help of their fins they create lift, and thrust based propulsion as the water currents advance through their body (Flammang, 2013). As illustrated in the Figure 40, the fins of a marine vertebrate evolve in order to increase the efficiency while swimming, with the caudal fin at particular angles decreasing the drag force, thus resulting in lift increment (Salumae and Kruusmaa, 2011). The advantage of the drag decrement at the effective angles of a caudal fin is the ability of the marine

vertebrate is to push its body through the water currents at acute angles without losing the ability of propulsion (Liu and Hu, 2005). The increment in lift from the caudal fin propulsion means that more power is generated through the caudal fin propulsion which decreases the drag as the marine vertebrate propagates through marine currents, and there is less opposing force (Jayne and Block, 1996). The pelvic and anal fins work by creating vortices behind the caudal fin which change the pressure distribution over the caudal fin, but the caudal fin maintains its balance through an extensive range of angles of attack (Luthy, 2005; Shirgaonkar et al., 2008).

The same principles could be applied in designing the horizontal axis tidal turbine blades inspired by a curved caudal fin: the friction between seawater currents and turbine blades would be reduced and the advancing turbine blades would rotate faster with less seawater current required to turn a turbine. Thus bio mimicry proves an excellent motivation to improve the tidal turbine efficiency, which is inspired from the wind turbine industry in this research. An attempt is made in this PhD thesis to design and analyse a curved caudal fin look-alike turbine blade, to improve the default straight tidal turbine blade.

2. Seawater Environment, Hydrodynamics of Horizontal Axis Tidal Turbines, and Bio-mimicry

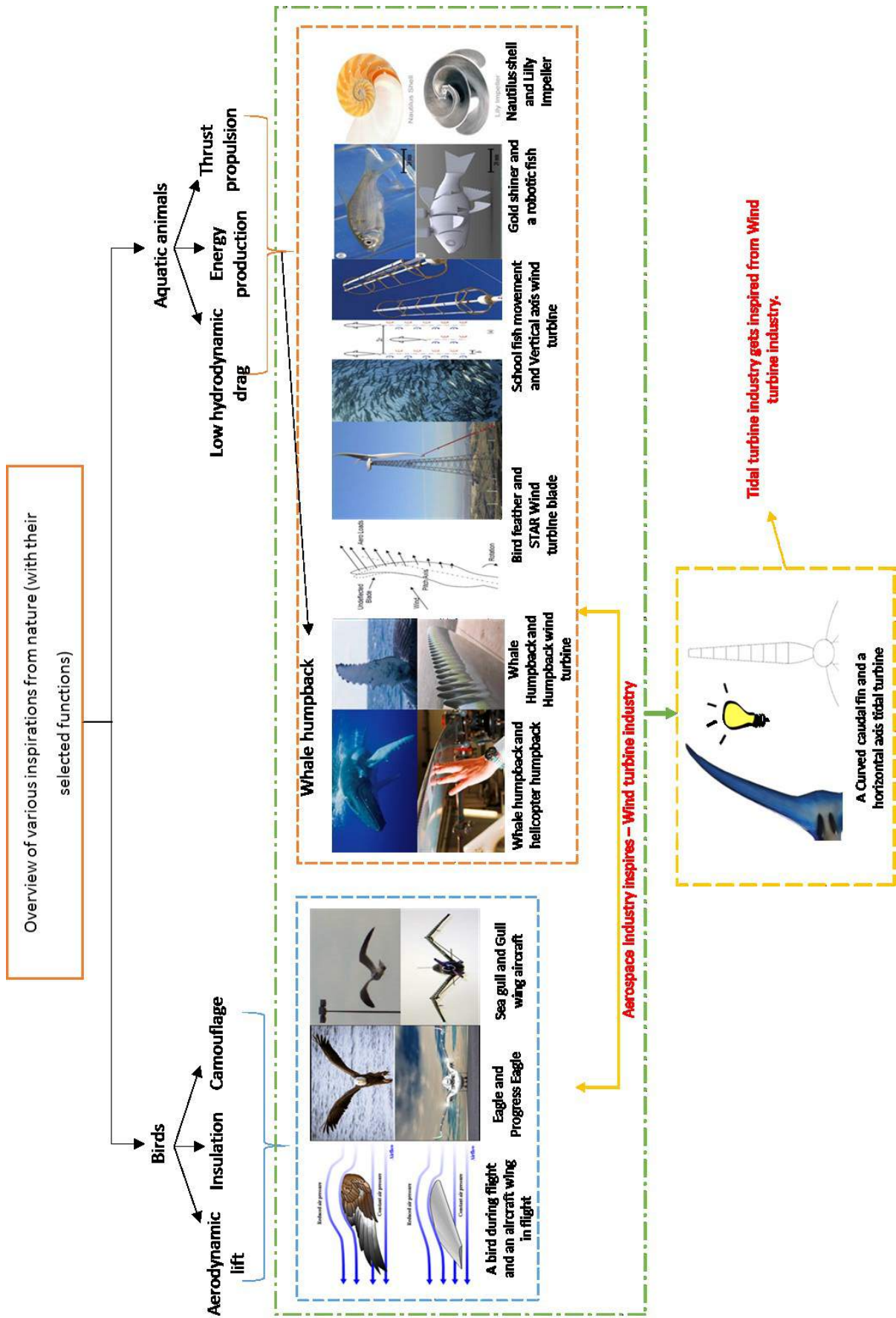


Figure 42 Biologically inspired application within various industries

## 2.6 Chapter summary

The above chapter examined the literature on the seawater environment, design and hydrodynamics of the tidal turbines, with a specific focus on HATT's along with their working principles. The numerical tidal characteristics that define the importance of site selection for the installation of the tidal turbine blades were also demonstrated. A brief literature review on bio-mimicry was also carried out to present the synopsis on the marine vertebrates. The non-dimensional forces like Lift, Drag, Power and Thrust coefficients were also explicitly discussed, along with the justification of the fish caudal fin to design a HATT. Finally, the important sensitivities related to the seawater environment, and HATT's were identified to perform sensitivity and comparative analysis at later stages of this research. The following chapter examines the background theory on Computational Fluid Dynamics, CFD analysis procedure and it concludes with the describing CFD based design methods applied in the tidal turbine blade industry.

## 3 Application of Computational Fluid Dynamics in tidal energy

### 3.1 Introduction

This chapter examines background theory in Computational Fluid Dynamics (CFD) and the understanding of CFD methods applied in tidal energy. This chapter starts with the description of the basic fluid dynamics theory and then follows on to turbulence modelling in CFD. The discretisation methods used in CFD, Errors and Uncertainties in CFD modelling are also explained. The CFD code used in this thesis is ANSYS CFX; the problem solving steps are also mentioned. This chapter concludes by explaining the CFD based design methods applied in tidal energy.

### 3.2 Principle CFD theories

The mathematical aspects of modelling any flow problem are based on the three laws of conservation:

- 1) Conservation of mass (continuity equation): The conservation of the mass can be mathematically represented as the continuity equation which is “in the given fluid volume, the rate of increase of mass inside that volume must be equal to the net mass flow rate into the volume across its face” (Versteeg & Malalasekera, 2007). Hence the continuity equation for a compressible fluid can be stated as:

$$\frac{\partial \rho}{\partial t} + \nabla \cdot (\rho \mathbf{u}) = 0 \quad \text{Eqn. 18}$$

In the case of an incompressible fluid the density  $\rho$ , is constant Eqn. 18 simplifies to;

$$\nabla \cdot (\mathbf{u}) = 0 \quad \text{Eqn. 19}$$

where  $\rho$  is the density of the fluid,  $u$  is the velocity of the fluid.

- 2) Conservation of momentum (Newton’s second law): The conservation of momentum can be derived by applying Newton’s second law, which states that the rate of change of the momentum for a fragment of fluid is equal to the sum of the forces on the fluid fragment. Hence the emerging momentum equations can be stated as.

$$\rho \frac{\partial \mathbf{u}}{\partial t} = \nabla \cdot (\boldsymbol{\tau}_{ij}) \quad \text{Eqn. 20}$$

But, the derivative on the left hand side of the equation 20 uses the particle derivative hence,

### 3. Application of Computational Fluid Dynamics in tidal energy

$$\frac{D}{Dt} = \frac{\partial}{\partial t} + (\mathbf{u} \cdot \nabla) \quad \text{Eqn. 21}$$

But for a Newtonian fluid i.e. the viscosity in the fluid is assumed to be constant and is also related to the linear strain rates in the fluid. Therefore the stress tensor can be defined as:

$$\tau_{ij} = -p\delta_{ij} + \mu \left( \frac{\partial u_i}{\partial x_j} + \frac{\partial u_j}{\partial x_i} \right) + \delta_{ij}\lambda_v \nabla \cdot \mathbf{u} \quad \text{Eqn. 22}$$

where,  $\lambda_v$  is the bulk viscosity of the fluid.

Thus after further simplifies to;

$$\rho \frac{\partial \mathbf{u}}{\partial t} = -\nabla p + \frac{\partial}{\partial x_j} \left[ \mu \left( \frac{\partial u_i}{\partial x_j} + \frac{\partial u_j}{\partial x_i} \right) + \delta_{ij}\lambda_v \nabla \cdot \mathbf{u} \right] \quad \text{Eqn. 23}$$

where, P is the pressure and  $\mu$  is the fluid viscosity. The left hand side of the above equation demonstrates the momentum variation with respect to the fluid acceleration. The right hand side of the equation represent the pressure gradient forces and also the tangential shear stresses. Assuming, both density and viscosity are constant Equation 23 becomes:

$$\rho \frac{\partial \mathbf{u}}{\partial t} = -\nabla p + \mu \nabla^2 \mathbf{u} \quad \text{Eqn. 24}$$

In the case of incompressible fluids, Eqn. 24 and the continuity equation coupled together can be solved for velocity and pressure. When considering temperature, in CFD analysis it can be combined together as well by using the energy equation mentioned in next section.

- 3) Conservation of energy (Energy is conserved): The law of conservation states that the total energy in a closed system is constant, it cannot be created nor can be destroyed, it can only be transformed from one form to another this is also called as the first law of thermodynamics Hence for a thermodynamically closed system the mathematical energy equation is:

$$\rho \frac{\partial e}{\partial t} = \frac{\partial}{\partial x_j} \left( k \frac{\partial T}{\partial x_j} \right) - \nabla \cdot (\rho \mathbf{u}) + \frac{\partial (u_i \tau_{ij})}{\partial x_j} \quad \text{Eqn. 25}$$

where E is the fluid specific energy (sum of kinetic and potential energy).

Considering the effects of static, total enthalpy and specific energy of the fluid (Patankar, 1980).

$$\frac{\partial (\rho h_0)}{\partial t} + \nabla \cdot (\rho h_0 \mathbf{u}) = \frac{\partial}{\partial x_j} \left( k \frac{\partial T}{\partial x_j} \right) + \frac{\partial p}{\partial t} + \frac{\partial (u_i \tau_{ij})}{\partial x_j} \quad \text{Eqn. 26}$$

When considering the thermal effects, the energy equation becomes the product of the kinetic energy and the velocity of the fluid.

$$\rho \frac{\partial e}{\partial t} = \frac{\partial}{\partial x_j} \left( k \frac{\partial T}{\partial x_j} \right) - \nabla \cdot (\rho \mathbf{u}) + \frac{\partial (u_i \tau_{ij})}{\partial x_j} \quad \text{Eqn. 27}$$

The above equations form an integral part of the CFD analysis, and are later used develop the foundations of the CFD analysis in Chapter 6.

### 3.3 Turbulence modelling in CFD

#### 3.3.1 Turbulent and Laminar Flow

Turbulence is the most general aspect occurring during the fluid motion in engineering practice, in which fluid gains rapid motion overlapping on the steady flow. This effect was first carried out by Osborne Reynolds in the 1880's and who established the discrepancy between laminar and turbulent flow through his experiments. A dimensionless number was later proposed as a result of those experiments which was named after him and called 'Reynolds number'. The Reynolds number is defined as "the ratio of the inertial forces to viscous forces in the given flow (Falkovich, 2011)" and is calculated using Equation 28.

$$Re = \frac{\rho V L}{\mu} \quad \text{Eqn. 28}$$

where  $\rho$  is the fluid density,  $V$  is the free stream velocity of the fluid,  $L$  is the characteristic length of the flow and  $\mu$  is the dynamic viscosity of the fluid. When the Reynolds number is low ( $Re < 2100$ , flow in a pipe with no interruptions between the layers) the fluid flow is called 'laminar flow'. Thus the heat and mass transfer and the diffusive transport of the momentum result in low velocity and pressure of the fluid which are independent from time (Date, 2005). When the Reynolds number is high ( $Re > 4000$ , for flow in a pipe when there is chaotic disruption between the layers) the fluid flow is called 'turbulent flow'. This results in low diffusion of momentum and rapid increase in velocity and pressure both in space and time. Figure 43 shows the laminar and turbulent flow as performed by Osborne Reynolds experiment.

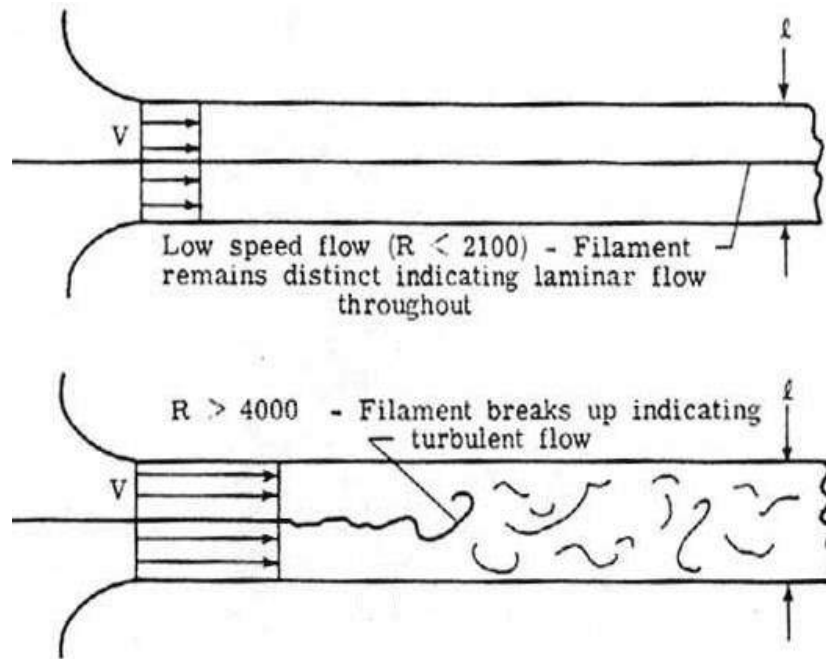


**Figure 43 Laminar and Turbulent flow (Reynolds, 1883)**

Therefore the turbulent flow for turbines can be stated as follows (Afgan *et al.*, 2013):

“The occurrence of turbulent flow in the rotation of turbine blades experiencing the irregular flow in which various fluid variables show arbitrary variation with time and space”.

Thus turbulent flow can occur either as the fluid progresses through a solid surface or in parallel streams when two fluids of same kind flow over one another. Swirling eddies of different sizes are incorporated in the turbulent flow condense the energy from mean flow through the process of vortex shedding as a result of energy dissipation. In turbulence modelling the turbulent flow is classified into two types as wall turbulence and free turbulence. Air flowing through the wing of an aeroplane and the flow expanding in pipe are two classic examples of shear flow on the turbulent wall as demonstrated in Figure 45. The turbulent wake formed behind a bluff body and turbulent jet nozzle discharges are examples of turbulence flow which aren't circumscribed as demonstrated in Figure 44.

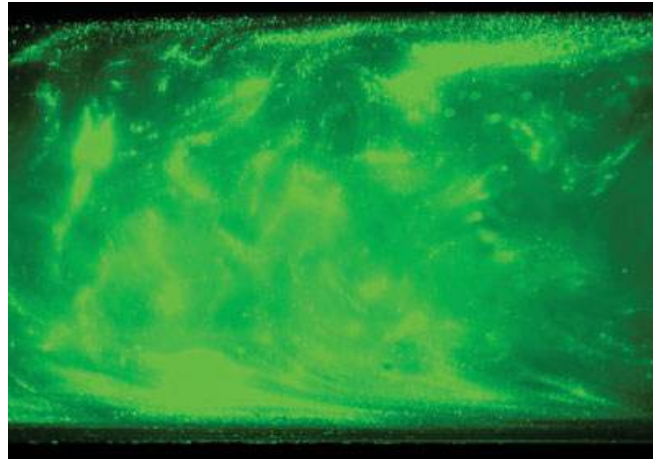


Figure 44 Wall turbulence in a pipe (Lathrop, 2006)

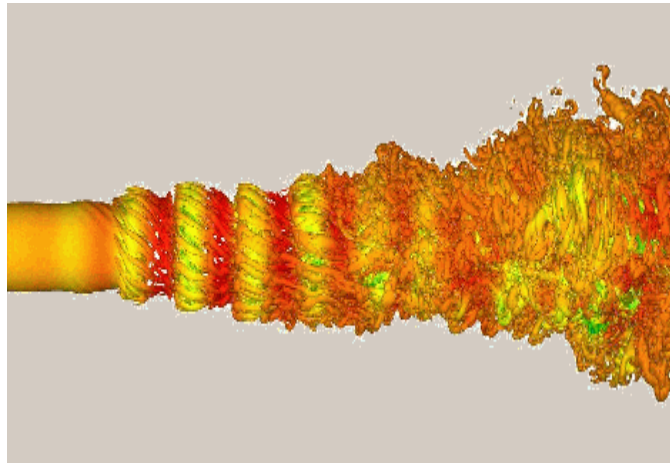


Figure 45 Free turbulence in a jet (Buhler *et al.*, 2010)

### 3.3.2 Numerical description of turbulence

The basic numerical descriptions of turbulence start with introducing the theory of turbulence termed as 'Reynolds decomposition which separates the average and fluctuating parts of a quantity'. For example, consider a flow variable  $\phi$  into the sum of a mean component  $\bar{\Phi}$  and a zero mean component  $\phi'$  which varies and fluctuates with time:

$$\phi(t) = \bar{\Phi} + \phi'(t) \quad \text{Eqn. 29}$$

where

$$\bar{\Phi} = \frac{1}{\Delta t} \int_0^{\Delta t} \phi(t) dt \quad \text{Eqn. 30}$$

### 3. Application of Computational Fluid Dynamics in tidal energy

The time interval  $\Delta t$  should be compelling. In theory,  $\Delta t \rightarrow \infty$  but practically it is impossible to have  $\Delta t$  'larger' than the largest eddies ( $t_1$ ) which give significant results, and thus this interprets the steady mean flows. For transient mean flows  $\Delta t$  should be 'smaller' than the time scales related to the mean flows ( $t_2$ ). Findikakis & Street (1982) suggest that  $t_1$  and  $t_2$  should diverge in 'considerable' orders of magnitude. In order to describe variances of the kinetic energy and its fluctuations on the velocity components it is defined as the kinetic energy contained in turbulence per unit mass:

$$ke = \frac{1}{2} (\overline{u'^2} + \overline{v'^2} + \overline{w'^2}) \quad \text{Eqn. 31}$$

Another equation which explains the variances of the fluctuations of the velocity, which is the square root of the variance velocity referenced through mean velocity:

$$Tur = \frac{(\frac{2}{3} ke)^{1/2}}{V_{in}} \quad \text{Eqn. 32}$$

where  $V_{in}$  is the inlet velocity.

This then allows clarifying the addition of the steady velocity components by taking the mean value and results in unsteady term are called "Reynolds Stresses".

#### 3.3.3 The Reynolds-Averaged-Navier-Stokes (RANS) equations

Traditional approaches to turbulence modelling began with time-averaging the equations of fluid motion and decomposition of Reynolds number, through which the instantaneous flow variables are disintegrated into its time-averaged and fluctuating quantities. Considering the momentum velocity variables  $u$  (mean component) and  $u'$  (fluctuating component) and time averaging them with an integral operation and commutative differentiation and as  $\bar{u}$  the fluctuating component is equal to zero in order to derive the time averaged mass and momentum equations (for an incompressible Newtonian fluid):

$$\mathbf{u} = \bar{\mathbf{u}} + \mathbf{u}' \quad \mathbf{v} = \bar{\mathbf{v}} + \mathbf{v}' \quad \mathbf{w} = \bar{\mathbf{w}} + \mathbf{w}' \quad \mathbf{p} = \bar{\mathbf{p}} + \mathbf{p}' \quad \text{Eqn. 33}$$

Thus using these notations the time averaged continuity equation for the mean flow can be written as:

$$\nabla \cdot (\bar{\mathbf{u}}) = 0 \quad \text{Eqn. 34}$$

and the time averaged momentum equation:

$$\rho \frac{\partial \bar{\mathbf{u}}}{\partial t} + \rho \frac{\partial}{\partial x_j} \overline{(u'_i u'_j)} = -\nabla \cdot \bar{\mathbf{p}} + \mu \nabla^2 \bar{\mathbf{u}} \quad \text{Eqn. 35}$$

which are generally known as the Reynolds-Averaged-Navier-Stokes (RANS) equations.

Due to the involvement of the product of two fluctuating velocities, there is an additional term associated with the turbulent eddy convective momentum transfer, called as Reynolds Stress:

$$\rho \frac{\partial \bar{u}}{\partial t} = -\nabla \cdot \bar{p} + \nabla \cdot \tau_{ij} \quad \text{Eqn. 36}$$

where

$$\tau_{ij} = \mu \left( \frac{\partial \bar{u}_i}{\partial x_j} + \frac{\partial \bar{u}_j}{\partial x_i} \right) - \rho \overline{u'_i u'_j} \quad \text{Eqn. 37}$$

The Newtonian viscous stress results in six additional turbulent stresses called as Reynolds stresses:

$$\tau_{xx} = -\rho \overline{u'^2} \quad \tau_{yy} = -\rho \overline{v'^2} \quad \tau_{zz} = -\rho \overline{w'^2} \quad \text{Eqn. 38}$$

and the three shear stresses:

$$\tau_{xy} = \tau_{yx} = -\rho \overline{u'v'} \quad \tau_{xz} = \tau_{zx} = -\rho \overline{u'w'} \quad \tau_{yz} = \tau_{zy} = -\rho \overline{v'w'} \quad \text{Eqn. 39}$$

The 'Reynolds stresses' are essentially non-zero values as they are the 'mean forces (per unit area) introduced on the mean flow by squared velocity fluctuations in turbulence'. The Reynolds stresses are coherent structure of turbulent flows and has additional unknowns due to their nature and thus results in the development of Reynolds stress turbulence models, which are discussed in following sections.

## 3.4 Turbulence models

### 3.4.1 Introduction

Versteeg & Malalasekera (2007) define turbulence modelling as 'A turbulence model is a computational procedure to close the system of mean flow equations, so that a more or less wide variety of flow problems can be calculated.' In tidal turbine simulations, while using CFD software they are simulated under the turbulent flows, mostly the turbulence variations are not of interest only the effects are sought after. Turbulence modelling is frequently used to clarify the solution of the governing equations of the turbulent flow, thus reducing the computational cost, but these turbulence models are required to substitute the scales of flow not necessarily resolving it). Turbulence models are also treated as 'semi-empirical' based on the presumption of the turbulent flow conditions.

### 3.4.2 The Boussinesq approximation

Turbulence modelling i.e. Reynolds stress modelling was first exercised by Joseph Boussinesq and hence the concept the ‘eddy viscosity’ was developed in 1887. Boussinesq recommended that turbulent (Reynolds) stresses are directly proportional to the mean flow of the closed system. As a result of Boussinesq’s hypothesis the turbulent eddy viscosity was introduced i.e.  $\mu_t > 0$ . Now the gradients can be written as:

$$\tau'_{ij} = -\rho \overline{u'_i u'_j} = \mu \left( \frac{\partial \bar{u}_i}{\partial x_j} + \frac{\partial \bar{u}_j}{\partial x_i} \right) - \frac{2}{3} \rho k \delta_{ij} \quad \text{Eqn. 40}$$

where,  $k = \frac{1}{2} (\overline{u'^2} + \overline{v'^2} + \overline{w'^2})$  is the turbulent kinetic energy, and  $\delta_{ij}$  is the Kronecker delta.

In Equation 40, also known as ‘The Boussinesq approximation’, the turbulent viscosity although not a fluid property has the same units and molecular viscosity and varies with the boundary condition of turbulent flow. The Kronecker delta assures the accurate formulation of the Reynolds stresses.

### 3.4.3 Prandtl’s mixing length models

Ludwig Prandtl in 1904 introduced a further concept of mixing length for simple 2D wall bounded thin shear flows where eddy viscosity varies to a distance from the wall and dissipation of turbulence is balanced everywhere. Thus the additional concept of ‘mixing length’ which includes axisymmetric jets, wakes and mixing boundary layers are the examples of the flows. Prandtl’s mixing length model for the turbulent eddy viscosity in the thin shear wall is given by:

$$\mu_t = \rho l_m^2 \left| \frac{\partial \bar{u}}{\partial y} \right| \quad \text{Eqn. 41}$$

where,  $\frac{\partial \bar{u}}{\partial y}$  is the partial derivative of the stream wise velocity ( $\bar{u}$ ) w.r.t y direction of wall,  $l_m$  is the mixing length, which varies according to the flow type.

As turbulence is a result of unsteady behaviour of flow, if it changes then mixing length model accounts those changes by changing  $l_m$ . The mixing length model is also known as the ‘law of the wall’, which is very precise for wall-bounded flow field problems which have small pressure gradients. The flows experiencing high turbulence i.e. recirculating flows (flows at higher angle of attack) the mixing length model gives incorrect results. As the mixing length model is incompetent of characterising flow separation and only calculates the mean flow characteristics of turbulent shear stress, it results in formation of accurate description of higher turbulence models which are described in following sections.

### 3.4.4 The turbulent kinetic energy governing equations

As a substitute for the mixing length model, it is a common practice to use turbulent kinetic energy in conservation equation to solve the additional transport phenomenon. To derive the equation for turbulent kinetic energy which is proportional to the square root of the kinetic energy of the fluctuating velocity a scalar product is taken with the Navier-Stokes equations and then it is subtracted from the fluctuating velocity vector from the RANS equations. Therefore the turbulent kinetic energy equation for an incompressible fluid after consequential adjustment:

$$\frac{\partial(\rho k)}{\partial t} + \nabla \cdot (\rho k \bar{u}) = \nabla \cdot \left( \underbrace{-\overline{p'u'}}_{(I)} + \underbrace{2\overline{\mu u's'_{ij}}}_{(IV)} - \underbrace{\frac{1}{2}\overline{\rho u'_i u'_i u'_j}}_{(V)} \right) - \underbrace{2\overline{\mu s'_{ij} \cdot s'_{ij}}}_{(VI)} - \underbrace{\overline{\rho u'_i u'_j} \cdot S_{ij}}_{(VII)} \quad \text{Eqn. 42}$$

In Equation 42  $\rho, U_j, k$  are the ‘knowns’ which are of interest for calculation. The ‘k equation’ also contains several higher orders of fluctuating velocity components which are of no interest as they cannot be resolved.

The **III – V** quantities serve as the transport/diffusion processes and modelled using gradient-diffusion assumptions.

The **VI** quantity represents the turbulent kinetic energy viscous dissipation which is the product of  $\rho$ , and the rate of turbulent kinetic energy per unit mass  $\epsilon$ :

$$\epsilon = 2\nu \overline{s'_{ij} \cdot s'_{ij}} \quad \text{Eqn. 43}$$

### 3.4.5 Standard k-ε model

The k-epsilon (k-ε) turbulence model is the most popular and used in CFD to analyse and simulate the turbulent flow conditions. It is a two-equation turbulence model as it describes the result for conservation equations using two transport equations k and epsilon. Launder *et al.*, (1975) developed this model which is an improvement to the mixing length model as it has good stability for high Reynolds number turbulent flow. The first transport model k-equation arbitrates the energy from the turbulent kinetic energy equation and is described as turbulent kinetic energy (k). The second transport model is the dissipation of turbulence (ε), which describes the rate at which turbulent kinetic energy dissipates. The experimental form for the standard k-ε model can be described as (Wilcox, 1994):

For turbulent kinetic energy  $k$ ,

$$\frac{\partial(\rho k)}{\partial t} + \nabla \cdot (\rho k \bar{u}) = \nabla \left[ \frac{\mu_t}{\sigma_k} \nabla \cdot k \right] + P - \rho \epsilon \quad \text{Eqn. 44}$$

For dissipation  $\epsilon$ ,

$$\frac{\partial(\rho \epsilon)}{\partial t} + \nabla \cdot (\rho \epsilon \bar{u}) = \nabla \left[ \frac{\mu_t}{\sigma_\epsilon} \nabla \cdot \epsilon \right] + C_{1\epsilon} \frac{\epsilon}{k} P - C_{2\epsilon} \rho \frac{\epsilon^2}{k} \quad \text{Eqn. 45}$$

where,  $u_i$  is the velocity component in parallel direction,  $E_{ij}$  is the rate of deformation,

$$\mu_t = C_\mu \rho \frac{k^2}{\epsilon} \text{ is the eddy viscosity, and } P = 2\mu_t S_{ij} \cdot S_{ij}$$

The above values are defined after iterating for numerous simulations of ‘data fitting’ for various range of turbulent flows. The  $k$ - $\epsilon$  is based on the Bousinessq’s approximation and gives excellent results for industrial flows, but gives poor performance to rotating and swirling flows i.e. fully developed flows in non-circular ducts.

#### 3.4.6 Wilcox’s $k$ - $\omega$ model

The Wilcox  $k$ - $\omega$  turbulence model is one of the first two-equation turbulence models projected to use the  $k$  (resolves the energy in turbulence) as one of the transport variable which is the turbulent kinetic energy and, the second transport variable  $\omega$  is the specific dissipation per unit kinetic energy generally termed as the frequency of the turbulence (Wilcox, 2008). This turbulence model also reports the developments of convection and diffusion of the turbulent energy. The fundamental advantage of the  $k$ - $\omega$  turbulence model is it can be integrated throughout the wall as it does not require usage of wall damping function. Kolmogorov first practised the use of variable  $\omega$  and is defined as  $\omega = \frac{\epsilon}{\beta k}$  where,  $\beta$  is a constant (Tikhomirov, 1991).

Turbulence Kinetic Energy:

$$\frac{\partial(\rho k)}{\partial t} + \nabla \cdot (\rho k \bar{u}) = \nabla \left[ \mu + \frac{\mu_t}{\sigma_k} \nabla \cdot k \right] + P - \beta^* k \omega \quad \text{Eqn. 46}$$

Specific Dissipation Rate:

$$\frac{\partial(\rho \omega)}{\partial t} + \nabla \cdot (\rho \omega \bar{u}) = \nabla \left[ \mu + \frac{\mu_t}{\sigma_\omega} \nabla \cdot \omega \right] + \gamma_1 (2\rho S_{ij} \cdot S_{ij} - \frac{2}{3} \rho \omega \frac{\partial \bar{u}_i}{\partial x_j} \delta_{ij}) - \beta_1 \rho \omega^2 \quad \text{Eqn. 47}$$

#### 3.4.7 Shear Stress Transport (SST) model

The SST model was developed by Menter (1993); it assimilates the inner and outer region of boundary layer in between the eddy viscosity and full turbulent viscosity formation. The SST model

draws up the best effects of k-ε (accurate precision of results in the far field region) and k- ω (good accuracy in providing results in the near wall region) it being used as low Reynolds number model without any blending functions changes the cross term function) also prevents being too sensitive to ‘inlet free stream turbulence’.

$$\begin{aligned} \frac{\partial(\rho\omega)}{\partial t} + \nabla \cdot (\rho\omega\bar{u}) & \qquad \qquad \qquad \text{Eqn. 48} \\ & = \nabla \left[ \mu + \frac{\mu_t}{\sigma_{\omega,1}} \nabla \cdot \omega \right] + \gamma_2 \left( 2\rho S_{ij} \cdot S_{ij} - \frac{2}{3} \rho \omega \frac{\partial \bar{u}_i}{\partial x_j} \delta_{ij} \right) - \beta_2 \rho \omega^2 \\ & + 2 \frac{\rho}{\sigma_{\omega,2} \omega} \frac{\partial k}{\partial x_k} \frac{\partial \omega}{\partial x_k} \end{aligned}$$

### 3.4.8 Large eddy simulation (LES)

Large eddy simulation (LES) is a higher Reynolds stress than has been discussed until now, also a popular turbulence model to solve the problems of turbulent flow. It was developed by Joseph Smagorinsky in 1963 to compute atmospheric air currents (Smagorinsky, 1963). LES functions on the Navier-Stokes equations to cut down the total time of the turbulent flow solution and hence reduce the computational over-head. The primary application of LES is based on ‘low pass filtering’ while other turbulence models discussed until now use time-averaging method to isolate the small and large scale eddies. This principle is applied to the Navier-Stokes equations to exclude the small scale eddies in the turbulent flow solution, and this reduces the computational overhead and thus remodelling the governing equations for the velocity field.

The LES procedure begins with election of a filtering function and an assertive cut-off width to produce the solution of a transient solution of all eddies with a length scale greater than the cut off width. After the election of the filtering function is completed, a spatial filtration procedure is performed on the time-dependent equations. The spatial filtering operation demolishes the small scale eddies in the turbulent which aren’t necessary for the calculation, thus allowing the flow configurations of the complex geometries like turbulent jets, turbines, vehicles with landing gears etc. The following sections describe the properties like Spatial Filter, governing equations involved in LES and numerical methods of LES (only two main types are covered due to scope of this project):

In LES, spatial filter can be applied by modes of a ‘filter function’ on the temporal field and implement a spatial filter procedure. The filter function is defined as:

$$\bar{\phi}(x, t) = \int_{-\infty}^{\infty} \int_{-\infty}^{\infty} \int_{-\infty}^{\infty} G(x, x', \Delta) \phi(x', t) dx'_1 dx'_2 dx'_3 \qquad \qquad \qquad \text{Eqn. 49}$$

where  $\overline{\phi}(x, t)$  is the filtered function,  $\phi(x, t)$  is the original (unfiltered) function, and  $\Delta$  is the cut-off filter width.

The two of the most common filtering functions for 3D LES simulations are box-filter

$$G(\mathbf{x}, \mathbf{x}', \Delta) = \begin{cases} 1/\Delta^3 & |\mathbf{x} - \mathbf{x}'| \leq \Delta/2 \\ \mathbf{0} & |\mathbf{x} - \mathbf{x}'| > \Delta/2 \end{cases} \quad \text{Eqn. 50}$$

and Gaussian filter:

$$G(\mathbf{x}, \mathbf{x}', \Delta) = \left(\frac{\gamma}{\pi\Delta^2}\right)^{\frac{3}{2}} \exp\left(-\gamma \frac{|\mathbf{x} - \mathbf{x}'|^2}{\Delta^2}\right) \quad \text{Eqn. 51}$$

The two important sub-grid-scale (SGS) LES turbulence models are described below:

#### The Smagorinsky-Lilly SGS model:

Smagorinsky (1963) proposed that the smallest eddies are isotropic and Boussinesq's hypothesis proves it. The Smagorinsky- Lilly SGS model was developed by Smagorinsky (1963), but the first LES simulation was simulated by Deardorff (1970) and is based on the Prandtl mixing length model to define the kinematic SGS viscosity summarised below:

$$\tau_{ij} = -2\mu_{SGS}\overline{S}_{ij} + \frac{1}{3}\tau_{ii}\delta_{ij} = -\mu_{SGS}\left(\frac{\partial\overline{u}_i}{\partial x_j} + \frac{\partial\overline{u}_j}{\partial x_i}\right) + \frac{1}{3}\tau_{ii}\delta_{ij} \quad \text{Eqn. 52}$$

The eddy viscosity in Smagorinsky-Lilly is described as:

$$\mu_{SGS} = \rho(C_{SGS}\Delta)^2|\overline{S}| \quad \text{Eqn. 53}$$

The Smagorinsky constant  $C_{SGS}$  usually has the values in between 0.17 – 0.21

#### Germano dynamic model:

Lilly (1992) proposed distinct decomposition to higher SGS turbulent stresses called Dynamic sub-grid scale model (DSGS) also called as Germano dynamic model. The DSGS model may be seen as an alteration to the Smagorinsky model, as it allows changing the Smagorinsky constant ( $C_{SGS}$ ) which varies in time and space. In DSGS,  $C_{SGS}$  is simulated per region and in each time-step based on two filters of flow variables which are defined as and also called as Germano identity:

$$L_{ij} - \frac{1}{3}L_{kk}\delta_{ij} = C_{SGS}^2 M_{ij} \quad \text{Eqn. 54}$$

where  $M_{ij} = -2\Delta_2^2|\overline{S}|^2\overline{S}_{ij} + 2\Delta_1^2|\overline{S}|^2\overline{S}_{ij}$

### 3.4.9 Flow modelling near the turbulence wall

Near wall (point  $P_w$ ) modelling of turbulent flow can be done via two techniques, being ‘low Reynolds number’ and ‘wall functions’. These approaches are resolution separated for near-wall shear stress boundary conditions, and are viscosity affected. Firstly, in the low Reynolds number modelling technique, the viscous layer is simulated numerically which includes the viscous sub layer ( $y_w^+ < 2$ ) and in boundary conditions for inlet velocity  $V_{in} = 0$ . In this approach, mixing length, one-equation, two equation turbulence models are evenly simulated across the entire turbulent near wall region. While simulating the turbulent using this approach, sometimes variations in the model coefficients might be required to obtain the high accuracy in the turbulent viscosity near wall area. Secondly, wall functions (which are also called as ‘high Reynolds number’) this ‘treatment’ was developed to reduce the computational overhead related to the thin layer in the equilibrium of the turbulent flows. When using wall functions in 3D turbulent flows with fine grids it increases the computational time for the near wall turbulence region. The distance between the grid point and the sub viscous wall must be  $y_w^+ > 35$  using the log law of the wall, and implementing the low Reynolds number can provide great accuracy. In the following sections, near wall treatments for k-omega turbulence models (SST K-omega included), and for LES models are discussed:

#### 3.4.9.1 Near wall flow modelling for k-omega models

As mentioned above, the wall function technique is established in the near wall flow behaviour, which can make simulations unresponsive w.r.t the mesh refinement of the wall. The boundary conditions for  $\kappa$  (kinetic eddy viscosity) and  $\omega$  are demonstrated below:

$$\frac{\partial k}{\partial n} = 0 \quad \frac{\partial \omega}{\partial n} = 0 \quad \text{Eqn. 55}$$

where,  $n$  is the boundary normal.

The centroid values for the cells adjacent to solid walls are defined as:

$$k_p = \frac{u_T^2}{\sqrt{C_\mu} y_p}, \quad \omega_p = \frac{\sqrt{k_p}}{C_\mu^{\frac{1}{4}} k y_p} \quad \text{Eqn. 56}$$

In ANSYS CFX, both standard k- $\omega$  and the SST K- $\omega$  models are available to simulate low and high Reynolds number. The boundary conditions for  $k$  and  $\omega$  are kept the same as in for k equation in k-epsilon. For ‘wall function meshes’  $y_w^+$  at the adjoining wall should be in the order of  $y_w^+ = 1$ , and for transient overlapping boundary layer, according to the log law it should be  $30 < y_w^+ < 300$  (CFX-Solver Theory guide, 2006).

### 3.4.9.2 *Near wall flow modelling for LES models*

Near wall flow modelling for LES is done by computing the eddy viscosity constraints. By applying the log-law wall to the fine mesh the universal wall distance becomes:

$$y_w^+ = \frac{y C_\mu^{1/4} k^{1/2}}{\nu} \quad \text{Eqn. 57}$$

Balaras and Benocci (1994) proposed a two layer zonal approach, which simulate the wall shear stresses in the LES zone to extract a separate modelling process. The wall shear stress can be obtained using the log law of the wall, this approach was later proved by Tessicini et al. (2005), in the study presented the wall shear stresses are typically solved at  $y_w^+ = 50$ . The turbulent boundary layer eddy viscosity later becomes:

$$\frac{\mu_t}{\mu} = k y_w^+ (1 - e^{-y_w^+/A})^2 \quad \text{Eqn. 58}$$

## 3.5 Discretisation in CFD

The partial differential equations (PDE's) which are also known as the governing equations of the fluid dynamics. Mathematical solutions for Navier-Stokes equations only prevail for simple cases such as flow in a pipe. As computers only understand numerical data and can manipulate accordingly the PDE's are discretised in both time and space to solve them. This operation of transformation of PDE's is called 'numerical discretisation'. The numerical discretisation in the unsteady terms always incurs errors which can be minimised to average levels; discretisation of the transient terms is done with respect to time in an imperceptible control volume and is called as 'discretisation in time'. The major techniques in CFD used for discretisation are Finite Element Method (FEM), Finite Difference Method (FDM), and Finite Volume Method (FVM). FEM and FDM are discussed briefly, while FVM is explained in more detail as it serves to be the most popular method used in CFD for discretisation.

### 3.5.1 Finite Element Method (FEM)

FEM is a mathematical technique for simulating the boundary value problems of differential equations. When using FEM, the domain is divided into small elements over the sub-domains, which use the calculus of variations to decrease the amount of errors to produce a steady solution. Initial values of the dependent variables are calculated based on the node elements. The dependent variables are then varied systematically (by assembling the global matrices) in whole domain and all the element equations are combined for the final calculation. The correspondences between these

dependent variables are considered only when the boundary conditions are enforced on the element equations massed into matrices.

The finite element method attains the equations for each independent element of the entire domain, where the residual errors which are caused due to the trial function are constructed into elemental part of the 'inner product'. The most common application of FEM is known as Finite Element Analysis (FEA), which is used in calculating the engineering performance of complicated domains like gas pipelines and cars (where domain changes during moving boundaries).

#### 3.5.2 Finite Difference Method (FDM)

The finite difference method uses Taylor series to convert partial differential equations into a numerical scheme by approximating the derivatives of an operator to at numerous points which vary in space and time. When using FDM, the computational domain is divided in space and time and the approximations are computed in space or time points for each of the variable. A differential operator determines the error in between the mathematical solution and the actual solution, which is termed as discretisation error.

#### 3.5.3 Finite Volume Method (FVM)

The Finite Volume method is the most prominent discretisation methods applied in numerical simulations of CFD. The FVM is established on the control volume formation of the computational domain where the domain is divided in different number of cells and elements; this method is roughly similar to the Finite Element method. Once the control volume (CV) is divided in to many mesh constituents (elements), the governing equations in their differential form which are integrated over each control volume to satisfy the laws of conservation. The primary advantage of FVM is that it conforms the final solution satisfies all the conservations laws of mass, momentum and energy 'for any number of control volumes' (Eymard *et al.*, 2008). ANSYS CFX (the CFD verification software used in this project) employs the finite element method to determine the shape functions for the source term discretisation, while solving the PDE's which consist of coefficients of discontinuity. Figure 46 demonstrates the 2D surface mesh elements over a CV.

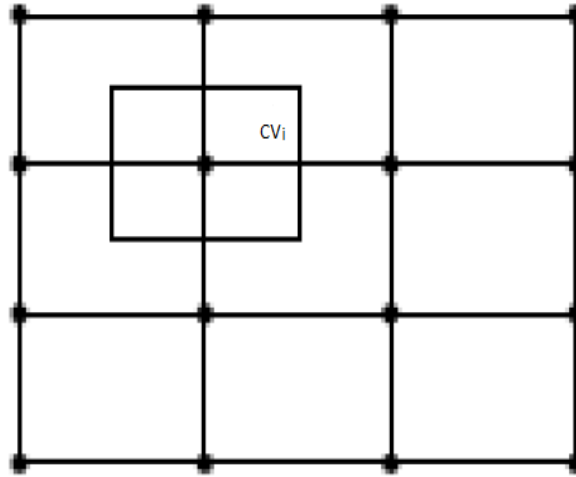


Figure 46 A 2D control volume with mesh elements

FVM converts the integral form of the governing equations identically as in FEM and those mathematical equations gives values of the adjoining points. Considering the discretisation of partial differential equations over a control volume:

$$\frac{d}{dt} \int_V \rho dV + \int_S \rho U_j dS_j = 0 \quad \text{Eqn. 59}$$

where  $V$  and  $S$  are the volume and surface regions of the control volume integration respectively.

$$\frac{d}{dt} \int_V \rho \bar{u}_i dV + \int_S \rho \bar{u}_j \bar{u}_i dS_j = - \int_S P dS_j + \int_S \mu_{eff} \left( \frac{\partial \bar{u}_i}{\partial x_j} + \frac{\partial \bar{u}_j}{\partial x_i} \right) dS_j + \int_V S_{M_i} dV \quad \text{Eqn. 60}$$

Equation 60 is obtained using 'Gauss's divergence theorem' over the control volume surface  $dV$  which also serves as the beginning point of the finite volume method.

The transient and the source terms in the control volume around the control volume are approximated, with the inclusion of the shape functions. Generally, the nodes in Equation 60 are tetrahedrons, hexahedrons, prism elements.

### 3.5.4 Transient term

The transient term in the governing equations are discretised in time in order to take the transient (temporal) effects into consideration for incompressible flows. The temporal effects are generally are simulated over each time step and the time difference being  $\Delta t$  thus the temporal discretisation for an incompressible flow, which is time dependent can be expressed as:

$$\frac{d}{dt} \int_V \rho \phi dV = V \frac{(\rho \phi)^{n+\frac{1}{2}} - (\rho \phi)^{n-\frac{1}{2}}}{\Delta t} \quad \text{Eqn. 61}$$

where  $n + \frac{1}{2}$  and  $n - \frac{1}{2}$  are the start and end of the time steps respectively.

The start and end of time steps for the First Order Backward Euler scheme are using the old and current time steps and are discretised as:

$$\frac{d}{dt} \int_V \rho \phi dV = V \left( \frac{\rho \phi - \rho^0 \phi^0}{\Delta t} \right) \quad \text{Eqn. 62}$$

The start and end of time steps for the Second Order Backward Euler scheme are discretised as:

$$(\rho \phi)^{n-\frac{1}{2}} = (\rho \phi)^0 + \frac{1}{2} ((\rho \phi)^0 - (\rho \phi)^0) \quad \text{Eqn. 63}$$

$$(\rho \phi)^{n+\frac{1}{2}} = (\rho \phi) + \frac{1}{2} ((\rho \phi) - (\rho \phi)^0) \quad \text{Eqn. 64}$$

### 3.5.5 Convection term

The convection term in the Navier-Stokes momentum equation is discretised by integrating the point values of the fluxes to the velocity components surrounding in the control volume as the momentum equation is linearized by mass flow rates. Now, integrating  $\phi$  over control volumes gives us the values of the velocity components at the grid nodes. This method which describes the face values in a given control volume for the adjacent nodal values is called ‘advection scheme’ calculated by  $\phi_{ip}$  as described in Equation 65:

$$\phi_{ip} = \phi_{up} + \beta \nabla \phi \cdot \Delta \vec{r} \quad \text{Eqn. 65}$$

where,  $\phi_{up}$  is the upwind node value,  $\beta$  blending factor constant and  $\Delta \vec{r}$  is the upwind node vector to the integration point. Depending on the numerical scheme chosen,  $\beta = 0$  for the first order upwind scheme, and  $\beta = 1$  for the central difference scheme. For CFD simulations in this PhD project used is ‘High Resolution scheme’ as it calculates the  $\beta$  value as closer to 1 without experiencing any non-physical oscillations, which is accurately bounded.

### 3.5.6 Pressure-Velocity coupling

Pressure quantity in the transport equation do not conform the transport equation therefore it is laterally given by the continuity equation. “When the accurate pressure is displaced in the momentum equation, the resulting velocity field satisfies the continuity-mass equation” (Eesa,

2009). Hence, while simulating the incompressible flows, velocity and pressure are coupled by an algorithm where the initial pressure is guessed to give the precise value of velocity to give ‘pressure correction’. Patankar (1980) states “the formation of this pressure field can give rise to the ‘checkerboard’ pressure field effect”. In CFX, Rhie Chow algorithm is employed to couple pressure and velocity. The guessed pressure can be calculated using the central difference method for the given control volume and can be described as:

$$u_e = \frac{u_P + u_E}{2} + \frac{1}{2}(d_P + d_E)(p_P - p_E) - \frac{1}{4}d_P(p_W - p_E) - \frac{1}{4}d_E(p_P - p_{EE}) \quad \text{Eqn. 66}$$

where  $u_e$  is the face velocity directly linked with pressure difference ( $p_P - p_E$ ) across the face  $e$ .

The three pressure terms shown in the equation 68 are the addition of a higher order term, and thus assuming the Rhie-Chow’s face velocity  $u_e$  interpolation:

$$u_e = \frac{u_P + u_E}{2} + \frac{d}{4}[4(p_P - p_E) - (p_W - p_E) - (p_P - p_{EE})] \quad \text{Eqn. 67}$$

where the pressure term is  $\frac{d}{4}(p_{EE} - 3p_E + 3p_P - p_W)$

### 3.6 Errors and uncertainty in CFD

The quality of the CFD simulation results depends on the severity of uncertainty and on the aggregate response of the errors. There are many causes for error and uncertainty in CFD analysis, which can be classified according to the rudiments for estimating these errors which can be minimised through verification and validation. The terms error, uncertainty, verification and validation are described in the following sections. An error can be defined as “A recognizable deficiency in any phase or activity of modelling and simulation that is not due to lack of knowledge” (Mehta, 1998). An uncertainty can be defined as “A potential deficiency in any phase or activity of the modelling process that is due to the lack of knowledge” (Mehta, 1998). The best practice and guidelines on CFD analysis are specified by American Institute of Aeronautics (AIAA, 1998), and European Research Community on Flow, Turbulence and Combustion (ERCOTAC, 2000) both are widely accepted and practised. Versteeg & Malalasekera (2007, in chapter 10) also provide a good reference on this topic.

#### 3.6.1 Differentiating errors and uncertainties

Errors can be differentiated as ‘local’ and ‘global’ errors. Local errors are referenced to a grid cell, whereas global errors are referenced to errors which occur in the entire computational flow domain.

An error can be further subcategorised as acknowledged error or unacknowledged error. Generally errors can be eliminated, but uncertainties cannot be.

#### 3.6.2 **Physical Modelling errors**

Physical modelling errors can be defined as an uncertainty in the actual flow exact solution of conservative equations due to studious simplifications of the model. These errors emerge due to choosing wrong turbulence model equations. Mehta (1998) states that error arise if the flow phenomenon is not understood properly, or the parameters used in the physical model are inappropriate. For instance, if  $k - \varepsilon$  turbulence model is used to model the flow behaviour of the boundary layer involving pressure gradient will always give wrong results.

##### 3.6.2.1 ***Round-Off computing errors***

Round-off computing errors occur due to floating numbers on the computer as the real numbers can only be stored in a computer using a finite level of accuracy. Nowadays, due to availability of the higher computational resources, the numbers are stored using '32 bits' or '64 bits', in commercial CFD codes with the results precision being 7 to 16 digits. Round-off computing errors are not compelling when correlating with other errors; these errors are usually considered important when calculating the difference between arithmetic operations. For example when a CFD user attempts to simulate the flow problem using a coarse mesh a residual can be of zero residual.

All the CFD simulations performed in this project were run using double precision, as the certainty of the geometric calculations was taken into consideration. These calculations were done when the solver settings were specified which included the range of the turbine mesh (meters) for the turbine and seawater domain.

##### 3.6.2.2 ***Iterative error of Convergence***

Iteration errors occur due to the iteration method difference between the exact solution and the when the iteration is stopped eventually. The error significance is measured after the completion of the simulations, by monitoring the variations of equation residuals. This error is often called as the Convergence error.

##### 3.6.2.3 ***Discretisation error***

Discretisation errors are defined as the errors which occur during the exact solution of the governing flow equations, and with the other turbulence models of the algebraic expression system in finite

### 3. Application of Computational Fluid Dynamics in tidal energy

volume of space and time. The mesh domain discreteness is demonstrated by time step involved. The discretisation error is also called as the 'numerical error', which also serves as the most major concerned error in CFD analysis, because the quality of CFD analysis is defined from the quality of the grid. When the mesh is refined it is naturally expected that the solution should become less responsive to the grid sensitivity and converge to continuum solution. This is also called as 'the grid convergence'.

#### 3.6.2.4 *Programming errors*

Programming errors occur due to the mistakes made while writing the CFD code, as it is the sole responsibility of the CFD programmers. Code errors can also be difficult to find, which often takes systematic reviewing of the parts of the code or sometimes entire code.

#### 3.6.2.5 *User errors*

User errors occur when the CFD codes are dealt improperly which automatically produces inaccurate solutions. Usage errors can occur during the generation of the model, grid generation or at the post-processing stage of the CFD analysis. These errors can be minimised by proper training and the CFD experience.

### 3.6.3 **Verification and Validation**

After describing the errors and uncertainty in CFD modelling; verification and the validation of the CFD analysis performed becomes necessary to prove the quality of the results obtained. Oberkamp & Tocarno (2002), and Mehta (1998) made a quality assessment and their terminologies are widely accepted in CFD research community.

#### 3.6.3.1 *Verification*

Verification can be defined as "The process of determining that a model implementation accurately represents the developer's conceptual description of the model and the solution to the model" (Mehta, 1998). The verification procedure begins with assessing the error occurred quantitatively during the discretisation of fine grids, implementation of the turbulence models, and errors while programming the CFD codes. Generally, grid refinement study is performed to describe and point out the errors. The spatial discretization error is analysed by simulating the grids to different resolutions which thus increases the computational overhead while increasing the options in CFD code. In CFX, Richardson exploration is used to estimate the far-field boundary error.

#### 3.6.3.2 **Validation**

Validation can be defined as “The process of determining the degree to which a model is an accurate representation of the real world from the perspective of the intended uses of the model” (Mehta, 1998). Validation in CFD refers to comparison of the CFD simulation with the experimental data in order to examine the modelling errors. CFD results validation against experimental data can be difficult sometimes as the available experimental data might be limited or is complex. Validation can also be defined as “solving the right equations” which also recognises the quantified errors and the uncertainty in CFD simulations. Oberkampf & Trucano (2002) demonstrated that validating CFD simulations against experimental data can be complicated, as the poor experimental data may scatter the CFD simulations.

### **3.7 Application of CFD in turbine blade design**

This section examines the background on CFD and its application in tidal turbine blade design studies. Generation of power from tides is very expensive and requires abundant money to build and manufacture tidal turbines. The entire tidal turbine system consists of turbine, a gearbox, an electric generator, and a control unit. Computational Fluid Dynamics is considered as a powerful means to provide a picture of the tidal turbine behaviour i.e. by plotting velocity, pressure graphs. The application of CFD in turbine blade design studies is a developed field of research and the concerned literature is very extensive. Hence, the main aim of this section was to explore the turbulence model selections, design variable selection, concerned TSR's, the non-dimensional distances from the inlet and outlet boundaries that have been used previously and advantages when compared with the experimental data (when available). However, the data occupied from the sources cited provide some or most of the needed information, for CFD simulations are discussed below.

#### **3.7.1 CFD in the tidal energy conversion**

Batten *et al.* (2008) developed a numerical model based on the BEM validated it with the experimental data achieved from tests carried out in a cavitation tunnel (by the same authors). The parametric deviations of the 3D rotor model including TSR and blade number were varied with different tidal velocities to predict the power and thrust values. Further qualitative appraisal was carried out by to predict the cavitation thus illustrating that output power reduces at higher TSR. Bahaj *et al.* (2006) designed a horizontal axis turbine to demonstrate the common characteristics in wind energy which are transported in tidal energy which is based on the conversion of kinetic energy

### 3. Application of Computational Fluid Dynamics in tidal energy

to electrical energy. The investigations of torque and thrust parameters were performed in a cavitation tunnel at QinetiQ, Haslar. Their studies concluded demonstrating tidal turbines should be designed within the range of  $TSR > 7$ , designing the turbine blades above that limit predicts acute drop in power and thrust of the turbines. Wang *et al.*, (2010) presented a 2D CFD investigation on the unsteady flow around NACA 0012 airfoil at low Reynolds number ( $Re < 10^5$ ). They simulated two sets of oscillating patterns with different frequencies, numerically. They concluded that CFD predicting the vortex shedding flow structure validates with experimental data when the blade is at very high angle of attack. They also commented on various numerical techniques like DNS, LES and RANS stating that DNS and LES despite being the most advanced turbulence models which all the time and space scales are resolved, are computationally more expensive. They concluded with saying SST-  $k-\omega$  model (which is used for the steady state CFD simulations in this research) predicts reasonable accuracy over  $k-\omega$  model with the experimental results for development of flow transition of high angles of attacks.

Having described the working theory of RANS and LES turbulence models in *Section 3.4*, it is now possible to investigate the application of these models in tidal turbine blades which have been used previously and their success when compared with the experimental data. The principal importance for the selection of these turbulence models are due to mesh definition and the generation of cells on the airfoil used. The references reviewed in following section give information with an examination of the details (CFD simulations). These sources provide almost all the information which is required to discuss the properties of RANS and LES. The characteristics of LES and RANS which include the treatment of flow from laminar to transition in the boundary layers are also demonstrated in Table 4.

Table 4 Summary of the SST and LES simulations from the literature with the data analysed

Data	Turbulence model	Flow velocity (m/s)	Turbine type	CFD/Experimental Based validation	Reference
$C_L, C_D, C_P$	SST	2	HATT	CFD and Experimental	Goundar and Ahmed (2013)
$C_{thrust}$ , cavitation, $C_{pre}$ , $C_P$	k-epsilon	-	HATT	CFD and Experimental	Wu <i>et al.</i> (2013)
$C_{thrust}$ , cavitation, Cpressure, $C_P$	k-epsilon	3	HATT	CFD - BEM	Masters <i>et al.</i> (2013)
$C_{Thrust}$ , $C_P$	SST and LES	-	HATT	CFD and Experimental	Afgan <i>et al.</i> (2013)
$C_T, C_P$	SST	2.5	HAWT	CFD and Experimental	Costa-Rocha <i>et al.</i> (2014)
$C_P, C_{Thrust}$ , cavitation	SST	-	HATT	CFD and Experimental	McSherry <i>et al.</i> (2011)
$C_P$	LES	10	VAWT	CFD	Li <i>et al.</i> (2013)
$C_L, C_P$	SST	3-6	HATT	CFD-BEM	Jo <i>et al.</i> (2014)
$C_P$ and various TSR	k-epsilon and SST	10	VAWT	CFD	Almohammadi <i>et al.</i> (2013)
$C_P$ and Power	SST	2.5	HATT	CFD	Kim <i>et al.</i> (2012)
$C_P$ , torque, Power	LES	1 and 2.1	HATT	CFD and Experimental	Kang <i>et al.</i> (2012)

### 3. Application of Computational Fluid Dynamics in tidal energy

The quantitative results accessed by Goundar & Ahmed (2013) analysed the characteristics of a 10m diameter 3 bladed HATT which gave the maximum efficiency of 47.5% at 2m/s. The tip of the blade was designed using a thinner airfoil with thickness of 24% to ensure that the blades do not experience cavitation. The TSR chosen was 4. The performance of the airfoils which behave differently whilst the turbine blade rotates and when is still, was accessed based on the lift, drag forces acting on the blade and the torque generated through the mechanical power. The mesh was generated using ANSYS ICEM CFD (12C x 20C rectangular grid), which was very fine near the blade wall region to obtain precise results, but no  $y^+$  values were given in the source. The CFD maximum efficiency, power output obtained from this research were later compared with the results accessed by Goundar & Ahmed (2013).

Wu *et al.* (2013) designed a highly efficient tidal stream turbine by changing the chord length distribution and the low stream velocity, using the Glauert theory. The tidal turbine designed by Wu *et al.* (2013) was to be installed in China, where the speed of the tidal currents in most of the areas are slow, therefore the turbine was designed to operate at a low speed in order to produce required torque and hence mechanical power. The data tidal turbine blade performance was accessed based on the pressure and lift coefficients hence demonstrating the two most important sensitivities that cause cavitation studies at different angles of attack especially for the leading edge.

An analytical study coupling BEM-CFD modelling was performed by Masters *et al.* (2013) on a tidal stream turbine to analyse the wake performance in non-uniform flow. To investigate the flow velocity speed across the complete flow domain, a mesh dependency study was carried out to demonstrate; when using the two different profile with same coarse mesh settings produces small changes in the power coefficients of the two different rotors. Their findings demonstrated the sensitivity analysis of wake dynamics (flow behaviour) on the tidal stream turbine deployment, by emphasizing the need of tidal site investigations before deployment of the actual tidal turbine in that site. The mesh dependency test for Straight blade case studies is also performed in this research to demonstrate whether the varying mesh resolution affects the overall efficiency.

A comparison between RANS (SST) and LES numerical solutions was presented by Afgan *et al.* (2013) for a 3 bladed HATT, validating the implemented sliding mesh technique for the unstructured mesh code over a range of TSR's. The CFD simulations were run using open source CFD code solver - *Code\_Saturne*. The accuracy of the LES solver was tested against the optimum design condition, investigating the wake and turbine performance. Costa Rocha *et al.* (2014) carried out a numerical investigation and calibrated SST turbulence model to test the operational performance of a 'small scale horizontal axis wind turbine (SS-HAWT).' They studied aerodynamic performance of the SS-

### 3. Application of Computational Fluid Dynamics in tidal energy

HAWT based on the turbulence intensity and characteristic length and varied  $\beta^*$  (*turbulence modelling constant*) which affects the friction over the blades. Grid sensitivity analysis exhibiting the  $y^+$  of less than 5, including the blade tip to eliminate the discretisation error from the solution, and thus reduce the computational burden. The sliding mesh procedure,  $y^+$  values, the turbulence model comparison (SST vs LES), pressure velocity coupling used by the above mentioned authors forms the basis of the CFD simulations presented in *Chapter 6* of this research.

McSherry *et al.* (2011) compared and validated thrust and power coefficients of a 3D CFD tidal turbine model with the laboratory experiments of the identical turbine also considering the mesh resolution and time step convergence in their studies. The power and thrust coefficients were measured for a range of pitch angles and tip speed ratios which had good agreement with the experimental data especially at 15° and 20° of pitch angle. The turbulence model used to model the pressure and near wall effects was ANSYS's Shear Stress Transport (SST) as it models the effect of turbulence and flow near airfoil surface accurately. This paper was of particular interest in this research, mainly because of the steady state CFD analysis done using ANSYS CFX, SST turbulence model, boundary conditions, unstructured mesh settings, and observations of thrust and power coefficients which have a major influence on the five steady state analysis case studies in this research.

Li *et al.* (2013) compared three different CFD modelling approaches on a vertical axis wind turbine in higher angles of attack. The aerodynamic definition of a straight bladed involving NACA 0018 foil was simulated using Large Eddy Simulation (LES) of high angle of attack flow. In symmetrical airfoils the stall angles appear in between 10° to 15. The computational domain was discretised using Finite volume method based in ANSYS FLUENT, and O-grid topology was adopted to reduce the number of grids and thus avoiding the far wake in the grid. The authors also commented on the efficacy of the SST turbulence model and considered it to be assuring when simulating the adverse pressure gradients in incompressible flow, but when compared SST to LES; LES is computationally more challenging than SST but produces more realistic 3D vortex diffusion and flow separation in unsteady flow computations. Force coefficients were calculated in the span wise distribution of the airfoil blades, thus proving LES as a better high fidelity CFD modelling technique than the traditional RANS approaches; which is also demonstrated by this research in the *Chapter 6*.

Jo *et al.* (2014) designed a horizontal axis tidal turbine based on BEM and calculated its efficiency performance to 40% with choosing 5 as the tip speed ratio. They also investigated the wake distribution in the unsteady velocity flow affecting the tidal turbine system. The CFD analysis was performed using SST turbulence model and the curves of  $C_p$  and torque generated from the shaft

### 3. Application of Computational Fluid Dynamics in tidal energy

were presented for different velocities. The airfoils were arranged in a sequential order with appropriate twist angles and chord lengths to predict the tidal turbine performance using CFD to predict its torque and  $C_p$ .

Almohammadi *et al.* (2013) examined four numerical techniques i.e. Grid Convergence Index (GCI), the fitting method, mesh refinement and General Richardson Extrapolation (GRE), to produce a mesh separated solution and for VAWT and generate power curve using CFD. The CFD solution was produced using two turbulence models, SST and RNG  $k - \epsilon$  turbulence models to compare the mesh independent convergence studies. They achieved the mesh independent solution after converging the mesh solution and examining the iterative convergence error. The power coefficient was predicted using the GRE method based on two functions of convergence criteria and the accuracy order of the solution obtained, and the power curve was obtained using the fitting method for both first and second order solutions of fitting method. The mesh dependent solutions which are adequately covered in their studies also share the same focus of the mesh independent study performed in this research.

A bi-directional vertical axis turbine performance was analysed by Kim *et al.* (2012) which was to be employed in a larger area of tidal channel. Hexahedral mesh was applied in the augmentation channel, and SST turbulence model was selected for turbulence modelling. The flow velocity increased massively through the augmented flow channel when the rotors were equally placed in the simulated tidal channel. Kang *et al.* (2012) simulated 3D turbulent flow around an axial tidal turbine, placed on the rectangular bed comprising of an open channel accommodating the CFD domain to carry out LES simulations. The convoluted turbine geometry comprising rotor and stator components with moving boundaries were managed by engaging the curvilinear immersed boundary (CURVIB) method. The CFD simulations were compared to the Marine Hydropower Turbine (MHK) by Verdant Power, New York, USA using systematic grid refinement and calculating the torque sensitivity analysis. The simulations of the turbine indicate pressure fields near the turbine blades generate the torque and extract power from the water column.

From the literature examined in the above section, it can be clearly seen that SST turbulence model is the most popular turbulence model used in the steady state analysis of tidal turbine blades, other parameters mesh type and size,  $y^+$  values, far-field boundary distances from the turbine blades play a pivotal role in the accurate prediction of power, torque, lift and drag coefficients. In the present context of study, SST turbulence model is used for the steady state, and LES-Smagorisky is used for transient analysis of all the designed blades, a mesh dependence study for the examination of the Straight blade at coarse, medium, and fine mesh sensitivities using SST, and  $k - \epsilon$  turbulence

models and is conducted to demonstrate the changes of power output and power coefficient for the designed blade.

#### 3.7.2 CFD based design studies in tidal energy

As the concept of tidal energy comparatively new to other renewable energy sources, this attracts researchers to focus on developing new blade configurations to give more power. Tidal turbine blade design studies are generally performed using blade element theory, which acquires the two-dimensional data engaged in the airfoils and the blade design is generated by considering the conservation of momentum along the entire rotor. This design studies approach is very fast and hence it has been widely used in blade design including the CFD analysis. Fugslang & Madsen (1999) designed a wind turbine blade using blade element theory by modifying the chord lengths of airfoils and their twist angles. Conventional blade design approaches like BEM theory combined with CFD analysis in design studies have been analysed in tidal turbine industry and have proven to be powerful and efficient for design and analysis of the tidal turbine blades.

In tidal turbine blade design, the design procedure can be explained in four stages: geometry creation, numerical (CFD) simulation, post-process operation. Generation of the blade geometry is a method related to transcribe the airfoil surface into numbers, which are then used as constraints (variables) in the design-analysis procedure. The sources provide almost all the information which is required to discuss the application of CFD based design in tidal turbine blades are highlighted in Table 5. The primary reason of investigating the sources mentioned in the Table 5, is to identify design variables combined with the traditional CFD-BEM methods that affect the overall power coefficient when designing and analysing a tidal turbine blade configuration.

**Table 5 Summary of the CFD based design techniques used in the literature with the data analysed**

Data	Design study method	CFD/Experimental Based validation	Turbine type	Reference
Chord length, blade thickness, $C_p$ , Safety factor, Blade weight	CFD-FEA	CFD and Experimental	HATT	Liu & Veitch (2012)
$C_D$ , $C_L$ , $C_P$	BEM-CFD	CFD	HAWT	Bavanish & Thygarajan (2013)
$C_{pre}$ $C_p$ and angular velocity	CFD based parametrisation	CFD	HATT	Liu & Bose (2013)
$C_D$ , $C_L$ , Power, Cpressure	BEM-CFD	CFD and Experimental	HAWT	Rajakumar & Ravidran (2012)
Torque, Power, $C_M$ , TSR	Traditional CFD	CFD	VATT	Asim <i>et al.</i> (2013)
Torque, Power, Pressure drop	Traditional CFD	CFD	HATT	Wang <i>et al.</i> (2012)
Chord length, twist distributions, and Power	EA-CFD-BEM	CFD and Experimental	HAWT	Benini & Toffolo (2002)

### 3. Application of Computational Fluid Dynamics in tidal energy

Liu & Veitch (2012) presented a design method in which the blade thickness of the tidal turbine rotor across the entire designed blade span considering the safety factor, highlighting the importance of tidal turbine blade fractures and the damages caused and hence resulting in the cost increment due to blade material failures. The designed tidal turbine had same chord lengths for each sections and the twist angle was larger at the root section, than the tip to ensure that the blade faces assemble smoothly with the hub surfaces, for surface meshing at the root airfoil section and later determining the pressure on each airfoil section of the blade. This approach of assigning the root airfoil twist angle larger than the tip airfoil tip angle is also adapted to all the designed blades in this research to ensure the structural integrity.

Bavanish & Thyagarajan (2013) performed aerodynamic optimisation on the HAWT to increase the power coefficient (turbine efficiency) based on the design constraints of the HAWT for a single wind velocity value. The aim of their design study was to reduce the cost to optimise the output power by considering the design constraints like rotor chord, twist and the structural thickness on the tip of the blades. BEM was used to find the correlation between the each airfoil drag and lift properties and the axial thrust was calculated for the individual airfoil. The design methodology was concluded with investigating the most important design parameters for e.g. blade twist angle, tip speed ratio, blade length, blade material affect the power coefficient of the rotor. A sensitivity analysis involving the geometric parameters like variable pitch values and blade tip parameterisation, for a HATT was conducted by Liu & Bose (2013). As the highest power output can be obtained on at the highest inlet water velocity, before the turbine starts experiencing stall a constant turbine shaft speed was maintained and eventually the shaft speed was optimised. The hydrodynamic performance of the proposed bi-directional tidal rotor was benchmarked on the annual power production based on the inlet water velocity application. The developed design procedure suggests that primary selection of blade twist angle, tip speed ratio are very crucial in tidal turbine blade design studies, which are also considered in this research.

Rajakumar & Ravindran (2012) developed a new technique for determining the aerodynamic performance of HAWT. The optimum twist was investigated for the given wind velocity and angular velocity of the blade based on the blade element theory (BET) distribution for various angles of attack. The power efficiency was derived using BET which illustrated that as the wind velocity increased the angular velocity of the blade increased until a constant power limit was reached which also increased its coefficient value. The CFD analysis was performed on the NACA 4410 and NACA 2415 to evaluate their aerodynamic properties and later validated. From the performance equations

### 3. Application of Computational Fluid Dynamics in tidal energy

developed the drag and tip loss factor was reduced, and the CFD simulations were compared to the existing methods available.

A novel Darrieus type VATT was mathematically simulated using CFD consisting of various number of rotor blades to simulate for various combination of diameters by Asim *et al.* (2013). They increased the torque interaction between rotor and stator thus resulting into increment of the overall power production. The incompressible flow of sea water creates pressure rise in the rotor-stator interaction which increases the torque, therefore they concluded their analysis by increasing the number of blades increases the power output of the Darrieus VATT by the rise in torque output. Wang *et al.* (2012) designed a composite HATT using high fidelity 3D CFD numerical analysis at different angular velocities of the rotor calculating the torque and power output for a particular flow speed. Due to the increase in pressure drop in the adjacent areas of the turbine blades it is possible to harness more energy out of the sea water. The unstructured mesh was refined in the surrounding areas of the turbine blades to simulate the flow field precisely, using the Sliding Mesh Method (SMM) available in ANSYS FLUENT which allows the use of explicit discretisation of the time steps in data interpolation in the blade angular rotation. The thrust force generated on the axial blades generated the pressure drop influencing the angular velocity to extract maximum available torque thus contributing to a novel manufacturing method to manufacture a composite HATT.

Benini & Toffolo (2002) developed a multi-functional evolutionary algorithm to design the stall regulation on HAWT. The optimisation strategy was divided into two parts: an aerodynamic model of the HAWT was designed and the performance was analysed using BEM theory equations, and an evolutionary algorithm was further implemented to give precise solution around the flow field in the HAWT based on the optimisation design variables. The design criteria were based on the decision variables like tip speed, chord length distribution and twist distribution. Thus by employing this approach it was possible to achieve the best annual energy production per square meter of the chosen wind park and the cost of energy was minimised theoretically.

All the results discussed above justify the most important design variable sensitivities that affect the overall power coefficient in the tidal turbine blade (3D level) design studies are blade twist angles, number of airfoil stations, angular velocity of blades, seawater velocity, tip speed ratio, blade material etc. As the rotational speed of the rotor is different at different flow velocities the power coefficient (depending on the water flow velocity) for each rotational velocity can be defined as and will be used to validate the turbine performance in this project (Bai *et al.*, 2014; Pinon *et al.*, 2012; Costa Rocha *et al.*, 2014; Afgan *et al.*, 2013; Jo *et al.*, 2014):

$$C_p = \frac{M\omega}{\frac{1}{2}\rho AV^3} \quad \text{Eqn. 68}$$

where  $\omega$  is the angular velocity of the turbine blade (rad/s),  $\rho$  is the seawater density (kg/m<sup>3</sup>),  $A$  is the project area of the rotor (m<sup>2</sup>),  $M$  is the torque acting on rotor (Nm).

By sketching the power coefficient ( $C_p$ ) versus different TSR's, it allows extraction efficient power production, thus as suggested by Jo et al. (2013), Costa Rocha et al. (2014), Batten et al. (2008) choosing TSR 5 for the design of the tidal turbine blades in this research.

### 3.8 Chapter summary

This chapter introduced the theory behind CFD analysis, and concepts related to design of tidal turbine blades when using CFD as a numerical modelling tool. The turbulence modelling techniques, basic fluid dynamics theory, CFD analysis procedure, the pressure-velocity coupling in ANSYS CFX is also described along with the common discretisation methods used in CFD. Various applications whilst using CFD in tidal energy conversion were also highlighted. This chapter finally concluded with the identification of the most important CFD based design variable sensitivities from the tidal turbine blade literature. The following chapter describes the design and analysis approach used to model the default HATT, and the CFD simulation set up chosen to analyse the performance of the designed blades is also explained.

## 4 Design and Analysis of tidal turbine blades

### 4.1 Introduction

This chapter examines the design, CFD simulation setup and the verification approach applied in this research to accomplish the objectives which were indicated in chapter one. This chapter begins with describing the direct design method, and then follows by specifying the design approach, and experimental analysis of the tidal turbine blade modelled. There is a brief discussion conducted sensitivity analysis on the chosen design variables, design approach, and this chapter concludes with the verification strategy applied to compare the CFD simulation results.

### 4.2 Direct design method

The direct design approach is used to design a product by collecting numerical data which can be analysed using mathematical based methods (Aliaga & Gunderson 2002). It also guides other researchers to figure out the mathematical and empirical aspects of the design process. The established research in mechanical engineering states that ignoring the empirical and mathematical processes is the main cause of inefficiency of the project. Using direct design methods in the area of mechanical engineering projects allows improved perceptiveness of the mathematical and empirical data collection (May *et al.*, 2014).

The elemental principles of the direct design method are based on data collection, data analysis, and verification or validation of the data (Shen *et al.*, 2012). A numerical modelling can be studied better using the direct design method, as the mathematical modelling requires the anticipating understanding of the problem (Wang *et al.*, 2012). By performing CFD analysis on the tidal turbine rotors and comparing the numerical results with the existing data in the literature, the critical research aims specify the choice direct design method. The final step when this method is to build the three dimensional model, where chosen experimental methods are tested and verified by further investigation, which then allows emergence of new data (Hudgins & Lavelle 1995). After the literature review is conducted, research questions are proposed and theoretical framework is proposed to build a numerical model. The potential relationships between the design variables are then identified to conduct the experimentation. The prime assumption of the researcher depends on the nature of the problem and then a solution can be proposed in the chosen numerical environment (Pugh, 1992).

The CFD results collected from the straight blade were comparatively analysed and evaluated with the Marlin look-alike curved caudal fin shape blade. The design and analysis process outlined in this research is summarised in Figure 47 and the stages are explained in the later sections.

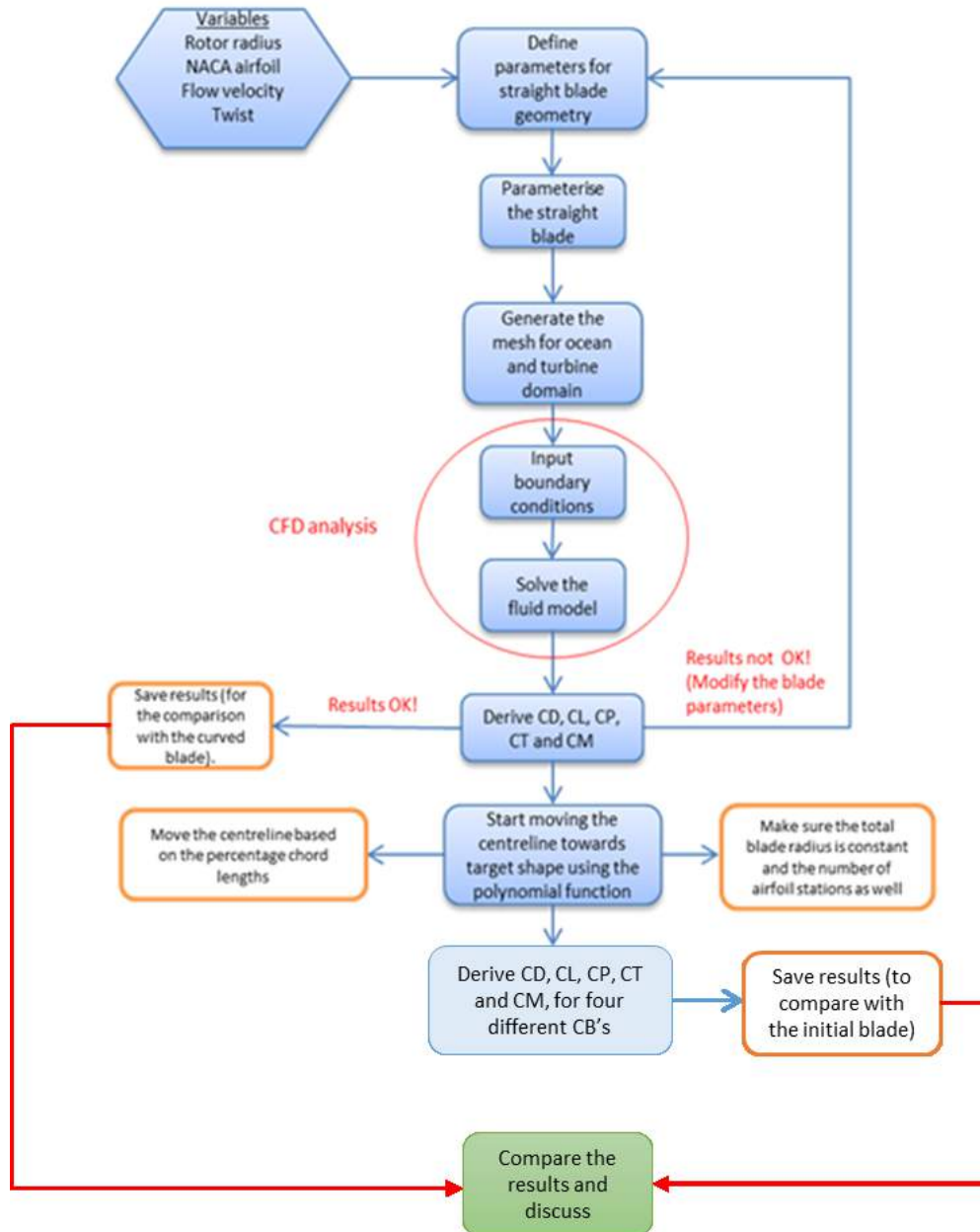


Figure 47 Graphical overview of the CFD process used in this research

## 4.3 Designing the default tidal turbine blade

### 4.3.1 Introduction

This section examines the design method applied in the three dimensional modelling of the default straight blade, the default twist distribution rule for the straight blade is explained.

### 4.3.2 Three dimensional default tidal turbine blade modelling based on literature

#### 4.3.2.1 *Three dimensional blade parameters and NACA airfoil span wise distribution*

The parameters that affect the tidal turbine blade are:

- a) Blade radius ( $r$ ),
- b) Total blade height ( $R$ ),
- c) NACA Airfoil selection,
- d) Twist angle distribution.

Thus, the top level parameters for defining a blade in three dimensions (3D) with their instances are defined in the Table 6.

**Table 6 Three dimensional blade parameters**

Instance Name	Initial Comments
Blade radius (r)	See figure 48 for further description
Total blade height (R)	See figure 48 for further description
NACA default airfoil selection	The default airfoil chosen is 0018.
Blade root airfoil twist angle ( $\beta$ and measured in $^{\circ}$ )	The default blade root airfoil twist angle is $16^{\circ}$ which is also the “maximum twist angle” limit for the root airfoil.
Blade tip twist angle ( $\beta$ and measured in $^{\circ}$ )	The default blade tip airfoil twist angle is $4^{\circ}$ which is also the “minimum twist angle” limit for the tip airfoil “The twist angle for the tip airfoil should be at least four times smaller than the root airfoil twist angle”.

Blade parameters like Total blade height, blade radius and hub circle can be illustrated in Figure 48.

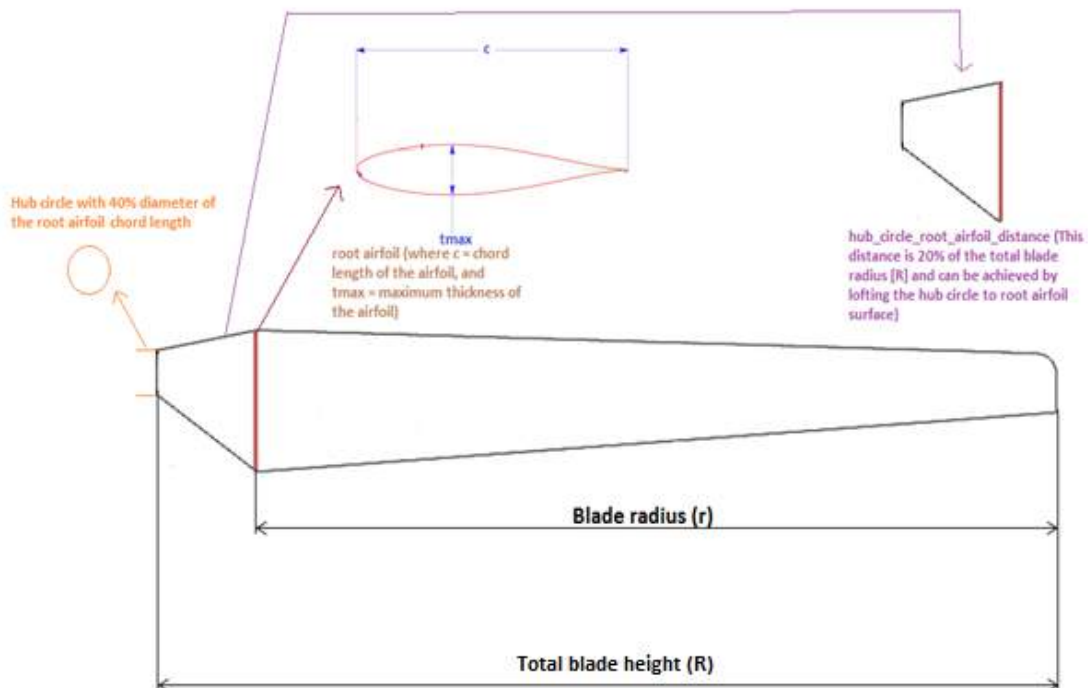


**Figure 48 Description of the blade parameters like Total blade height, blade radius, root chord, and the distance from hub circle to root airfoil.**

The span wise distribution of the airfoils is done at every 10% of the blade. The distance between hub circle and the root airfoil is 20% of the total blade height (R). The diameter of the hub circle is 40% of the root airfoil chord length. For e.g. if the root airfoil chord length is 1000mm then the hub circle diameter would be 400mm (the hub circle is a cylindrical surface which is to be lofted with the root airfoil). Figure 49 shows the airfoil distribution along the blade span.

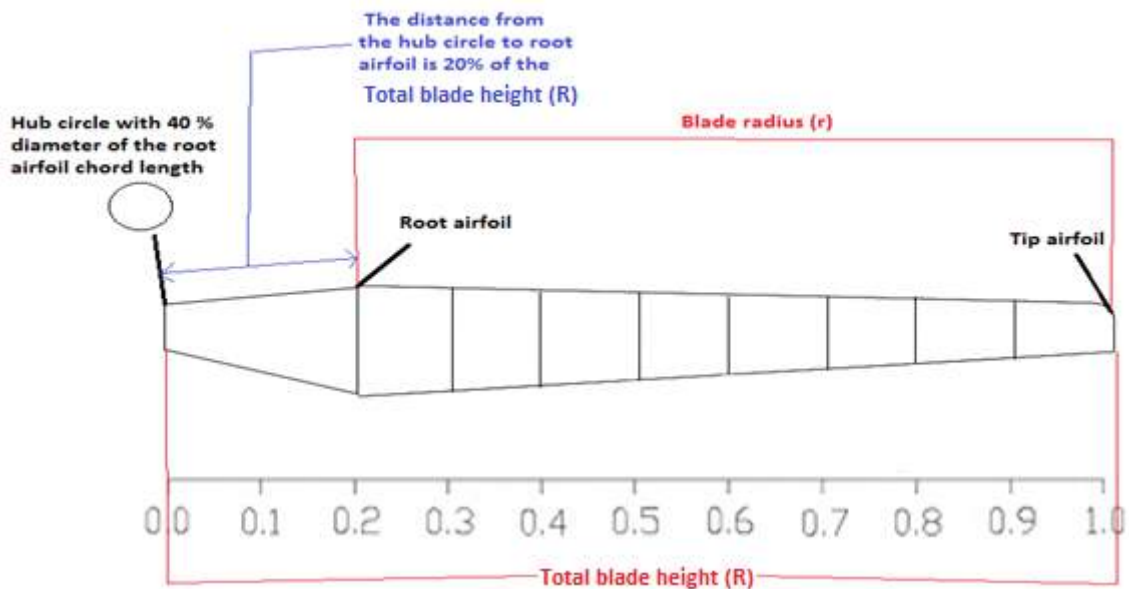


**Figure 49 Blade span airfoil distribution**

After defining the default value of the root airfoil chord length (1000mm), the remaining airfoil chord length distribution is done using a constant reduction factor of **0.08R** (Kim *et al.*, 2013; Wu *et al.*, 2013; Batten *et al.*, 2008; Batten *et al.*, 2006) which is named as **Blade chord length reduction factor** (which is not considered as a design variable due to the scope of the project), and is used to calculate the chord lengths of remaining airfoils. For e.g. if the root airfoil chord length is 1000mm, For station 1 the airfoil chord length will be 920mm ( $1000 - 80$ ), similarly for station 3 the airfoil chord length will be 840mm ( $940 - 80$ ) and so on until the tip airfoil chord length is calculated (See worked example in the following section).

#### 4.3.2.2 *The twist distribution along the default straight blade*

It is now possible to define the twist distribution for each individual airfoil in the turbine blade. The blade twist angle is higher at the root airfoil because it experiences less rotational forces on the

blade and it gradually starts decreasing towards the entire span of the blade. As the angular velocity of the blade is highest on the tip of the blade the blade twist angle is at least four times smaller than the root airfoil twist angle. Thus a twist distribution rule can be created for example **(NOTE: The centre axis goes with the airfoils):**

NACA-AIRFOIL-ROOT-TWIST-ANGLE =  $16^\circ$  (default)

NACA-AIRFOIL-TIP-TWIST-ANGLE =  $4^\circ$  (default)

BLADE-TWIST-ANGLE-DECREMENT = 4 times

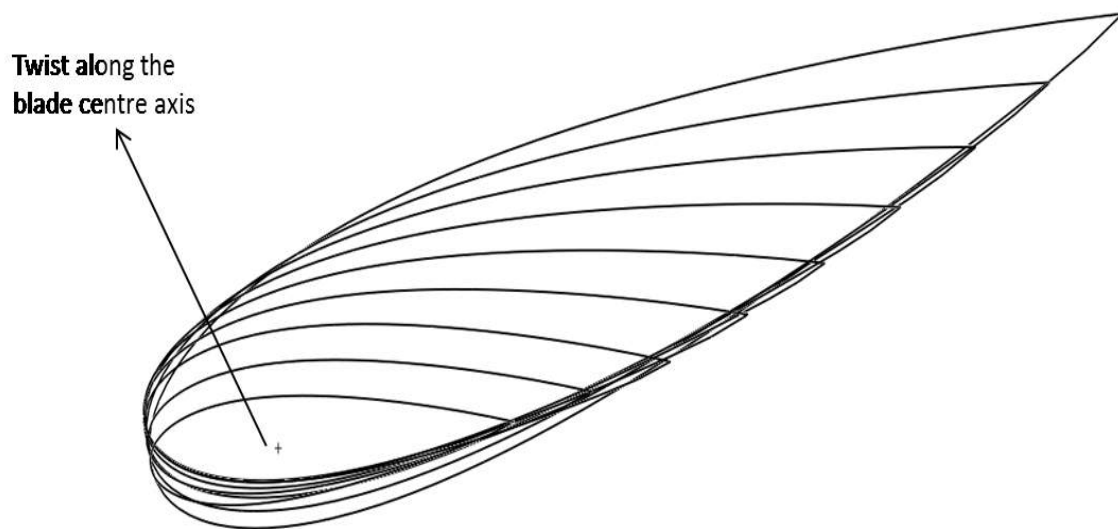


**Figure 50 NACA airfoils twisted about the central axis in blade**

#### 4.3.2.3 *An example blade design*

After describing all the necessary parameters to design a tidal turbine blade, **an initial default blade** can now be defined in the following sections.

**Table 7 Default blade parameters**

Input parameter	Value
Hub-circle-diameter	40% of the root airfoil chord length works out to be "400mm" in this example
Hub-circle-root-airfoil-distance	20% of the Total blade height (R) works out to be "1480mm" in this example
Root-airfoil-chord-length	1000mm (default)
Root-airfoil-max-thickness	18% (maximum thickness with the chord length ratio)
Total-Blade-Radius	7400mm (default; the total blade height has a maximum value of 11000mm and, minimum value of 1500mm)

Using the 10% rule (to create number of airfoil stations), it is now possible to define the NACA stations for the entire blade which is illustrated in the Figure 51.

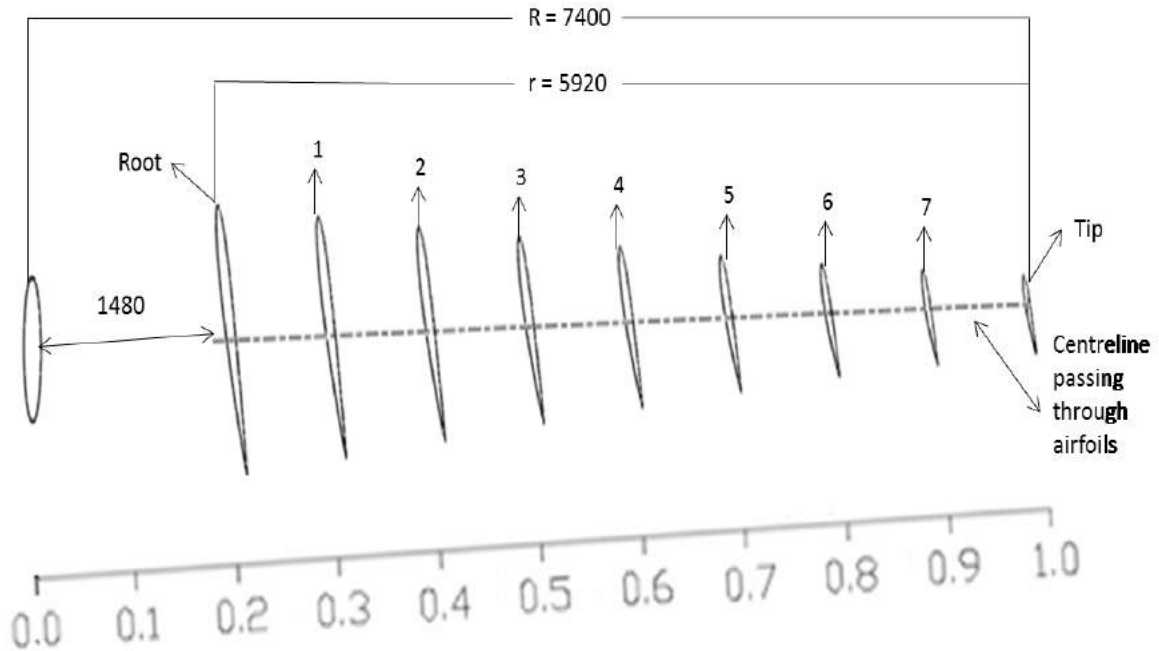


**Figure 51 Defining the NACA airfoil stations along the entire length of the blade**

As, all the stations of the turbine utilise NACA 0018 airfoils but have different parameters values for each instance. The NACA stations are placed at the 10% value of the blade as visualised in Figure 52, therefore the remaining R values are shown in the last column of the following table.

**Table 8 NACA Airfoil stations with the R values (worked at the 10% rule)**

Instance name	Max-camber	Max-camber-position	Max-thickness	R value from hub circle (mm)
NACA-AIRFOIL-ROOT	0.0	0.0	18	1410
NACA-AIRFOIL- STATION -1	0.0	0.0	18	1970
NACA-AIRFOIL- STATION -2	0.0	0.0	18	2530
NACA-AIRFOIL- STATION -3	0.0	0.0	18	3090
NACA-AIRFOIL- STATION -4	0.0	0.0	18	3660
NACA-AIRFOIL- STATION -5	0.0	0.0	18	4220
NACA-AIRFOIL- STATION -6	0.0	0.0	18	4790
NACA-AIRFOIL-STATION-7	0.0	0.0	18	5320
NACA-AIRFOIL-TIP	0.0	0.0	18	5920

The distance between hub circle and the root airfoil chord is 1480mm (20% of the total blade distance, defined according to literature). The root airfoil station has an R value of 5920mm (Total blade height – hub circle root airfoil distance), Station 1 has the R value which is 10% of 5920 (which yields) 5328mm (5920 - 592) and so on until we reach the value of 1410mm for the tip airfoil station.

The next step is to use calculated R values from the hub circle values and “stack” the airfoils along the blade centreline; so that the each individual airfoil can be added a twist angle. Once the coordinate systems for all the airfoil stations are located, the NACA profiles should be referenced to the blade centreline. The calculation method for defining the variable twist angle for each an individual airfoil is already explained in the above section. After the stations are positioned and defined, it is now possible to define the twist angle for each airfoil using the Table 9.

**Table 9 Twist angle values for each NACA airfoil station**

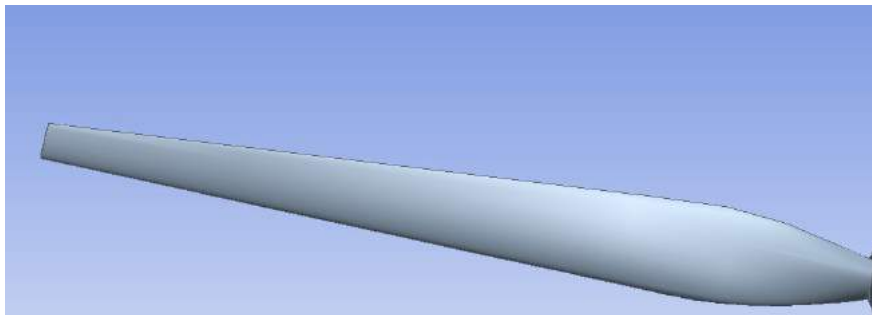
Instance name	Twist distribution [°]
NACA-AIRFOIL-ROOT-TWIST-ANGLE	16
NACA-AIRFOIL-STATION-1-TWIST-ANGLE	14
NACA-AIRFOIL-STATION -2-TWIST-ANGLE	12
NACA-AIRFOIL-STATION-3-TWIST-ANGLE	10
NACA-AIRFOIL-STATION-4-TWIST-ANGLE	8
NACA-AIRFOIL-STATION-5-TWIST-ANGLE	6
NACA-AIRFOIL-STATION-6-TWIST-ANGLE	4
NACA-AIRFOIL- STATION-7-TWIST-ANGLE	4
NACA-AIRFOIL-TIP-TWIST-ANGLE	4

The chord lengths for the default blade are defined according to the literature. The entire blade can be summarised in the Table 10.

**Table 10 Complete blade parameters**

Station number and name	R (mm)	Chord length, c (mm)	Twist distribution (°)	NACA airfoil
<b>NACA-AIRFOIL-ROOT</b>	1410 (Default)	1000 (Default)	16 (Default)	0018
<b>NACA-AIRFOIL-STATION -1</b>	1970 (Calculated)	920 (Calculated)	14 (Calculated)	0018
<b>NACA-AIRFOIL-STATION -2</b>	2530 (Calculated)	840 (Calculated)	12 (Calculated)	0018
<b>NACA-AIRFOIL-STATION -3</b>	3090 (Calculated)	760 (Calculated)	10 (Calculated)	0018
<b>NACA-AIRFOIL-STATION -4</b>	3660 (Calculated)	680 (Calculated)	8 (Calculated)	0018
<b>NACA-AIRFOIL-STATION -5</b>	4220 (Calculated)	600 (Calculated)	6 (Calculated)	0018
<b>NACA-AIRFOIL-STATION -6</b>	4790 (Calculated)	520 (Calculated)	4 (Calculated)	0018
<b>NACA-AIRFOIL-STATION-7</b>	5320 (Calculated)	440 (Calculated)	4 (Calculated)	0018
<b>NACA-AIRFOIL-TIP</b>	5920 (Calculated)	360 (Calculated)	4 (Calculated)	0018

The final step is to create a loft through all the airfoils, and the lofted geometry is demonstrated in Figure 52.

**Figure 52 Lofted surface blade profiles**

## 4.4 CFD simulations setup

### 4.4.1 Introduction

This section examines the CFD simulation methods employed on the tidal turbine blade designed in this research. This section starts with the introduction of the computational mesh domain built to analyse the designed rotor, the reasons for having high density in the turbine domain area. A brief description of the mesh independency study is also given. The steady state CFD simulations are performed using the SST turbulence model and transient simulations are performed using LES-Smagorinsky. After simulating the initial tidal turbine rotor a third order polynomial function is introduced on the centreline passing through the airfoils for moving the straight blade to the curved caudal fin shaped blade. Finally, sensitivity analysis is performed on the most important design variables and perturbation of the initial blade design to a curved caudal fin shape blade is explained.

### 4.4.2 2D CFD study of NACA 0018 airfoil

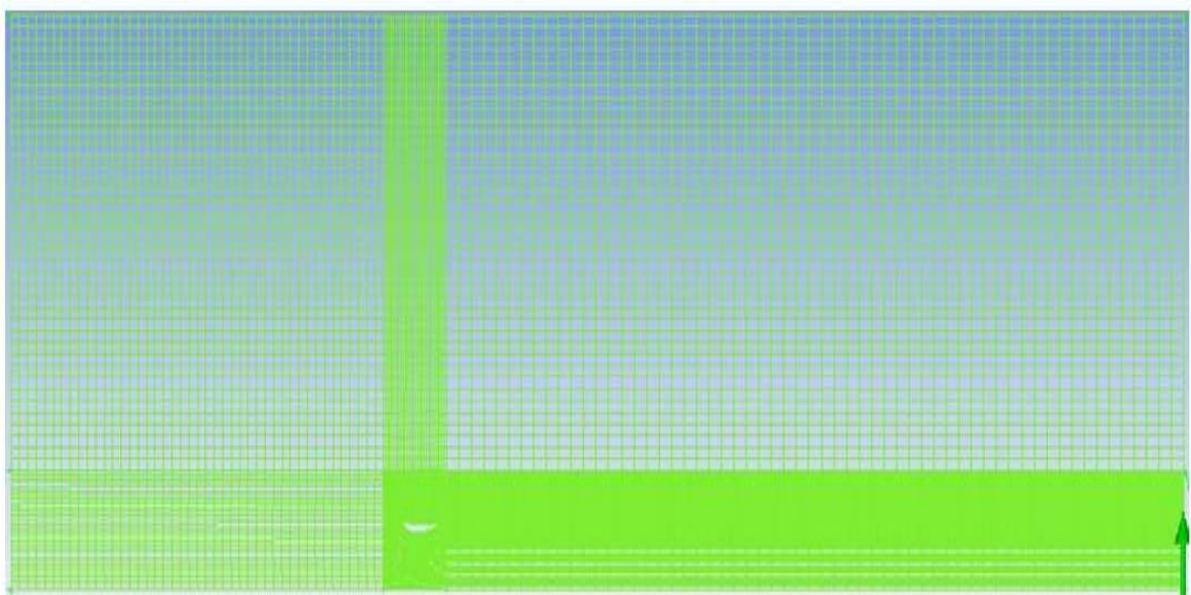
The verification and the comparison of the NACA 0018 airfoil steady state simulations were performed using the case studies of Mehmood *et al.* (2012). The reasons for choosing this airfoil in this research are because of its wide use in tidal turbine blade design, and the steady state experimental data availability for comparison purposes. The airfoils travel in a tangential direction in axial path to the tidal current flow, and hence the airfoil chord length is not parallel to the flow as with the VATT, but travelling across it. As the fluid velocity increases over the airfoils, the 'convex surface' results in lower pressure on the 'suction' side when compared to the 'pressure side' of airfoil. Therefore applications for tidal energy have not used symmetrical airfoils to model a bio-mimicked HATT blade. The use of "non-symmetrical" airfoils to design the HATT's is also known. For example, Bai *et al.* (2014) and Wu *et al.* (2013) designed tidal turbine blades using non-symmetrical airfoils which have a descending convex bend in the middle of the leading edge and the camber inverting point towards the trailing edge. These airfoils are generally designed to have huge unfavourable torque values which also produce a lower lift coefficient at the same time. As the tidal current flow increases around the cylindrical leading edge, a pressure drop is produced which gives negative pressure inclination. For the given airfoil design, if the water velocity and the angle of attack are higher on the upper surface of the airfoil, a higher "drag" force when a HATT completes a full rotation and also causes "lift" fluctuations. The benefit of designing blade like a Blue Marlin caudal fin is that higher lift and power coefficients would be generated at both lower and higher tidal current velocities.

What is needed therefore, is a HATT blade system designed using a symmetrical airfoil, which would produce greater lift coefficient, and power output throughout the year i.e. for lower and higher tidal current velocities. An attempt is made in this PhD thesis to design and analyse a curved caudal fin look-alike turbine blade, to improve the default straight tidal turbine blade.

Before performing the 2D steady state simulations, some preliminary assumptions were made regarding the density of the sea water, and the mesh density due to the lack of mention in the chosen source. The 2D CFD simulations were performed using CFX, and the numerical model was validated replicating the structured grid generation from Mehmood *et al.* (2012). The design of the replicated grid is discussed in following sections, and the O-C grid using the same boundary conditions.

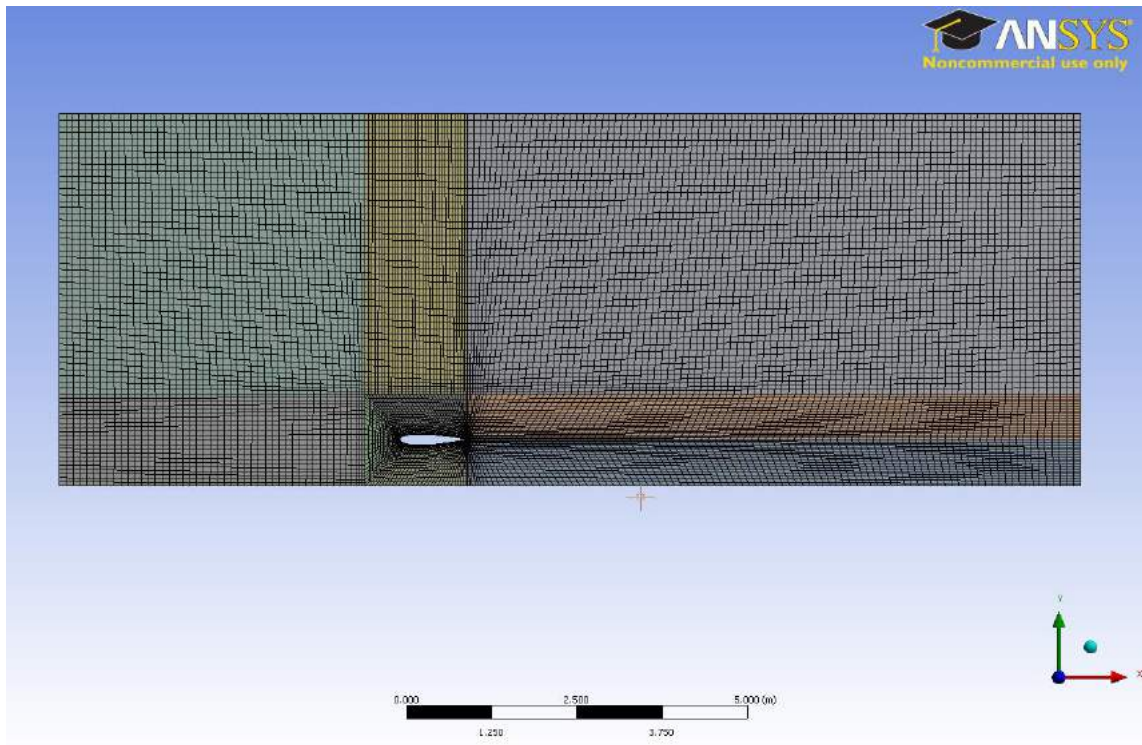
##### 4.4.2.1 *The design of the rectangular replicated grid*

The development of the structured rectangular grid was designed as much as possible to replicate the structure of the grid created by Mehmood *et al.* (2012), to maintain the order of verification of the mathematical model applied in this project. The mesh block cutting scheme was employed to calculate the effect of the length and rotational angle on the maximum velocity interacting on the NACA 0018 airfoil. The most important factor when defining the boundary conditions is that there must be significant distance from the airfoil edges to the inner and outer domains of the grid. The radius of the inlet distance, and outlet distance from airfoil was five times the length of the airfoil and ten times the length of the airfoil respectively.



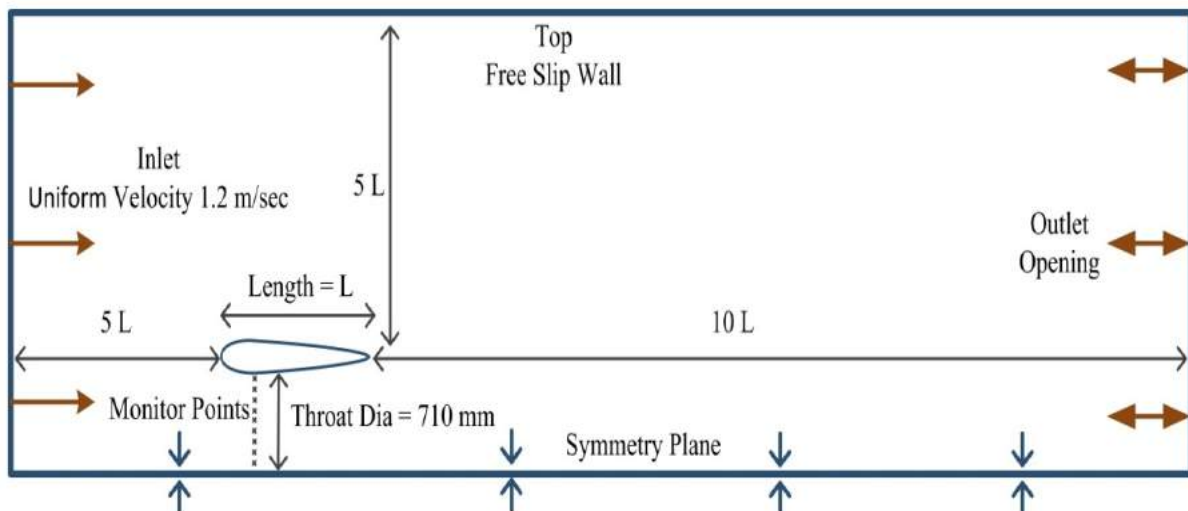
**Figure 53 Mesh block cutting scheme (Mehmood *et al.*, 2012)**

Figure 54 show the replication of the mesh settings used by (Mehmood *et al.*, 2012).



**Figure 54 Mesh created for NACA 0018 1m 0 degree of angle of attack**

The bottom wall of the generated grid was selected to be the symmetry plane (in real world it acts as seawater bed), the top wall of the rectangular grid was selected as 'free slip wall', and the steady state simulations were performed using SST turbulence model in CFX. Figure 55 shows the schematic of the boundary conditions used by Mehmood *et al.* (2012), and Figure 56 shows the replication of the boundary conditions used by the same authors.



**Figure 55 schematic of the boundary conditions (Mehmood *et al.*, 2012)**

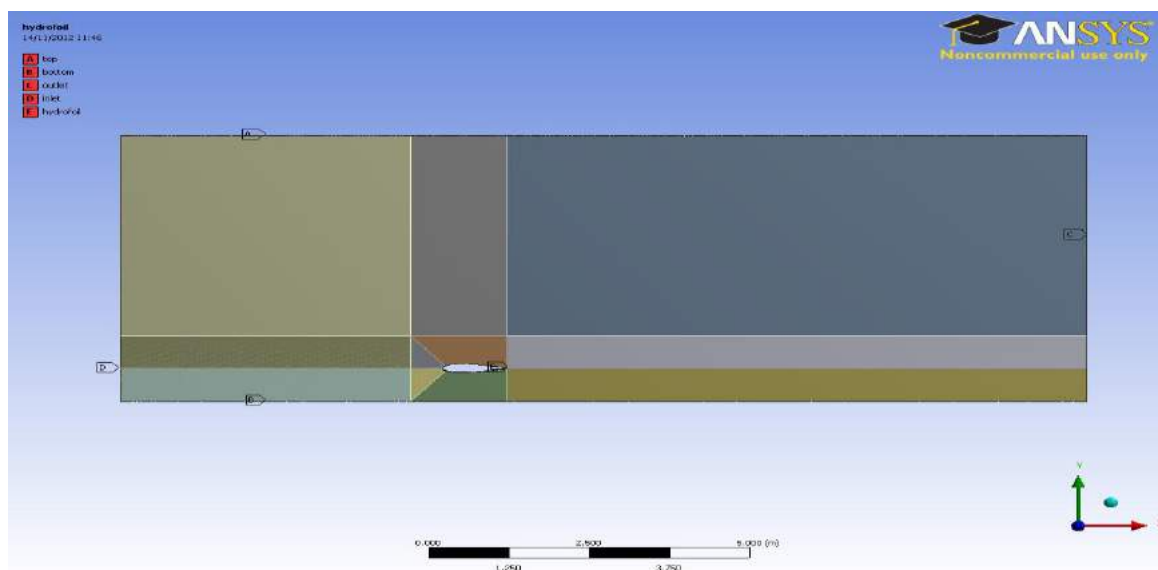


**Figure 56 boundary conditions defined using named selections in CFX**

The verification and the comparison of the 2D steady state simulations performed are discussed in the Chapter 5.

#### 4.4.3 Design of the computational domain

The initial straight turbine blade geometry is simulated in a rectangular mesh domain with a few important parameters. Firstly, the circular domain outside the tidal turbine blades is known as ‘turbine disc’, is developed with high mesh density to monitor the rotational movements of the rotor. The development of the turbine disc was done to meet the computational accuracy; the turbine disc and the entire rotor are named as the ‘turbine domain’. The outer domain of the turbine domain is the ‘seawater domain’, more details of the development of the turbine and seawater computational grid domains are discussed below.

##### 4.4.3.1 The seawater domain

The rectangular computational grid was used to model the seawater domain, consisting of the turbine domain. The seawater domain extends ‘5 times the turbine diameter’ at the inlet and ‘10 times of the turbine diameter’ at the outlet, and the height of the rectangular grid is ‘five times of the turbine diameter (Figure 57); which replicates the computational grid used in the modelling of 2D NACA 0018 case studies.

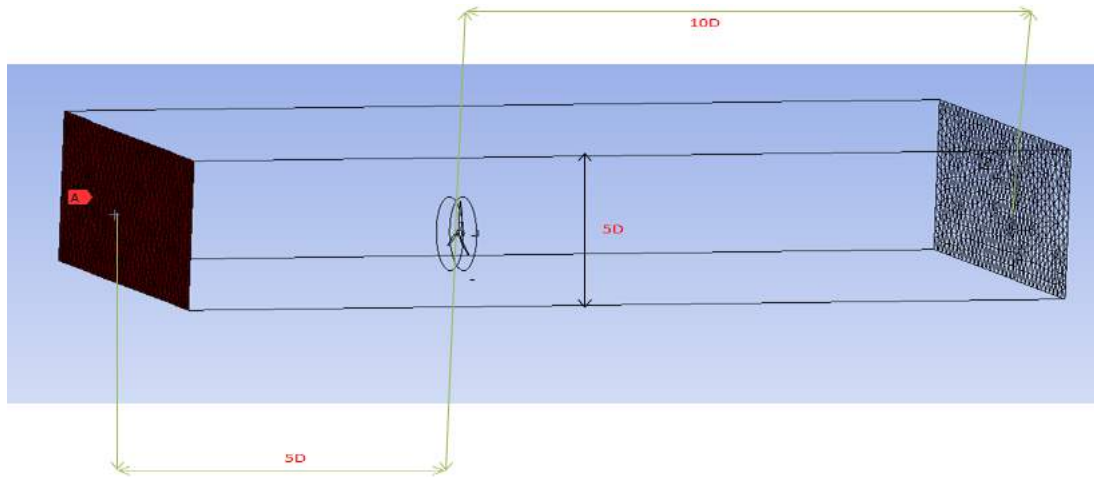


**Figure 57 Inlet, outlet and height extension from the tidal turbine blades**

The details of the mesh cells, node counts mesh spacing and the mesh growth ratio is discussed in the Chapter 6.

#### 4.4.3.2 *The turbine domain*

The turbine domain was designed as 'rotating domain in CFX (Figure 58)', and then a full 360° mesh surrounding the tidal turbine blades. An unstructured tetrahedral mesh was constructed around this domain as the flow would be highly non-linear and the rotational effects are to be considered, therefore using structured mesh or hexahedral mesh would not be useful. The latter two mesh techniques described would be useful if the flow wasn't in an assertive direction, and as tidal turbine geometry is convoluted, which would result in skewing the mesh cells.

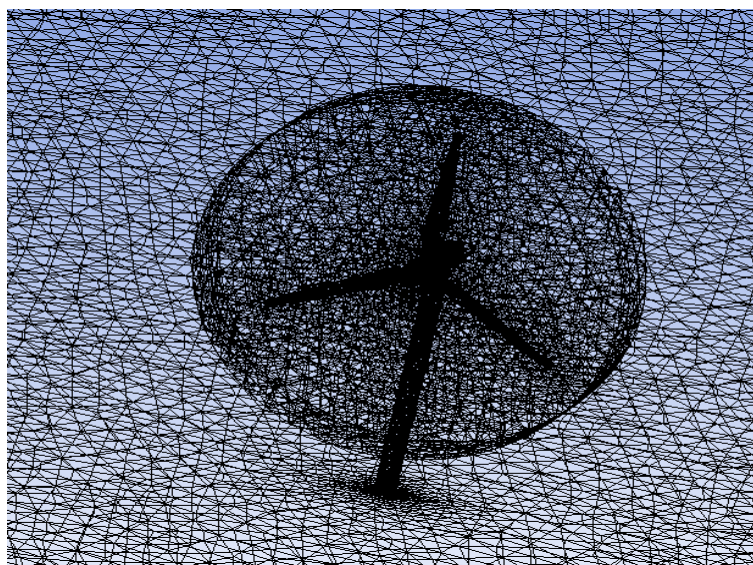


**Figure 58 Rotating turbine domain around blades using unstructured mesh**

## 4.5 Strategy to move the default straight blade to the curved caudal fin shaped blade

After parameterising the initial tidal turbine geometry, it is now possible to move the initial straight blade geometry towards the target shape by using the centreline polynomial function. A centreline was introduced (See Figure 51) in which all the airfoil centres, starting from the root airfoil chord and ending on the tip airfoil chord are built about the centreline.

### 4.5.1 Mesh Independency study and boundary conditions

A mesh independency study was carried out on the Straight Blade using the standard  $k-\epsilon$  model, and SST model to establish the accuracy of the CFD solution. The SB was analysed using three different meshes coarse, medium, and fine thus simulating six different mesh sizes using two turbulence models. Mesh resolution plays an important role in the final CFD results and is highly sensitive towards the power coefficients of the HATT, hence after the grid convergence study the best mesh in terms of computational time and results was employed in further numerical analysis carried out in this research. The default turbulence model chosen is SST to perform steady state CFD analysis on the tidal turbine blades. To perform unsteady (transient) CFD analysis, LES-Smagorinsky was used which is a well-known turbulence model which gives an accurate picture of the flow field around turbine blades. The default value for inlet sea water velocity is defined as 2.5m/s.

#### 4.5.1.1 Derive $C_L$ , $C_P$

After completing the CFD analysis, the dimensionless coefficients  $C_L$  (Lift Coefficient),  $C_P$  (Power Coefficient), are derived. General notes as regards to obtained results:

- The  $C_P$ ,  $C_L$ , have to be calculated in all the cases.
- The  $C_P$  value should come as high as possible although the maximum  $C_P$  value that can be theoretically achieved is 0.593 for any rotating machine (The Betz limit).
- The  $C_P$  value of the improved curved caudal fin tidal turbine blade is to be compared with the  $C_P$  values of the standard HATT models in the literature.

#### 4.5.1.2 Moving centreline

The 3D curved caudal fin blade is characterised by a set of centroids as discussed in Appendix B. In this program the centroid of the NACA airfoil centres from a 3D shape as predicted by the MATLAB program (Turbinegenerator.m). The NACA4gen.m (NACA 4 digit Airfoil Generator, MathWorks, 2014)

and `centroid.m` (Geom2d, MathWorks, 2014) programs were downloaded from MathWorks website, to generate four digit NACA airfoil co-ordinates, and to compute the centre of mass for a set of points respectively. The explanations for the commands used in the programs are described in the Appendix B.

The `Turbinegenerator.m` program computes the centre of mass (gravity) for the set of airfoils used in modelling the curved caudal fin blade. The weighted centroid uses the pixel intensities in the airfoil region which weights in the centroid calculation. NACA 0018 is a symmetrical four digit airfoil, and the centre of mass lies on the line of symmetry and has a homogeneous centre of mass distribution. The airfoil stations were induced to rotate freely around its centre of mass due to the hydrodynamic forces under the action of an incompressible flow of seawater. The 3D curved caudal fin shape generated from the Matlab program is reproduced below in the Figure 59.

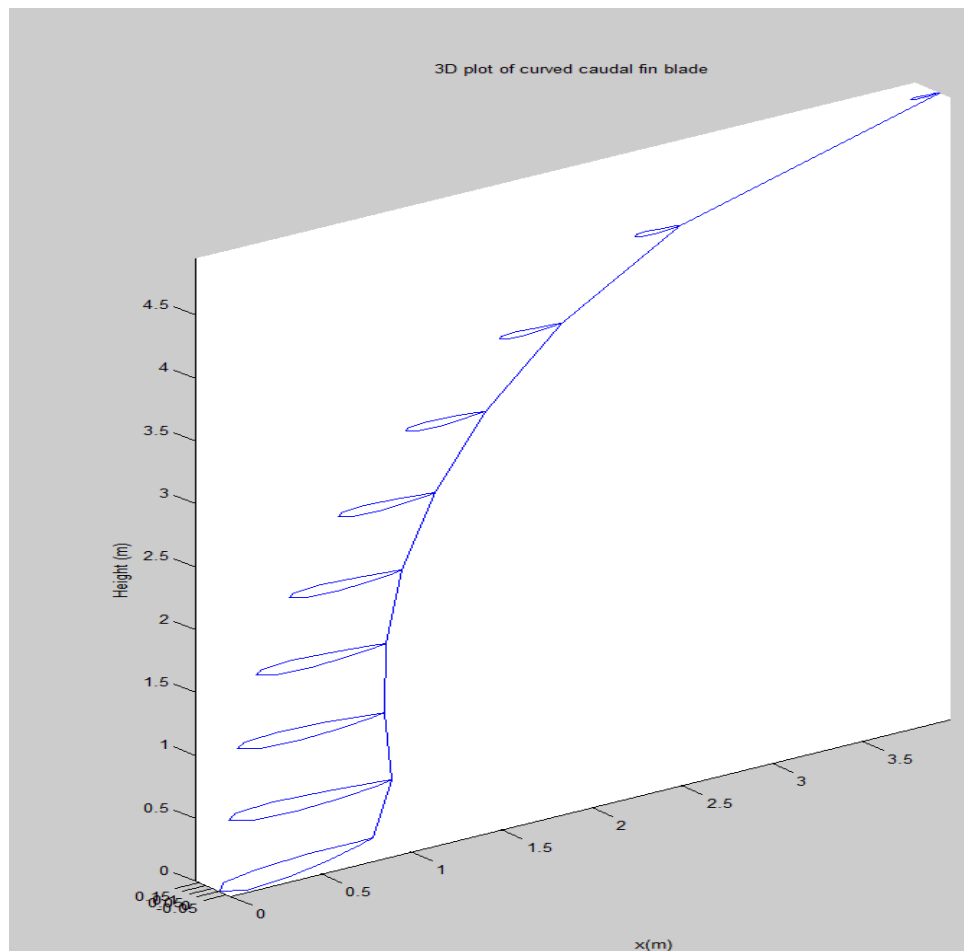


**Figure 59 3D plot of the curved caudal fin blade reproduced by MATLAB program.**

The twist angle which acts as the function of the blade incremental length, is further modified by to create a smooth twist by fitting a third order polynomial function. In order to get the desired curve

for the initial tidal turbine blade to move towards the curved caudal fin shape (the target shape), a third order polynomial function is defined on the central axis curve which is:

$$x = 0.0034y^3 + 0.0678y^2 + 0.3209y + 0.0043 \quad \text{Eqn. 69}$$

The above equation is considered to be the centreline polynomial function of the curved blade caudal fin (tail). Each NACA profile centre is built about the centreline, the centreline then acts as master and each profile datum sit along its length divided by the height and the numbers of stations, the blade height stay constant as the default straight blade. Using this approach it would be easy to model the curved shape blade and reduce the computational overhead. All the NACA profile sections are considered parallel to the x-axis i.e. the normal of each NACA section should be y-axis. The chord length values defined in Table 11 are for the target shape which is an assumption of 'a caudal fin' shape. Fitting the third order polynomial on the skeleton of the caudal fin look-alike centreline, starting at the root airfoil centre and passing through all the airfoil stations till the tip airfoil centre entails the blade bending and thus creation of the curved caudal fin shaped blade. The straight blade comprising of the symmetrical airfoil stations which have straight mean camber and using the Cartesian coordinates in a twisted in span wise direction makes it possible to achieve the desired caudal fin shaped blade, which can also be called as span wise curvature.

The initial values of the caudal fin NACA profile chord lengths are defined in Table 11; the default profile chosen is NACA 0018.

**Table 11 default values for defining the curved blade shape**

X- Offset	Y – Offset	Chord length, c (mm)	NACA airfoil
0	0	1645	0018
0.2285	0.6	1337	0018
0.4998	1.2	1091	0018
0.8145	1.8	924	0018
1.197	2.4	808	0018
1.678	3	663	0018
2.2164	3.6	509	0018
2.7833	4.2	353	0018
3.489	4.8	0	0018

The X-offset and Y-offset values are used to construct the approximate axis profile. Thus, for the purposes of programming, the nearest third order polynomial equation is defined above  $y$  using polynomial regression analysis in MS-Excel, and is demonstrated in the Figure 60.

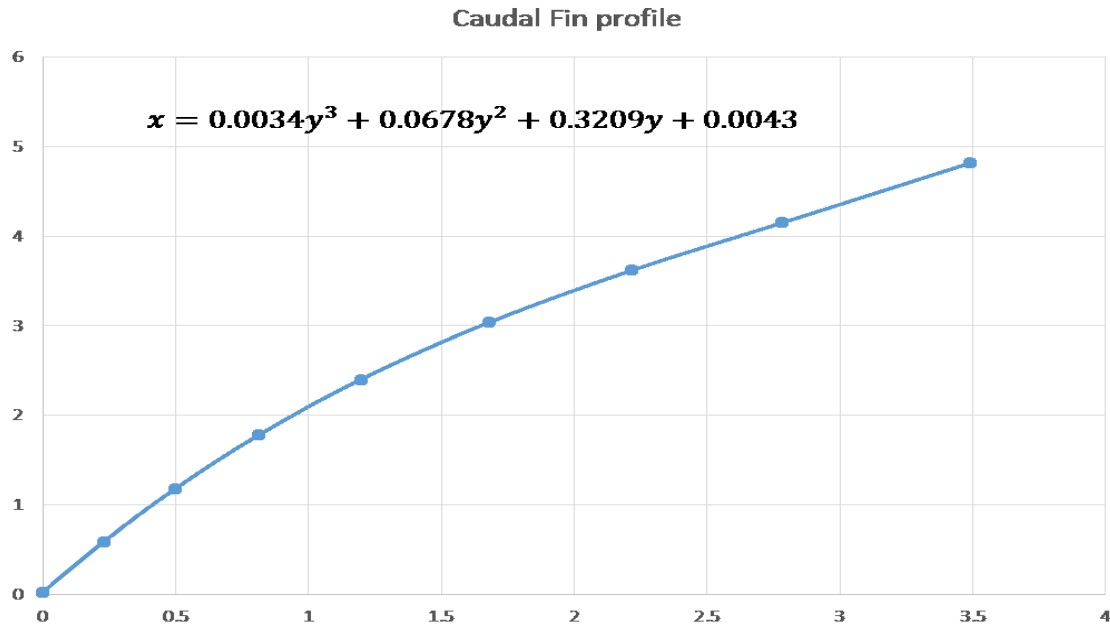


**Figure 60 the  $y$  equation graph which constructs the third order polynomial**

## 4.6 Design strategy and sensitivity analysis

A direct approach for the design and analysis of the curved shape blade has been used here because, the user can select the design parameters and the design evaluation can be conducted based on the assessment criteria (in our case highest  $C_p$ ), including variable sensitivities. This method is considered to be iterative i.e. which allows the selection of design variables and the performing the CFD analysis. This approach is the most popular approach in all the mechanical engineering problems. Thus using this direct based design approach the output function is to find the maximum power coefficient of the designed tidal turbine rotors at the simulated inlet velocity so that annual energy production is maximised automatically.

The most important design variables that affect the overall efficiency ( $C_p$ ,  $C_D$ ,  $C_L$ ,  $C_T$ ,  $C_M$ ) of the horizontal axis tidal turbine system are chord lengths of airfoils, twist distribution, overall span of the blade, angle of attack, angular velocity of the blade, blade material, and the fluid velocity acting on the blade (Afgan *et al.*, 2013; Batten *et al.*, 2008; Clancy, 1978; Pinon *et al.*, 2012; Betz, 1966, MCT; 2008; Jo *et al.*, 2014). The design variables selected for the design study of the designed tidal

turbines blades are chord lengths (which are varied in a linear progression to achieve the target curved blade), the blade span is kept constant (in order to allow the comparison of the blade performance), and the blade twist rule which is also varied in all the four percentage based stages of curved blade design to find the more power coefficient producing blade shape. After simulating the straight blade, when moving the centreline using the third order polynomial function the number of blade stations, the twist rule is varied along with the chord length values for each airfoil station. The third order polynomial equation will always make sure that the percentage wise chord length blade values will always resemble like a curved shape blade, and the total blade height stays constant (Figure 61).

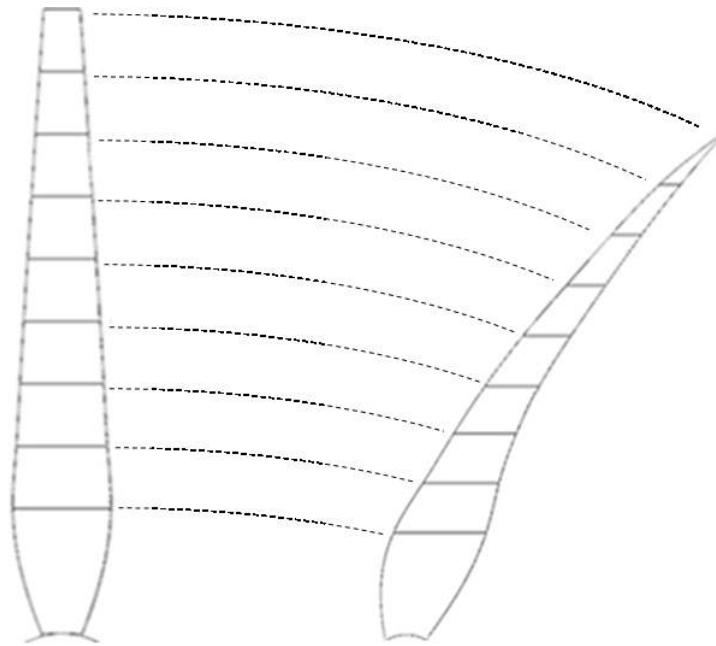


**Figure 61 chord length variation of the straight blade to achieve the curved blade**

The chord lengths of the straight blade can be varied in linear or non-linear progression along the span wise direction to achieve the curved caudal fin blade. The curved caudal fin shaped blade also has a thicker base than the straight blade to mount the caudal fin shaped blade on the rotor without having to use additional support. The blade twist is also varied along all the airfoil stations making the curved caudal fin shaped blade produce more energy from the tidal currents. The twist angle mounted on the airfoil stations for the caudal fin shaped blade can be lower than the region of what is mounted on the traditional tidal turbine blades, for the caudal fin shaped blade to produce higher efficiency in certain low tidal current velocities. This is particularly suitable for the caudal fin shaped blade because of the increasing concave bend and is thinner at the tip, and thus should be dimensioned to have sufficient strength at the blade tip. The movement of the centreline towards

achieving the target shape in percentage based chord lengths and the strategy to move the curved blade backwards to the straight blade is explained in Chapter 6 section 6.5.

### 4.6.1 Saving the results of the curved blade

After performing the CFD analysis, the results of the best (maximum  $C_p$ ,  $C_l$ ) curved blade shape should be saved; for the comparison with the default analysed straight blade, and the HATT models available in the tidal turbine blade literature. This saving is to show the comparison between the CFD based design study curved blade experiment with the original analysed straight blade to see its improvements in  $C_p$ ,  $C_l$  have been generated.

## 4.7 Comparison of the CFD results

The function of this section is to draw together the numerical results of the straight blade and the curved caudal fin shape blade and compare them. The CFD results obtained from the straight will be compared separately with all the design four curved shaped blades to form a design study. The results comparison between the CFD simulations of the straight blade and the curved caudal fin shaped blade will prove the novelty of this research and design study difference between the steady state and unsteady CFD analysis of the turbine blades, and thus eliminate the unnecessary sensitivities to allow the future users to analyse the any shape of the tidal turbine blade at any potential location. The potential reasons for the differences in the CFD results of the both models, are nevertheless constant, both at '3D blade level (blade radius, total blade height, NACA airfoil, twist angle)', and at the 'rotor level (assumptions, made using BEM theory), but it is possible to eliminate some of the sensitivities by the degrees of comparisons between the CFD result sets, for example different velocities, and different speed ratios.

### 4.7.1 Power, lift coefficient comparisons

The comparison of the CFD results will be concluded by comparing the straight blade and the more curved blade power, and lift coefficients at different angles of attack. The blade element results produced by the initial designed HATT (according to the literature) whose comparison will be labelled as SB – (Straight blade), and the blade modelling and the complete CFD results for the straight blade tidal turbine model will be presented in the Chapter 6, as well as the complete CFD curved blade turbine models will be labelled CB - (Curved blade). Differences between the SB/CB CFD results will be compared with the good agreement of the power coefficient. Finally, a further set

of results of  $C_p$  from the maximum power coefficient obtained curved blade shape will be compared to the standard HATT models available in the tidal turbine literature.

### **4.8 Chapter summary**

The above chapter highlighted the design, analysis, and verification approaches used in this research. The direct design approach which is used to design and analyse the default HATT, and curved blades was also explained. Important blade level parameters like total blade height, twist rule were also explained. The CFD simulations set up for 2D, and 3D environment with the grid domain characteristics, and boundary conditions were also explained. The design strategy to move the default straight blade to the curved caudal fin shape using a novel third order polynomial function was demonstrated. A grid independency study carried out on the Straight Blade to investigate the effects of mesh resolution on the final CFD results was also demonstrated. Finally, the verification and comparative analysis approach used in this research was explained. The following chapter demonstrates the two dimensional CFD analysis on NACA 0018 and the validation study done against the literature. A further comparative analysis of the validated case study is done with different grid settings in a time dependent flow problem.

## 5 CFD analysis of airfoils

### 5.1 Introduction

In this chapter, the CFD analysis of the NACA 0018 airfoil is explained which forms a major part to designing the default horizontal axis straight tidal turbine blade geometry; and forms a significant percentage of the CFD simulation work carried out in this research. The NACA airfoil study looks at the four digit NACA 0018 airfoil behaviour under steady state, and transient water flow conditions. These studies are performed because when designing the a tidal turbine blade, it is very important to rigorously predict the hydrodynamic forces and moments enforced on the turbine blade, otherwise the verification of a complete horizontal axis tidal turbine CFD simulation becomes problematic, because of the data available for satisfactory numerical model verification.

To verify and compare the implemented numerical model, the steady state airfoil CFD data generated is correlated with Mehmood *et al.* (2012) thus enabling us to compare properly the numerical model used in this research. The presented chapter involves discussion of the following parts, the geometry specification, mesh generation, and the numerical model approach used to calculate and compare the hydrodynamic performance of the NACA 0018 airfoil. The two dimensional hydrodynamic coefficient like drag is described and tabulated for comparison in the latter stages. The airfoil CFD simulations described in this chapter are undeviatingly applied to the 3D CFD simulations of the default straight blade and the curved blade shape, because seawater flow can be accurately modelled as it is an incompressible fluid; and for the same Reynolds number a 2D CFD simulation performed on the airfoil at constant water velocity and density should give exactly the same predictions at 3D CFD simulation level (when modelled using the same airfoil), for the lift, drag and moment coefficients. Finally, the 2D CFD simulation results are discussed, tabulated, compared with the experimental data, as well as the grid change generated data, for steady state as well as transient CFD analysis.

### 5.2 The NACA 0018 airfoil

The NACA 0018 airfoil section was selected as the starting point in the design for the current verification and comparison study of the airfoils, fundamentally because they are suited for low Reynolds number, high lift applications, and are prone to less cavitation in the tidal turbine industry. Present 2D NACA validation data came from the CFD tests performed by Mehmood *et al.* (2012). The

data analysed by the authors was termed as “excellent” and also claimed that there was no previous study available in the literature concentrating on the effect of the NACA airfoil and the water low angle of attack on the airfoil at the same time.

No specific details were given on the sea water density to characterise the turbulence and flow effects on the airfoil used. Mehmood *et al.* (2012) carried out the NACA 0018 2D modelling using MATLAB, and was experimented at 14 different lengths and 17 different angles of attack at uniform velocity of 1.2m/s. In this present study two case studies are modelled and tested for the validation and structure purposes;

- 1) NACA 0018 length = 500mm; angle of attack = 0°, and 15°,
- 2) NACA 0018 length = 1000mm; angle of attack = 0°, and 16°.

The grid generation and experimental values obtained are discussed in the following sections.

### 5.3 Geometry specification

The generation of the rectangular structured grid was possible due precise schematic of the boundary conditions (Figure 5, pp 4554, Mehmood *et al.*, 2012). ANSYS Design modeller was used to model the rectangular grid around the NACA 0018 airfoil (Figure 62), and the model was meshed using ANSYS Meshing to create the structured mesh. The NACA 0018 airfoil coordinate points were imported into the Design Modeller (DM), a smooth curve was defined using ‘spline’ through the imported coordinate points. A rectangular plate was then designed around the airfoil, and thus creating a ‘boolean’ to create a smooth geometry for cleaner mesh generation.

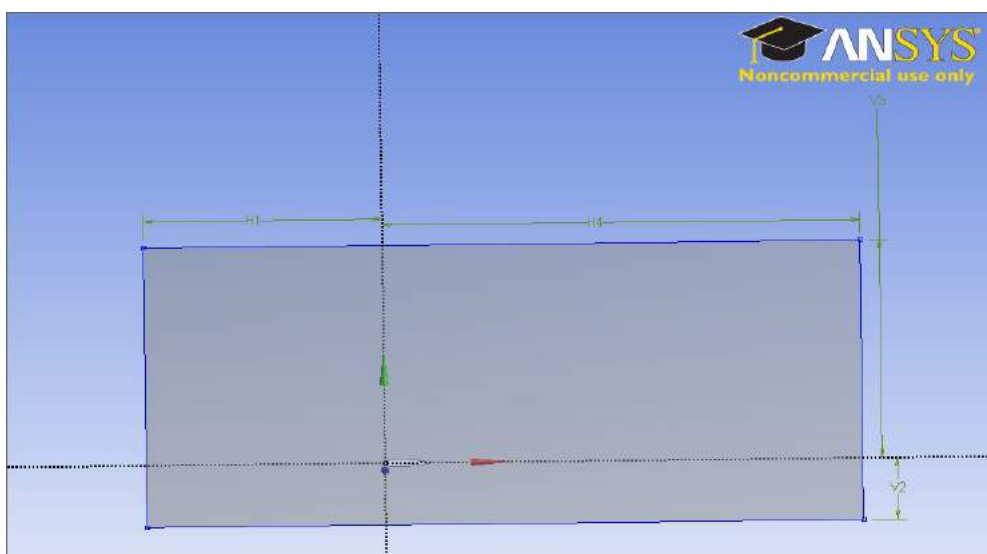


Figure 62 NACA 0018 geometry specification replicating Mehmood *et al.* (2012) geometry

The NACA airfoil curve generated with the rectangular plate was then imported into the ANSYS Meshing program to construct the structured mesh. While generating the mesh special considerations were made because of the curvature radius present on the airfoil to provide smoother mesh on the entire 2D geometry. It was noticed that ANSYS Meshing's default practice is to create a polyhedron geometric structure, based on the splines imported from the ANSYS DM. Thus the mesh was projected on the airfoil curves instead of the splines to obtain a steady mesh. Figure 63 shows the dimensions of the NACA 0018 0.5m and angle of attack 0°.

Details View	
[-] Details of Sketch1	
Sketch	Sketch1
Sketch Visibility	Show Sketch
Show Constraints?	No
[-] Dimensions: 4	
<input type="checkbox"/> H1	2.5 m
<input type="checkbox"/> H4	5 m
<input type="checkbox"/> V2	0.71 m
<input type="checkbox"/> V3	2.5 m
[-] Edges: 4	
Line	Ln7
Line	Ln8
Line	Ln9
Line	Ln10

Figure 63 NACA 0018 0.5m and angle of attack zero degree dimensions

## 5.4 Grid generation

The structured grid for the rectangular domain is a single block design which is based on the mapping of the flow direction, in ANSYS Meshing and due to this reason 11 blocks were created around the airfoil (Figure 64). The block structured mesh, uses multiple blocks created around the airfoil to make sure that the grid lines are normal to the airfoil wall, this practice is also recommended in the *CFX Reference Guide*. Three blocks were used instantly around the airfoil, which then extended the thickness to chord length ratio to 0.1, which is also called as the 'boundary layer blocks'. The mesh spacing along the airfoil edges were defined using the 'geometric' growth rate laws. This law obligates the number of edges on the airfoil and specifies the spacing and developing ratios at both the ends of airfoil edges. The stretching ratio was selected to be 1.1 along the airfoil wall and 1.05 in the normal wall direction.

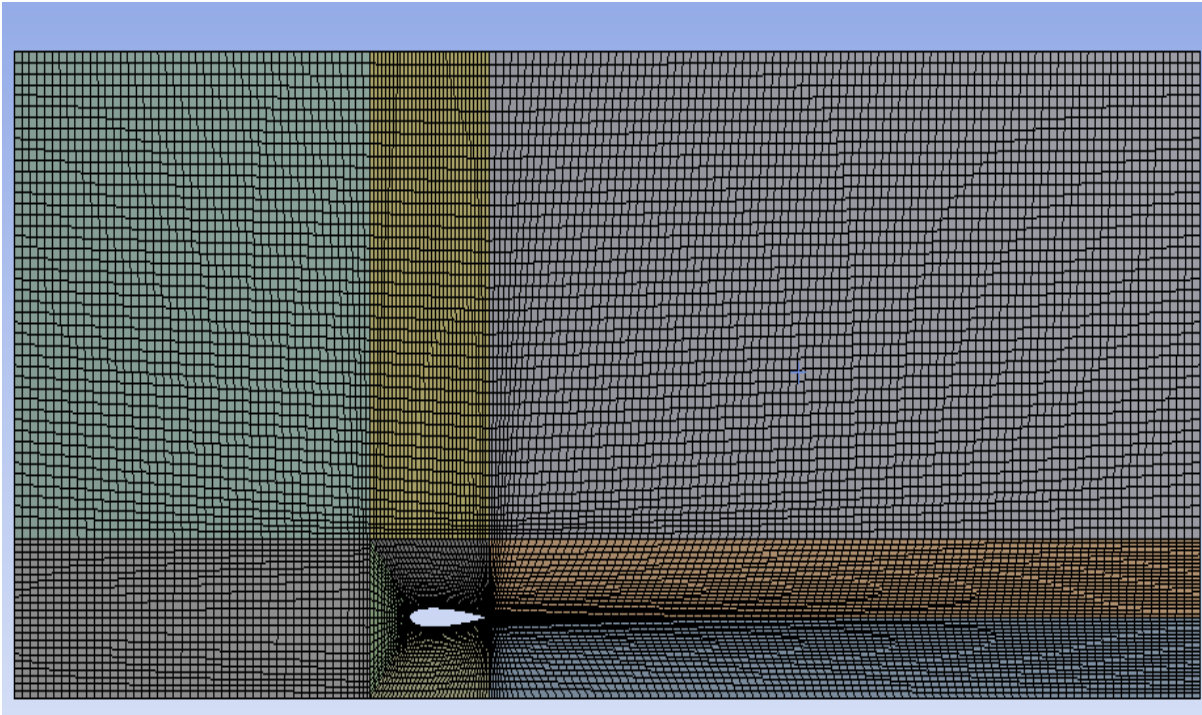


**Figure 64 Block cutting mesh view**

Mapped face meshing was used on the airfoil edges which have 7 faces and 14 vertices at the specific ends of each face. The block edge parameters used in designing the block grid edges are discussed in the Table 12 where all the curvature angles, and the growth rate were kept to default for all the edges.

**Table 12 Block edge parameters**

Edge Sizing	Number of Edges	Behaviour Type	Number of Divisions	Bias Type	Bias factor
<b>A</b>	1	Hard	1	No Bias	0
<b>B</b>	2	Soft	20		5
<b>C</b>	1	Soft	20		5
<b>D</b>	1	Soft	20		5
<b>E</b>	2	Soft	30	No Bias	0
<b>F</b>	1	Soft	20	No Bias	0

## 5.5 Boundary conditions, turbulence model, mesh convergence study

The boundary conditions set up in CFX, the mesh convergence and boundary conditions applied were as follows:

- 1) Inlet velocity = 1.2m/s (uniform), 'medium' turbulence intensity of 5%, and eddy viscosity = 10
- 2) The outlet pressure (static) was defined as 0 Pa, which is relative to 1atm,
- 3) Airfoil walls were defined as no slip walls, the bottom wall defined as symmetry, front and back face were defined as inlet and outlet walls respectively.

The airfoil wall is based 5 chord lengths of the airfoil (in both the cases of comparison), the outlet distance is 10 chord lengths of the airfoil (again in both the cases of comparison). As expected, the immediate intensity would vary the individual airfoil intensity resulting into the boundary errors and lead on to the grid convergence study. The non-dimensional wall distance  $y^+$  value is less than 10 to have optimal mesh spacing. As no specific water density value was specified by Mehmood *et al.* (2012), the sea water density was assumed to be  $\rho = 1025 \text{ kg/m}^3$  and the dynamic viscosity  $\mu = 0.00107 \text{ kg/(m.s)}$ . [These values are the sea water values at 25°C, which are inputted in CFX].

SST turbulence model was chosen to predict to the accurate hydrodynamic flow and pressure gradients on the airfoil, and also because of its good prediction of the boundary layer separation. It is a standard practice in the aerospace industry that the two dimensional validation of symmetrical airfoils, is done by using the Spallart-Allmaras turbulence irrespective of the inlet fluid (Singh *et al.*, 2012), but Versteeg & Malalasekera (2007, p. 91) state that "Spallart-Allmaras turbulence lacks sensitivity to transport processes in rapidly changing flows" (which is exactly the case with regards to the sea water flowing through horizontal axis tidal turbine blades), thus SST was decided to be used for the validation of the steady state simulations of the initial default 3D tidal turbine blade, as well as the curved shape blade.

All the incompressible 2D simulations performed in the four case studies show slight differences in the Reynolds number and the total advection time, occurring are highlighted in the Table 13. The residuals also show some oscillation frequency, it might be because of the elemental transient behaviour of the sea water flow solution and or additional far-field boundary related pressure conditions.

**Table 13 Reynolds number and advection time differences for case studies performed**

NACA 0018 Case study	Reynolds number	Advection Time (s)	Dynamic Viscosity (kg/ms)	Inlet velocity (m/s)
<b>0.5m 0°</b>	$3.314 \times 10^6$	2.407	$1.07 \times 10^{-3}$	1.2
<b>0.5m 15°</b>	$3.381 \times 10^6$	2.511	$1.07 \times 10^{-3}$	1.2
<b>1m 0°</b>	$5.067 \times 10^6$	3.669	$1.07 \times 10^{-3}$	1.2
<b>1m 16°</b>	$5.206 \times 10^6$	3.807	$1.07 \times 10^{-3}$	1.2

## 5.6 Comparison of the steady state simulations

Having discussed the boundary conditions, verification of the block cutting mesh, this section explores the comparison of the four case study simulations performed in this chapter. The comparison performed from the report of Mehmood *et al.* (2012) is listed in the Table 14.

**Table 14 Available data set for validation**

Data set available	Remarks
<b>Drag and Drag coefficient, angle of attack, different airfoil chord lengths, velocity streamlines in CFX</b>	NACA 0018 data

The data set chosen allowed specific comparison between the four case studies performed with the data of Mehmood *et al.* (2012), Figure 65 (Mehmood *et al.*, 2012; Figure 19) and Figure 66 shows a comparison of the maximum velocity streamlines for NACA 0018 chord length 500mm and angle of attack 15°. The CFD simulations predict that the occurrence of the stall at higher angles of attack causes the high lift coefficient is expected result for the RANS based CFD simulations. The comparison of the maximum velocity is also presented for all the four case studies presented along with the coefficient of velocity. It can also be seen that coefficient of velocity declines a bit when compared to the zero degree of angle of attack and with the chord length increase.

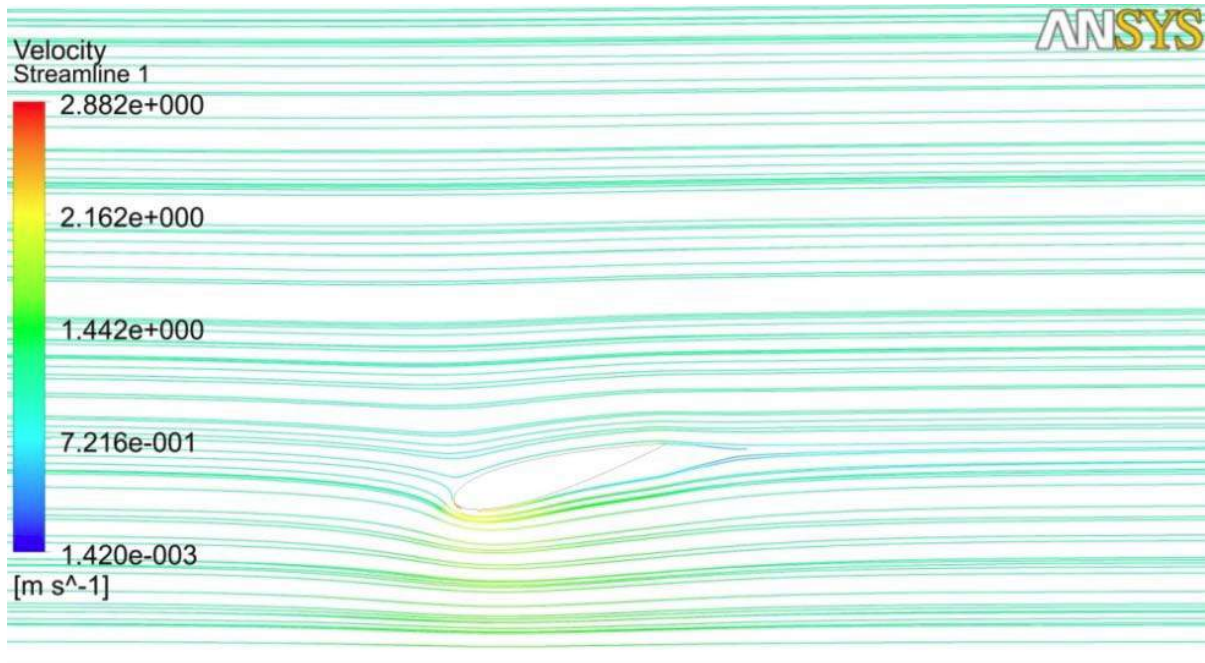


Figure 65 Velocity streamline of NACA 0018 0.5m and AOA 15° (Mehmood *et al.*, 2012)

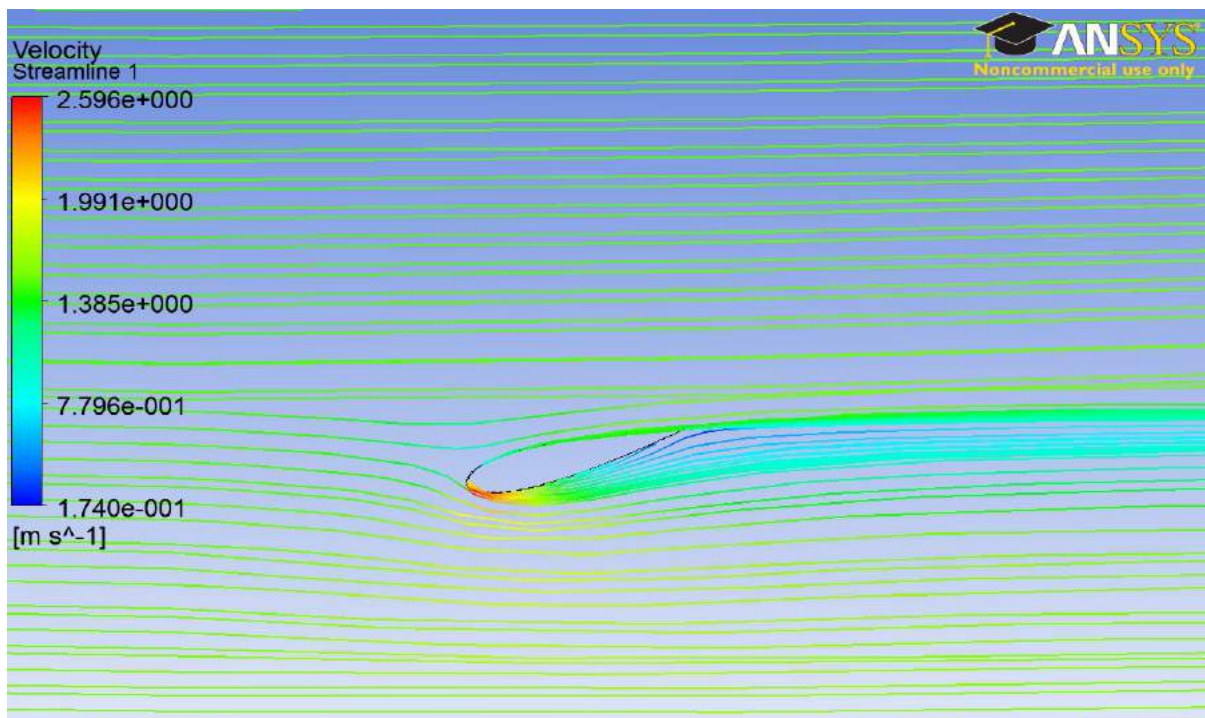


Figure 66 Velocity streamline for NACA 0018 chord length 500mm and angle of attack 15 degrees

Figure 67 (Mehmood *et al.*, 2012; Figure 25), and Figure 68 show the comparison of the maximum velocity streamlines for NACA 0018 chord length 1000mm and angle of attack 16°.

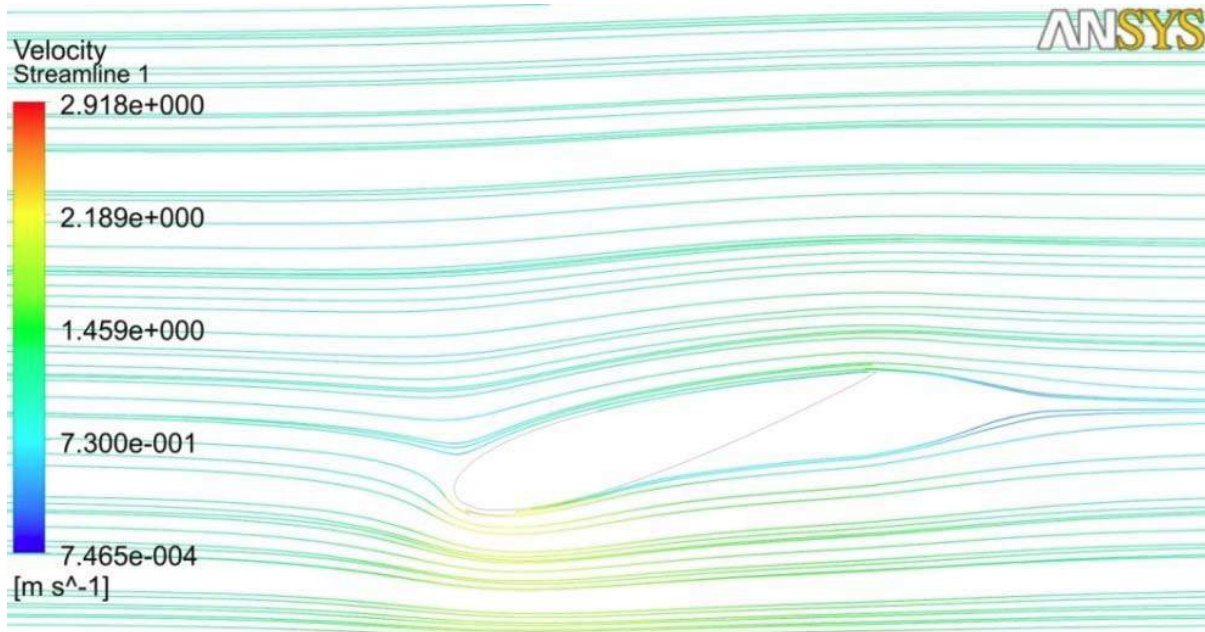


Figure 67 Velocity streamline for NACA 0018 length 1000mm and AOA 16° (Mehmood *et al.*, 2012)

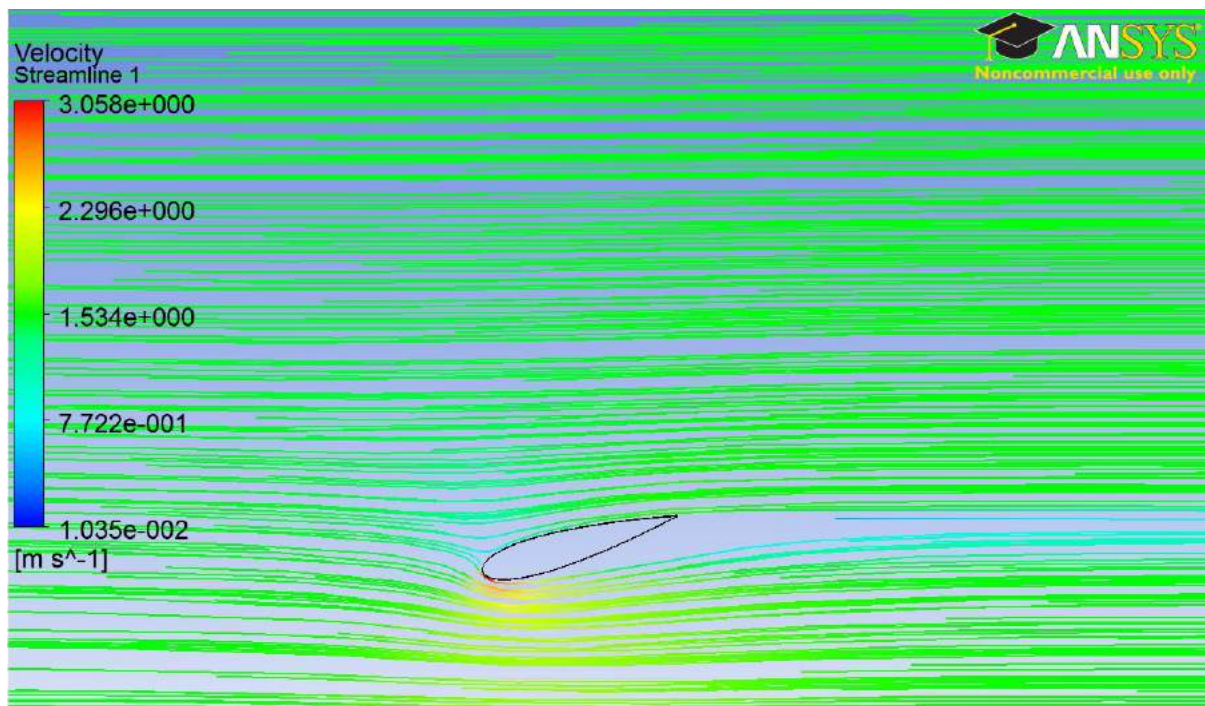
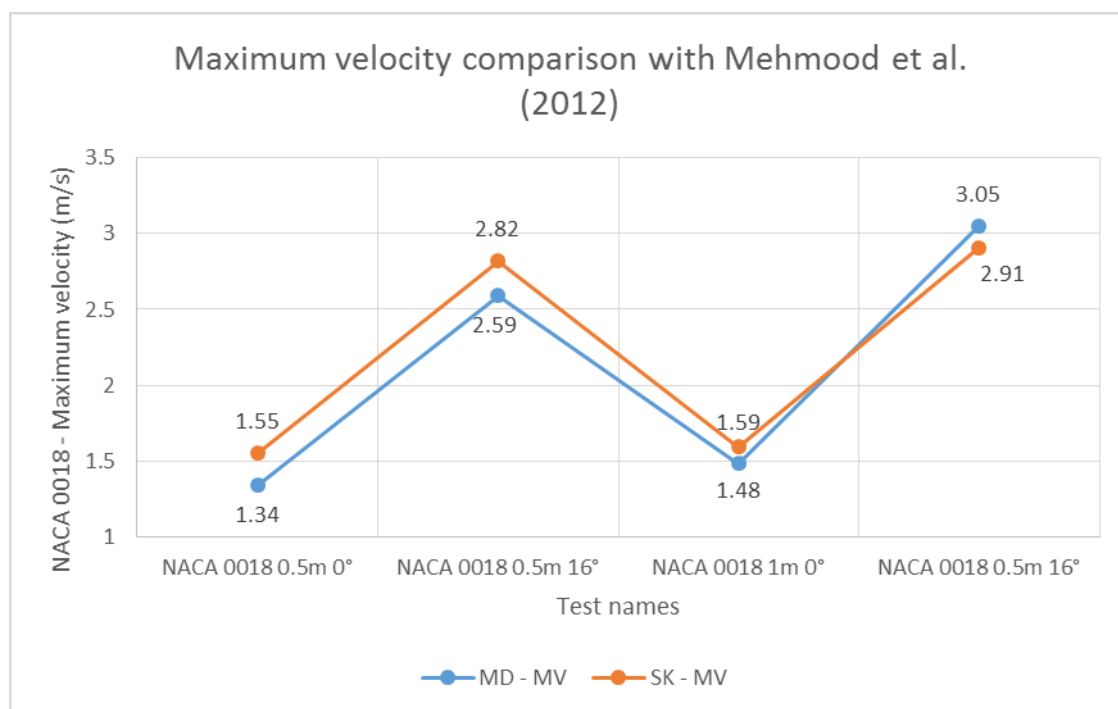


Figure 68 Velocity streamline for NACA 0018 chord length 1000mm and angle of attack 16 degrees

A comparison of the maximum velocity results (at different angles of attacks), drag force comparison (at different angles of attack) is demonstrated in Figures 69 and 70 respectively. Where 'MD-MV' is

the Mehmood *et al.* (2012) maximum velocity values for the specific case study, and 'SK – MV' is the author's maximum velocity values for the case studies performed in this chapter. There is good agreement despite of the few assumptions made in the design and modelling of the block cutting mesh, as drag is an important parameter while considering design of the tidal turbine blades in the real as well as the CFD world, as it increases with the increasing angle of attack. The CFD analysis of the zero-lift i.e. minimum drag values would be defined as the further validation and continuation of the studies presented in this chapter. However, by conducting the 2D NACA studies it is clear that for perfectly turbulent flow CFD results are always over projected for the maximum lift in comparison to the Mehmood *et al.* (2012) data agreement.



**Figure 69 Comparison of the maximum velocity values at different angles of attack**

In Figure 69, maximum sea water velocity at the bottom of the NACA 0018 airfoil is sketched against the angle of attack for the four case studies performed in this chapter. This graph clearly shows that maximum velocity values are approximately linear and show a good correlation in comparison with Mehmood *et al.* (2012) maximum velocity values for respective angles of attack. Thus, it can be concluded that maximum velocity increases with the increase in the chord length and the angle of the NACA 0018 airfoil, which in return also increases the mass flow rate at the inlet and the overall drag force values along the 'X-Axis' which is demonstrated in the Figure 70.

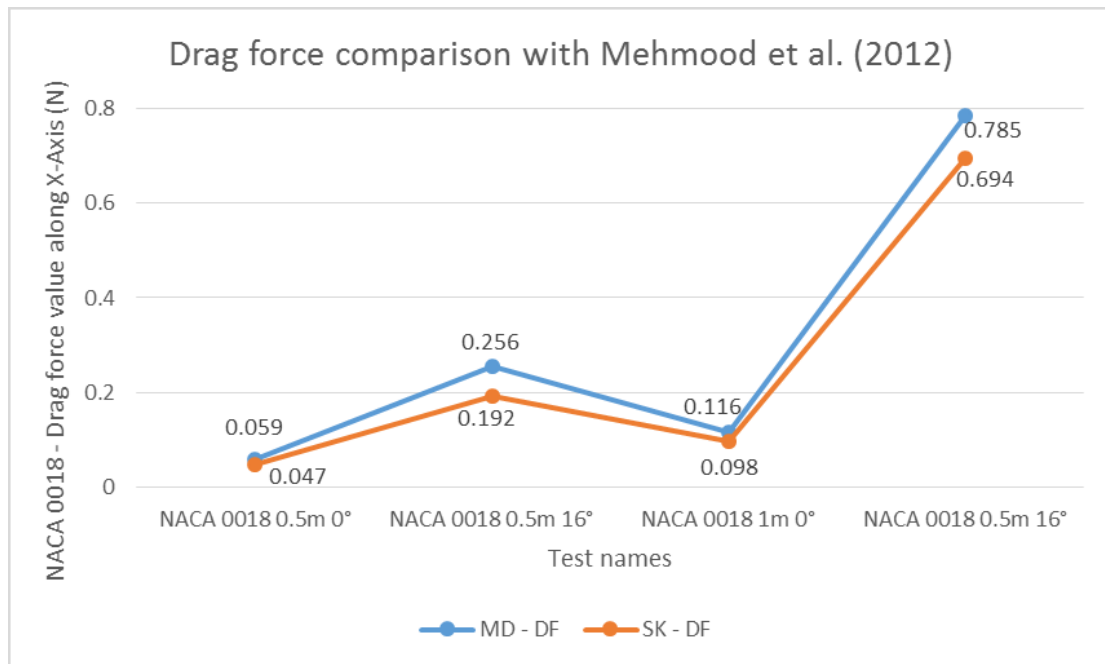


**Figure 70 Comparison of the drag values at different angles of attacks**

In Figure 70, the drag force values along the X axis of the NACA 0018 airfoil are plotted against various angles of attacks, for the four case studies performed in this chapter. As drag force is an important parameter which also governs the airfoil behaviour, the above graph clearly shows the linear correlation with the empirical data. Where 'MD-DF' are the Mehmood et al. (2012) drag force values along the X axis for the specific case study, and 'SK - MV' are the author's drag force values along the X axis values for the case studies performed in this chapter.

Succinctly, the validation of the steady state 2D CFD simulations of the NACA 0018 airfoil summarise the following:

- As illustrated in Figures 65 - 68 the maximum velocity values can be seen at the leading edge the airfoil, the agreement with the comparative data is within 5% for the maximum velocity/angle of attack. The CFD results could influence the over anticipation of the maximum velocity and the angle of attack where it occurs. As the sea water density and other values are also assumed, the results clearly show excellent correlation, further assumptions could also lead the poorer results, but was unknown and not necessary at this time.
- The anticipation of the drag force values show excellent compliance with the Mehmood et al. (2012) results. It is also observed that the maximum drag values tend to increase with the increasing of angle of attack. Overall, it can be concluded that CFD analysis of the 2D NACA

0018 airfoil show good agreement, and the same boundary conditions can be applied for the steady state simulation of the 3D default straight blade.

## 5.7 Two domain grid design and verification of the O-C grid

After the verification and the validation of the NACA 0018 airfoil case studies, the CFD analysis of the 2D NACA 0018 is further CFD analysis is carried out by designing O-C grid which is an adapted method to validate the 2D NACA validation in the wind turbine industry. The primary reason for performing this further verification of the 2D NACA CFD studies: firstly; it allows the author to investigate the efficacy of the SST turbulence under different grid conditions whilst keeping all the boundary conditions same, and secondly it allows the comparative analysis of the different grid results for the steady state CFD analysis, as the author planned to perform comparative analysis of the default 3D HATT (designed according to the literature), and the curved shape blade, for the  $C_L$ ,  $C_T$ ,  $C_P$ . In this section, the CFD simulations are only presented for one case study 'NACA 1m 0 degree angle of attack' and the results of the block cutting mesh are compared to the O-C grid case study.

The generation of the computational mesh domain was done using ANSYS meshing again, then comparison for drag, lift, and moment coefficient, a comparison which was not discussed for the NACA 0018 airfoil validation (as the data for lift and moment was not available for the validation). A density based solver was used maintaining the existing boundary conditions used in the validation of NACA 1m 0degree angle of attack, as this is a density based problem this also enables to have the same length of the computational domain as in the previous study without losing the numerical accuracy in the results. A C-grid is an element of the single block structure, it was created using 'three point arc' and remaining three blocks were created using the 'three point rectangle' to create multiple blocks around the NACA 0018 airfoil. Three projections were created to divide the geometry in four different parts to achieve higher meshing accuracy. The inlet distance from the airfoil was five times the chord length of the airfoil, and the outlet distance was ten times replicating the block cutting mesh settings (Figure 71). The two dimensional structured grid contains 15300 elements in total. The stretching and aspect ratio was chosen to be 1.05 along the airfoil wall and 1.1 in the normal wall direction for the remaining O-C grid.

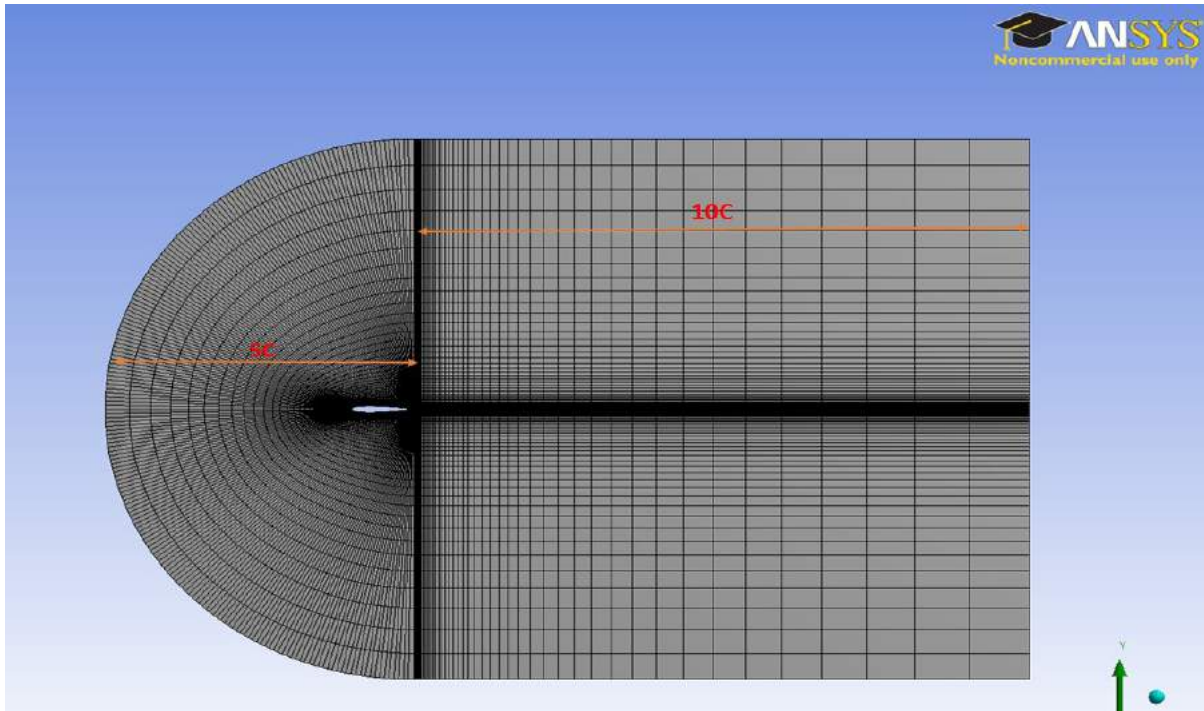


**Figure 71 Boundary spacing for inlet and outlet walls**

The two dimensional CFD simulations of the O-C grid were performed using ANSYS Fluent (v 14) which uses FVM in CFD analysis. The spatial discretisation for the flow, turbulent kinetic energy, specific dissipation rate, and momentum all of them were done using 'second order upwind scheme', as this is a time integration problem. The time step intervals and the grid refinement ratio is kept constant and small enough to avoid any maximum velocity loss due to the incompressible fluid in the flow field. The solution initialisation was computed from the inlet as all the initial values were all the inlet velocity and intermittency values were checked. Drag force coefficient surface monitor was defined in order to check the convergence is guaranteed convergence, as drag coefficient is the final coefficient to converge as compared to other aerodynamic coefficients. The 2D CFD simulations were performed only for zero degree of angle of attack, as this problem is solved in a density based solver the Reynolds number is kept constant whilst maintaining the thermodynamic properties like sea water density and dynamic viscosity as the block cutting mesh case study. Figure 72 shows the velocity vectors near the NACA 0018 airfoil respectively simulated for the O-C grid.

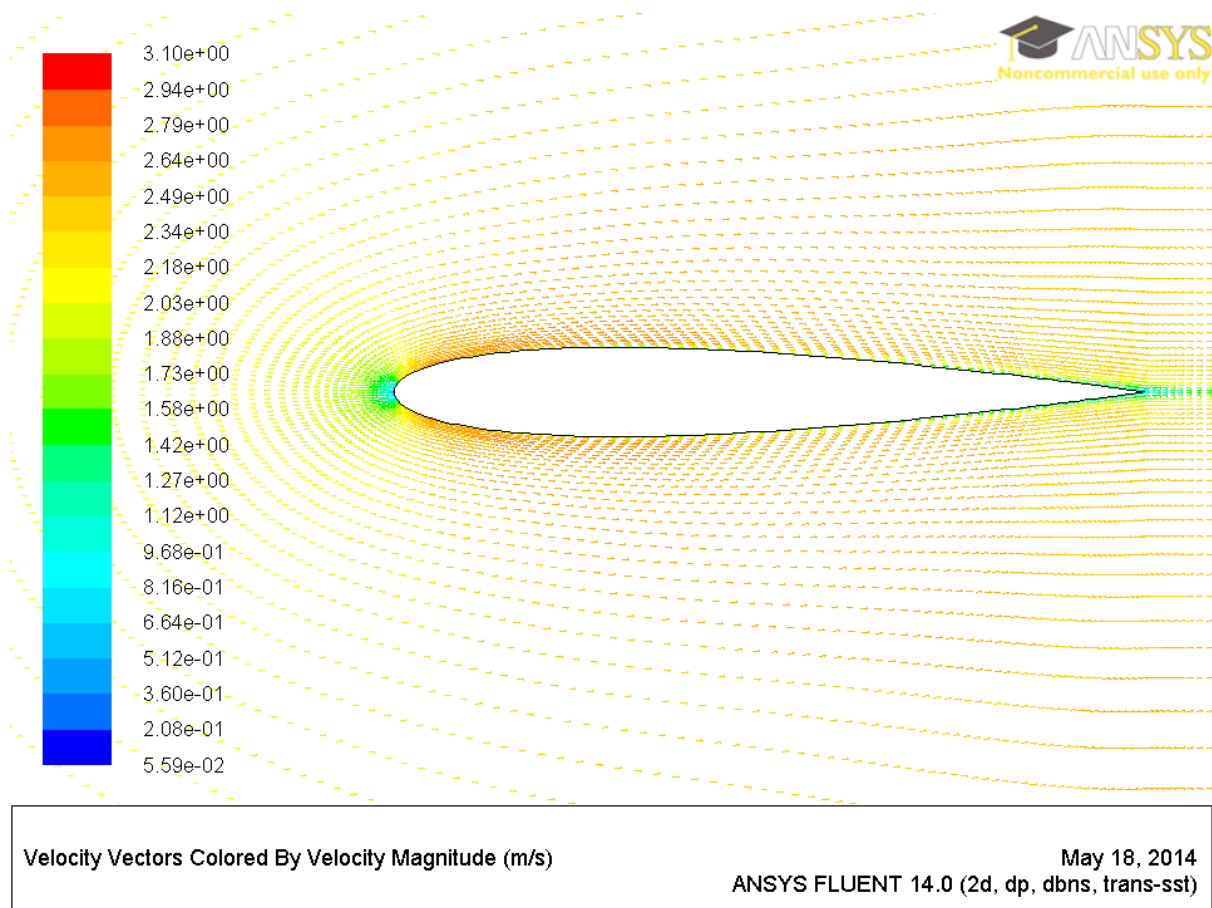


**Figure 72 Velocity vectors around the NACA 0018 airfoil**

The mesh density around the edges of the airfoil was refined to acquire the maximum possible turbulence kinetic energy, as this airfoil was later going to be used for three dimensional modelling purposes and tidal energy generation is based on the kinetic energy conversion. As mentioned earlier, the boundary conditions were kept constant with the block cutting mesh experiments where the temperature was 25°C. The airfoil walls were selected as the no slip walls and this included the inlet wall to achieve the highest Reynolds number possible. The convergence criteria was set to  $1 \times 10^{-5}$  for all the RMS residuals. The drag coefficient was calculated to ensure that convergence criteria was met. The verification of the O-C structured grid was done using the steady state CFD simulations presented above, with adapting the existing boundary conditions (block cutting mesh), the only difference in this grid the inner (airfoil) domain was fixed as a no slip wall and the outer (O-C) grid domain was relatively zero to the pitch angle. The case compare feature in ANSYS Workbench results is used to compare the CFD results for these two cases. The node residuals where the k, omega and the intermit theta residual are 'very high' when converging. The block cutting mesh CFD solution converges in 108 iterations and has 28822 nodes; whereas the O-C grid CFD simulation converges in 267 iterations, and has 15300 nodes. Thus it can be seen that despite O-C grid

computational domain having more surface area than the block cutting mesh case study, as the block cutting mesh was divided into 11 multiple blocks around the airfoil to study the flow effects increased the number of nodes for that case study. Thus, a clearer picture of the transient (real world) situation will be demonstrated in the next chapter for the three dimensional modelled tidal turbine blades.

## 5.8 Chapter summary

This chapter demonstrated the validation of the 2D NACA 0018 airfoil case studies, with a view to setting the 3D CFD simulations for this research. The steady state 2D CFD simulations were conducted using SST, which also formed the basis of the 3D tidal turbine blade steady state CFD simulations presented later on in the next chapter. The 2D CFD results provided with the drag coefficient increment with the increasing angle of attack for the block structured grid case study validation. A further comparative analysis was conducted using a different mesh setting to verify the flow problem in a time dependent solution showing the pressure differences on the upper and lower airfoil surfaces. The next chapter demonstrates the three dimensional steady state and transient CFD analysis done of the straight blade and all the designed curved caudal fin blades along with the used turbulence modelling sections, and thus identifying the improved efficiency curved caudal fin blade. The strategy to move the curved blade backwards to the straight blade is also highlighted. Finally, the power coefficient obtained from the curved caudal fin blade design is compared with the literature and discussed.

## 6 CFD based design studies of tidal turbines

### 6.1 Introduction

The objective of this chapter is to explain the design studies of the HATT and present the CFD analysis in order to obtain the numerical prediction of the power, and lift coefficients to compare the performance of both straight and curved caudal fin blade shapes. The design of the HATT is followed by classification of the sensitivity analysis of the design variables chosen for design studies in this research. A mesh independency study is also carried out on the Straight Blade to investigate the effects of the mesh resolution on the CFD results. The best mesh in terms of computational costs, is further employed for the numerical analysis performed in this research. The steady state and transient analysis of all the designed blades explained, followed by the comparison of the power coefficients obtained from the designed blades. The lift distribution on the blade spans which is caused due to the variations in the pressure is also illustrated. The computational overhead required to simulate the transient LES-Smagorinsky is informed by the understanding of the implementation of the CFD based design studies for five different shaped blades.

### 6.2 Design of the default straight blade

The designed default horizontal axis tidal turbine blade is formulated in three phases namely, theoretical, hydrodynamic and CFD. The design variables which define a horizontal axis tidal turbine blade are as follows:

1. Blade span (Total blade height),
2. Airfoil distribution (Number of airfoil stations),
3. Airfoil chord lengths,
4. Twist angle distribution
5. Blade material and anatomical features (which include hub, nose, blade stand and their thickness distribution).

The rotor diameter is also a design variable which is retrieved at the theoretical design phase of the tidal turbines parallel with number of blades, hub and nose height, diameter, angular velocity. After determining the above mentioned parameters the rotor span can be fixed. In the hydrodynamic

phase, the airfoil, chord length, and the twist angle distribution are determined. The design of the computational mesh, material and fluid flow properties are defined in the CFD analysis phase.

### 6.3 Classification of the sensitivity analysis variables

The design variables that define a tidal turbine blade are classified into distinct and assigned groups:

- Distinct: In this group design variables with single value like rotor diameter, number of blades, TSR, and angle of attack are classified.
- Assigned or distributed: In this group design variables which are assigned along the entire span of blade like number of airfoil stations, respective airfoil chord lengths, twist distribution etc. are defined in this section, which can also be represented as real numbers.

As the blades are designed using a direct design approach, all the design variables are selected and then the respective values are assigned for the designed blade based on the series of the design study criteria, thus steady state and transient CFD analysis is done on all the five designed blades (based on the percentage wise chord lengths), and all the analytical Navier-Stokes equations are solved using the turbulence models SST (for steady state CFD simulation), LES (for transient CFD simulation), for each and every blade case study. As the hydrodynamics of the tidal turbines blades are very complicated, the applied variable chord lengths and the pre-twist values are installed on the blade axis spinal variation in four stages, to determine directly the blade geometry that will achieve highest power coefficient. Thus the curved blade geometry which has achieved the highest power coefficient will then be further formulated to be compared and discussed with the HATT models in the tidal turbine literature.

### 6.4 Boundary conditions, turbulence models, and seawater properties

In order to produce maximum power from the designed horizontal axis tidal turbine blades the chord lengths and the twist angles were varied along the outward direction of the horizontal axis tidal turbine blade. To obtain the ideal cross-sectional blade shape with largest  $C_L/C_D$  called as lift to drag ratio was also considered. The boundary conditions slightly vary for steady state and transient CFD simulations performed for all the five case studies, due to the extra precision required for solving LES related simulations. The fluid was defined as seawater and the boundary conditions for the steady state analysis for all the five cases using SST turbulence model were as follows:

- 1) Inlet seawater velocity = 2.5m/s (uniform), 'high' turbulence intensity of 10%, and eddy viscosity = 10
- 2) The outlet pressure (static) was defined as 0bar,
- 3) The blade was defined as a 'Rotating Wall', with no slip wall condition, for mass and momentum option,
- 4) The bottom, and side walls were defined as the free slip walls to incorporate the accuracy when solving the continuity equation.
- 5) The front, and back wall were defined as inlet and outlet walls respectively.

The SST turbulence model was chosen to predict the accurate hydrodynamic flow and pressure gradients on the airfoil, and also because of its good prediction of the boundary layer separation; whilst verifying the steady state simulations of this research. As the water velocity decreases the pressure on the frontal area of the turbine increases, which in return causes the mass flow rate to deviate sideways and exploit the kinetic energy available in the water to make tidal turbine blades to rotate. This thus proves a challenging case to validate the SST turbulence model, because of the number of the flow characteristics involved in the experimentation. The flow modelling near to the leading edge experiences a laminar separation bubble due to the turbulence, and at the trailing edge recirculation of the flow is experienced.

The boundary conditions for the transient analysis for all the five cases using LES turbulence model were as follows:

- 1) Inlet seawater velocity = 2.5m/s (non-uniform), there is no turbulence intensity option available as LES filters the turbulence with stream wise periodic boundaries,
- 2) The outlet pressure (static) was defined as 1bar, which is also called as zero boundary condition,
- 3) The blade was defined as a 'Rotating Wall', with no slip wall condition, for mass and momentum option,
- 4) The bottom, and side walls were defined as the free slip walls to incorporate the accuracy when solving the continuity equation.
- 5) The front, and back wall were defined as inlet and outlet walls respectively.

LES uses a spatial filtering operation for the separation of the smaller and larger scale eddies rather than time-averaging the transient solution, which makes it computationally more expensive and challenging to solve the unsteady flow calculations, and can also lead to inaccurate simulation if the mesh or boundary conditions are set incorrectly. In order to avoid the spatial discretisation error,

which is also called as mesh/grid convergence study, the mesh settings used for the verification purposes used a non-linear grid refinement ratio  $\sqrt{2}$  which is also recommended in the *CFX Reference guide*, each mesh element had a double refinement ratio. Although, the correlation between the order of convergence is slightly higher, the solution is globally converged at all the degrees of freedom. The exact reason for the varying convergence order is because of the assumptions made on the sea water density and mesh settings as the available information in the verification was limited. Ideally, another assumption would be due to a specific flow feature which was not resolved for the chosen grid, which would affect the modelling changes, and is a minor criterion which can be neglected (Gretton, 2009). As CFX, follows the Richardson extrapolation grid convergence method for comparison, which states that maximum spatial error for drag or lift can be less than or equal to 5%, this would not affect the generation of power or the HATT efficiency.

The blade is based on 5 diameter lengths of the blade (in all the cases of the verification, and comparison), the outlet distance is 10 diameter lengths of the blade (again in all the cases of the verification, and comparison).

## 6.5 Design of the curved caudal fin blades

As explained in the previous sections, a direct blade design and CFD analysis approach was employed as it normally imposes a fixed blade topology and hydrodynamic characteristics to give a robust CFD solution for the designed blade. As the formulated design study is based on the CFD analysis and is set to find the maximum power coefficient from the designed blades, a particular inlet velocity is set at which the results are numerically calculated. The end objective function of the chosen direct blade design method was to compare the highest power coefficient obtained curved caudal fin blade with the literature, also calculating the annual power production of the straight blade design, and the highest power coefficient curved caudal fin blade design, for the chosen Pentland Firth, UK tidal energy site. As the yearly power production of the designed tidal turbine blades is determined by the tide characteristics of that particular site as well as the installed tidal turbine blade system, seawater density is a feasible function of the seawater velocity. The following sections elaborate on the design study strategy implemented as the centreline is moved in percentage chord length basis, including the strategy to move the curved caudal fin blade shape backwards to straight blade shape.

### 6.5.1 Moving the centreline in percentage chord lengths and constant blade radius

As the chord lengths for the target shape (a curved caudal fin shape); the polynomial centreline was moved in the percentage chord lengths in order to reach the target shape. For the initial experimentation, “the percentage chord lengths were moved in 0%, 25%, 50%, 75%, and 100%”. Where 0% would be the initial straight blade chord lengths, and then the chord lengths are increased in 25%, 50%, and 75%. So for the convenience and start up experimentation “the same blade is optimised, the total blade height and number of stations are kept constant until the best design (maximum power coefficient of the blade system is found)”. It is now possible to calculate the percentage wise chord length values; a linear progression function was defined to calculate the percentage chord length using following equation which is demonstrated as follows:

$$R_v = \left[ \left( \frac{Ed_{val} - St_{val}}{100} \right) (R_p) \right] + St_{val} \quad \text{Eqn. 70}$$

where  $R_v$  is the required chord length value,  $Ed_{val}$  is the end value of target shape chord length value,  $St_{val}$  is the starting chord length value of the initial blade,  $R_p$  is the required chord length percentage.

For example The NACA-AIRFOIL-ROOT (Default blade) chord length:  $St_{val} = 1000\text{mm}$ , and target shape NACA-AIRFOIL-ROOT chord length:  $Ed_{val} = 1645\text{mm}$  and the starting percentage value:  $R_p = 25$ ; then substituting these values in the Equation 70 we get the  $R_v$  as 1161.25mm (for the root chord length of 25% curved blade). The baseline airfoil used in all the stations is NACA 0018, for initial experimental studies and the third order polynomial function is introduced at the percentage stages. The third order polynomial function will stay constant in order for the percentage based geometries to resemble like Marlin fish caudal fin. As, 9 airfoil stations were defined for the default straight blade, initial experimentation will also include 9 airfoil stations for each four percentage stages this can be highlighted in Table 15.

**Table 15 Percentage based chord length values in four stages**

Station name and number	R (mm)	Straight blade 0% chord length, c (mm)	25% chord length, c (mm)	50% chord length, c (mm)	75% chord length, c (mm)	Target shape 100% chord length, c (mm)
<b>NACA-AIRFOIL-ROOT</b>	1410 (Default)	1000 (Default)	1161.25 (Calculated)	1322.50 (Calculated)	1483.75 (Calculated)	1645 (Default)
<b>STATION-1</b>	1970 (Calculated)	920 (Calculated)	1024.25 (Calculated)	1128.50 (Calculated)	1232.75 (Calculated)	1337 (Default)
<b>STATION-2</b>	2530 (Calculated)	840 (Calculated)	902.75 (Calculated)	965.5 (Calculated)	1028.25 (Calculated)	1091 (Default)
<b>STATION-3</b>	3090 (Calculated)	760 (Calculated)	801 (Calculated)	842 (Calculated)	883 (Calculated)	924 (Default)
<b>STATION-4</b>	3660 (Calculated)	680 (Calculated)	712 (Calculated)	744 (Calculated)	776 (Calculated)	808 (Default)
<b>STATION-5</b>	4220 (Calculated)	600 (Calculated)	615.75 (Calculated)	631.5 (Calculated)	647.25 (Calculated)	663 (Default)
<b>STATION-6</b>	4790 (Calculated)	520 (Calculated)	517.25 (Calculated)	514.5 (Calculated)	511.75 (Calculated)	509 (Default)
<b>STATION-7</b>	5320 (Calculated)	440 (Calculated)	418.25 (Calculated)	396.5 (Calculated)	374.75 (Calculated)	353 (Default)
<b>STATION-TIP</b>	5920 (Calculated)	360 (Calculated)	272.50 (Calculated)	185 (Calculated)	97.50 (Calculated)	24.37 (Default)

### 6.5.2 Strategy to move the curved blade shape backwards to straight blade shape

As tidal turbine blade power coefficient is very sensitive to the blade twist, chord length distribution and mainly the total blade height, and changing the value of each and every design variable would be very time consuming and the computational overhead required when simulating to check the relationship between the design variables is massive. To overcome this problem, perturbation of the default blade design method was used. Using this method a new candidate design was produced using the percentage based chord lengths; by a random deviation of the initial default straight blade rather than generating a random blade from scratch. This method was applicable as the design variables were distributed (i.e. chord, twist angle, and span). Using this method percentage based chord lengths were selected and the third order polynomial function will stay the same making sure that the blade span or total blade height will stay same as the default straight blade.

Thus it was possible to define an design study strategy to move the target shaped curved caudal fin blade backwards to the straight blade shape using a linear progression function based on the target shape curved blade which is designed using “image processing (to preserve the total blade height) for all the designed blades”, the linear progression function can be demonstrated as follows:

$$T_{ASTN} = T_{SXC} \times \left( \frac{R_p}{100} \right) \quad \text{Eqn. 71}$$

where  $T_{ASTN}$  is the required airfoil station value,  $T_{SXC}$  is the target shape X-coordinate value for the particular airfoil station,  $R_p$  is the required chord length percentage.

The NACA-AIRFOIL-ROOT (target shape) X-coordinate value = 595.568, and target shape, and the starting percentage value:  $R_p = 25\%$ ; then substituting these values in Equation 73 we get the  $T_{ASTN}$  as 148.92 (for the root chord length of 25% curved blade). The third order polynomial function will stay constant in order for the percentage based geometries to resemble like a curved caudal fin. As 9 airfoil stations were defined for the default straight blade, the curved blade shape design experimentation will also include 9 airfoil stations for each blade axis spinal variation. Thus after calculating the X and Y-offsets for the blade spinal axis variation the backward design strategy can be plotted in Figure 71.

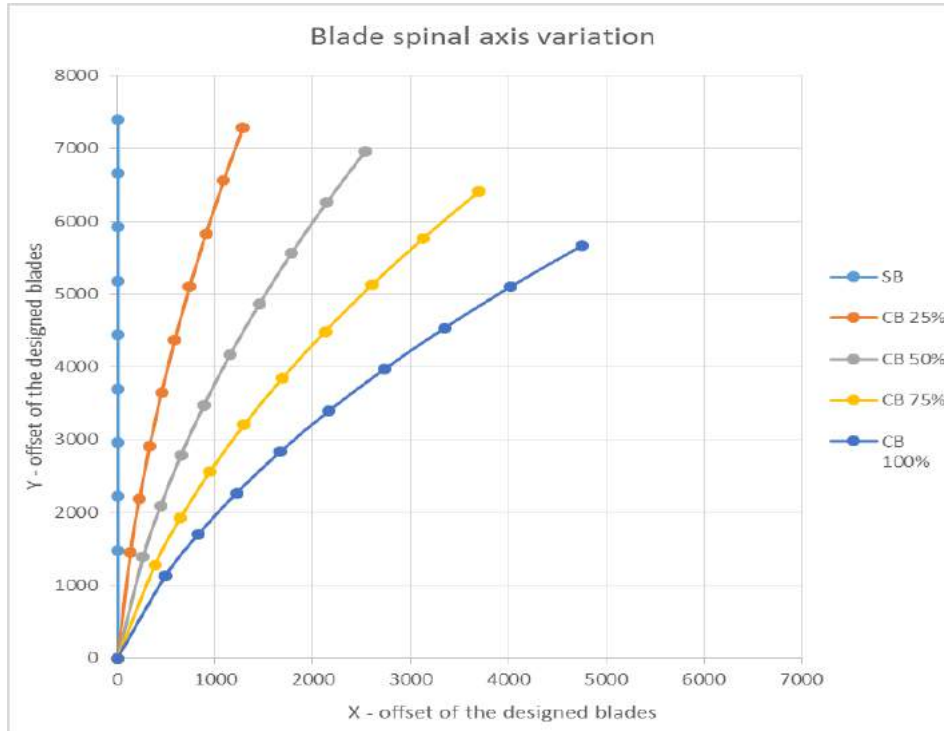


**Figure 73 Blade Spinal axis variation**

The perturbation from the initial straight blade to the target curved blade shape is done by setting following parameters in order to create robust CFD simulations for each of the designed blade, and optimised at the same time:

- Maintain constant total blade height, number of airfoil stations for all the blades,
- Considering the lower and upper limits for twist angle for all the blades,
- Performing mesh independency study, steady state, and transient CFD analysis for all the blades,
- Comparing the power, and lift coefficients, and thus putting forward the highest power coefficient obtained curved caudal fin blade to compare and discuss with tidal turbine literature.

In the computed bisection, each design variable was weighted as the average of its corresponding parents i.e. the parents being default straight blade and target shape curved caudal fin blade. After the generation of the five blade geometries, they were analysed in steady state and transient simulations to calculate their numerical performance. After the convergence of each solution the pressure, velocity plots are generated along with the non-dimensional coefficients. The following

section elaborates on the mesh independency study, steady state analysis, mesh convergence values, and the CFX set up values.

## 6.6 Mesh independency study

To establish the accuracy of the CFD solution, and to keep the computational costs low the Straight Blade was analysed using: the standard k- $\epsilon$  model, and SST model. This case study was selected because the Straight Blade is further designed as the curved caudal fin shaped blade using the third order polynomial (which has constant total blade height, number of airfoil stations), at uniform  $V_{in} = 2.5\text{m/s}$ , and  $\lambda = 5$ . The grid convergence study was performed by developing three different meshes: with coarse grid, medium grid, and fine grid for all six different meshes of the Straight Blade in order to predict the power, lift coefficients, and torque with respect to normalised mesh cells to determine how the mesh quality affects CFD simulation results.

The number of nodes, the simulation time, for the three cases simulated using SST model are highlighted in Table 16, and the other three cases simulated using standard k- $\epsilon$  model are listed in Table 17. Table 16, and 17 summarise the key characteristics of the meshes, and it is very clear that CFD simulation time greatly depends on the number of mesh nodes considered. The six meshes generated have near wall resolution i.e.  $y^+ < 10$  by using the standard wall function approach to avoid unsatisfactory results when using standard k -  $\epsilon$  model.

**Table 16 Mesh size, CFD simulation time, and estimated  $C_p$  for SST model at  $\lambda = 5$**

Mesh Resolution	Coarse mesh (M1)	Medium mesh (M2)	Fine mesh (M3)
Number of nodes	79859	151740	230439
CFD simulation time	4hrs 10mins	6hrs 16mins	9hrs 53mins
Estimated $C_p$	0.3816	0.4169	0.4218

**Table 17 Mesh size, CFD simulation time, and estimated  $C_p$  for k- $\epsilon$  model at  $\lambda = 5$**

Mesh Resolution	Coarse mesh (M4)	Medium mesh (M5)	Fine mesh (M6)
Number of nodes	44064	92767	139506
CFD simulation time	1hr 36mins	4hrs 41mins	5hrs 38mins
Estimated $C_p$	0.2271	0.2586	0.2693

In the case of investigated meshes of the Straight blade, the turbine domain has an increased mesh resolution due to the blades being exposed to the complex flow separation. The mesh is refined in the grids from M1 to M6 where M1, M2, M3 represent coarse, medium, and fine mesh generated for the SST turbulence model; and M4, M5, M6 represent coarse, medium, and fine mesh generated for the standard k- $\epsilon$  turbulence model. The estimated power coefficient increased from 0.2271 to 0.4218 as shown in Figure 74.

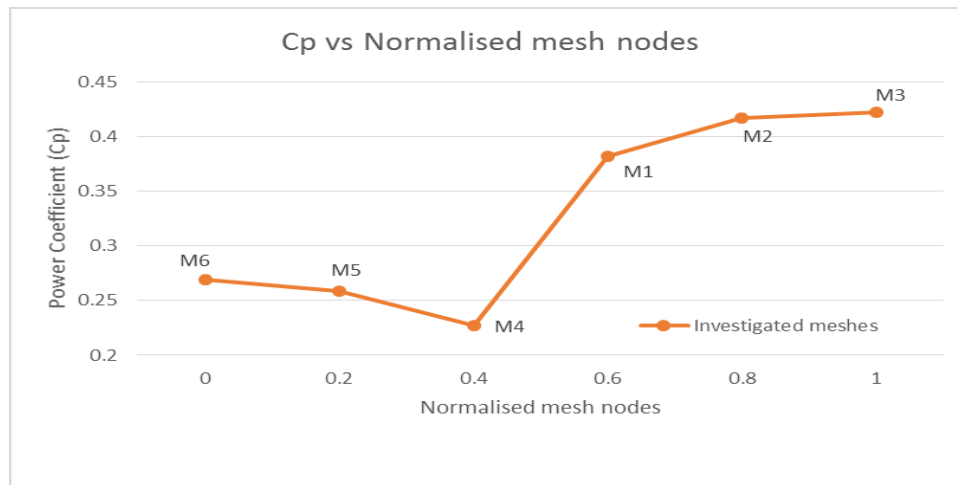


**Figure 74** the power coefficients of all the investigated meshes in mesh independency study

It is important to note that the mesh resolution plays a pivotal role in the final CFD results, the mesh nodes need to be small in order to resolve the boundary layer on the blade surfaces. The highest  $C_p$  obtained from the mesh independent study conducted is 0.4218 for M3 from SST model. M2 and M3 account in nearly 1% difference in the estimated power coefficients, but the final CFD simulation time required for convergence of the two meshes has massive difference when employed conventional mesh independency method. The power coefficients obtained from the standard k- $\epsilon$  model are almost 15% to 20% lower than the SST model power coefficients, which is caused due to the poor performance of k- $\epsilon$  model in near wall regions and in the adverse pressure gradients i.e. the fluid flow near the turbine blade surfaces; which causes the k- $\epsilon$  model to underestimate the power coefficient.

It is clear from the final CFD simulation results obtained in the mesh independence study that the simulation time is highly dependent on the number of mesh nodes, and the turbulence model selected. As shown in Fig. 74 the CFD solution when using k- $\epsilon$  model for all the meshes (M4, M5, and M6) employed under predicts power coefficient when compared with the SST model. M1 relatively leads to reasonable prediction of the power coefficient on the Straight Blade, whereas M2, and M3 it can be seen that the power coefficient of M3 is slightly better than M2. Due to the slight difference

medium mesh (M2) is the best mesh in terms of computational costs and is further employed for the numerical analysis carried out in the following section of turbulence model comparison study.

### 6.6.1 Turbulence model comparison study

To understand the sensitivity of the CFD solution a consecutive study was carried out with reference to above mentioned turbulence models at medium sized meshes. From the mesh dependency test conducted it has been found that SST model performs superiorly in adverse pressure gradient situations than the standard k- $\epsilon$  model; because SST model is a unification of k- $\epsilon$  model and k- $\omega$  model for free stream and inner boundary layer problems respectively. Figure 75 shows the torque coefficient related to each of the two turbulence model analysed for medium mesh. As shown in Fig. 74 the SST model medium mesh has higher  $C_M$  than the standard k- $\epsilon$  model in all the 9 different TSR's. It can also be seen that the torque coefficient of SST medium mesh model increased by more than 25%, when compared to the standard k- $\epsilon$  model medium mesh.

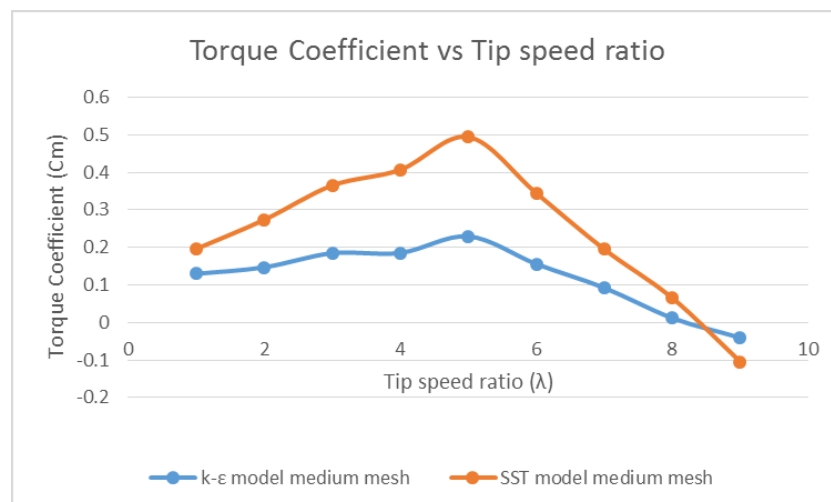


**Figure 75 Torque coefficient versus Tip speed ratio for k- $\epsilon$  and SST model medium meshes**

The highest  $C_M$  is achieved at  $\lambda = 5$  for both the cases,  $C_M$  increases with the increasing TSR and acts as a function of TSR. It can also be noted that the non-linearity in the torque coefficient occurs after TSR of 5, and the k- $\epsilon$  model fails to capture this, due to the boundary layer and turbulence quantities to the blade wall.

Figure 76 shows that the power coefficient increases steadily until  $\text{TSR} \approx 5$ , at which it shows the peak  $C_p \approx 0.4169$  for the SST model medium mesh; after which it shows a drastic reduction with the increasing  $\lambda > 6$ . The curve for the k- $\epsilon$  model medium mesh shows that it predicts lower power

coefficient to a satisfying level of accuracy, and also under predicting the values with increasing  $\lambda$ . However, the numerical  $C_p$  prediction by the SST model medium mesh observed values are approximately 20% higher than the k- $\epsilon$  model medium mesh simulation, the range  $5 \leq \lambda \leq 6$  was also validated by Bahaj et al. (2007), McSherry et al. (2011); and considered to be optimum range for HATT's. The standard k- $\epsilon$  model is incapable of capturing the account of rotational forces and their effects on the turbine blades, and due to the near wall physics implementation. Thus, the  $C_p$  prediction by SST model is more reasonable and acceptable when compared to the power coefficient predictions by the standard k- $\epsilon$  model.

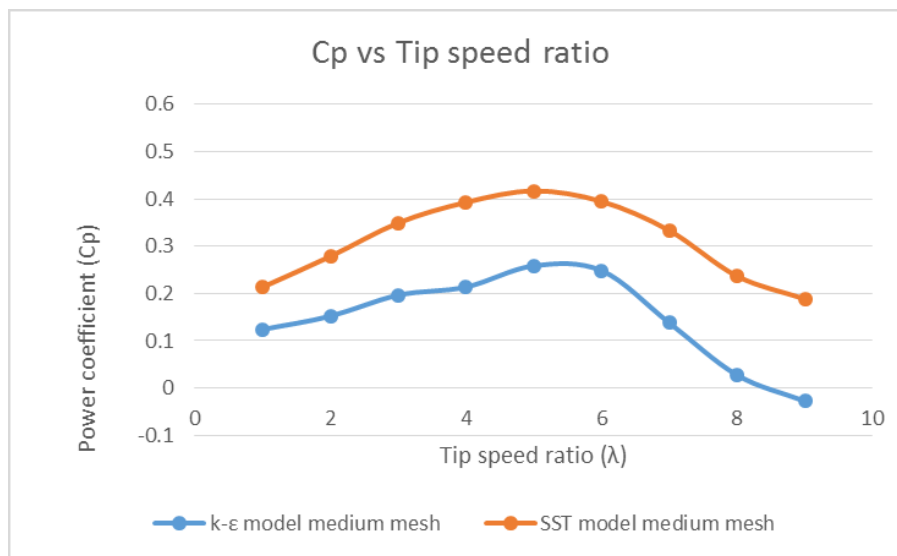


**Figure 76 Power coefficient versus Tip speed ratio for k- $\epsilon$  and SST model medium meshes**

As a result, of the mesh independency test conducted it can be concluded that the overall power coefficient shown by the SST turbulence model are more reasonable than the standard k- $\epsilon$  model, for all the cases considered. Therefore in order to avoid any misleading CFD results the standard k- $\epsilon$  model is not employed in any further CFD tests conducted in this research. The power coefficient of a HATT is highly sensitive to the turbulence model chosen for the CFD analysis; however the mesh independent CFD solution for SST medium mesh satisfactorily achieves the mesh independency over the SST fine mesh solution which requires a massive computational overhead. Hence, medium mesh is used to conduct the steady state and transient analysis in further sections; for all the blade design case studies.

## 6.7 Steady State CFD analysis using Shear Stress Transport model

The three dimensional modelling and steady state simulations presented in this section are conducted using ANSYS CFX, using the Shear Stress Transport model to solve the Reynolds Averaged Navier Stokes (RANS) equations for the unstructured mesh approach used on the developed five models to predict the highest efficiency generating blade. The computational mesh is finer near the turbine disc area, and coarser on the seawater domain modelled in the unstructured pattern to improve the accuracy of the CFD simulation, as the seawater flow passing through the twisted initial straight blade and the curved blades is highly incompressible and complicated due to varying twist and the chord lengths around the entire span of the blade. Figure 77 shows the blade meshing including the hub and tips of the blade.

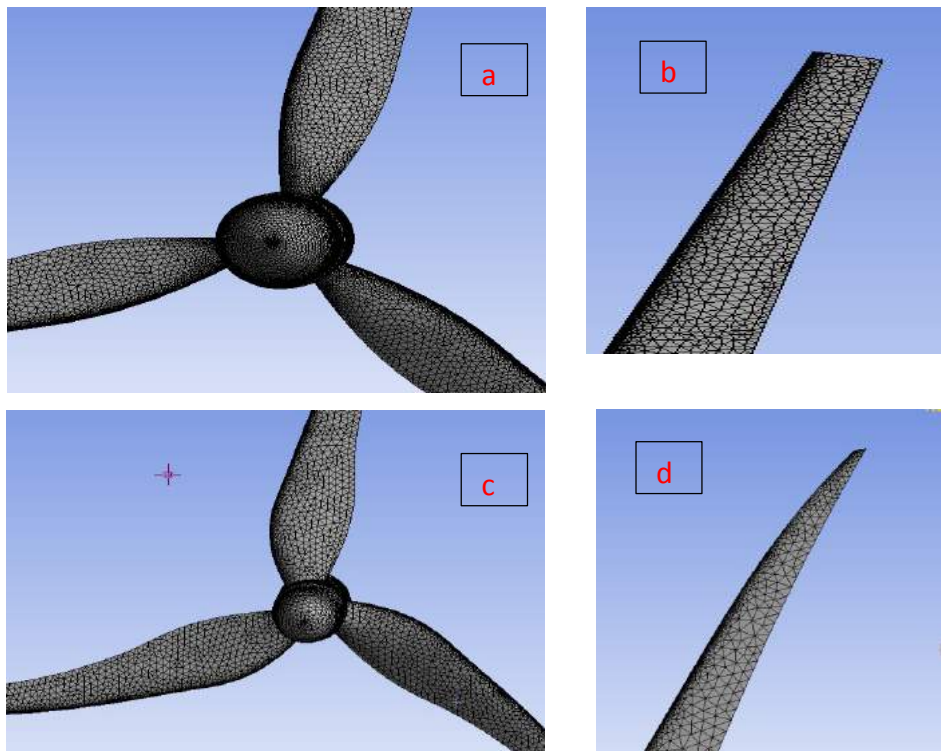


**Figure 77 a) Meshed SB with blades and hub, b) SB meshed tip, c) Meshed CB 75% with blades and hub, d) CB 75% meshed tip**

In ANSYS CFX, the pressure-velocity coupling was done using “Rhie Chow Option”, which is equivalent to the SIMPLE algorithm used for pressure-velocity coupling in ANSYS FLUENT, all interpolation and advection values were set as “High Resolution” for Continuity, Momentum, Density and Turbulence Kinetic energy, which is equivalent to Second Order Upwind Interpolating

Scheme values in ANSYS FLUENT. In the meshing aspect, some controls were modified of the meshing controls in order to suit the concentration on the curved shaped blades because of the additional bend on the surface. Those functions are summarised below and the respective characteristics are presented in Table 18.

- **Mesh growth rate:** The increment in the mesh element edges and the layer of elements associated with it.
- **Maximum and minimum mesh size:** The maximum and the minimum mesh size ANSYS mesher will address after meshing operation is completed.
- **Maximum mesh size:** The maximum mesh size ANSYS mesher will address after the meshing operation is completed.
- **Curvature normal size:** The maximum span angle allowed to a mesh element to address.

**Table 18 Mesh Parameters for all the designed blades (SST)**

Blade Model	Mesh growth rate	Maximum mesh size (mm)	Minimum mesh size (mm)	Curvature normal angle (°)	Number of nodes
SB	1.2	2500	75	15	151740
CB 25%	1.15	2100	50	13	195647
CB 50%	1.10	1800	45	11	226846
CB 75%	1.05	1500	40	10	252839
CB 100%	1.0	1150	35	10	309461

It can be noticed from the above table that the number of nodes of the CB 100% case study are almost twice that of SB case study this is due to the flow being considerably complicated and the blade surfaces being bent for the curved blade shape. The minimum mesh size was also reduced for the CB case studies as that of the SB case study to improve the near wall resolution and the CFD solution to produce an acceptable level of spatial resolution. There was a slight over prediction of the convergence of the computational model as the entire seawater domain is 222m long, and the

secondary effect of the thrust losses were expected, due to inception of angular velocity of the blade at the designed TSR.

As the seawater flow velocity progressed over the blade pressure side the pressure increased especially on the tip of the blade as it was affected due to the rotational velocity being the highest on the tip. At the same time flow velocity at the same time decreased; which further resulted in arduous movements on the blade suction surface except on the trailing edge of the blades. Figure 78 shows the comparison of the blade pressure distribution on the case studies performed (blades rotate anti-clockwise).

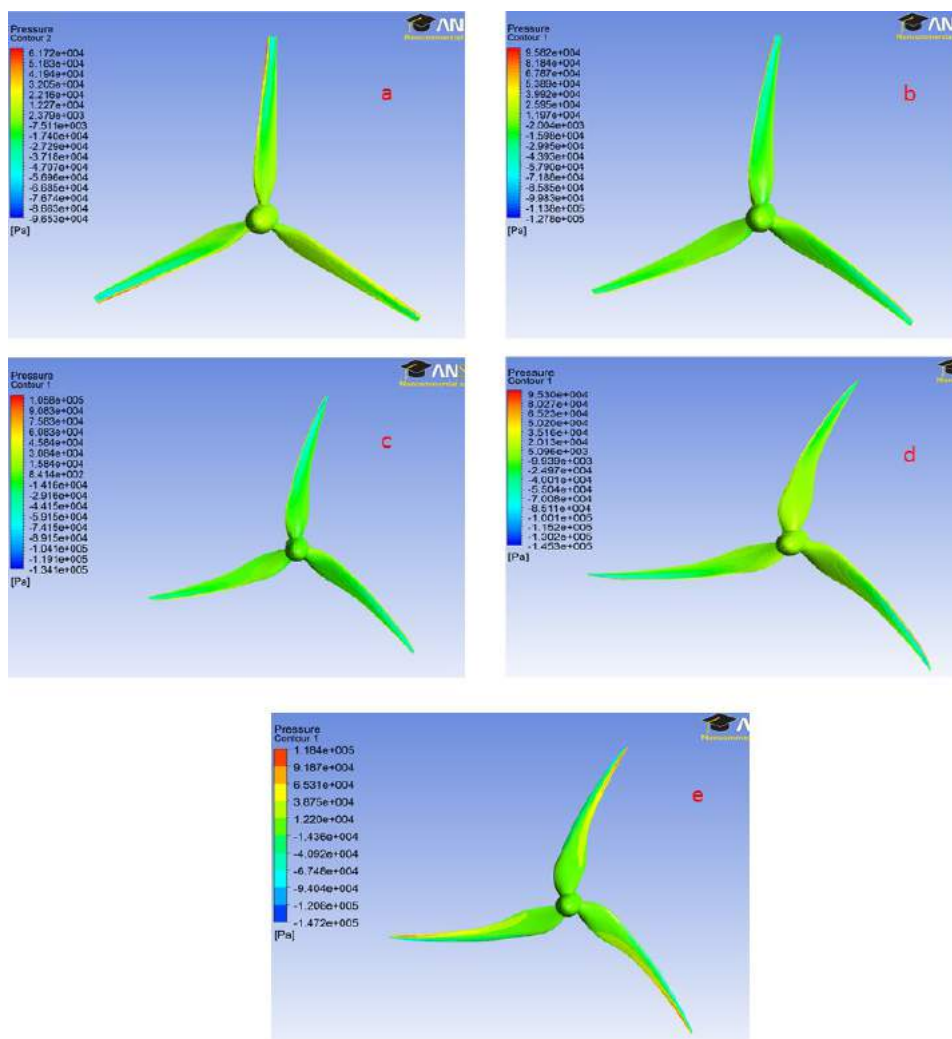


**Figure 78 Blade pressure distributions (pressure side) on a) SB, b) CB 25 %, c) CB 50%, d) CB 75%, and e) CB 100%**

The above figure compares the steady state pressure distribution on the five blade designs designed, the numerical simulations show how the seawater flow behaves on the trailing and the leading edge

on the pressure side of the blade. It can also be seen that the positive blade tip vortex are seen on the pressure side of the blade, this is because of the high turbulence intensities generated from the trailing edge of the airfoil and thus creating downstream interaction of the Reynolds shear stress and turbulent boundary layer formation.

The NACA 0018 airfoil, a high lift generating airfoil, generates lift from the pressure difference created by the fluid and blade interaction. The varying lift coefficient distribution can also be demonstrated by plotting the mid-height coefficient of lift distributions for all the five blade designs. CB 75% shows the highest lift coefficient at 0.5 blade span location with a peak value of 0.182, and CB 100% shows the lowest lift coefficient value of 0.0835 amongst all the blades designed in this research. Another interesting fact that can be noted from the Figures 78, and 79 that is the pressure is higher on the outer radius of trailing edge of the CB 100% (target shape blade), as compared to the other four blade geometries; this may be because the target shape is modelled as an assumption of the fish caudal fin and causing the flow reattachment. The pressure near the tip region of all the five case studies increases as compared to the rest of the blade, and leading edge contributes to the pressure distribution increase on the pressure side, but at the same time the trailing edge causes the negative pressure distribution increase on the suction side; thus contributing in lift force decrement and torque force reduction as well. As seen on the pressure distribution of the CB 100% blade there is a pressure rise on the trailing edge of blade pressure, which causes turbulence, and the fluid flow on the blade surface reduces and thus causes increment in the drag and torque gets reduced due to the turbulence generated.

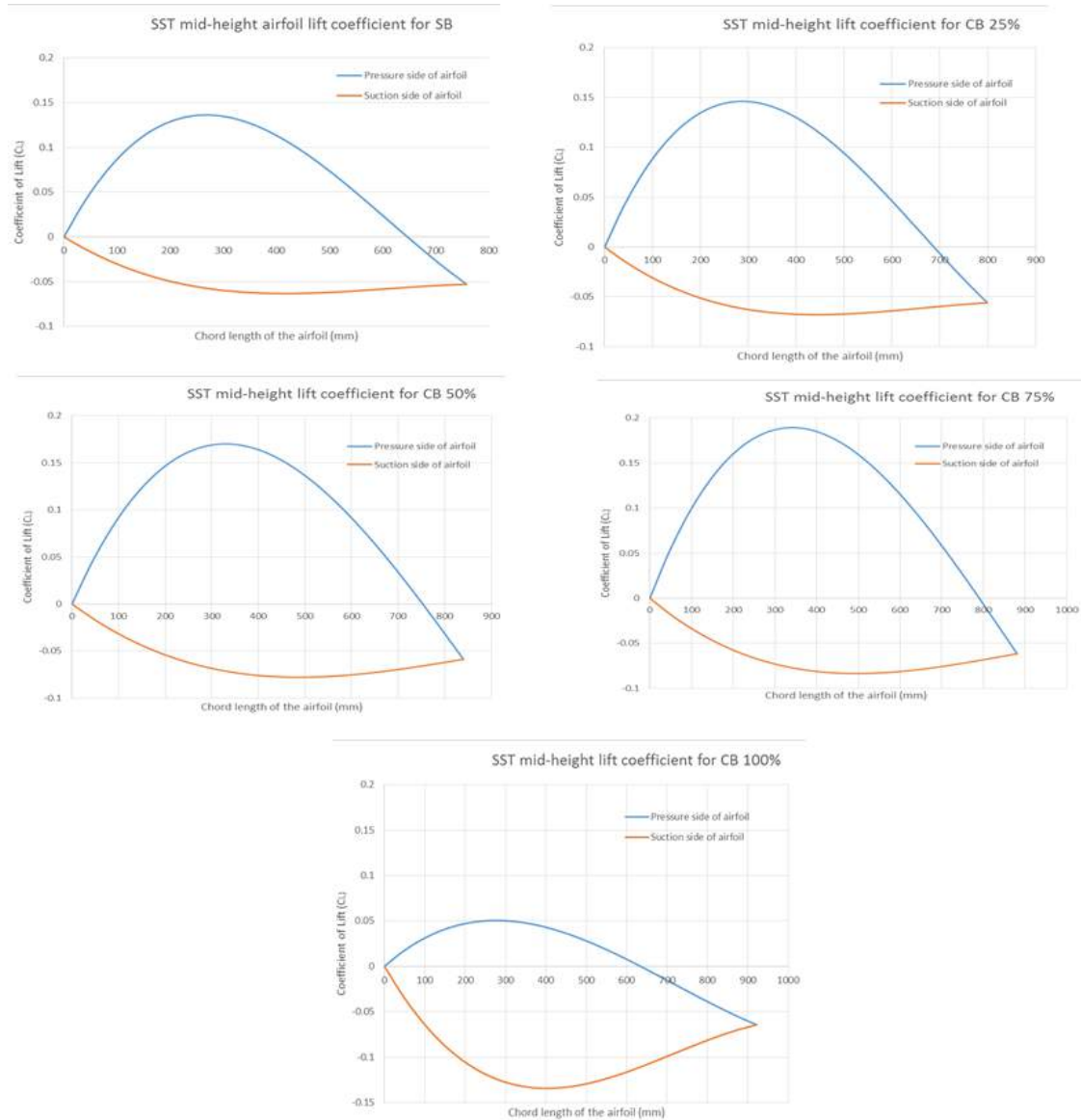


**Figure 79 SST mid-height lift coefficient distribution for five blade designs**

The variations in the pressure distribution yield the varying lift coefficient distribution on the blade span which can be seen in Figure 80. The lift coefficient increases with the increase in blade span until 0.8 blade span location, after which it results in drastic reduction near the blade tip. The peak lift coefficient is observed in the blade spans of 0.75 to 0.8 where the total lift increases with the increasing pressure. Although the lift coefficient varies in magnitude for all the blade designs, it can be observed that CB 100% results in lower lift coefficients when compared with the rest of the 4 blade designs at all the positions of the blade span. Therefore it can be concluded from the steady state analysis that the target shape blade i.e. CB 100% would cause drag increase, and the angle of attack would be higher than the Lift-to Drag ratio causing torque reduction and leading to lower

power coefficient, and as the bend on the blade increases, the negative pressure on the suction side rises which automatically decreases the power output.

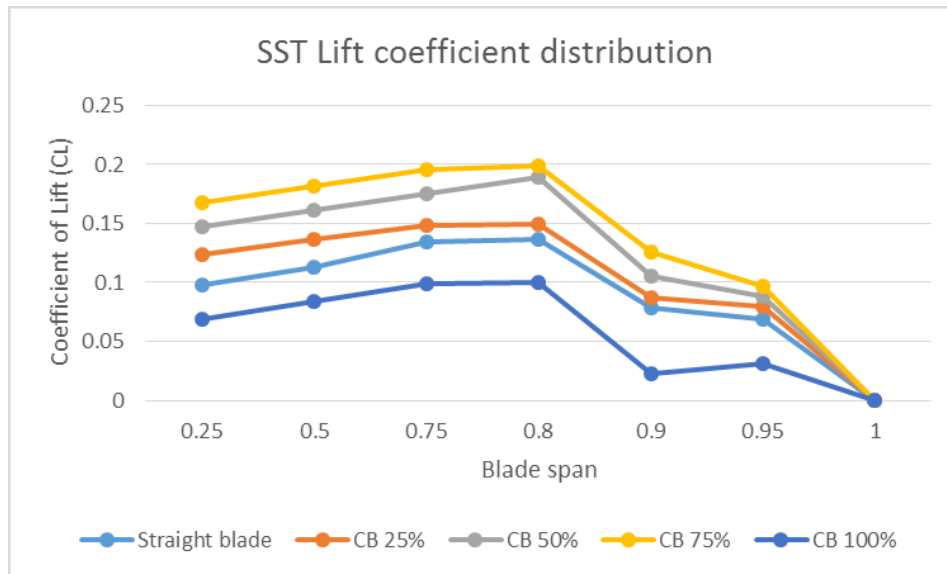


**Figure 80 SST model lift coefficient distribution for 5 designed blades**

Figure 81 shows blade rotational velocity and streamlines on the five case studies performed. It can be seen that the fluid velocity expands as it passes through the turbine and causing it to produce maximum efficiency.

6. CFD based design studies of tidal turbines

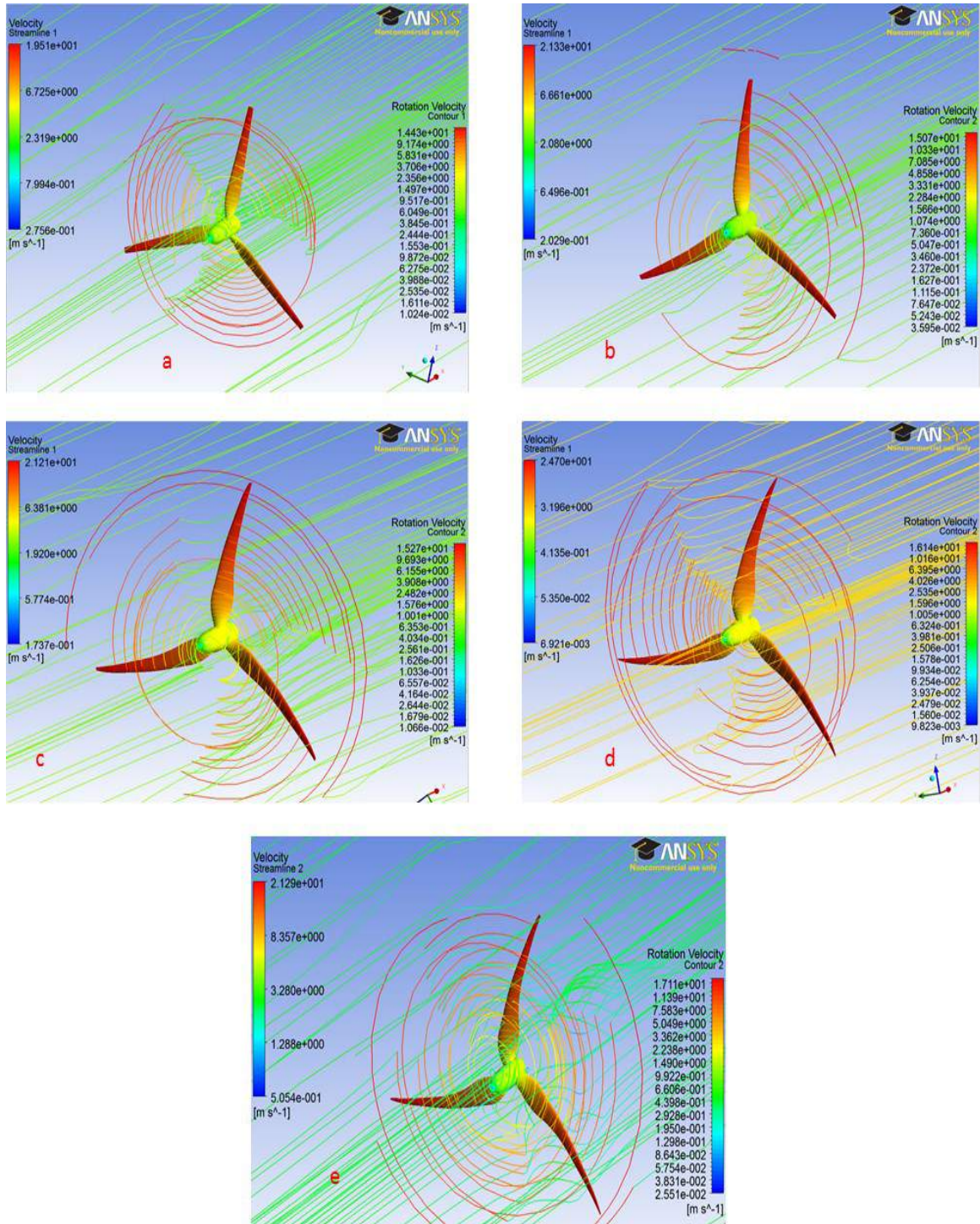


Figure 81 Steady state blade rotational velocity, streamlines for a) SB, b) CB 25 %, c) CB 50%, d) CB 75%, and e) CB 100%

## 6.8 Transient CFD analysis using the LES-Smagorinsky model

In this section transient simulations for the designed five blades using the LES-Smagorinsky sub-grid scale model and fine unstructured mesh in an integrated time step are presented. In order to enable series of LES simulations on the finer mesh generated the maximum time step was set large to enable the turbine blades to rotate very near from one time step to the next, by using the convergence acceleration techniques available of the iterative solver in ANSYS CFX, using the parallel message passing interface (MPI) available to benefit from the substantially-lateral numerical platform which substantially increased the computational overhead as the time step was 12 times smaller than the usual RANS simulation. For all the five design case studies that have been performed using LES, the time step used for the simulation required for the flow to pass entirely through the turbine was about 0.15million time steps with the time step size for each case being  $3 \times 10^{-5}$  which coincides with approximately 10 blade rotations for the TSR = 5 for all the five cases, which is equivalent to  $4.89 \times 10^5$  seconds or 135.83 hours for each mesh running on mesh partition of the 4 processors for each geometry tests conducted. The Multiple Frames of Reference (MFR) was applied on the turbine disc analysis as it was a rotating domain based on the general grid interface (GGI), available in CFX.

The turbulence intensity at the inlet of the computational domain was defined as 15% (typical seawater value), it should be noted that the non-uniform velocity of 2.5 m/s was applied to all the five blade case studies; and the tidal turbine blade geometry is a high turbulence intensity case. The turbulence intensity gradually decreased at a distance of four rotor diameters downstream from inlet to 13.68% due to the velocity instability, and the turbulence level at the rotor leading edge was observed to be 12.82%. This gradual decrease was expected due to the higher rotational velocity of the blades, which correspond to the blade tip. At the solid boundaries (blade geometry) the near wall node was  $y^+ = 50$  (Balaras and Benocci, 1994; Tessicini et al., 2005); because of the two zonal layer LES approach used, and the refined fine mesh in the tidal turbine domain was embedded into the ocean flow domain. As the non-uniform mesh (fine) requires a different cut-off filter for the near wall flow regions, the mesh generated for all the five case studies is the cube root volume of the entire seawater domain and the values are demonstrated in Table 19.

**Table 19 Mesh parameters for the designed blades (LES-Smagorinsky)**

Blade Model	Mesh growth rate	Maximum mesh size (mm)	Minimum mesh size (mm)	Curvature normal angle (°)	Number of nodes
<b>SB</b>	1.0	1150	65	10	427552
<b>CB 25%</b>	0.85	950	45	9	514842
<b>CB 50%</b>	0.7	820	40	7	690137
<b>CB 75%</b>	0.55	760	38	6	851326
<b>CB 100%</b>	0.4	680	35	6	912470

The unsteady convergence is an iterative process of the LES-Smagorinsky simulation, and the calculation needs to be monitored in order to confirm the progressive tracking of the imbalances (scaled residuals), or variables on specific points (ERCOFTAC, 2000; Versteeg and Malalasekera, 2007). The residuals convergence criterion for each time step was set to  $10^{-5}$ , and in this research two monitors were used:

- Scaled residual monitors for mass and momentum of the iterative process;
- Lift coefficient  $C_L$  trend as a function of the iteration number for LES-Smagorinsky solution.

The CFD solution is considered to have converged when the mass and momentum residuals present a constant trend under  $10^{-5}$  value which is illustrated in the Figure 82 where the residuals represent the downward trend of the scaled residuals for the CB 75% LES-Smagorinsky solution.

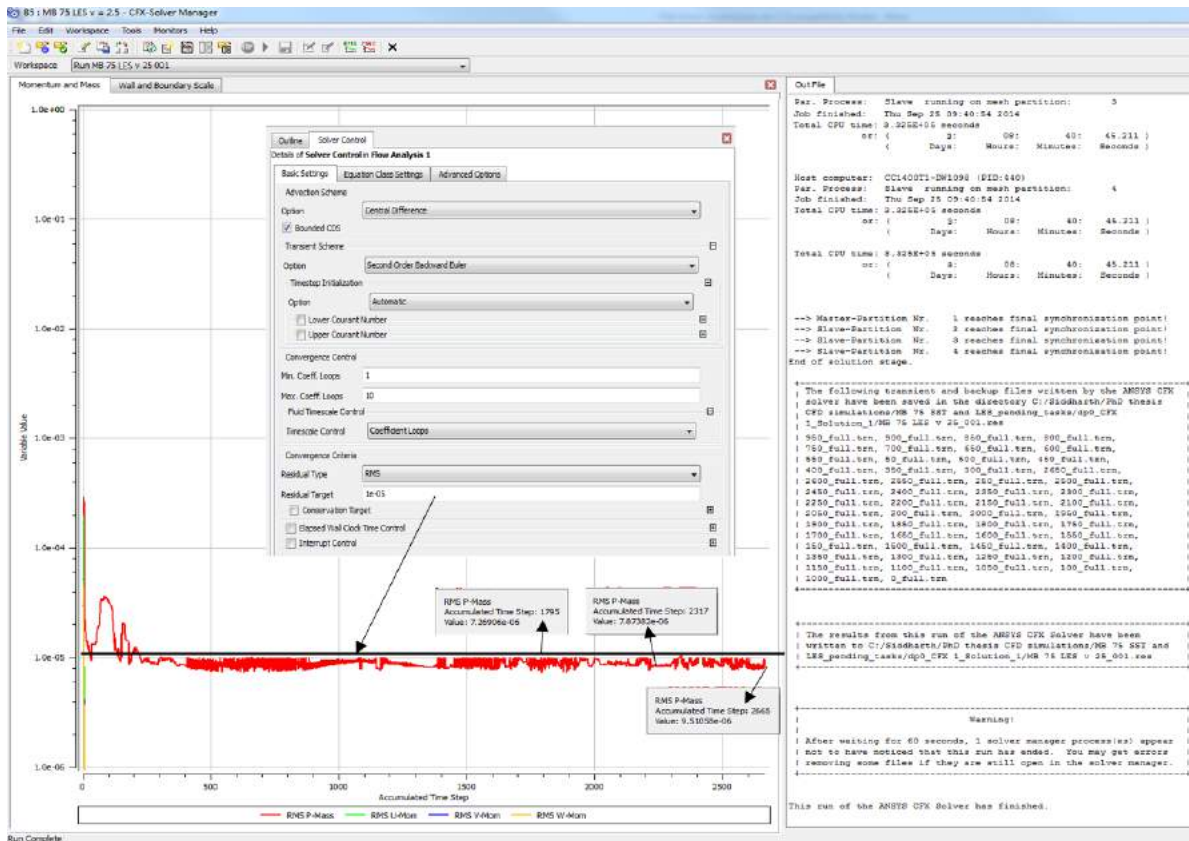


**Figure 82 CB 75% LES-Smagorinsky convergence monitoring with respect to the defined convergence criteria.**

It can be clearly seen that the residuals mark the continual removal of the unwanted imbalances, and thus causing the CFD iterative process to converge rather than diverge for e.g. the mass residual at the time step number 1795 reached the convergence value of  $7.269e-06$ , and  $9.51e-06$  on the time step 2665 when the transient solution was stopped. The discretised mass, momentum equations are presumed to be converged when they reached the convergence criterion and didn't change with the further iterations. Besides monitoring the scaled residuals the mass flow balance between the inlets and outlets were also verified for all the transient CFD simulations performed in this research to ensure the continuity in the solution; which is a standard practise in CFD analysis whilst monitoring the unsteady convergence (CFX solver guide, 2006; Oberkampf and Trucano, 2002). Another variable which was monitored to verify the unsteady convergence of the LES-Smagorinsky solution was the lift coefficient ( $C_L$ ) history over iterations which is illustrated in the Figure 83 for CB 75%. There was no appreciable change observed in the lift coefficient after 1100 timesteps, but the solution was still monitored for more than 1500 time steps as the lift coefficient elevations to the fixed value of 0.1795. It can also be noted that although the CFD simulation was run on LES-Smagorinsky there wasn't enough turbulence structure captured.

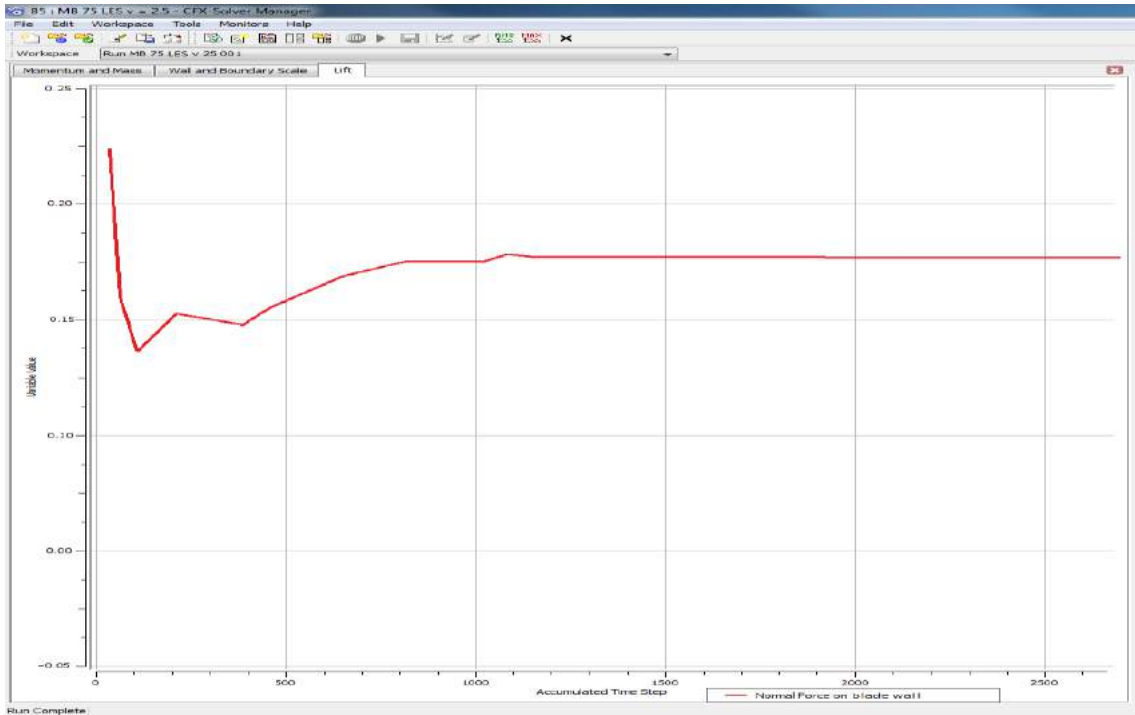


**Figure 83 Lift coefficient history convergence monitoring for the CB 75% transient solution.**

The objective of the performing LES transient simulations is to compare the results obtained with the steady state SST simulations to obtain grid converged power, and lift coefficient values to produce and efficient blade configuration, the turbine pressure contours (LES-Smagorinsky) are summarised below in Figure 84. It can be seen from the below pressure contour plots that due to the incoming incompressible seawater flow the difference between the pressure side and the suction side of the blade becomes smaller as the rotational velocity increases on the upper part of the blade, which in comparison to steady state simulations, increases the net lift and torque. Although the SST turbulence model showed similar pressure movement on the blade, the pressure difference when compared with the LES-Smagorinsky simulations on the pressure side and suction side of the blade the data obtained from the SST simulations is slightly concealed by anticipation of the TSR, and also leads to lower coefficients of power, lift, and thrust, and the airfoil-chords also experience pressure drop due to the integral flow coefficient of the seawater.

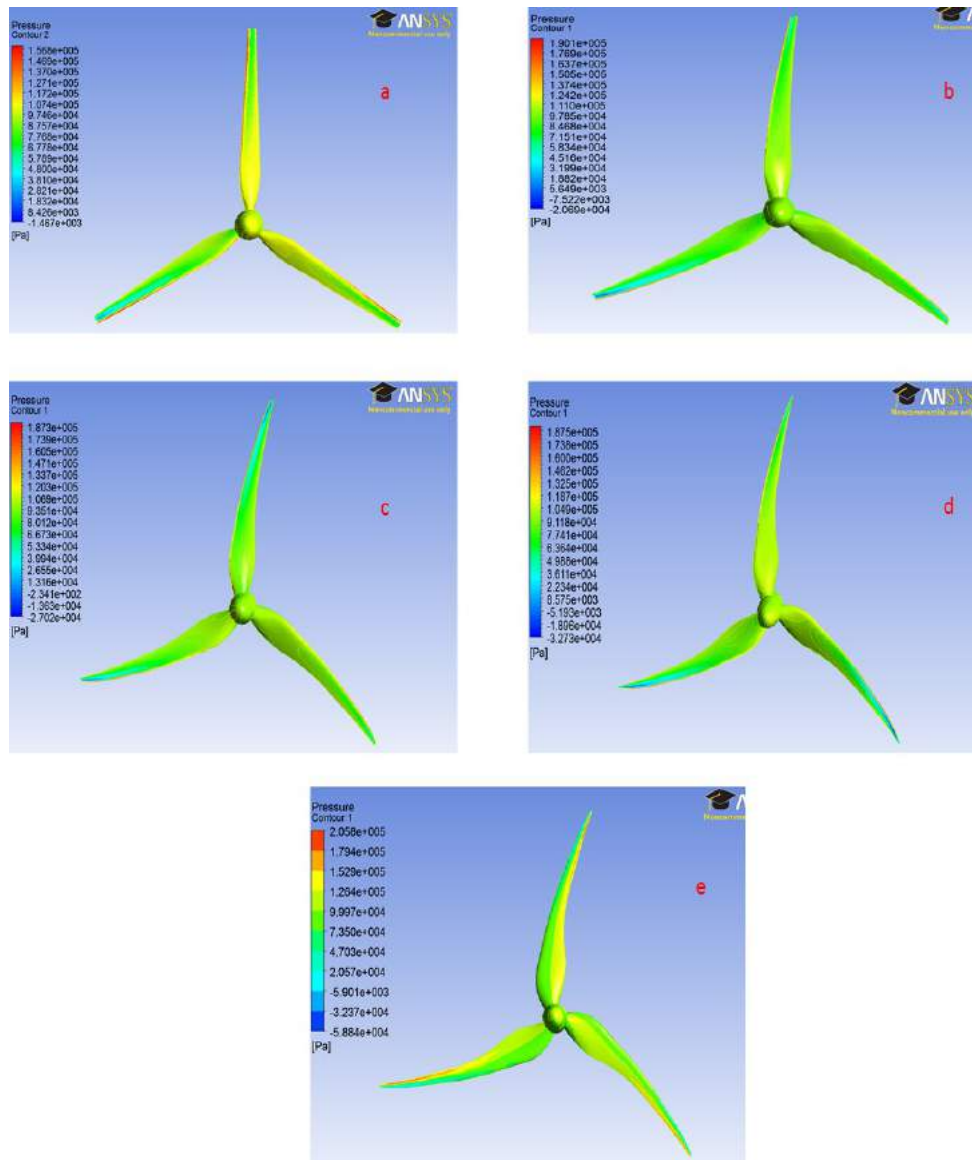


**Figure 84 Transient blade pressure distributions (pressure side) on a) SB, b) CB 25 %, c) CB 50%, d) CB 75%, and e) CB 100%**

After comparing the blade pressures of the SST and LES, the pressure prediction on the tip of the blade where the rotational velocity of the blade is at its highest also causing higher lift on the pressure side of the blade, and also risking the chances of facing cavitation, it can be concluded that SST model slightly under predicts in giving the real world picture than the LES transient simulations. It can be seen that lift distribution on the suction side of the mid-height is larger than on the pressure side of the airfoil, which would increase drag force on the CB 100% (target shape) as compared to the other four geometries is significantly higher, making it directly proportional to the bend on the blade. Thus, the overall aim for tidal turbine blade is to reduce the drag force in order to

achieve the higher lift to drag ratio. It also further shows that the most affected region by the seawater is the tip chord of the blade along with its leading and trailing edge, due to the unsteady vibrations of the blade are demonstrated in Figure 85. The blade tips experience the highest pressure, and also causes the flow separation in the pressure side and suction side of the blade of the curved blades. The drag increment for the CB 100% was expected seeing the negative pressure on the suction side on the tip, proving to generate cavitation in extreme velocity conditions.

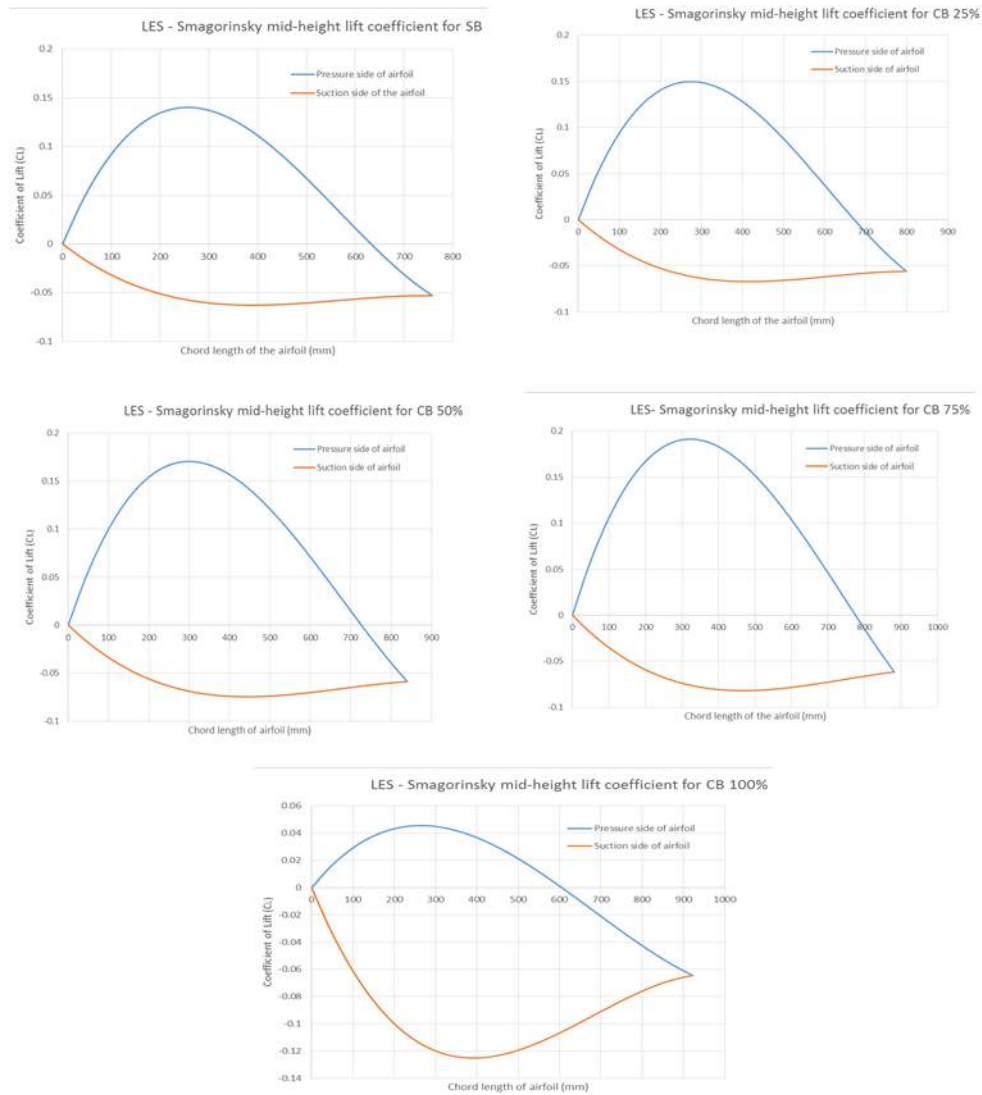


**Figure 85 LES – Smagorinsky mid-height lift coefficient distribution for five blade designs**

The substantial pressure rise on the leading edges of the pressure side of the blade may lead to dynamic stall due to increment in lift, and comparably cause homogeneous pressure distribution along the horizontal direction of the turbine blades; which is illustrated in the Figure 86 by varying lift coefficient on the 5 designed blade spans. The highest lift coefficient is observed in the blade spans of 0.75 to 0.8 in a similar trend of SST simulations, before drastically decreasing at 0.9 blade

span. CB 100% also shows the lowest lift distribution as compared to the other 4 blade designs which was also demonstrated by SST simulations. The lift distribution of CB 75% yields the peak lift coefficient amongst other blades designed in this research.

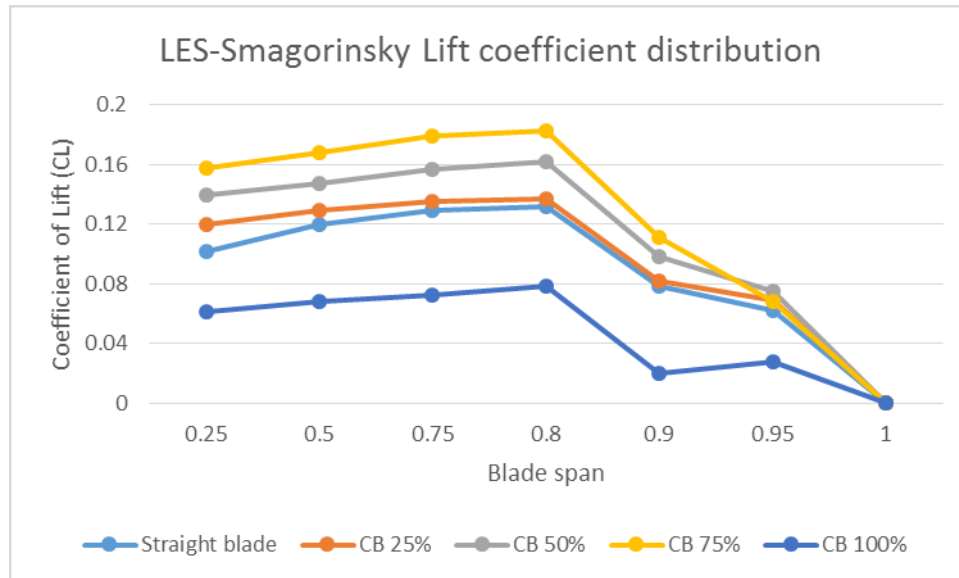


**Figure 86 LES-Smagorinsky model lift coefficient distribution for the 5 designed blades**

Thus LES simulations have demonstrated that the kinetic energy contained in the seawater flow is extracted by the upper stream of the blade, and also the pressure prediction tends to be more realistic as there is no flow divergence in real life HATT's. The prediction of the lift caused due to the large separation of the flow and the pressure surface of the blades consequently increases the predicted power coefficients, and causes less discrepancy in the vorticity of the pressure field. Thus interestingly LES solutions with a high computational overhead show a clear phenomenon of the pressure changes on the blade, and avoids over prediction of the lift and power coefficient. Therefore it can be concluded that pressure distribution on the rotating blade is predominantly a crucial output constraint for the lift, and thrust generation and also harnessing the power from the seawater, and is not affected by the other rotor parts like hub, generator etc. This also makes LES a promising computational turbulence model and exploring the potential to become a dominant engineering tool for the design studies of the HATT's in real world; the only drawback being the geometric complexity in estimating the boundary conditions, computational overhead required to solve the CFD simulation.

Figure 87 shows the Transient rotational velocity swirls and the streamlines for the five blade designs.

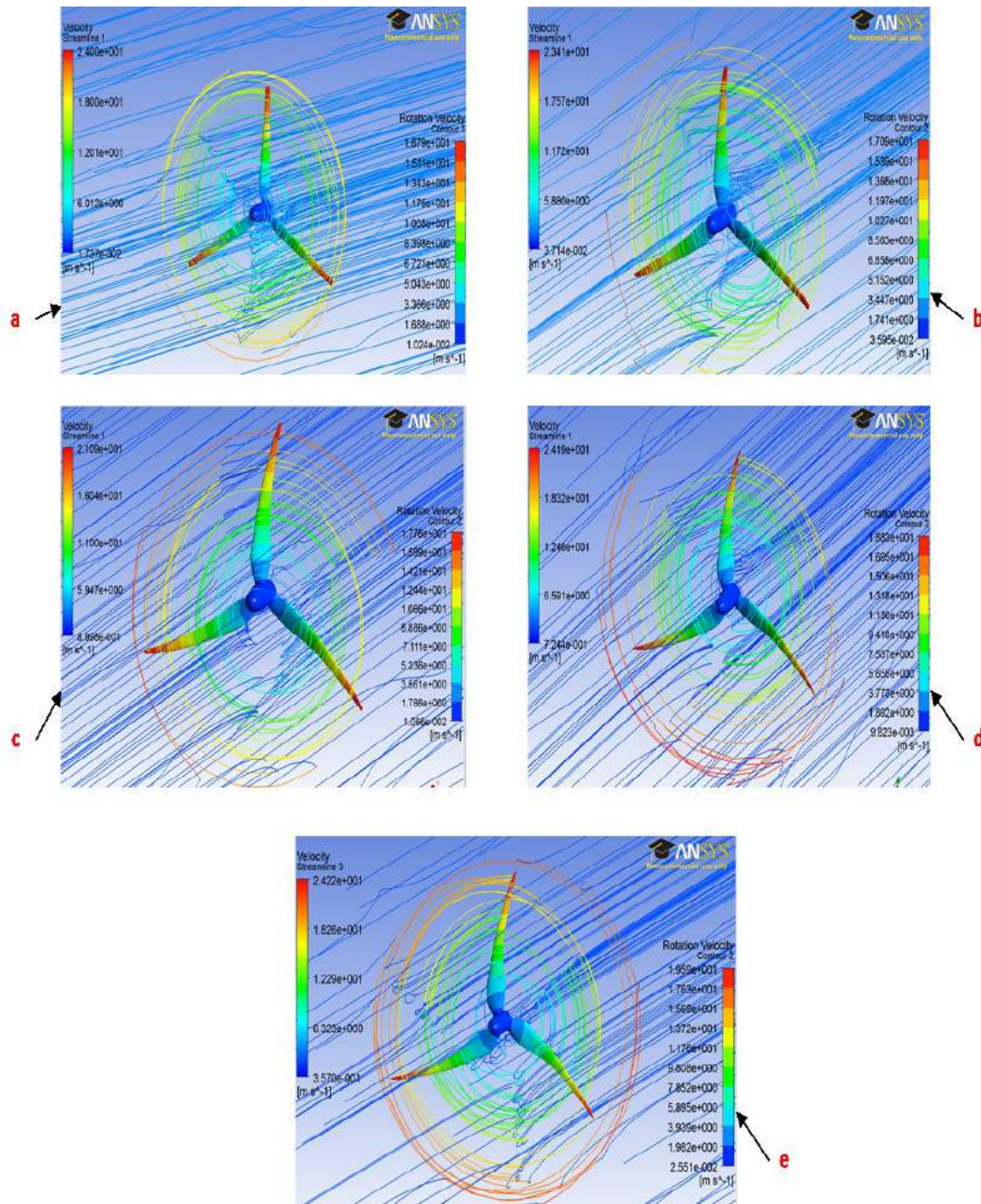


Figure 87 Transient blade rotational velocity, streamlines for a) SB, b) CB 25 %, c) CB 50%, d) CB 75%, and e) CB 100%

## 6.9 Comparison of the forces on the straight blade and curved blades

The purpose of this section is to discuss the results obtained from CFD simulations conducted on all the five design case studies. The comparison of the non-dimensional forces lift, power coefficients their variations produced by the SST simulations are demonstrated in following figures. The

differences in the SST-CFD results at the turbine level are due to assumptions made during the design and analysis, but it is possible to put forward a comparative analysis, for example at different angles of attack.

The performance of SST and LES-Smagorinsky turbulence models are examined by plotting the Lift coefficient against various angles of attack and are demonstrated in Figure 88. There is a gradual decrease in the lift coefficient after the 6 degrees of angle of attack for all the cases, as the flow becomes highly non-linear and the rotational velocity of the blades is at its maximum. The mass flow rate of the seawater is a function of the cross sectional area of the turbine blades and its velocity, therefore the bend on the curved blades makes the mass flow rate to drop the lift coefficient after 6 degrees of angle of attack.

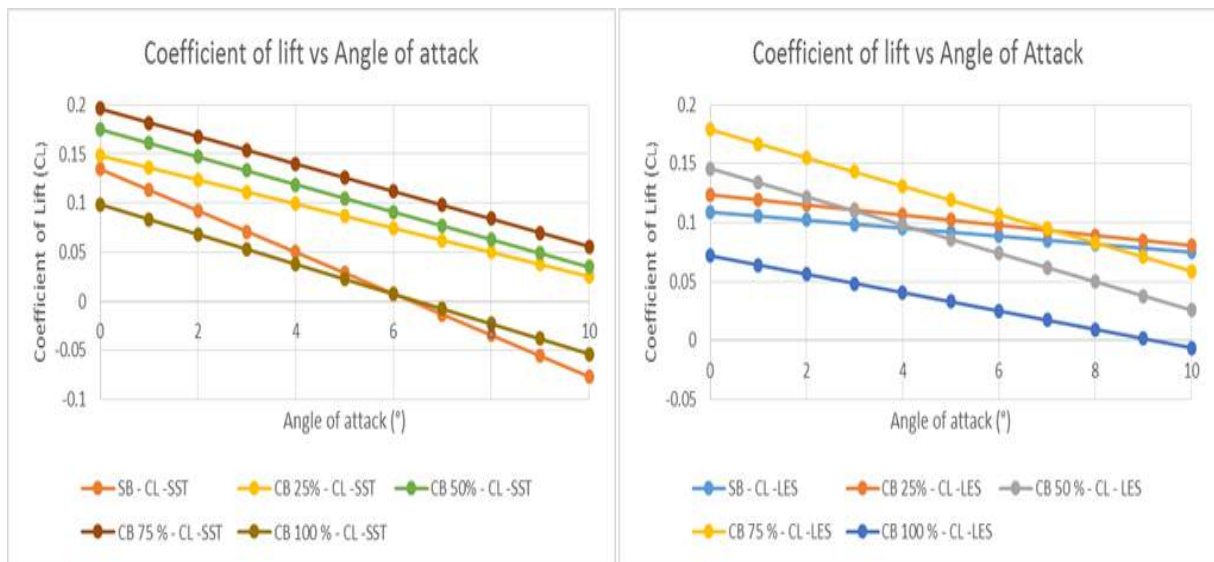


**Figure 88 Lift coefficient versus angle of attack for SST and LES CFD simulations, at inlet velocity 2.5m/s**

Thus it can be concluded that with the increase in the angle of attack the turbine blades would rotate faster, but at the same time due to the kinetic energy available in the seawater, drag force on the blade would increase as well, causing a reduction of the overall power coefficient of the turbine blade.

The output power notably depends on the inlet seawater velocity, this can be demonstrated from Figure 89. The attributes of the turbine blade power are determined by the number of blades, angular velocity, chord lengths, and most importantly the total blade height i.e. the surface area of the blade. Although the CB 100% yields almost 15% more power than the SB in case of all the flow

velocities, this does not necessarily mean that it would yield the highest power coefficient for the designed blades.

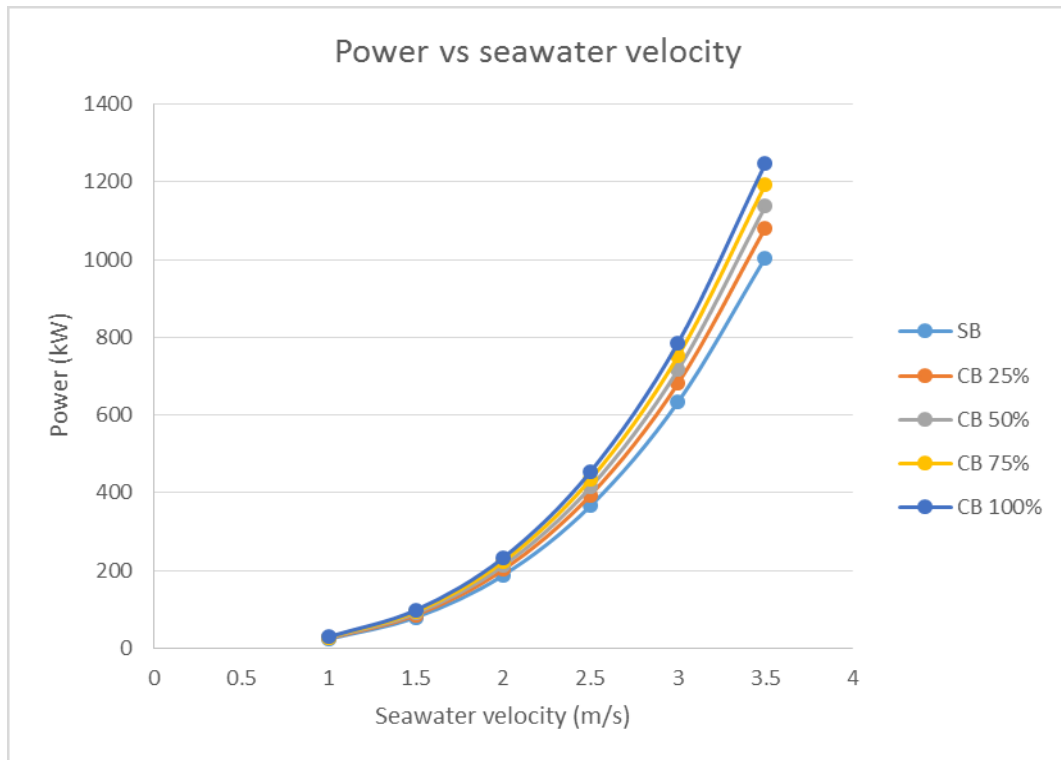


**Figure 89 SST - power versus seawater velocities for the designed five blades**

Figure 89 shows the theoretical prediction of the power is done for the velocities using SST turbulence model that range annually in the Pentland Firth, UK tidal site. The annual output power is one of the most important characteristics that determines the tidal turbine blade performance throughout the year. As the rotational velocity on the curved blade increases so does the power output, however, it also increases the pressure on the suction side of the blade causing it to increase the drag force at the same time.

The results of the blade performance i.e. the power coefficients of the modelled five sets of blades are compared in the Figure 90. The results show good agreement, which demonstrates satisfactory correlation between the different turbulence models used. The CB 75% has the highest power coefficient of 0.5178 i.e. the most efficient curved blade amongst CB 25%, CB 50%, CB 75%, and CB 100%, at the rated seawater flow velocity 2.5m/s, and TSR 5.

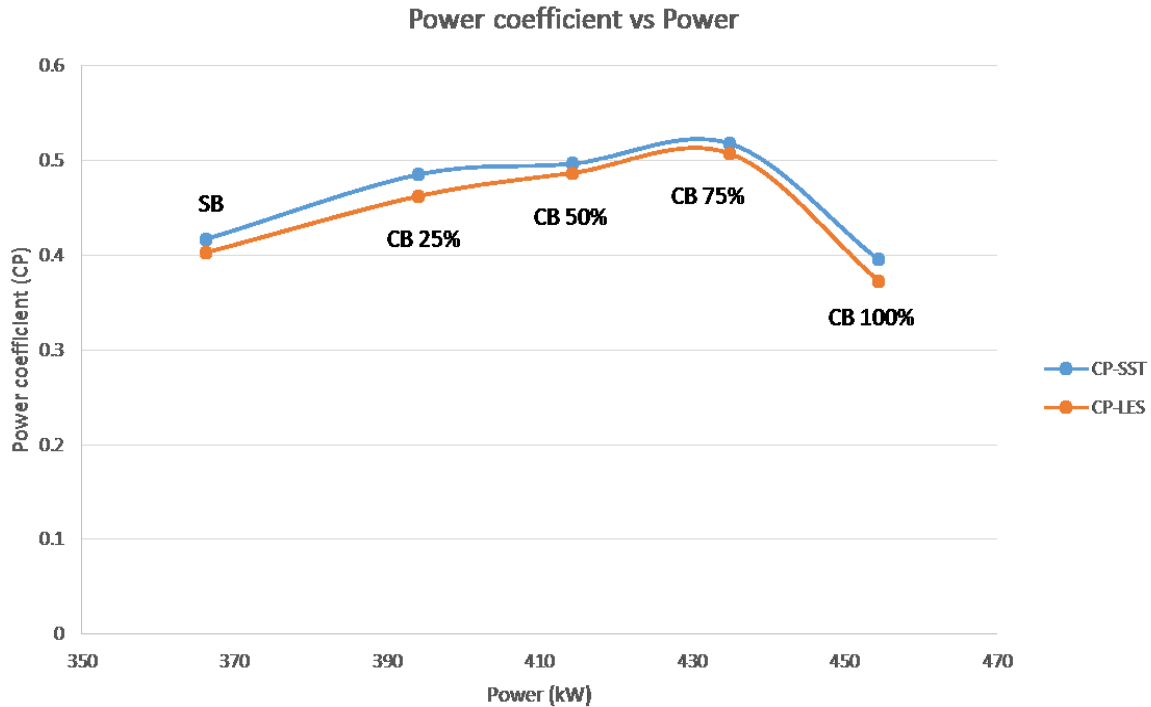


**Figure 90 Power coefficient versus output power for the designed five blades**

The SB produces 366 kW of power and a power coefficient of 0.4028, whilst the CB 100% produces approximately 20% more output power than the SB, and approximately 15% more power than the most efficient (in this research) CB 75%, but the power coefficient for the target shape blade i.e. CB 100% is 0.3951 and 0.3728 for the SST and LES-Smagorinsky CFD simulations respectively. As 75% of turbine blade efficiency i.e. the power coefficient is generated from the mid section of the designed blade to the tip of the blade, in the case of CB 100% the tip of the blade experiences highest negative pressure on the suction side of the blade, and the tip of that blade being the thinnest out of all the blades designed in this research. Significant differences are seen for the power coefficient and output power curves from the five sets of tests. A peak power coefficient is shown by CB 75%, and greater power extraction is shown by CB 100%. Thus it can be concluded that a blade design producing highest power output does not necessarily produce an improved power coefficient. The CB 75% showed the most consistent and efficient set of data from the SST and the LES-Smagorinsky CFD tests. It is noted that there is little difference between the results from the LES-Smagorinsky CFD simulations, but these results thus confirm the accuracy of the comparative analysis while using two different turbulence modelling techniques. Therefore, the CB 75% will be put forward to allow the overall efficiency i.e. the power coefficient comparison with the standard (suitable) HATT models available in the tidal turbine literature.

Goundar and Ahmed (2013) designed a three bladed 10m diameter HATT, and achieved a maximum efficiency of 47.5% with power output of 150kW, for the constant seawater velocity of 2m/s. The CB 75% is also three bladed and has a 14.2 diameter, and yields an efficiency of 51.78% for LES simulations with a power output of 435kW; which is higher than the overall efficiency achieved by Goundar and Ahmed (2013). At the same time the benefit of designing a blade like a curved caudal fin generates higher lift and power coefficients at lower and higher tidal current velocities and this has been demonstrated with the CFD simulations presented above. The STAR blade to generate low cost electricity from wind designed by Larwood & Zuteck (2006) implements swept blade design parameters and produces annual power output which ranges from 1.5 to 3MW. The designed turbine blades are 71 to 126m in diameter and have rated generator speed of 1800rpm, and the designed swept wind turbines produce 10 to 15% more power than the standard wind turbines available in the market at this time. A direct comparison of the results obtained from this research with the STAR blade would not be feasible, as the maximum diameter a tidal turbine can have is 22m (Batten *et al.*, 2008; Batten *et al.*, 2006), and as the designed CB 75% is 14.4m in diameter; so it is out of scope of this research to compare the CB 75% with the STAR blade. A general comparison of the annual power output can be made, i.e. designing the curved caudal fin blades produces at least 10% more annual power output than the standard straight blades which has been shown by both the studies i.e. by this research, and by Larwood & Zuteck (2006).

Thus it can be proved that bio-mimicking the Blue Marlin Fish caudal fin look-alike turbine blade i.e. curved blade 75%, produces greater efficiency than the default straight blade which was designed according to the tidal turbine blade literature, and meets the objectives of this research.

### **6.10 Chapter summary**

This chapter presented the verification and comparative analysis between the designed blades to find the most efficient curved caudal fin blade design in this research. The grid convergence study was conducted using two different turbulence models to investigate the mesh resolution effects on the CFD results. The standard k- $\epsilon$  model under predicts the power coefficients under all the different mesh conditions, the turbulence model comparison study in between the k- $\epsilon$  model and SST model highlights that the former model performs poorly in the adverse pressure gradients. Hence a comparative CFD analysis was performed on the five designed blade case studies using SST turbulence for steady state simulations, and LES-Smagorinsky for transient simulations. Blade chord lengths were varied for all the designed blade configurations to achieve the curved caudal fin blade

shape. The integrated third order polynomial function on the centreline which passed through the airfoils made sure that the the designed curved blades represented like a caudal fin and the total blade height stayed constant. The meshing of the curved blade was problematic due to its curve. To overcome this problem all the curved blade geometries were divided into sections to produce section-by-section meshing. The CFD solution for LES-Smagorinsky was run on the finer mesh than the SST, with double precision iterative convergence, and it had massive computational overhead. The pressure distribution plays an important role in determining the power coefficient of the designed turbine blade, which causes the varying lift coefficient distributions across blade spans. The lift coefficient increases with the increasing blade span and the peak lift coefficient is observed in the blade spans of 0.75 to 0.8, before drastically dropping down at 0.9 of the blade spans of each blades. The power coefficient of the SB was 0.4028% (SST), and 0.4169 (LES-Smagorinsky), and the most efficient curved blade from the five cases was CB 75% showing a power coefficient of 0.5073% (SST), and 0.5178 (LES-Smagorinsky). Finally, the power coefficient of the CB 75% was compared with the standard HATT's available in the literature thus achieving the objectives of this research, by the CB 75% producing more efficiency. The next chapter highlights the novel contributions of this research, the overall conclusions of this research, and the future recommendations suggested.

## 7 Conclusions

### 7.1 Thesis Contributions

The major novel contribution made through this research is to design, and analyse a horizontal axis tidal turbine blade by bio-mimicking a curved caudal fin shape. A standard HATT blade was defined using traditional methods comprising symmetrical airfoil, twist angle distribution, and a centreline passing through the airfoil centres. A third order polynomial function was defined on the centreline axis of the straight blade in order to create the caudal fin shaped blade; translating the blade spinal axis into percentage wise chord lengths generates a further three sets of caudal fin shaped blade geometries. A strategy to move the curved caudal fin shaped blade back towards the straight blade ensures that the total blade height stays constant for all the blade geometries.

Another original contribution made is to compare power coefficients obtained from the most efficient curved caudal fin blade (CB 75%) with the straight blade and the tidal turbine literature standard HATT models, to highlight that a HATT blade designed by bio-mimicking a curved caudal fin shape which would generate higher lift and power coefficients throughout the season i.e. for lower and higher tidal current velocities. One of the new contributions from this thesis is to demonstrate CFD based design case study approach of the horizontal axis tidal turbine blades by using bio-mimicry. Another fundamental aspect of the CFD analysis on the horizontal axis tidal turbine blade performed in this research considers the mesh independency study on the Straight Blade to demonstrate the sensitivity of the CFD design case study towards mesh resolution and turbulence model selection.

The most fundamental challenge which this research faced was to validate the CFD methodology for the case studies performed with the real world data. This is also the most significant problem faced in the wind turbine industry, to which this research could contribute. To overcome this challenge, a comparative analysis was performed for the straight blade and CB 75% with the tidal turbine literature which thus helps the future tidal turbine blade designers in knowledge transfer, particularly on turbulence model selection, and mesh resolution.

It can also be proved that bio-mimicking the caudal fin shape produces an improved horizontal axis tidal turbine blade shape, when compared to the existing standard HATT models in the literature. As the numerical predictions are so close for the all the design and analysis case studies, it can be questioned whether is it really worth simulating the designed blade case studies in higher turbulence models, due to the computational overhead required.

## 7.2 Overall thesis conclusions

This research should be of great interest to academics, researchers, engineers in tidal energy, and also other renewable energy consultants, as it brings together the concepts of the seawater environment, hydrodynamics of horizontal axis tidal turbines, bio-mimicry, CFD and various numerical modelling techniques, in order to develop a novel HATT blade shape.

For flexibility and simplicity reasons the HATT design study is divided into three sections design, analysis, and verification. The reasons for choosing the NACA 0018 airfoil for comparison and three dimensional modelling purposes are also summarised. A brief introduction on the direct design approach which was used in three dimensional modelling of the initial straight blade according to the literature. The blade level parameters like total blade height, twist rule and the NACA airfoil selection were also demonstrated. The CFD simulation approach highlights the CFD based design study of NACA 0018 airfoil, the design and analysis of the rectangular grid domain, and the boundary conditions. The creation of the computational domain describing the inlet and outlet distance from the turbine blade is also explained. After introducing the strategy to move the default straight blade to the curved caudal fin blade, a brief description is given on the chosen turbulence models, and how the centreline is moved in order to achieve the improved target blade shape using the defined third order polynomial function. Finally, the verification and the comparative analysis approach to allow the comparison of the power coefficients obtained from the designed blades against the literature.

The verification of the two dimensional NACA airfoil case studies, which also formed the basis of the three dimensional HATT steady state CFD analysis using SST turbulence model was conducted. The comparison of the steady state simulations showed excellent correlation with the source, at the four angles of attack at which the case studies were performed. From the tests performed the drag coefficient increased with the increasing angle of attack, although some assumptions had to be made whilst modelling the block structured grid. The maximum velocity values which appear at the bottom of the airfoil are within the 5% of the comparison data. A comparative analysis was also performed for the two domains i.e. the rectangular block structured grid, and to verify the O-C grid using the second order scheme for flow, turbulent kinetic energy, and momentum values, as the flow problem simulated was time independent. The two dimensional airfoil concluded with the pressure comparison, and showing the surface area differences on the upper and lower airfoil surfaces.

A three dimensional verification and comparative analysis was performed on the designed five blades, to find the most efficient curved caudal fin blade, after the completion of the two dimensional CFD airfoil analysis. A mesh independency study was carried out on the straight blade to determine the mesh sensitivity and its effects on the CFD simulation results. The grid convergence study was simulated using two turbulence models the standard k- $\epsilon$  model, and SST turbulence model at coarse, medium, and fine mesh resolution thus simulating six different mesh sizes. The highest  $C_p$  was obtained for M3 using SST turbulence and the lowest  $C_p$  for M6 using k- $\epsilon$  model. The standard k- $\epsilon$  model under predicts the power coefficients and the simulation time is highly dependent on the mesh and turbulence model chosen for CFD analysis. The SST medium mesh offers the best level of accuracy in terms of computational costs and accounts for 1% difference in the  $C_p$  when compared to the SST fine mesh case study.

The steady state analysis was performed using SST turbulence model and transient analysis was LES-Smagorinsky a higher order turbulence model, on all the five sets of blades. The most important design variable sensitivities were classified using direct design approach to satisfy the design study criteria in this research was achieving the highest power coefficient. Using the defined third order polynomial function, the centreline was moved in 25%, 50%, 75% and 100 percentage stages whilst ensuring that the total blade height stayed constant to find the most efficient curved caudal fin blade shape. The verification study defined for the straight blade and curved caudal fin blade steady state and transient simulations concluded as follows:

- In ANSYS CFX, the pressure-velocity coupling was done using Rhie-Chow Option and all the advection values were set to high resolution. The meshing of the curved blade geometries proved to be complicated due to the bend on the curved caudal fin blades. The minimum mesh size was also reduced by almost 20% to produce a fully developed flow field.
- The steady state pressure distribution showed pressure rise from the mid-section to the tip of the blade and upstream pressure being higher on the leading edge of the blade in all the cases except the CB 100% showed the upstream pressure being higher on the trailing edge of the blade. This showed that CB 100% would experience higher drag force than the other blade shapes.
- The variation in pressure distributions yields to the varying lift coefficient distribution across blade spans. It was observed that the lift coefficient reached its peak in the blade span of 0.75 to 0.8 where the total lift increases with the increasing pressure. CB 100% resulted in the lowest lift coefficient distribution amongst the rest of the designed four blades, in both SST and LES-Smagorinsky CFD based design studies.

- The LES-Smagorinsky solution required a finer solution than the steady state solution as LES uses spatial filter operation to simulate the transient simulation, the solution was run for at least 2 turbine blade revolutions in order to generate accurate data for power, and lift coefficients, which would then be compared with the SST simulation results.

The CFD results produced by the SST and LES-Smagorinsky were compared with each other to demonstrate the effectiveness of the computational simulations. Thus the two most important conclusions that can be drawn from the defined CFD based design study strategy are:

- Pressure distribution is a predominant output for determining the lift, and power coefficients, and also to define the most efficient blade. Lift coefficient distribution across blade spans showed a similar trend of the peak lift coefficient being observed at 0.75 to 0.8 of the total blade span before drastically dropping down at 0.9 onwards due to the increasing rotational velocity of the blades.
- The unsteady convergence is an iterative process of the transient solution which needs to be monitored in order to calculate the accuracy of the transient CFD solution. This was done by monitoring the scaled residuals for mass, and momentum and observing lift coefficient as a function of the iteration. The removal of unwanted imbalances over time steps result in the CFD solution to converge, and do not change with further iterations.
- The power coefficient of the straight blade increases from 0.4028% (SST) to 0.4169% (LES-Smagorinsky), and for the CB 75% 0.5073% (SST) to 0.5178 (LES-Smagorinsky). It can thus be concluded that although LES-Smagorinsky provides a better result than the SST simulations, but has massive computational overhead involved in it. The CFD results allow a further comparison of the power coefficients; proving that a curved caudal fin shaped tidal turbine blade produces more efficiency than the standard HATT's at lower and higher tidal current velocities.

### 7.3 Future work suggestions

Some areas for further research in several important areas on HATT's are discussed below. The areas listed below are according to the significant impact on the HATT design and analysis.

### 7.3.1 **Development of a decision support methodology for optimisation through KBE-CFD closed loop system**

A design, analysis, and optimisation automation closed loop system is under development using KBE-CFD principles to design a robust tidal turbine blade design which would be optimal throughout the year. The designed closed loop system would automatically parameterise blade geometry, generate automatic mesh, and the numerical results by itself. The purpose of developing the KBE-CFD closed loop system was to allow the future tidal turbine blade designers to produce a decision support methodology, and analyse any tidal turbine blade performance at any location in the world.

Therefore a suggestion can be made to use design and optimise a tidal turbine using non-symmetrical airfoils, and analyse the tidal turbine blade performance for the seasonal velocities for a different location. The optimisation loop integrated in the closed loop system uses Genetic Algorithm (GA) to find the optimal solution, without having to design and analyse every single designed blade.

### 7.3.2 **CFD simulations for cavitation analysis**

Cavitation is one of the major problems faced in horizontal axis tidal turbine blades, which causes damage to the tidal turbine blades in form of erosion at the tip of the blade. It causes as a mechanical damage to the turbine due to the bubble occurrence in the uncontrolled ambient conditions under the ocean.

In order to increase the overall performance of the existing tidal turbine blades the cavitation phenomenon can be controlled using appropriate materials in the tidal turbine blade design. Therefore, combining existing CFD simulations with the numerical methods which solve three dimensional cavitation problems, by refining the axisymmetric flows through nonlinear theory hydrodynamic cavitation of the horizontal axis tidal turbine blade is a major future recommendation to consider.

### 7.3.3 **Structural analysis for designed tidal turbine blades**

To complete the optimisation cycle, it is very important to perform structural analysis of the tidal turbine blades. The mechanical stresses acting on the tidal turbine blades during its operation under seawater create cyclic loading as a result of the pressure variation due to the angular velocity of the blades. When investigating the mechanical strength of the designed tidal turbine blade, it is very

important to calculate the aerodynamic stress distribution, and the conducting the material fatigue analysis to ensure optimal durability and overall performance of the tidal turbine blade.

Therefore optimising the structural strength as its objective strength needs to be coupled with the CFD analysis to give multi-disciplinary optimisation and thus establishing the parametric finite element modelling of the tidal turbine blades. Thus inclusion of the finite element modelling of horizontal axis tidal turbine blades reduces the complexity when considering manufacturing, and increases overall power coefficient.

### 7.3.4 **Manufacturing of the designed horizontal axis tidal turbine blades**

The direct commercialisation of the horizontal axis tidal turbines is still a big question for major investors in the tidal energy industry, due to the heavy investments required. Deployment of the HATT's is still in its infancy, although the peak power coefficient obtained from the curved blade 75% is 50.73% for SST simulation and 51.78% for the LES simulation; therefore the question Whether the CB 75% blade design identified in this research will be manufactured and deployed under seawater for real energy production? Clearly, the ultimate goal of the designed caudal fin HATT is to manufacture and produce the required parts from the model. After conducting the structural analysis of the designed blade which is also closely linked with the manufacturing, and is considered to be very cost effective solution in the production of the blade. Therefore consideration of the choice of material, costing, and generation of Bill of Materials (BOM), during manufacture of the tidal turbine blades is also of prime importance.

## **Appendix A: GB Patent Application: GB1421623.8**

### **A TIDAL TURBINE BLADE**

**Authors: Siddharth Suhas Kulkarni, Craig Chapman, Hanifa Shah**

#### **ABSTRACT**

A curved caudal fin shaped blade for use on horizontal axis tidal current turbines, the blade designed by bio-mimicking a caudal fin is disclosed. The method of transforming a traditional horizontal axis tidal turbine comprises the symmetrical airfoil of the blade and forming the blade having the symmetrical airfoil, twist angle distribution, and centreline passing through the airfoil centres. A third order polynomial function is defined on the centreline axis of the straight blade in order to create the curved caudal fin shaped blade; translating the blade spinal axis into percentage wise chord lengths generates a further three sets of caudal fin shaped blade geometries. The strategy to move the caudal fin shaped blade back towards the straight blade ensures that the total blade height stays constant for both the geometries.

Figure 1 to accompany Abstract.

1/5

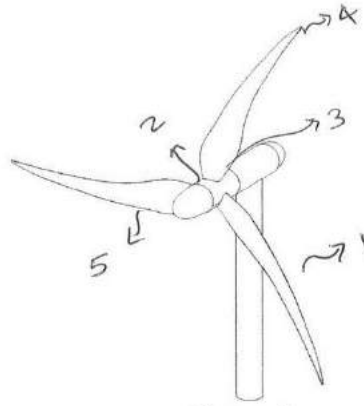


Figure 1

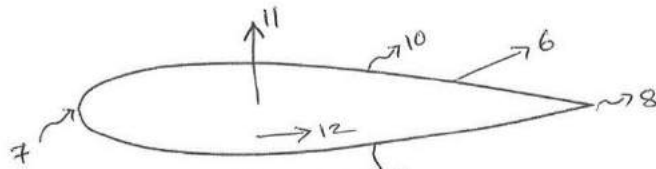


Figure 2

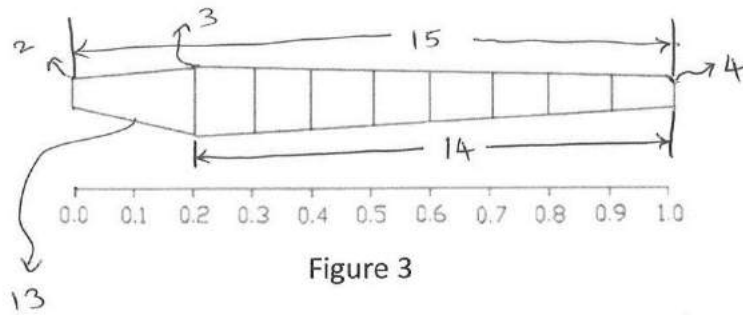


Figure 3

2/5

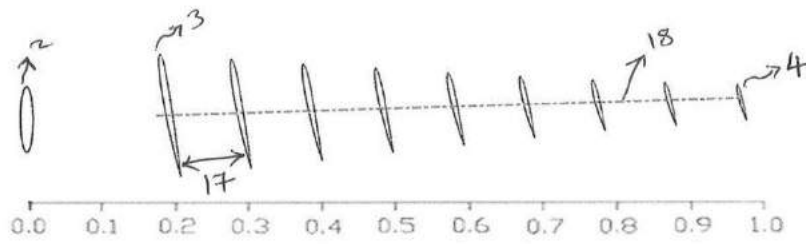
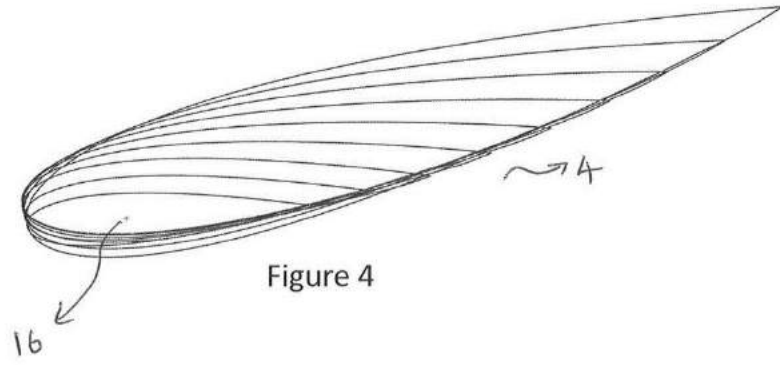


Figure 5

3/5

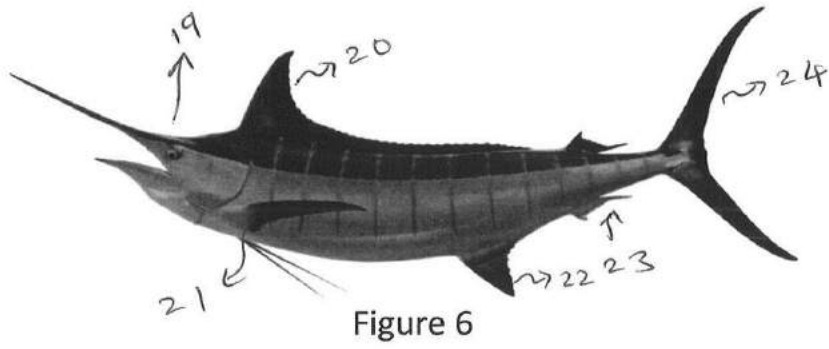


Figure 6

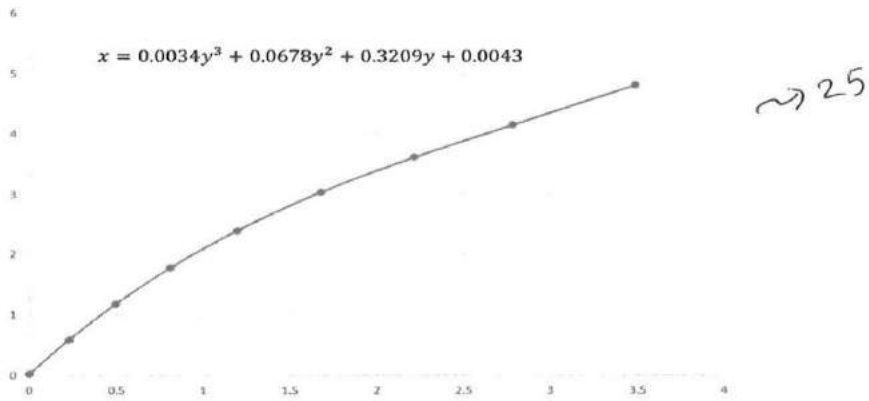


Figure 7

4/5

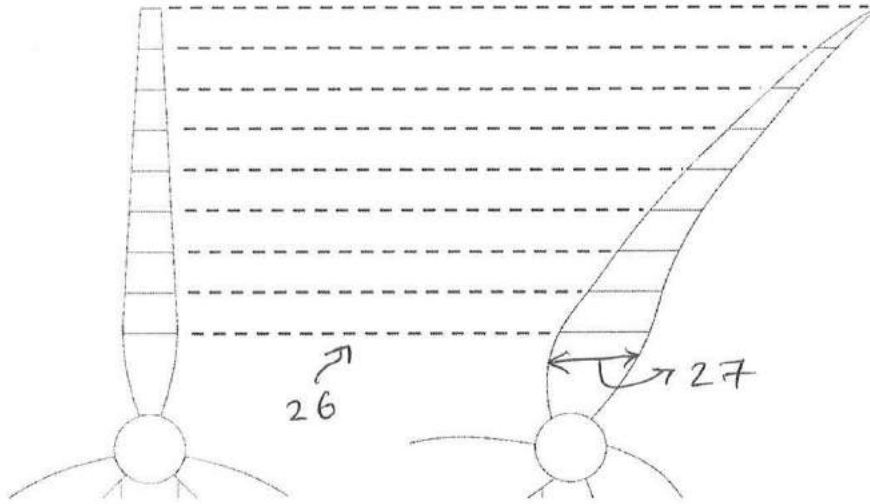


Figure 8

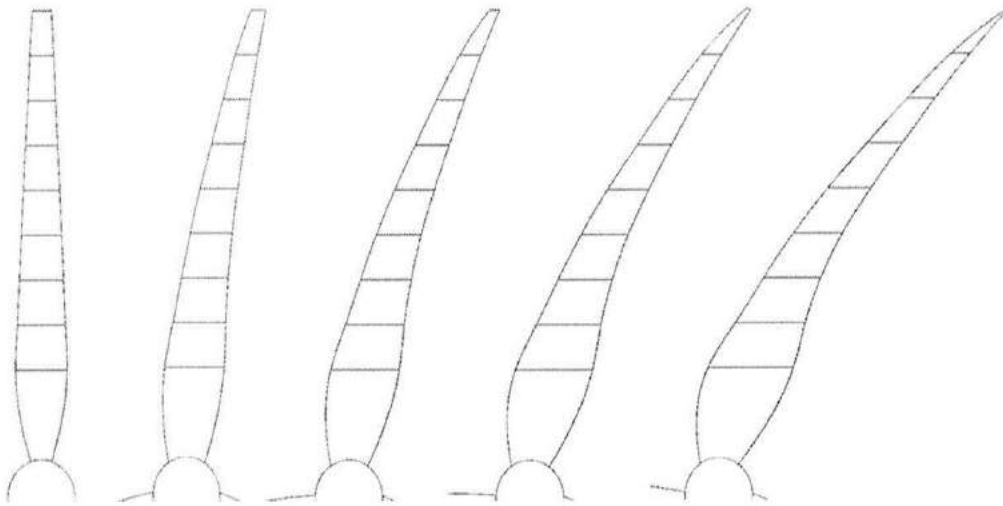
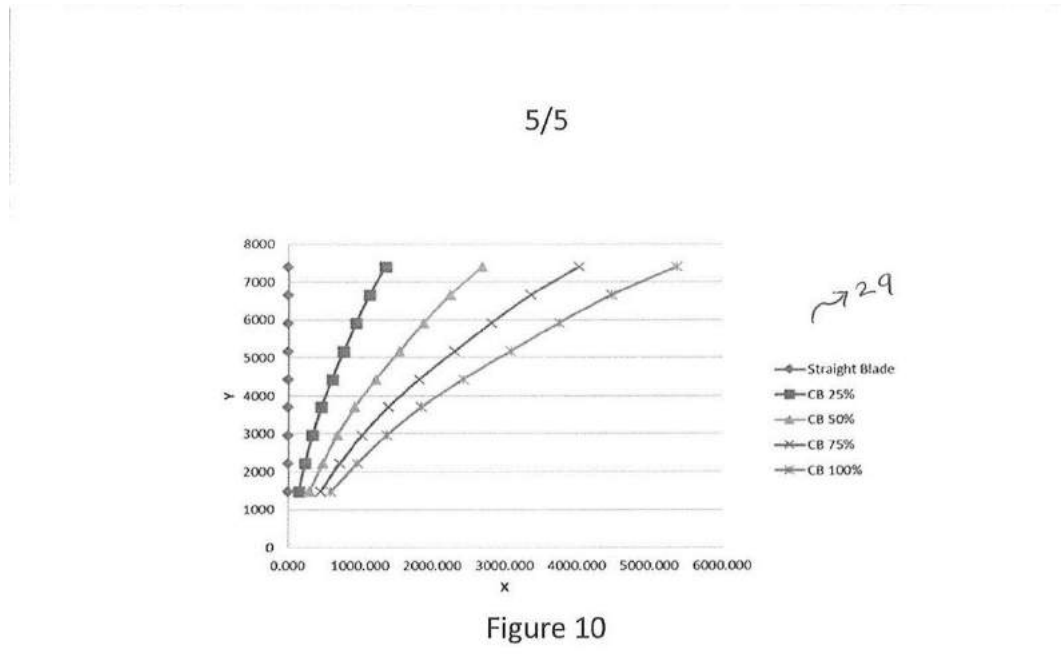


Figure 9

28



## FIELD OF THE INVENTION

The present invention in general relates to the horizontal axis tidal turbine blades, and in particular to bio-mimicking the curved caudal fin to design a HATT [1] in which the curved blade is twisted from the root airfoil station [3] to the tip airfoil station [4] using a novel third order polynomial function to replicate the curved caudal fin [24] shape of one of the fastest travelling fish in the ocean.

## BACKGROUND OF THE INVENTION

Currently, the global energy requirements are met by consumption of the fossil fuels. As the heavy dependence on fossil fuel increases it is becoming a major concern and countries worldwide have now realised the need to incorporate renewable energy sources in their energy policies as an alternative to the fossil fuels (Shields *et al.* 2009). Fossil fuels are very limited with their potential and with the current percentage of fuel consumption, these resources would deplete in coming decades. Thus realising the change in energy policy, renewable energy technologies have become favourable alternative to traditional energy sources. Tidal energy is a renewable electricity source based on the conversion of kinetic energy of moving water into mechanical power. It has fewer CO<sub>2</sub> emissions; it has minimal reliance on fossil fuels (Bryden *et al.* 2007). Solar power, tidal energy, geothermal energy, and wind power are the primary sources of sustainable energy (Yuksel, 2008). Tidal energy has advantages over wind energy, mainly because it is predictable and due to sea water being

denser than wind, the available energy can be up to 835 times greater than wind power (Bryden and Couch, 2006).

As a result of this growing interest in the tidal energy, many new tidal turbine blade designs have been created to harness electricity from tidal currents. Tidal turbines are generally classified into two types horizontal axis tidal turbines [1] (“HATT’s”), and vertical axis tidal turbines (VATT’s). Both HATT’s and VATT’s are capable of generating power through the rotation of the turbine blades. HATT’s are also called as axial flow tidal turbines, as they have rotational axis parallel to the tidal current flow; which makes them operate in one direction only. They can be designed using both symmetrical and asymmetrical airfoils; the blades are generally fitted to the hub, to kinetic energy from the water to mechanical energy, and shaft to produce power and gearbox. A traditional HATT has a larger root airfoil chord length [3] and it starts tapering towards its tip airfoil chord length [4], it also has a twist angle [16] along its entire span to keep the relative angle of attack constant (Mycek *et al.* 2013).

On the other hand, bio-mimicry or bio-mimetics has proved to be an excellent motivation to solve complex human problems, by imitating the nature. The design process starts by looking at nature’s ecosystem, self-healing abilities or a particular organism, to produce a design solution of the human need. The classic example of the bio-mimicry is the Humpback Whale wind turbine blade of designing an efficient wind turbine blade adapting Humpback whale’s flippers and tubercles (Fish & Battle, 1995; Fish *et al.*, 2011). As 80% of the propulsive efficiency i.e. the swimming speed of the Blue Marlin fish is caused due to its high lift generating caudal fin [24], which makes it one of the fastest propelling fishes under ocean, and also enables it to be efficient even at the low velocities). Thus, a tidal turbine blade design which replicates the caudal fin would produce an improved HATT [1] producing higher efficiency throughout the year i.e. even for the lower tidal flow velocities. Finally, the overall power coefficient of the designed curved blade would be higher throughout the season.

## **BRIEF DESCRIPTION OF THE INVENTION**

According to the main aspect of an embodiment, this invention provides a bio-mimicked curved caudal fin shape curved blade [1], for the use on horizontal tidal turbines to provide improved efficiency throughout the year than the traditional symmetrical and asymmetrical tidal turbine blades. The blade comprises of a twisted bend from the root airfoil to the tip airfoil stations [16]. The curved caudal fin shaped blade [1] has a thinner tip than most of the

traditional tidal turbine blades, which makes it rotate faster even at low tidal flow velocities, making it improved annual power producing HATT.

According to the first aspect of the invention, a traditional tidal turbine blade (which is called Straight Blade or SB in this invention) is designed using a “symmetrical” airfoil [6], comprising of 9 airfoil stations placed at ten percent [17] of designed default HATT. The SB has been using a twist rule [16] with maximum twist angle defined on the root airfoil [3], and minimum twist angle defined on the tip airfoil [4]. As the rotational velocity of the blade is highest at its tip, the twist angle [5] defined on the tip is at least four times smaller than the root airfoil twist angle. The bend on the caudal fin blade shape is achieved using a novel third order polynomial function [25] passing through the centre of each airfoil, and airfoil stations are stacked long the blade centreline [18] third order polynomial function to resemble the caudal fin shape. A further 3 sets of curved caudal fin shaped blades were generated in percentage wise chord lengths [29] to demonstrated the strategy to move the straight blade towards the target shape curved caudal fin shaped blade.

The above mentioned features and aspects of the present invention will be made clear with the references in the following description, and affixed claims. The added drawings, which are integrated in and aggregated in the parts of the specified blade assembly. The advantages, the third order polynomial equation, the strategy to move the curved caudal fin shaped [1] blade backwards to the straight blade, are illustrated in the embodiments of this invention, and the composition with the explanation, deliver the fundamentals of this invention.

## **BRIEF DESCRIPTION OF THE DRAWINGS**

Figure 1 is an isometric view of the bio-mimicked caudal fin blade system.

Figure 2 is a schematic of a symmetrical airfoil which is used as a default airfoil on a horizontal path which rotates around the hub axially (PRIOR ART).

Figure 3 is a perspective view of the symmetrical airfoil distribution in ten percent of the blade radius of the straight blade with the hub distance of the present disclosure.

Figure 4 is a top plan view of the twist angle distribution on the straight blade in the present invention.

Figure 5 is the perspective view of the centreline passing through the individual airfoil station of the straight blade of the present disclosure.

Figure 6 is the schematic of the Blue Marlin fish along with its propulsion attributes (PRIOR ART).

Figure 7 is the skeleton (centreline) of the caudal fin shaped blade fitted with third order polynomial function in the present invention.

Figure 8 is the transitional views of the straight blade to caudal fin shape tidal turbine blade of the present disclosure.

Figure 9 is a schematic of the percentage wise chord length blade progression to the caudal fin shaped blade of the present disclosure.

Figure 10 the skeleton of the strategy to move caudal fin shaped blade backwards (spinal axis variation) to the straight blade in this present invention.

## **DETAILED DESCRIPTION OF THE INVENTION**

References now will be made to the designed curved caudal fin shaped blade [1] in detail to embodiments of the invention, which includes all the examples of which are demonstrated in the drawings. The curved caudal fin shaped blade [1] twisted [4] from the root airfoil [3] to the tip airfoil [4] of which the explanation in this invention is provided and not the limitations of this invention. The features described as total blade height (R) [15], blade radius [14], twist angle distribution [16], airfoil stations would be intended to describe the modifications and variations made through this invention can be used for one embodiment with another embodiment. Thus it is aimed that present invention covers within the scope of the affixed claims, and their proportionate.

Figure 1 shows the isometric view of the designed curved caudal fin shaped horizontal axis turbine blade inspired by bio-mimicking a caudal fin.

Referring to Figure 2 (after Mohamed, 2012), according to a first aspect of the invention, a “symmetrical” [6] airfoil was used to design the straight blade in this invention. Generally in tidal energy industry, a symmetrical airfoil [6] is used to design both HATT’s and VATT’s (Etemadi *et al.* 2011; Rossetti & Pavesi, 2013), due to the angle of attack variation over the full turbine blade rotation and the mainly because of the high cavitation properties (Liu & Veitch, 2011). The word “symmetrical” means that the mean camber of the airfoil is straight and is same as the chord length of the airfoil. Previous examples of the use of symmetrical airfoils in tidal turbine blade design can be found in Masters *et al.* (2013), Yang & Shu

(2012), and are also well known to the skilful people in this art. The airfoils travel in a tangential direction in axial path to the tidal current flow, and hence the airfoil chord length is not parallel to the flow like VATT's, but travelling across it. As the fluid velocity increases over the airfoils, the 'convex surface' results in lower pressure on the 'suction' [10] side when compared to the 'pressure side' [9] of airfoil. Therefore using symmetrical airfoils [6] to model a bio-mimicked HATT blade has not been performed to harness energy from the tidal currents. The use of "non-symmetrical" airfoils to design the HATT's are also known. For example, Bai *et al.* (2014), and Wu *et al.* (2013) designed tidal turbine blades using non-symmetrical airfoils which have descending convex bend in the middle of leading edge [7] and the camber inverting point towards the trailing edge [8]. These airfoils are generally designed to have huge unfavourable torque values which also produce lower lift coefficient at the same time. As the tidal current flow increases around the cylindrical leading edge, it results in pressure drop and gives negative pressure inclination. For the given airfoil design, if the water velocity, the angle of attack are higher on the upper surface of the airfoil, it results in higher "drag" [12] force when a HATT completes a full rotation and also causes "lift" [11] fluctuations. The benefit of designing blade like a curved caudal fin would generate higher lift and power coefficients at lower and higher tidal current velocities with less vibrations and would be easy to manufacture.

What is needed, therefore is a HATT blade system designed using a symmetrical airfoil [6], which would produce more lift coefficient, and annual power output throughout the season i.e. for lower and higher tidal current velocities, and can be easily manufactured as well.

Referring now to Figure 3, shown is the symmetrical airfoil [6] distribution along the entire span of the straight blade [15]. The top level design parameters that define the three dimensional straight blade are blade radius [14], total blade height [15], symmetrical airfoils [6], and twist angle distribution [16]. The span wise distribution of the airfoils is done at every 10% of the blade [17]. The distance between hub circle [2] and the root airfoil [13] is 20% of the total blade height [15]. The diameter of the hub circle [2] is 40% of the root airfoil [3] chord length. For e.g. if the root airfoil chord [3] length is 1000mm then the hub circle [2] diameter would be 400mm (the hub circle [2] is a cylindrical surface which is to be lofted with the root airfoil [3]). After defining the default value of the root airfoil chord length [3] (1000mm), the remaining airfoil chord length distribution is done using a constant reduction factor of  $0.08R$ , which is named as Blade chord length reduction factor and is used to calculate the chord lengths of remaining airfoils. For example, if the root airfoil [3] chord

length is 1000mm, For station 1 the airfoil chord length will be 920mm (1000 – 80), similarly for station 3 the airfoil chord length will be 840mm (940 – 80) and so on until the tip airfoil [4] chord length is calculated. The rotor diameter is also a design variable which is retrieved at the theoretical design phase of the tidal turbines parallel with number of blades, hub and nose height, diameter. After determining the above mentioned parameters the rotor span can be fixed. Later on, the airfoil, chord length, and the twist angle distribution [16] are determined.

As shown in Figure 4, a top plan view of the twist angle [4] defined on all the airfoil stations. The blade twist angle is higher at the root airfoil [3] because it experiences less rotational forces on the blade and it gradually starts decreasing towards the entire span of the blade. As the angular velocity of the blade is highest on the tip [4] of the blade the blade twist angle is at least four times smaller than the root airfoil twist angle. Thus a twist distribution rule [16] can be created for example:

NACA-AIRFOIL-ROOT-TWIST-ANGLE = 16° (default)

NACA-AIRFOIL-TIP-TWIST-ANGLE = 4° (default)

BLADE-TWIST-ANGLE-DECREMENT = 4 times

This is a default value which starts from the Root airfoil twist and ends on the tip airfoil, for e.g. if root airfoil twist value is chosen 15° then the tip twist angle will be five times smaller which would then give 3° as the value for tip twist angle. **(NOTE: The centre axis goes with the airfoils).** As the tidal current flow velocity progresses towards the turbine blade, the blade pressure side [9] pressure increases especially at the tip [4] of the blade as it is being affected by the rotational velocity being the highest on the tip [4] of the blade. At the same time having lower blade twist angle at the tip airfoil station [4] would result in positive tip blade vortex on the pressure side of the blade which is the expected behaviour in the high turbulence intensity tidal current flow. The blade tips [4] also experience the highest pressure, which also causes the flow separation in the pressure side [9] and the suction side [10] of the blade. Due to the discussed reasons the blade twist [5] is varied across all the airfoil stations and therefore allowing the straight blade and the curved caudal fin shaped blade to produce the highest efficiency throughout the season.

Figure 5, shows the creation of the straight blade concept along with the centreline [18] passing through it. In order for a tidal turbine rotor to produce enough annual power output,

the total blade height needs to have a maximum value of 11000mm, and minimum value of 1500mm (Kim *et al.*, 2013; Batten *et al.*, 2008; Batten *et al.*, 2006). As, all the stations of the turbine utilise symmetrical airfoils [6] but have different parameters values for each instance. The NACA stations are placed at the 10% value of the blade [17] as visualised in Figure 5, and the distance between hub circle and the root airfoil chord is 1480mm (20% of the total blade distance, to provide structural strength for the blades to survive high rotational velocities). For example, the root airfoil station has an R value of 5920mm (Total blade height – hub circle root airfoil distance), Station 1 has the R value which is 10% of 5920 (which yields) 5328mm (5920 - 592) and so on until we reach the value of 1410mm for the tip airfoil station. The next step is to use calculate R values from the hub circle [2] values and “stack” the airfoils along the blade centreline [18]; so that the each individual airfoil can be added a twist angle [5]. Once the coordinate systems for all the airfoil stations are located, the NACA profiles should be referenced to the blade centreline [18]. The calculation method for defining the variable twist angle for each an individual airfoil is already explained in the above section.

Shown in Figure 6 is a drawing of a Blue Marlin [19] (after King Sailfish Mounts, 2014) with its propulsion characteristics. The swimming and locomotion characteristics of marine like most other mammals differ in size, weight, shape, nonetheless they all live and survive in the unsteady currents in the ocean. Thus certain marine vertebrates function accurately in unsteady and fast seawater currents, the Blue Marlin fish, *Makaira nigricans* swimming speed has been recorded up to 80 km/h (50 MPH), thus these marine vertebrates employ the thrust manoeuvring or in other words they use their ‘fins’ for the propulsion (Lenarz & Nakamura, 1972). The locomotion of the marine vertebrate Blue marlin fish is generally based on the five fins namely; caudal [24], anal [23], pelvic [22], pectoral [21], and dorsal fins [20] which are located around its body, and the movements caused because of these flexible fins act as the main source for propulsion at high swimming efficiency. The pectoral [21] and pelvic [22] fins contribute to the manoeuvrability to swim at low velocity marine currents, with ‘the caudal fin [24]’ actually causing the essential thrust for propulsion (Tokic & Yue, 2012). The caudal fin [24] propulsion may represent a ship is rudder at high speed or an airplane movement operating with the same forces like pitch and thrust, including the transfer mechanisms like drag [12] and lift [11]. The pressure related forces drag [12] and lift [11] originate due to the inequality of the water flow acting on the fish body. This propulsion is also termed as the Body and/or Caudal Fin (BCF) propulsion (Wilga & Lauder, 2001),

which may cause surface area increment or decrement; thus, the swimming movements may differ from species to fish species. Dorsal fins [20] are the easiest to locate in marine vertebrates as they are found in the dorsal part of the spinal cord in fish. The dorsal fins [20] protect the fish from rolling, and help in turning, thus controlling the body at low speeds or to a complete stop (Jayne *et al.*, 1996). The anal fins [23] are located ventrally in the anus region of the fish, and help managing the body orientation to maintain the stability when the swimming velocity increases (Zhou *et al.*, 2008). The caudal fin [24], which is also termed the tail fin, is located at the end of the fish's body (caudal pinnule), and is the main fin that produces thrust propulsion through seawater (Windsor *et al.*, 2010). The propulsive efficiency of the Blue Marlin ranges in between "0.85 to 0.91%" (Barbara *et al.*, 1992; Watanabe & Sato, 2008; Luthy, 2004).

Referring to Figure 7, In order to get the desired curve for the initial tidal turbine blade to move towards the Marlin look alike curved caudal fin blade [1] (the target shape), a third order polynomial function is defined on the central axis curve which is:

$$x = 0.0034y^3 + 0.0678y^2 + 0.3209y + 0.0043 \quad \text{Eqn. 1}$$

The above equation is considered to be the centreline polynomial function of the curved blade caudal fin (tail) [25]. Each NACA profile centre is built about the centreline [18], the centreline [18] then acts as master and each profile datum sit along its length divided by the height and the numbers of stations stay constant as the default straight blade. Using this approach it would be easy to model the curved shape blade and reduce the computational overhead. All the NACA profile sections are considered parallel to the x-axis i.e. the normal of each NACA section should be y-axis. The skeleton which is fitted on the midpoint of the each airfoil has a decrease in the chord length in the blade span wise direction which increases the surface area of the curved caudal fin shaped blade [1]. According to a further aspect of the invention, fitting the third order polynomial on the skeleton of the caudal fin look alike centreline [25], starting at the root airfoil [3] centre and passing through all the airfoil stations till the tip airfoil [4] centre entails the blade bending and thus creation of the curved caudal fin shaped blade. The straight blade comprising of the symmetrical airfoil stations which have straight mean camber and using the Cartesian coordinates such that of the leading edge [7] of the symmetrical airfoil [6] in a twisted span wise direction makes it possible to achieve the desired curved caudal fin shaped blade, which can also be called as span wise curvature.

As shown in the Figure 8, the chord lengths of the straight blade can be varied in linear or non-linear progression [29] along the span wise direction to achieve the caudal fin shaped blade. The curved caudal fin shaped blade [1] also has a thicker base [27] than the straight blade to mount the caudal fin shaped blade on the rotor without having to use additional support. The blade twist [4] is also varied along all the airfoil stations making the caudal fin shaped blade to produce more energy from the tidal currents. The twist angle [4] mounted on the airfoil stations for the curved caudal fin shaped blade [1] can be lower than the region of what is mounted on the traditional tidal turbine blades, for the caudal fin shaped blade to be useful and producing improved in certain low tidal current velocities. This is particularly suitable for the curved caudal fin shaped blade [1] because of the increasing concave bend and is thinner at the tip [4] and thus should be dimensioned to have sufficient strength at the tip of the blade. The most important design variables that affect the overall efficiency of the horizontal axis tidal turbine system are chord lengths of airfoils, twist distribution [16], overall span of the blade [15], angle of attack, angular velocity of the blade, blade material, and the fluid velocity acting on the blade (Afgan *et al.*, 2013; Clancy, 1978; Pinonet *et al.*, 2012; Betz, 1966, Jo *et al.*, 2014). The design variables selected to move the straight blade towards the curved caudal fin shaped blade are airfoil chord lengths, the total blade span, and twist angle distribution; however the other important design variables that construct a HATT are outside of the scope of this invention.

Referring to Figure 9, the percentage wise chord length computed bisectonal blade progression [28] is demonstrated by mathematically determining a linear progression function to calculate the percentage wise chord lengths. As shown in Figure 9, there are five different sets of designed HATT's, the chord lengths of the caudal fin shaped blades are bigger than the initial straight blade. This embodiment also differs from the initial straight blade as the upper and lower airfoil chord length values are changed radically to replicate a curved caudal fin using symmetrical airfoil [6] stations. For the default design purposes, the percentage chord lengths were moved in 0%, 25%, 50%, 75%, and 100%". Where 0% would be the initial straight blade chord lengths, and then the chord lengths are increased in 25%, 50%, and 75%, at the same time the total blade height [15] is kept constant when moving the caudal fin skeleton [29] and the defined third order polynomial function [25] makes sure that the curved geometries always represent a caudal fin shaped blade. The designer then determines the percentage chord length values [28] using following equation:

$$R_v = \left[ \left( \frac{Ed_{val} - St_{val}}{100} \right) (R_p) \right] + St_{val} \quad \text{Eqn. 2}$$

where  $R_v$  is the required chord length value,  $Ed_{val}$  is the end value of target shape chord length value,  $St_{val}$  is the starting chord length value of the initial blade,  $R_p$  is the required chord length percentage.

For example The NACA-AIRFOIL-ROOT (Default blade) chord length:  $St_{val} = 1000\text{mm}$ , and target shape NACA-AIRFOIL-ROOT chord length:  $Ed_{val} = 1645\text{mm}$  and the starting percentage value:  $R_p = 25$ ; then substituting these values in the Equation 2 we get the  $R_v$  as 1161.25mm (for the root chord length of 25% curved blade). As, 9 airfoil stations were defined for the default straight blade, initial experimentation will also include 9 airfoil stations for each four percentage stages [28].

Referring now to Figure 10, caudal fin blade spinal axis skeleton [29] is shown, which is consequently generated by the second embodiment which is particularly suitable for the designer to move the curved caudal fin shaped blade [1] backwards to the straight blade. As tidal turbine blade power coefficient is very sensitive to the blade twist [4], chord length distribution and mainly the total blade height [15], and optimising each and every design variable would be very time consuming and the computational overhead required when experimenting to check the relationship between the design variables and optimisation is massive. To overcome this problem, perturbation of the default blade design method was used. Using this method a new candidate design was produced using the percentage based chord lengths [28]; by a random deviation of the initial default straight blade rather than generating a random blade from scratch. This method was applicable as the design variables were distributed (i.e. chord, twist angle, and total blade height). Using this method percentage based chord lengths [28] were selected and the third order polynomial function will stay the same assuming that the span or total blade height [15] will stay same as the straight blade, and can be defined using following equation:

$$T_{ASTN} = T_{SXC} \times \left( \frac{R_p}{100} \right) \quad \text{Eqn. 3}$$

where  $T_{ASTN}$  is the required airfoil station value,  $T_{SXC}$  is the target shape X-coordinate value for the particular airfoil station,  $R_p$  is the required chord length percentage.

For example the NACA-AIRFOIL-ROOT (target shape) X-coordinate value = 595.568mm, and target shape, and the starting percentage value:  $R_p = 25\%$ ; then substituting these values in Equation 3 we get the  $T_{ASTN}$  as 148.92mm (for the root chord length of 25% curved blade).

As shown in the examples above, a curved caudal fin shaped blade [1] is designed by using a symmetrical airfoil [6], and by transforming the exiting straight blade by introducing a centreline [18] which passes through all the airfoil centres. By integrating a third order polynomial [25] on the centreline allows the twisting of the blade from root airfoil [3] to the tip airfoil [4], and it is possible to model the Blue Marlin caudal fin look alike blade; thus allowing a designer using CAD. Bio-mimicking a curved caudal fin to design a horizontal axis tidal turbine blade [1] is particularly suitable to produce improved efficiency for higher and lower velocities i.e. throughout the year. The modelled curved caudal fin shaped blade are dimensioned to have sufficient strength to withstand incompressible tidal current velocities. The curved caudal fin shaped also has thicker chord length values [27] at the root airfoil [3] station than compared to the straight blade design, and they gradually decrease in the span wise direction to resemble a curved caudal fin.

One of the present invention benefits is that a designer can move the straight blade or any traditional blade to model a caudal fin shaped blade in any percentage wise chord lengths [28] required using the percentage wise chord length [28] formula. It is also possible to find an improved curved caudal fin shaped by performing further optimisation studies. A strategy to move the curved caudal fin shaped blade backwards to the straight blade also allows a designer to easily orient and model the blade shapes in parallel using the caudal fin spinal axis orientation [29] formula and the strategy. The configuration of the curved caudal fin shaped blade of the present disclosure follow the same placement of airfoils at ten percent of the blade [17], and the twist angle [5] is also varied in the span wise direction. It should be understood that, the curved caudal fin shaped blade tip airfoil [4] station is thinner than the straight blade, and may be remodelled for the manufacturing purposes as there wouldn't be any major energy loss by increasing the chord length values up to 10% thicker. The caudal fin shaped blade described here is suitable for a use on power output of 50 to 1300 kW, and tidal current velocities of 0.5 to 3.5 m/s underwater tidal turbines.

While a particular embodiment or all the illustrations that have been described for the straight blade and the caudal fin shaped blade in detail, it is to be understood and will be appreciated are within the scope of the invention are intended to be included herein. While in the

embodiments described above some of the features can be modified, lengthened, replaced, and it will be clear to any person skilled in the art that modifications or adjustments not shown are possible without departing from the spirit of the invention as demonstrated through this invention. The invention is therefore to be considered limited solely by the scope of the appended claims.

What claimed is:

1. A method to design a curved caudal fin shaped blade for the use on horizontal tidal turbine blades by bio-mimicking a fish caudal fin, said blade comprising:
  - a) determining a straight blade having a symmetrical airfoil by
    - i. selecting a symmetrical airfoil to define root airfoil station and the tip airfoil station;
    - ii. placing the designed airfoil stations in ten percent of the blade;
    - iii. the hub circle diameter is forty percent in diameter of the root airfoil chord length;
    - iv. the distance between the hub circle and the root airfoil is twenty percent of the total blade height;
    - v. defining the airfoil chord length distribution using a constant reduction factor "0.08R", and calling it blade chord length reduction factor;
  - b) determining twist angle distribution by
    - i. creating a twist angle distribution rule for root airfoil and tip airfoil;
    - ii. the created twist rule for the straight blade has blade twist angle on the tip airfoil is at least four times smaller than the root airfoil; and
  - c) forming a straight blade tidal turbine system with the above mentioned parameters.
2. The design of a straight bladed tidal turbine as claimed in claim 1 wherein

- a) a centreline is passed through all the airfoil stations defined starting from the root airfoil to tip airfoil, and stacking the airfoils along the centreline to locate the airfoil station coordinate systems, and later referencing them to the blade centreline.
  - b) the step of translating the airfoil station of the symmetrical airfoil comprising the translation of the chord lengths in the blade span wise direction in linear progression, by the same distance placement of the airfoil stations.
- 3.** An approach to move the straight blade towards Blue Marlin caudal fin look alike blade as claimed in claim **1** comprising:
- a) a Blue Marlin caudal fin look alike i.e. a curved caudal fin shaped blade is designed by
    - i. defining a third order polynomial function on the central axis curve called as the blade spinal axis and bending the airfoil stations to the caudal fin axis according to the following equation:
 
$$x = 0.0034y^3 + 0.0678y^2 + 0.3209y + 0.0043$$
    - ii. twisting the blade from root airfoil to the tip airfoil using the above equation to design the caudal fin shaped blade, with the symmetrical chord lengths of the caudal fin shaped blade being slightly thicker at the root airfoil and thinnest at the tip.
    - iii. developing a caudal fin shaped blade by using horizontally defined airfoil chord lengths, twist angle variation for all the airfoil stations and keeping the total blade height constant as the straight blade.
  - b) forming a caudal fin shaped blade with the determined steps as above.
- 4.** A strategy to create further set of curved caudal fin look alike HATT's as claimed in claim **3** comprising:
- a) a further set of a curved caudal fin shaped blades are created using the percentage wise chords, and the chord lengths of the caudal fin shaped blades get bigger than the previous percentage wise value, according to the following equation:

$$R_v = \left[ \left( \frac{Ed_{val} - St_{val}}{100} \right) (R_p) \right] + St_{val}$$

b) the blade caudal fin spinal axis enables generation of an approach to move the caudal fin shaped blade back to the straight blade making sure that the blade span will stay constant for both the blades, according to the following equation:

$$T_{ASTN} = T_{SXC} \times \left( \frac{R_p}{100} \right)$$

5. The curved caudal fin shaped blade according to claim 3, is designed by bio-mimicking the Blue Marlin fish caudal fin, and the root airfoil chord length value is slightly bigger than the straight blade designed.
6. The curved caudal fin shaped blade according to claim 3, where in the total blade height has a similar value to the straight blade.
7. The caudal fin shaped blade according to claim 3, is twisted from the root airfoil to the tip airfoil to resemble a curved caudal fin.
8. The curved caudal fin shaped blade according to claim 1, wherein the hub circle distance is also in forty percent diameter of the root airfoil chord length of the curved caudal fin shaped blade.
9. The straight blade according to claim 1, wherein the said blade is suitable for use at the twist angles ranging from 16 to 4°.
10. The curved caudal fin shaped blade according to claim 1, wherein the distance between the hub circle and the root airfoil is twenty percent of the total blade height of the caudal fin shaped blade.
11. The curved caudal fin shaped blade according to claim 3, wherein said blade is suitable to have blade span ranging from 1500mm to 11000mm.
12. The curved caudal fin shaped blade according to claim 3, wherein the root airfoil has the maximum chord length value of the blade span, and gradually decreases towards each of the said tip airfoil being the thinnest to resemble a curved caudal fin.

- 13.** The curved caudal fin shaped blade according to claim **3**, wherein the defined third order polynomial function on the blade spinal axis will ensure that the said blade will always look alike a caudal fin when varied in percentage wise chord lengths.
- 14.** The curved caudal fin shaped blade according to claim **4**, wherein the said blade can be designed at any percentage wise chord length value ranging from 0 to 100%.
- 15.** The curved caudal fin shaped blade according to claim **14**, wherein the said blade will have the same blade span for the designed percentage wise chord length blade value.

## Appendix B: Matlab programs

### Turbinegenerator.m

```
% l - meters (m) . The incremental length of the turbine blade ( l <=
%          totallength)
% totalLength - (m) total length of the blade
% tipThick - (m) the thickness of the blade tip
% L0 - (m) the length were tapering starts
% tipCurveL - (m) length were the blade-tip starts to curve
% tipCurveR - (m) the radius of curvature of the blade-tip
% 0018 - NACA airfoil code - Airfoil used for 0018
% cl - the percentage length where twisting stops
% theta(l) - twist angle as a function of blade incremental length
% twistAng - (rad) calculated by theta(l)

close all;clear all
totalLength=5; % total length - in metres
baseThick=1; % the thickness of the base - in metres
tipThick=0.15; % thickness at the tip - in metres
L0=0; % starting length (where you reduce the thickness - in metres
l=0:0.1:totalLength;n=0;
tipCurveL=1; % the place where blade tip curves backwards - in metres
tipCurveR=totalLength-tipCurveL; % the radius of curvature of the tip

% defining variables for naca4gen.m
iaf.designation='0018';
% designation='0018';
iaf.n=5;
iaf.HalfCosineSpacing=1;
iaf.wantFile=1;
iaf.datFilePath='./'; % Current folder
iaf.is_finiteTE=0;
blade = naca4gen(iaf);

% plot(af.x,af.z,'bo-')
s=5;
l1=length(blade.xU);l2=length(blade.xL(2:end));
xyz=[blade.xU blade.zU;blade.xL(2:end) blade.zL(2:end)];
lxyz=length(xyz);
[IDX, C0]=kmeans(xyz,1); % this calculates the centroid of the airfoil
% Write the coordinates to a text file
% calculate the location of the tip curve center of mass
tipCurveCenter=[C0(1)+tipCurveR, tipCurveL];
theta0=10; % the starting pitch angle at the root in deg
cl = 0.10 ; % default is 0.15 (15% the length)
theta=@ (l) -(theta0/(cl*totalLength))*l+theta0;
% set the folder to write the turbine profile data.
cd('C:\Users\id913531\Desktop\Caudal fin geometry');
% Change this folder to a folder on your desktop. The script will write
for l=0:.55:totalLength
    n=n+1;
    nstr=num2str(n); % changing the n to string
    % calculations
    thickC=(baseThick-tipThick)/(L0-totalLength)*l+baseThick;
    tempXYZ=thickC*xyz;
    z(n,1)=1;
    % this is for aligning the centroids of the airfoils
    Ct=centroid(tempXYZ);
```

```

if l>=tipCurveL
    %         at this point, the blade will start to curve back along a
    %         circular path of 0.85
    theta=asin((l-tipCurveCenter(2))/tipCurveR);
    xShift=[tipCurveR-tipCurveR*cos(theta) 0];
else
    xShift=[0 0];
end
if l<cl*totalLength % if the l is less than cut-off length
    twistAng=theta(1)*pi/180;
    M=[cos(twistAng) -sin(twistAng); % rotation matrix
        sin(twistAng)  cos(twistAng)];
else
    M=eye(2);
end
%         shift center of mass
tempXYZ=tempXYZ+repmat((C0+xShift-Ct),lxyz,1);
%         rotate by twistAng
tempXYZ=M*(tempXYZ');
%         final value  subrated the shift of the center of mass

profile(n,[:,:])=[tempXYZ' 1*ones(lxyz,1)];
profileLine(n,:)=profile(n,1,1) profile(n,1,2) 1];
tempM(:,:)=profile(n,[:,:]);
end

```

### Naca4gen.m

Naca4gen.m program (NACA 4 digit Airfoil Generator, MathWorks, 2014), which was adapted and modified to suit the requirements of this research. The full explanation of the commands used are explained as follows:

```

function af = naca4gen(iaf)

% INPUTS-----
%         iaf.designation = NACA 4 digit iaf.designation (eg. '0018') -
STRING !
%         iaf.n = no of panels (line elements) PER SIDE
(upper/lower)
% iaf.HalfCosineSpacing = 1 for "half cosine x-spacing"
%                       = 0 to give "uniform x-spacing"
%         iaf.wantFile = 1 for creating airfoil data file (eg.
'naca0018.dat')
%                       = 0 to suppress writing into a file
%         iaf.datFilePath = Path where the data file has to be created
%                       (eg. 'af_data_folder/naca4digitAF/')
%                       use only forward slash '/' (Just for OS
portability)
%
% OUTPUTS-----
% Data::::::::::::::::::::::::::::::::::::::::::::::::::::::::::::::::::
%         af.x = x cordinate (nx1 array)
%         af.z = z cordinate (nx1 array)
%         af.xU = x cordinate of upper surface (nx1 array)
%         af.zU = z cordinate of upper surface (nx1 array)
%         af.xL = x cordinate of lower surface (nx1 array)
%         af.zL = z cordinate of lower surface (nx1 array)

```

```

%      af.xC = x cordinate of camber line (nx1 array)
%      af.zC = z cordinate of camber line (nx1 array)
%      af.name = Name of the airfoil
%      af.header = Airfoil name ; No of panels ; Type of spacing
%                  (eg. 'NACA0018 : [50 panels,Uniform x-spacing]')
%
%
% File::::::::::::::::::::::::::::::::::::::::::::::::::::::::::::::::::
% First line : Header eg. 'NACA4412 : [50 panels,Half cosine x-spacing]'
% Subsequent lines : (2*iaf.n+1) rows of x and z values
%
% Typical Inputs::::::::::::::::::::::::::::::::::::::::::::::::::::::::::
% iaf.designation='0018';
% iaf.n=56;
% iaf.HalfCosineSpacing=1;
% iaf.wantFile=1;
% iaf.datFilePath='./'; % Current folder
% iaf.is_finiteTE=0;

% % [[Calculating key parameters-----]]
t=str2num(iaf.designation(3:4))/100;
m=str2num(iaf.designation(1))/100;
p=str2num(iaf.designation(2))/10;

a0= 0.2969;
a1=-0.1260;
a2=-0.3516;
a3= 0.2843;

if iaf.is_finiteTE ==1
    a4=-0.1015; % For finite thick TE
else
    a4=-0.1036; % For zero thick TE
end

% % [[Giving x-spacing-----]]
if iaf.HalfCosineSpacing==1
    beta=linspace(0,pi,iaf.n+1)';
    x=(0.5*(1-cos(beta))); % Half cosine based spacing
    iaf.header=['NACA' iaf.designation ' : [' num2str(2*iaf.n) 'panels,Half
cosine x-spacing]'];
else
    x=linspace(0,1,iaf.n+1)';
    iaf.header=['NACA' iaf.designation ' : [' num2str(2*iaf.n)
'panels,Uniform x-spacing]'];
end

yt=(t/0.2)*(a0*sqrt(x)+a1*x+a2*x.^2+a3*x.^3+a4*x.^4);

xc1=x(find(x<=p));
xc2=x(find(x>p));
xc=[xc1 ; xc2];

if p==0
    xu=x;
    yu=yt;

    xl=x;
    yl=-yt;

```

```

    zc=zeros(size(xc));
else
    yc1=(m/p^2)*(2*p*xc1-xc1.^2);
    yc2=(m/(1-p)^2)*((1-2*p)+2*p*xc2-xc2.^2);
    zc=[yc1 ; yc2];

    dyc1_dx=(m/p^2)*(2*p-2*xc1);
    dyc2_dx=(m/(1-p)^2)*(2*p-2*xc2);
    dyc_dx=[dyc1_dx ; dyc2_dx];
    theta=atan(dyc_dx);

    xu=x-yt.*sin(theta);
    yu=zc+yt.*cos(theta);

    xl=x+yt.*sin(theta);
    yl=zc-yt.*cos(theta);
end
af.name=['NACA ' iaf.designation];

af.x=[flipud(xu) ; xl(2:end)];
af.z=[flipud(yu) ; yl(2:end)];

indx1=1:min( find(af.x==min(af.x)) ); % Upper surface indices
indx2=min( find(af.x==min(af.x)) ):length(af.x); % Lower surface indices
af.xU=af.x(indx1); % Upper Surface x
af.zU=af.z(indx1); % Upper Surface z
af.xL=af.x(indx2); % Lower Surface x
af.zL=af.z(indx2); % Lower Surface z

af.xC=xc;
af.zC=zc;

lecirFactor=0.8;
af.rLE=0.5*(a0*t/0.2)^2;

le_offs=0.5/100;
dyc_dx_le=(m/p^2)*( 2*p-2*le_offs );
theta_le=atan(dyc_dx_le);
af.xLEcenter=af.rLE*cos(theta_le);
af.yLEcenter=af.rLE*sin(theta_le);

%% [[Writing iaf data into file-----
]]
if iaf.wantFile==1
    F1=iaf.header;
    F2=num2str([af.x af.z]);
    F=strvcat(F1,F2);
    fileName=[iaf.datFilePath 'naca' iaf.designation '.dat'];
    dlmwrite(fileName,F,'delimiter','')
end

```

**Centroid.m**

Centroid.m program (Geom2d, MathWorks, 2014), which was adapted and modified to suit the requirements of this research. The full explanation of the commands used are explained as follows:

```
function center = centroid(varargin)
%CENTROID Compute centroid (center of mass) of a set of points
%
%   PTS = centroid(POINTS)
%   PTS = centroid(PTX, PTY)
%   Computes the ND-dimensional centroid of a set of points.
%   POINTS is an array with as many rows as the number of points, and as
%   many columns as the number of dimensions.
%   PTX and PTY are two column vectors containing coordinates of the
%   2-dimensional points.
%   The result PTS is a row vector with Nd columns.
%
%   PTS = centroid(POINTS, MASS)
%   PTS = centroid(PTX, PTY, MASS)
%   Computes center of mass of POINTS, weighted by coefficient MASS.
%   POINTS is a Np-by-Nd array, MASS is Np-by-1 array, and PTX and PTY are
%   also both Np-by-1 arrays.
%
%   Example:
%   pts = [2 2;6 1;6 5;2 4];
%   centroid(pts)
%   ans =
%       4     3
%
%   See Also:
%   points2d, polygonCentroid
%
% -----
% Author: David Legland
% e-mail: david.legland@grignon.inra.fr
% created the 07/04/2003.
% Copyright 2010 INRA - Cepia Software Platform.
%
%
%   HISTORY
%   2009-06-22 support for 3D points
%   2010-04-12 fix bug in weighted centroid
%   2010-12-06 update doc

%% extract input arguments

% use empty mass by default
mass = [];

if nargin==1
    % give only array of points
    pts = varargin{1};

elseif nargin==2
    % either POINTS+MASS or PX+PY
    var = varargin{1};
    if size(var, 2)>1
```

```

        % arguments are POINTS, and MASS
        pts = var;
        mass = varargin{2};
    else
        % arguments are PX and PY
        pts = [var varargin{2}];
    end

elseif nargin==3
    % arguments are PX, PY, and MASS
    pts = [varargin{1} varargin{2}];
    mass = varargin{3};
end

%% compute centroid

if isempty(mass)
    % no weight
    center = mean(pts);

else
    % format mass to have sum equal to 1, and column format
    mass = mass(:)/sum(mass(:));

    % compute weighted centroid
    center = sum(bsxfun(@times, pts, mass), 1);
    % equivalent to:
    % center = sum(pts .* mass(:, ones(1, size(pts, 2))));
end

```

## References

- Abdulrahim M., and Lind R. (2004). Flight testing and response characteristics of a variable Gull-Wing morphing aircraft. American Institute of Aeronautics and Astronautics (AIAA), Navigation, and Control Conference and Exhibit 16 – 19 August, Providence, Rhode Island. 1 – 16.
- Afgan I., McNaughton J., Rolfo S., Apsley D., Stalard T., Stansby P., (2013). Turbulent flow and loading on a tidal stream turbine by LES and RANS. *International Journal of Heat and Fluid Flow*. Vol. 43, 96 - 108.
- Aliaga M., Gunderson B., (2006). *Interactive Statistics*. 3<sup>rd</sup> Edition, Pearson, London.
- Almohammadi K., Ingham D., Ma L., Pourkashan M., (2013). Computational Fluid Dynamics (CFD) mesh independency techniques for a straight blade vertical axis wind turbine. *Energy*. Vol. 58, 483 – 493.
- Ansys Inc., (2006). ANSYS CFX-Solver Theory Guide. <  
<http://product.caenet.cn/Uploadfiles/12872437250986625020081129090050986.pdf> > Date Accessed: 15/11/2013.
- Anyi M., Kirke B., (2010). Evaluation of small axial flow hydrokinetic turbines for remote communities. *Energy for Sustainable Development*. Vol. 14, 110 – 116.
- Arns A., Wahl T., Haigh D., Jensen J., Pattiaratchi C., (2013). Estimating extreme water level probabilities: A comparison of the direct methods and recommendations for best practise. *Coastal Engineering*. Vol. 81 51 – 66.
- Ashwill T., Kanaby G., Jackson G., Zuteck M., (2010). Development of the Swept Twist Adaptive Rotor (STAR) Blade. 48<sup>th</sup> American Institute of Aeronautics and Astronautics (AIAA), Aerospace Sciences Meeting, Orlando, Florida. 4 – 7.
- Asim T., Mishra R., Ubbi K., Zala K., (2013). Computational Fluid Dynamics based optimal of vertical axis marine current turbines. 2<sup>nd</sup> International Through-life Engineering Services Conference, Procedia CIRP. 323 – 327.
- Bahaj A., Batten W., McCann G., (2007). Experimental verifications of numerical predictions for the hydrodynamic performance of horizontal axis marine current turbines. *Renewable Energy*. Vol. 32 2479–2490.

Bahaj A., Molland A., Chaplin J., Batten W., (2006). Power and thrust measurements of marine current turbines under various hydrodynamic flow conditions in a cavitation tunnel and a towing tank. *Renewable Energy*. Vol. 32, 407–426.

Bai X., Avital E., Munjiza A., Williams J., (2014). Numerical simulation of a marine current turbine in free surface flow. *Renewable Energy*. Vol. 63, 715 – 723.

Balaras E., Benocci C., (1994). Applications of Direct and Large Eddy Simulation, Advisory Group for Aerospace Research and Development (AGARD). 21-26.

Barbara B., Booth D., Carey F., (1992). Direct measurement of the swimming speeds and depth of Blue Marlin. *Journal of Experimental Biology*. Vol. 166, 267 – 284.

Baston S., Harris R., (2011). Modelling the hydrodynamic characteristics of tidal flow in the Pentland Firth. EWTEC 2011, Southampton, UK, 5–9 September 2011.

Batten W., Bahaj A., Molland A., Chaplin J., (2008). The prediction of the hydrodynamic performance of marine current turbines. *Renewable Energy*. Vol. 33, 1085 – 1096.

Bavanish B., Thyagarajan K., (2013). Optimisation of power coefficient on a horizontal axis wind turbine using bem theory. *Renewable and Sustainable Energy Reviews*. Vol. 26, 169-182.

Behrendt A., Fahrbach E., Hoppema M., Rohardt G., Boebel O., Klatt O., Witte H., (2011). Variations of Winter Water properties and sea ice along the Greenwich meridian on decadal time scales. *Deep Sea Research II*. Vol. 58, 2524 – 2532.

Ben Elghali S., Benbouzid M., Charpentier J., (2007). Marine tidal current electric power generation technology: State of the art and current status. Electric machines and Drives Conference, Antalya. IEMDC. IEEE International. 1407 – 1412.

Benini E., Toffolo A., (2002). Optimal design of horizontal axis wind turbines using blade element theory and evolutionary computation. *Journal of Solar Engineering*. Vol. 124, 357 – 363.

BERR Marine Atlas, (2008). Department of Business, Enterprise and regulatory reform, Atlas of the UK marine renewable energy resource, BERR, London <<http://www.renewables-atlas.info>> Date Accessed: 21/03/2013.

Betz A. (1966). *Introduction to the Theory of Flow Machines*. (D. G. Randall, Trans.) Pergamon Press, Oxford.

- Betz A., (1920). Das Maximum der theoretisch möglichen Ausnutzung des Windes durch Windmotoren. *Gesamte Turbinenwesen*. 307 – 309.
- Bhusan B. (2009). Biomimetics: lessons from nature – an overview. *Philosophical Transactions of the Royal Society A*. Vol., 367 1445 – 1486.
- Black & Veatch Ltd., (2005). Phase II UK tidal stream energy resource assessment. Issue 3. Carbon Trust, UK. 5 – 31.
- Blunden L., Bahaj A., (2007). Tidal energy assessment for tidal stream generators. Proceedings of the Institution of Mechanical Engineers. *Journal of Power and Energy*. Vol. 221, 137 – 46.
- Bryden I., Couch S., (2006). ME-1 marine energy extraction: tidal resource analysis. *Renewable Energy*. Vol. 31, 133 -139.
- Bryden I., Couch S., Owen A., Melville G., (2007). Tidal current resource assessment. Proceedings of the Institution of Mechanical Engineers Part A. *Journal of Power and Energy*. Vol. 221, 125 – 135.
- Bühler S., Luginsland T., Obrist D., Kleiser L., (2010) Parallel simulation of compressible jets including nozzle modelling. Proceedings in Applied Mathematics and Mechanics. Vol. 10, 597 – 598.
- Cai Y., Huang G., Yeh S., Liu L., (2011). A modeling approach for investigating climate change impacts on renewable energy utilization. *International Journal of Energy Research*. Vol. 36, 764 – 777.
- Chaineux M., Charlier R., (2008). Women's tidal power plant Forty candles for Kislaya Guba TPP. *Renewable and Sustainable Energy Reviews*. Vol. 12, 515 – 2524.
- Charlier R., (2003). Sustainable co-generation from tides a review. *Renewable and Sustainable energy reviews*. Vol. 7, 187 – 213.
- Chen Y., Lu C., Wu L., (2006). Modelling and computation of unsteady turbulent cavitation flows. *Journal of Hydrodynamics*. Vol. 18, 559 – 566.
- Cherniawsky J., Foreman M., Kang S., Scharroo R., Jane Eert A., (2010). 18.6-year lunar nodal tides from altimeter data. *Continental Shelf Research*. Vol. 30, 575 -587.
- Clancy L., (1978). *Aerodynamics (Pitman aeronautical engineering series)*. Pearson, FT Prentice Hall, New York.

- Clark R., (2007). *Elements of tidal-electric engineering*. John Wiley and Sons, IEEE Press, New Jersey.
- Cooper W., Hinton C., Ashton N., Saulter A., Morgan C., Proctor R., Bell C., Huggett Q., (2006). An Introduction to the UK Marine renewable atlas. *Maritime Engineering*. Vol. 159, 1 – 7.
- Costa Rocha P., Barbosa Rocha H., Carneiro Moura F., Vieira da Silva M., Valente Bueno A., (2014).  $k - \omega$  SST (shear stress transport) turbulence model calibration: A case study on a small scale horizontal axis wind turbine. *Energy*. Vol. 65, 412 -418.
- Date A., (2005). *Introduction to Computational Fluid Dynamics*. Cambridge University Press, New York.
- Deardorff J., (1970). A numerical study of three-dimensional turbulent channel flow at large Reynolds numbers. *Journal of Fluid Mechanics*. Vol. 41, 453–480.
- Eesa M., (2009). CFD studies of complex fluid flows in pipes. University of Birmingham, Department of Chemical Engineering, PhD thesis, 10- 32.
- Etemadi A., Emami Y., AsefAfsar O., Emdadi A., (2011). Electricity generation by the tidal barrages. *Energy Procedia*. Vol. 12, 928 – 935.
- Eymard R., Gallouët T., Herbin R., (2008). *Finite volume methods Schemes and Analysis*. April 2008, Course at the University of Wroclaw, Wroclaw, 34 - 69. <  
[http://www.math.uni.wroc.pl/~olech/courses/skrypt\\_Roberta\\_wroclaw.pdf](http://www.math.uni.wroc.pl/~olech/courses/skrypt_Roberta_wroclaw.pdf) > Date Accessed:  
 10/06/2013.
- Falkovich G., (2011). *Fluid Mechanics*. Cambridge University Press, Cambridge.
- Ferrer E., Willden R., (2011). Development and validation of a high numerical solver for cross-flow turbine hydrodynamics. In proceedings 9<sup>th</sup> European Wave and Tidal Energy Conference (EWTEC), Southampton, UK.
- Findikakis A., Street R., (1982). Mathematical description of turbulent flows. *Journal of the Hydraulics division proceedings of the American society of civil engineers*. Vol. 108, 887 – 903.
- Fish F., (2009). Biomimetics: determining engineering opportunities from nature. Proceedings of SPIE Conference, San Diego, CA, Society of Photo-Optical Instrumentation Engineers (SPIE). Vol. 7401, 1 – 11.

- Fish F., Battle J., (1995). Hydrodynamic design of the humpback whale flipper. *Journal of Morphology*. Vol. 225, 51 – 60.
- Fish F., Weber P., Murray M., Howle L., (2011). The tubercles on Humpback Flippers: Application of Bio-Inspired Technology. *Integrative and Comparative Biology*. Vol. 51, 203 – 213.
- Flammang B., (2013). The fish tail as a derivation from axial musculoskeletal anatomy: an integrative analysis of functional morphology. *Zoology*. Vol. 117, 86 – 92.
- Flygtus, USA, (2011). < <http://www.flygtus.com/3424270.pdf> > Date accessed: 13/03/2014.
- Fraenkel P., (2007). Marine Current Turbines: Pioneering the development of marine kinetic energy converters. Proceedings of IMechE Part A: *Journal of Power and Energy*. Vol. 221, 159–169.
- Franenkel P., (1999). *Tidal currents: a major new source of energy for the Millennium EEZ Technology*. 4<sup>th</sup> Edition London; ICG publishing Ltd.
- Fugslang P., Madsen H., (1999). Optimisation method for wind turbine rotors. *Journal of Wind Engineering and Industrial Aerodynamics*. Vol. 80, 191 – 206.
- Garrett C., Cummins P., (2013). Maximum power from a turbine farm in shallow water. *Journal of Fluid Mechanics*. Vol. 714, 634 – 643.
- Geom2d, MathWorks, (2014). < <http://au.mathworks.com/matlabcentral/fileexchange/7844-geom2d/content/geom2d/geom2d/centroid.m> >. Date Accessed: 25/06/2013.
- Germano M., (1992). Turbulence: the filtering approach. *Journal of Fluid Mechanics*. Vol. 238, 325 – 336.
- Gim O., Lee G., (2013). Flow characteristics and tip vortex formation around a NACA 0018 foil with an end plate. *Ocean Engineering*. Vol. 60, 28 – 38.
- Goundar J., Ahmed M., (2013). Design of a horizontal axis tidal current turbine. *Applied Energy*. Vol. 111, 161 – 174.
- Gretton G., (2009). The hydrodynamic analysis of a vertical axis tidal turbine. The University of Edinburgh, PhD thesis, 249 – 261.
- Groves G., Reynolds R., (1975). An orthogonalized convolution method of tide prediction. *Journal of Geophysical Research*. Vol. 80, 4131-4138.

- Hameed M., Afaq S., (2013). Design and analysis of a straight bladed vertical axis wind turbine blade using analytical and numerical techniques. *Ocean Engineering*. Vol. 57, 248 -255.
- Han J., Lee J., Kim D. (2009). Bio-Inspired flapping UAV Design: A University perspective. *Health Monitoring of Structural and Biological Systems*. Proceedings of SPIE Vol. 7295 1 – 12.
- Herzfeld M., Andrewartha J.A., (2010). Modelling the physical oceanography of D’Entrecasteaux Channel and the Huon Estuary, south-eastern Tasmania. *Marine and Freshwater Research*. Vol. 61, 568–586.
- Huang D., Wu G., (2013). Preliminary study on the aerodynamic characteristics of an adaptive reconfigurable airfoil. *Aerospace Science and Technology*. Vol. 27, 44 – 48.
- Hudgins D., Lavelle J., (1995). Risk management in design engineering bids. Conference: Industrial Engineering Research conference, Nashville, TN, 25-26 May, 1 – 9.
- Iyer A., Couch S., Harrison G., Wallace A., (2013). Variability and phasing of tidal current energy around the United Kingdom. *Renewable Energy*. Vol. 51, 343 – 357.
- Jahromi M., Maswood A., Tseng K., (2011). Long term prediction of tidal currents. *IEEE Systems journal*. Vol. 5, 146 – 155.
- James S., Seetho E., Jones C., Roberts J., (2010). Simulating environmental changes due to marine hydrokinetic energy installations. OCEANS conference, Seattle, WA, 20– 23 September, 1–10.
- Jayne B., Block G., (1996). Function of the dorsal fin in bluegill sunfish: Motor patterns during four locomotor behaviors. *Journal of Morphology*. Vol., 228, 307- 326.
- Jo C., Lee J., Rho Y., Lee K., (2014). Performance analysis of a HAT tidal current turbine and wake flow characteristics. *Renewable Energy*. Vol. 65, 175 - 182.
- Johnson K., Pao L., Balas M., Fingersh L., (2004). Stability analysis of an adaptive torque controller for variable speed wind turbines, in Proceedings of the Conference in Decision and Control, Atlantis, Paradise Island, Bahamas, December 14 – 17, 4316–4323.
- Kang S., Borazjani I., Colby J., Sotiropoulos F., (2012). Numerical simulation of 3D flow past a real-life marine hydrokinetic turbine. *Advances in Water Resources*. Vol. 39, 33 – 43.

Karasev A., Mitenev V., Shulman B., (1996). Ecological popularities of the parasite fauna of cod and Pollock in the vicinity of the Kislava inlet tidal power plant, western Murmam (The Barents Sea). *Sarsia*. Vol. 80, 307 -312.

Keck H., Sick M., (2008). Thirty years of numerical flow simulation in hydraulic turbomachines. *Acta Mechanica*. Vol. 201, 211-229.

Kim B., Kim W., Lee S., Bae S., Lee Y., (2013). Development and verification of a performance based optimal design software for wind turbine blades. *Renewable Energy*. Vol. 54, 166 -172.

Kim H., Lee S., Fujisawa N., (2006). Computation of unsteady flow and aerodynamic noise of NACA 0018 airfoil using large-eddy simulation. *International Journal of Heat and Fluid Flow*. Vol. 27, 229 – 242.

Kim K., Ahmed M., Lee Y., (2012). Efficiency improvement of a tidal current turbine utilising a larger channel of area. *Renewable Energy*. Vol. 48, 557 – 564.

King Sailfish Mounts., (2014). < [http://www.kingsailfishmounts.com/saltwater-fish-mounts-marlin-blue-c-1\\_54.html](http://www.kingsailfishmounts.com/saltwater-fish-mounts-marlin-blue-c-1_54.html) > Date Accessed: 04/03/14.

Kvale E., Fraser G., Archer A., Zawistoski A., Kemp N., McGough P., (1994). Evidence of seasonal precipitation in Pennsylvanian sediments of the Illinois Basin. *Geology*. Vol. 22, 331–334.

Lanchester F., (1915). A contribution to the theory of propulsion and the screw propeller. *Transactions of the Institution of Naval Architects*. LVII. 98 - 116.

Larwood S., Zuteck M., (2006). Swept Wind turbine blade aero elastic modelling for loads and dynamic behaviour. [White paper] American Wind Energy Association, Wind Power, Washington. 1 – 17.

Lathrop D., (2006). Fluid Dynamics: Turbulence lost in transience. *Nature*. Vol. 443, 36 – 37.

Launder B., Reece G., Rodi W., (1975). Progress in the development of a Reynolds stress turbulence closure. *Journal of Fluid Mechanics*. Vol. 68, 537 – 566.

Lee J., Park S., Kim D., Rhee S., Kim M., (2012). Computational methods for performance analysis of horizontal axis tidal turbines. *Applied Energy*. Vol. 98, 512 – 523.

- Leffler K., Jay D., (2009). Enhancing tidal harmonic analysis: Robust (hybrid L1/L2) solutions. *Continental Shelf Research*. Vol. 29, 78-88.
- Lenarz W., & Nakamura E., (1972). Analysis of length and weight of three species of Billfish from the western Atlantic ocean. Proceedings of the International Billfish Symposium, Kailua-Kona, Hawaii, 9-12 August.
- Li C., Zhu S., Xu Y., Xiao Y., (2013). 2.5D large eddy simulation of vertical axis wind turbine in consideration of high angle of attack flow. *Renewable Energy*. Vol. 51, 317 – 330.
- Lilly D., (1992). A proposed modification of the Germano subgrid-scale closure method. *Physics of Fluids*. Vol. 4, 633–636.
- Liu J., Hu H., (2005). Mimicry of sharp turing behaviours in a robotic fish. Proceedings of IEEE International conference on Robotics and Automation, Barcelona, Spain, April, 3329 – 3334.
- Liu P., Bose N., (2013). Parametric analysis of Horizontal axis tidal turbine hydrodynamics for optimum energy generation. 3<sup>rd</sup> International Symposium on Marine Propulsors Symposium, Launceston. 242-256.
- Liu P., Veitch B., (2011). Design and optimisation for the strength and integrity of tidal turbine rotor blades. *Energy*. Vol. 46, 393 – 404.
- Liu P., Veitch B., (2012). Design and optimisation for strength and integrity of tidal turbine rotor blades. *Energy*. Vol. 46, 393 – 404.
- Long J., (1992). Stiffness and damping forces in the intervertebral joints of the blue marlin (*Makaira nigricans*). *Journal of Experimental Biology*. Vol. 162, 131 – 155.
- Lunar Energy Ltd., (2008). Renewables boost as Lunar Energy seals £500m deal; 2008. <<http://www.lunarenergy.co.uk/News.php>> Date Accessed: 02/04/2013.
- Luthy S., (2005). Toward identification of larval sailfish (*Istiophorus platypterus*), white marlin (*Tetra abidus*), and the blue marlin (*Makaira nigricans*), in the western North Atlantic Ocean. *Fish Bulletin*. Vol. 103, 588 – 600.
- Lynchos G., Fletcher J., Davies P., (2010). Properties of Ocean bitterns with regard to liquid-desiccant cooling. *Desalination*. Vol. 250, 172 -178.

- Lynne D., Talley G., Pickard W., Emery J., Swift H., (2011). *Descriptive Physical Oceanography*. 6<sup>th</sup> edition, Physical properties of water – Chapter three, Elsevier Ltd, London, 29-65.
- Manwell J., McGowan J., Rogers A., (2002). *Aerodynamics of Wind Turbine, Wind Energy Explained-Theory Design and Application*, John Wiley & Sons Ltd, London.
- Mason-Jones A., O'Doherty D., Morris C., Byrne C., Prickett P., Gorsvenor R., Owen I., Tedds S., Poole R., (2012). Non-dimensional scaling of tidal steam turbines. *Energy*. Vol. 44, 820 – 829.
- Masters I., Malki R., Williams A., Nicholas Craft T., (2013). The influence of flow acceleration on tidal stream turbine wake dynamics: A numerical study using a coupled BEM–CFD model. *Applied Mathematical Modelling*. Vol. 37, 7905 – 7918.
- May E., Wu R., Kelland M., Aman Z., Kozielski K., Hartley P., Maeda N., (2014). Quantitative kinetic inhibitor comparisons and memory effect measurements from hydrate formation probability distributions. *Chemical Engineering Science*. Vol. 107, 1 – 12.
- McSherry R., Grimwade J., Jones I., Mathias S., Wells A., Mateus A., (2011). 3D CFD modelling of tidal turbine performance with validation against laboratory experiments. The European Wave and Tidal Energy Conference 2011, Southampton, UK, 1 – 7.
- MCT, Marine Current Turbines Ltd. (2008). SeaGen Tidal Energy System Reaches Full Power - 1.2MW;  
<[http://www.marineturbines.com/3/news/article/17/seagen\\_tidal\\_energy\\_system\\_reaches\\_full\\_power\\_1\\_2mw/](http://www.marineturbines.com/3/news/article/17/seagen_tidal_energy_system_reaches_full_power_1_2mw/)> Date Accessed: 01/04/2013.
- MCT, Marine Current Turbines Ltd. (2009). SeaGen completed: World's First Megawatt-Scale Tidal Turbine Installed <[www.marineturbines.com](http://www.marineturbines.com)> Date Accessed: 01/04/2013.
- Mehmood N., Liang Z., Khan J., (2012 a). CFD study of 2D model of diffuser for harnessing tidal energy. *Advanced Materials Research*. Vol. 482 – 484, 2270 – 2274.
- Mehmood N., Liang Z., Khan J., (2012). CFD study of NACA 0018 for diffuser design of tidal current turbines. *Research Journal of Applied Sciences, Engineering and Technology*. Vol. 4, 4552 – 4560.
- Mehta U., (1998). Credible Computational fluid dynamics simulation. *The American Institute of Aeronautics and Astronautics (AIAA) Journal*. Vol. 36, 665 – 667.
- Menter F., (1993). *Zonal two equation k-omega turbulence models for aerodynamic flows*.

NASA Technical Reports. 93-2906. <

<http://ntrs.nasa.gov/archive/nasa/casi.ntrs.nasa.gov/19930013620.pdf> > Date Accessed:

14/04/2013.

Mohamed M., (2012). Performance investigation of H-rotor Darrieus turbine with new airfoil shapes. *Energy*. Vol. 47, 522 – 530.

Murthy P., Holla V., Kamath H., (2000). Unsteady Navier-Stokes solutions for a NACA 0012 airfoil. *Computational Methods Applied Mechanical Engineering*. Vol. 186, 85 – 99.

Mycek P., Gaurier B., Germain G., Pinon G., Rivoalen E., (2013). Numerical and experimental study of the interaction between two marine current turbines. *International Journal of Marine Energy*. Vol. 1, 70 – 83.

NACA 4 digit Airfoil Generator, MathWorks, (2014).

<<http://au.mathworks.com/matlabcentral/fileexchange/19915-naca-4-digit-airfoil-generator/content/naca4gen.m>>. Date Accessed: 25/06/2013.

Nagy K., Kormendi K., (2012). Use of renewable energy sources in light of the “New Energy Strategy for Europe 2011-2020”. *Applied Energy*. Vol. 96, 393 – 399.

Nishizawa Y., Shengning C., Elson R., Ushiyama I., (2013). An experimental study on performance of curved-plate bladed rotor. *Renewable Energy*. Vol. 49, 6 – 9.

Nova Scotia Power, (2013).

<<http://www.nspower.ca/en/home/aboutnspower/mediacentre/NewsRelease/2013/biomassplant.aspx>> Date Accessed: 15/03/2013.

Oberkampf W., Trucano T., (2002). Verification and Validation in Computational Fluid Dynamics. *Progress in Aerospace Science*. Vol. 38, 209 – 272.

Ocean Flow Energy Ltd., (2008). Development status

<<http://www.oceanflowenergy.com/development-status.htm>> Date Accessed: 01/04/2013.

OSPO, NOAA, Office of Satellite and Product Operations, National Oceanic and Atmospheric Administration. Sea Surface Temperature (SST) Contour charts. <

<http://www.ospo.noaa.gov/Products/ocean/sst/contour/index.html>> Date Accessed: 05/03/2013.

- Patankar S., (1980). *Numerical fluid flow and heat transfer*. Taylor and Francis, Hemisphere Publishing Corporation, New York.
- Pinon G., Mycek P., Germain G., Rivoalen E., (2012). Numerical simulation of the wake of marine current turbines with a particle method. *Renewable Energy*. Vol. 46, 111 – 126.
- Pugh P., (1992). Working Top-Down: Cost estimating before development begins. *Journal of Aerospace Engineering*. Vol. 206, 143 – 151.
- Rajakumar S., Ravindran D., (2012). Iterative approach for optimising coefficient of power, coefficient of lift and drag of wind turbine rotor. *Renewable Energy*. Vol. 38, 83 – 93.
- Reynolds O., (1883). An experimental investigation of the circumstances which determine whether the motion of water shall be direct or sinuous, and the law of resistance in parallel channels. *Philosophical Transactions of the Royal Society*. 935 – 982.
- Robinson E., Byrne G., (2008). Methodology for modelling tidal turbine characteristics. IEEE transactions. Oceans 2008 Conference, 15 – 18 September, Quebec City, QC, 1 – 5.
- Robinson M., Valdes P., Haywood A., Dowsett H., Hill D., Jones S., (2011). Bathymetric controls on Pliocene North Atlantic and Arctic sea surface temperature and deepwater production. *Palaeogeography, Palaeoclimatology, Palaeoecology*. Vol. 309, 92 -97.
- Rodriguez I., Lehmkhul O., Borrell R., Olivia A., (2013). Direct Numerical simulation of a NACA0012 in full stall. *International Journal of Heat and Fluid Flow*. Vol. 43, 194 – 203.
- Rossetti A., Pavesi G., (2013). Comparison of different numerical approaches to the study of the H-Darrieus turbines start up. *Renewable Energy*. Vol. 50, 7 – 19.
- Rourke F., Boyle F., Reynolds A., (2009). Tidal energy update 2009. *Applied Energy*. Vol. 87, 398 – 409.
- Salumae T., Kruusmaa M., (2011). A flexible fin with bio-inspired stiffness profile and geometry. *Journal of Bionic Engineering*. Vol. 8, 418 – 428.
- Sfakiotakis M., Lane D., Davies B., (1999). Review of Fish Swimming modes for aquatic locomotion. *IEEE Journal of Oceanic Engineering*. Vol.24, 237 – 252.

- Shen H., Li S., Chen G., (2012). Quantitative analysis of surface deflections in the automobile exterior panel based on a curvature-deviation method. *Journal of Materials Processing Technology*. Vol. 212, 1548 – 1556.
- Sheth S., Shahidehpour M., (2005). Tidal energy in electric power systems. Power Engineering Society General Meeting, IEEE, 12 – 15 June, Vol. 1, 630 – 635.
- Shields M. , Woolf D., Grist E., Kerr S., Jackson A., Harris R., Bell M., Beharie R., Want A., Osalusi E., Gibb S., Side J., (2011). Marine renewable energy: The ecological implications of altering the hydrodynamics of the marine environment. *Ocean and Coastal management*. Vol. 54, 2-9.
- Shields M., Dillion L., Woolf D., Ford A., (2009). Strategic priorities for assessing ecological impacts of marine renewable energy devices in the Pentland Firth (Scotland, UK). *Marine Policy*. Vol 33, 635 – 642.
- Shirgaonkar A., Curet O., Patankar N., Maclever (2008). The hydrodynamics of ribbon-fin propulsion during impulsive motion. *The Journal of Experimental Biology*. Vol. 211, 3490 – 3503.
- Singh R., Ahmed M., Zullah M., Lee Y., (2012). Design of a low Reynolds number airfoil for small horizontal axis wind turbines. *Renewable Energy*. Vol. 42, 66 – 76.
- Smagorinsky J., (1963). General Circulation Experiments with the Primitive Equations. *Monthly Weather Review*. Vol.91, 99–164.
- Stern N., (2007). Stern review on the Economics of Climate change. <[http://www.hm.treasury.gov.uk/sternreview\\_index.htm](http://www.hm.treasury.gov.uk/sternreview_index.htm)> Date Accessed: 20/01/2012.
- Stoddard F., Eggleston D., (1985). *Wind Turbine Engineering Design*. New York: Van Nostrand Reinhold.
- Suleman A., Crawford C., (2008). Design and testing a biomimetic tuna using shape memory alloy induced propulsion. *Computers and Structures*. Vol. 86 – 491 – 499.
- Sutherland G., Foreman M., Garrett C., (2007). Tidal current energy assessment for Johnstone Strait, Vancouver Island. Proceedings of the institution of Mechanical engineers. *Power and Energy*. Vol. 221, 147 -157.
- Tang H., Skraatz S., (2011). Marine Hydrokinetic energy systems and their performance indicators. 1 – 10, < <http://www-ce.ccnycuny.edu/cfd/C11.pdf> > Date Accessed: 06/05/2012.

- Tessicini F., Li N., Leschziner M., (2005). Large Eddy simulation of the three dimensional flow around a hill-shaped obstruction with a zonal near-wall approximation. *International Journal of Heat and Fluid Flow*. Vol. 28, 894 -908.
- The Canadian Encyclopaedia, (2013). <<http://www.thecanadianencyclopedia.com/articles/tidal-energy>> Date Accessed: 17/03/2013.
- Tikhomirov V., (1991). Selected works of A. N. Kolmogorov - Equations of turbulent motion in an incompressible fluid. *Mathematics and Its Applications (Soviet Series)*. Vol., 25, 328 – 330.
- Tocardo B.V. Tidal Turbines (2013) <[http://www.tocardo.com/products\\_and\\_services/t500.html](http://www.tocardo.com/products_and_services/t500.html)> Date Accessed: 01/11/2013.
- Tokic G., Yue D., (2012). Optimal shape and motion of undulatory swimming organisms. *Proceedings of the Royal Society B*. Vol. 279, 3065 – 3079.
- UK Hydrographic Office, (2013). Admiralty charts, UKHO, Taunton, UK, <<http://catalogue.ukho.gov.uk/home.asp>> Date Accessed: 20/03/2013.
- UNESCO, (1983). Algorithms for computation of fundamental properties of Ocean. UNESCO technical papers in marine science, Paris, 1 – 51.
- United States Patent, 6835108 (2004). Oscillating appendage for fin propulsion. <<http://www.patents.com/us-6835108.html>> Date accessed 10/01/2014.
- University of Reading: What is Biomimetics? <<http://www.reading.ac.uk/biomimetics/about.htm>> Date accessed: 18/04/2014.
- Vennell R., (2011). Estimating the power potential of tidal currents and impact of power extraction on flow speeds. *Renewable Energy*. Vol. 36, 3558 – 3565.
- Vennell R., (2013). Exceeding the Betz limit with tidal turbines. *Renewable Energy*. Vol. 55, 277 – 285.
- Versteeg, H., & Malalasekera W., (2007) 2<sup>nd</sup> edition. *Introduction to computational fluid dynamics: the finite volume method*. Addison-Wesley, London.
- Vu T., Retieb S., (2002). Accuracy Assessment of current CFD Tools to predict Hydraulic turbine efficiency. Hill Chart Proceedings of the 21st IAHR Symposium On Hydraulic Machinery and Systems, Lausanne.

- Wakeling J., (2001). Biomechanics of fast starting swimming in fish. *Comparative Biochemistry and Physiology*. Vol. 131, 31 – 40.
- Wang J. Piencha J., Muller N., (2012). A novel design of composite water turbine using CFD. *Journal of Hydrodynamics*. Vol. 24, 11 - 16.
- Wang S., Ingham D., Ma., Pourkashnian M., Tao Z., (2010). Numerical investigations on dynamic stall of low Reynolds number flow around oscillating airfoils. *Computers and Fluids*. Vol. 39, 1529 – 1541.
- Wang S., Yan C., Xiao F., (2012). Quantitative energy performance assessment methods for existing buildings. *Energy and Buildings*. Vol. 55, 837 – 888.
- Watanabe Y., Sato K., (2008). Functional dorsoventral symmetry in relation to lift based swimming in the Ocean sunfish *Mola mola*. *PLOS ONE*. Vol. 3, e3446.
- Watts C., Docherty J., MacRae A., McGookin E., Smith S., Souza C., Steen J., Trinder J., Vance K., Xi D. (2006). The design and construction of the submersible hybrid autonomous rover craft (SHARC). Paper presented at The Student Autonomous Underwater Challenge – Europe (SAUC-E), Faculty of Engineering, University of Glasgow, Scotland.
- WhalePower (2014). “Information on the WhalePower whale humpback technology” <<http://www.whalepower.com/drupal> > Date Accessed 03/01/2014.
- Wilcox D., (1994). *Turbulence modelling for CFD*. 2<sup>nd</sup> Edition, DCW Industries, Inc. La Canada, California.
- Wilcox D., (2008). Formulation of the k-omega Turbulence Model Revisited. *The American Institute of Aeronautics and Astronautics (AIAA)*. Vol. 46, 2823 – 2838.
- Wilga C., Lauder G., (2001). Functional morphology of the pectoral fins in bamboo sharks *Chiloscyllium plagiosum*: Benthic versus pelagic station holding. *Journal of Morphology*. Vol. 249, 195 – 209.
- Windsor S., Norris S., Cameron S., Mallinson G., Montgomery J., (2010). The flow fields involved in hydrodynamic imaging by blind Mexican cave fish (*Astyanax fasciatus*). Part I: open water and heading towards a wall. *The Journal of Experimental Biology*. Vol. 213, 3819 – 3831.
- Wu B., Zhang X., Chen J., Xu M., Li S., Li G., (2013). Design of high efficient and universally applicable of tidal stream turbine. *Energy*. Vol. 60, 187 – 194.

Yang B., Shu X., (2012). Airfoil optimisation and experimental validation in helical vertical axis turbine for power generation from marine current. *Ocean Engineering*. Vol. 42, 35 – 46.

Yuksel I., (2008). Global warming and renewable energy sources for sustainable development in Turkey. *Renewable Energy*. Vol. 33, 802 – 812.

Yuksel I., Kaygusuz K., (2011). Renewable energy sources for clean and sustainable energy policies in Turkey. *Renewable and Sustainable Energy reviews*. Vol. 51, 4132 – 4144.

Zhou C., Tan M., Gu N., Cao Z., Wang S., Wang L., (2008). The design and implementation of a biomimetic robot fish. *International Journal of Robotic Systems*. Vol. 5, 185 – 192.